Crystal and magnetic structures of multiferroics from powder diffraction data

Von der Fakultät Mathematik und Physik
der Universität Stuttgart
zur Erlangung der Würde eines
Doktors der Naturwissenschaften (Dr. rer. nat.)
genehmigte Abhandlung

vorgelegt von

Martin Etter

aus Stuttgart

Hauptberichter:	Prof. Dr. B. Keimer
Mitberichter:	Prof. Dr. P. Michler
Mitberichter:	Prof. Dr. R. E. Dinnebier
Tag der Einreichung:	24.06.2015
Tag der mündlichen Prüfung:	18.09.2015

Max-Planck-Institut für Festkörperforschung

Stuttgart, 2015

Contents

Abstract

In the present thesis, three different perovskites with potential multiferroic behavior were investigated mainly by X-ray and neutron powder diffraction methods.
Rietveld refinements of room temperature synchrotron X-ray and neutron diffraction measurements of the $Bi_{1-x}Sr_xFeO_{3-\delta}$ perovskites (with x = 0 to x = 0.5) revealed that above a composition of $x \geq 0.2$, the crystal structure can be regarded as cubic with the centrosymmetric space group $Pm\bar{3}m$, which prohibits the occurrence of proper ferroelectricity. Structural and magnetic investigations of high temperature high resolution neutron powder diffraction data showed, that the magnetic structure of the $BiFeO_3$ end member of the $Bi_{1-x}Sr_xFeO_{3-\delta}$ solid solution series must be described by a spin cycloid, whereas the $Bi_{1-x}Sr_xFeO_{3-\delta}$ perovskites above a composition of $x \geq 0.2$ possess a G-type antiferromagnetic ordering of the magnetic moments, which can be described by using a 4 times larger unit cell with the Shubnikov group I_c4/mcm (140.550) in the BNS setting. The critical Néel temperatures were determined from the temperature dependent neutron powder diffraction data and compared to the results from differential scanning calorimetry measurements.
For the $LaFeO_3$ perovskite the crystal structures of three polymorphs were determined from pressure dependent synchrotron X-ray powder diffraction measurements using four different data sets which are distinguishable by the used pressure media and the maximal applied pressure. From these data sets, two structural phase transitions at approximately 20.5(6) GPa and at approximately 38 GPa were found, where the first phase transition is of second order and the second phase transition is of first order. From Rietveld refinements it could be determined that the structural second order phase transition is a phase transition from the lower symmetric space group $Pbnm$ to the higher symmetric space group $Ibmm$. This observance was intriguingly underlined by the application of different crystallographic approaches, like e.g. the recently developed approach of rotational symmetry modes of a rigid body, which revealed that this phase transition can be described by the rotation of the FeO_6 octahedron and a shift of the lanthanum cation. For the first order phase transition it could be proved by Rietveld refinements, that this phase transition can be described by an isostructural phase transition, which can be attributed to a pressure induced high-spin ($S = \frac{5}{2}$) to low-spin ($S = \frac{1}{2}$) transition of the Fe^{3+} cation, which leads to a volume decrease of the FeO_6 octahedron and therefore to a volume drop of approximately 3% of the crystallographic unit cell. In addition to the investigation of the different phase transitions in $LaFeO_3$, sequential and parametric Rietveld refinements

were performed in order to determine the equation of state (EoS) parameters for the volume and the lattice parameters. Applying a Murnaghan EoS up to the hydrostatic limit of the pressure dependent volume gave a bulk modulus of $B_0 = 172(2)$ GPa, a first pressure derivative of the bulk modulus of $B_0' = 4.3(3)$ and a volume at ambient conditions of $V_0 = 242.87(1)$ Å^3. Corresponding values for the lattice parameters were determined by an adapted inverted Murnaghan EoS as well as by a newly developed adpated inverted third order Vinet EoS approximation.
The third and last investigated perovskite $BiCu_3Cr_4O_{12}$ was recently synthesized and belongs to the class of quadruple perovskites. The temperature dependent synchrotron X-ray powder diffraction investigations showed, that on cooling at approximately 188 K, the crystal structure becomes heavily distorted and that a reversible cubic to monoclinic phase transition from the centrosymmetric space group $Im\bar{3}$ to the centrosymmetric space group $C2/m$ takes place. Moreover, it could be shown from bond valence sum calculations that this structural phase transition is accompanied by a charge disproportionation and charge ordering of the chromium cations. Simultaneously, a paramagnetic to ferrimagnetic phase transition could be observed, which was unveiled by magnetization and magnetic susceptibility measurements.

CHAPTER 1

Introduction

Multiferroic materials (multiferroics), especially those who exhibit a strong (linear) magnetoelectric coupling between a(n) (anti-)ferromagnetic and a(n) (anti-)ferroelectric order at room temperature, are promising candidates in order to develop new magnetoelectronic devices. For instance, these devices can be used as new types of currentless magnetic field sensors [1, 2] or new types of magnetic data storages, where the magnetic bits can be written by small electric fields [2]. Besides single phase multiferroics, which exhibit a direct magnetoelectric coupling effect, different multi phase approaches are currently investigated, where the magnetoelectric coupling is indirectly mediated by e.g. strain effects [3–5]. Such a combination of piezomagnetic / magnetostricitve and piezoelectric / electrostrictive materials can be regarded as future-oriented, as the strength of the indirect magnetoelectric coupling can probably be epitaxially tailored [4–6].

Before a potential multiferroic material can be utilized in a magnetoelectric device, its structural and physical properties as well as the possible magnetoelectric coupling mechanisms have to be known in detail. Consequently, the first step in the investigation of such materials is to perform X-ray and neutron single crystal or powder diffraction measurements in order to reveal the underlying crystal and/or magnetic structure. In general, it is often more convenient to carry out such experiments using powders, as in many cases the synthesis, the handling and the required measurement geometry for such samples is much simpler compared to single crystals. Furthermore, single crystal diffraction experiments require specimens of an appropriate size, which are often not available. With respect to the simplified measurement geometry for powders, it is also more convenient to carry out *in situ* diffraction measurements, from which the behavior of multiferroic materials under different temperature and/or pressure conditions can be studied. Especially the temperature and/or pressure dependent phase transitions are of importance, as they can provide information about the onset of ferroic or even multiferroic orders [7]. Moreover, if the phase dependent crystal and magnetic structures are determined correctly, then the underlying symmetries can give crucial information about the allowed or disallowed occurrence of ferroic orders and

their potential couplings[1] [7]. Therefore a thorough characterization by diffraction methods has a high relevance.

The accepted method in order to determine crystal and/or magnetic structures from powders is the Rietveld method [10], where a least-squares algorithm is used in order to refine an artificial powder diffraction pattern, which is calculated from crystal and/or magnetic structure models, against an experimentally observed one. The parameters which are obtained from such a refinement, especially the atomic coordinates can give for instance insights in the structural changes during phase transitions. However, as the temperature and/or pressure dependent interplay between the different atoms in a crystal structure often is exceedingly complicated, different crystallographic approaches for the modeling of the atomic coordinates must be employed. These approaches constrain the different atoms either by symmetry dependent considerations or by given bond lengths and bond angles, which in many cases leads to a more intuitive description of the collective temperature and/or pressure dependent motion of the atoms.

Altogether it becomes apparent, that the micro- and macroscopic physical properties of a solid are intimately connected with the adopted crystal structure and its corresponding symmetry. Therefore diffraction experiments and in particular powder diffraction experiments are among the techniques which are at the forefront with respect to the investigation of many interesting materials including multiferroics.

In the present thesis, promising perovskite candidates with potential multiferroic behavior are investigated mainly by X-ray and neutron powder diffraction methods. In chapter 2, a description of the theoretical and experimental details of the used powder diffraction method is given. In addition, an introduction to all employed methods like the Rietveld method, symmetry modes and magnetic structure descriptions is presented, followed by a short introduction to phase transitions and ferroic and multiferroic materials.

In chapter 3, a solid solution series of $Bi_{1-x}Sr_xFeO_{3-\delta}$ is investigated *in situ*, in order to shed light on the temperature dependent structural and magnetic properties of these perovskites, by determining the crystal and magnetic structures from synchrotron X-ray and neutron powder diffraction measurements. Furthermore the antiferromagnetic to paramagnetic phase transition is explored in detail by temperature dependent neutron powder diffraction and differential scanning calorimetry measurements.

In chapter 4, an *in situ* high pressure synchrotron X-ray powder diffraction study of

1 A prominent example for such a symmetry dependent prediction is for instance given by the $BiFeO_3$ perovskite, where the symmetry of the long-range spin cycloid prohibits a linear magnetoelectric coupling [3, 4, 8, 9].

the $LaFeO_3$ perovskite is carried out, where besides the structural investigations along the room temperature isotherm, different crystallographic approaches with respect to the modeling of the atomic coordinates were tested, in order to give a comprehensive picture of the pressure induced structural phase transitions. In addition, the bulk modulus and corresponding values for the lattice parameters of the $LaFeO_3$ perovskite are determined from a Murnaghan equation of state (EoS) and a newly developed inverted third order Vinet EoS approximation.

In chapter 5, a recently synthesized $BiCu_3Cr_4O_{12}$ quadruple perovskite is structurally analyzed by *in situ* temperature dependent synchrotron X-ray powder diffraction measurements. The occurring structural low temperature phase transition, which is accompanied by a charge disproportionation, charge ordering effects and a paramagnetic to ferrimagnetic transition is characterized in detail by bond valence sum calculations as well as magnetization, magnetic susceptibility and electric resistivity measurements.

CHAPTER 2

Theoretical and experimental basics

Excerpts of the sub-chapters "2.1 Basics and History of Powder Diffraction" and "2.2 The Rietveld Method" are published with additional information of the entire history of powder diffraction in the manuscript: "*M. Etter & R.E. Dinnebier - A Century of Powder Diffraction: a Brief History*" [11].

2.1 Basics and history of powder diffraction

Early experiments with light were already carried out by the Greek philosophers [12], although it is believed that the Italian Francesco Maria Grimaldi (1618-1663) was the first who investigated the diffraction of light more rigorously. In his book "Physico mathesis de lumine, coloribus, et iride, aliisque annexis libri duo" from 1665 which was published after his death, he described the shape of a light cone, after the light has passed through a pinhole [13]. In fact, he was also the first who used the term "diffraction" in order to name the physical properties of his light scattering experiments.

Over the centuries, the investigation and description of light was a quite continuous development, as just the narrow spectral range of visible light was accessible (The infrared spectral range and the ultraviolet spectra range were discovered rather late by Friedrich Wilhelm Herschel (1738-1822) around 1800 and Johann Wilhelm Ritter (1776-1810) in 1801, respectively). This changed dramatically in 1895, when Wilhelm Conrad Röntgen (1845-1923) discovered his "X-rays", while he was experimenting with discharge tubes [14, 15]. This new kind of rays rapidly attracted the interest of a lot of researchers and for almost two decades there was a debate among them whether these new rays consist of particles or electromagnetic waves.

In 1912, Walter Friedrich (1883-1968), Paul Knipping (1883-1935) and Max von Laue (1879-1960) conducted their famous X-ray diffraction experiment, in which they produced a single crystal diffractogram by irradiating a copper sulfate crystal with the (polychromatic) light from a X-ray tube [16–19]. With this experiment they could

prove two physical principles at once: first of all that a single crystal is built by regular blocks (which is a required condition that diffraction effects can occur) and secondly that the X-rays are waves with a wavelength on the order of the distances between the building blocks of the crystal [11, 20, 21]. In fact, the idea for the experiment is ascribed to von Laue who also gave the first theoretical description of the observed phenomenon [16–18, 20–22]. In the theoretical part of their jointly publication [16–18], von Laue introduced the famous equations which are named after him:

$$\vec{a} \cdot (\vec{s} - \vec{s}_0) = h \cdot \lambda \quad , \tag{2.1}$$

$$\vec{b} \cdot (\vec{s} - \vec{s}_0) = k \cdot \lambda \quad , \tag{2.2}$$

$$\vec{c} \cdot (\vec{s} - \vec{s}_0) = l \cdot \lambda \quad . \tag{2.3}$$

Here, $\vec{s}_0$ is the unit vector of the primary beam, $\vec{s}$ is the unit vector of the scattered beam, h,k,l are the Miller indices, $\vec{a}, \vec{b}, \vec{c}$ are the primitive lattice vectors and λ is the wavelength. Due to the usage of unit vectors for the incident and the outgoing beam, the scalar product of a primitive lattice vector with a beam vector, reduces to a projection of the primitive lattice vector (which is equal to the distance of two points) onto the beam vector. For constructive interference the difference between the two projections must be equal to a multiple of the wavelength (see figure 2.1a). For a crystal structure in three dimensions diffraction occurs, if all three Laue equations are fulfilled simultaneously.

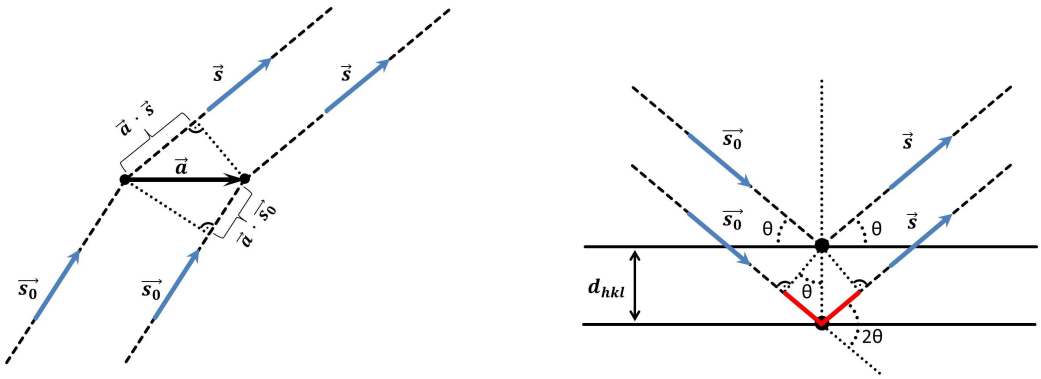

(a) Laue picture **(b)** Bragg picture

Figure 2.1: Visualization of the a) Laue equation and the b) Bragg equation with two point scatters. For the Bragg equation the optical path which must be a multiple of the wavelength is shown in red. Please note that the visualization of the Bragg equation is only a simple representation as the point scatters can lie anywhere on the lattice planes as they must not necessarily lie above each other [23, 24].

Already in the same year of the discovery of Friedrich, Knipping and von Laue, another mathematical description of the diffraction condition was given by Sir William Lawrence Bragg (1890-1971) who published his own equation [25], which is equivalent

to the Laue equations:

$$2 \cdot d_{hkl} \cdot \sin\theta = n \cdot \lambda \quad . \tag{2.4}$$

The geometrical interpretation of this equation is similar to the interpretation of the Laue equations. If the sine of the scattering angle θ multiplied by the doubled lattice plane spacing d_{hkl} is equal to a multiple of the wavelength λ (n is a positive integer), then diffraction occurs (see figure 2.1b)).

Although Bragg's and von Laue's description are equivalent, nowadays Bragg's equation is often preferred, due to its natural linkage of the lattice plane spacing d which is a function of the lattice parameters $a, b, c, \alpha, \beta, \gamma$ of the unit cell and the Miller indices h, k, l with the scattering angle θ and the wavelength λ.

In addition to the Laue equations, von Laue gave in his milestone publication from 1912 also an equation for the structure factor amplitude F [16–18], which is required for the calculation of the intensity of a h,k,l-dependent Bragg reflection. The calculation of the complex structure factor F depends on an individual atomic form factor f, the Miller indices h, k, l and the relative atomic coordinates x, y, z of each atom n in the unit cell:

$$F_{hkl} = \sum_n f_n \cdot e^{2\cdot\pi\cdot i\cdot(h\cdot x_n + k\cdot y_n + l\cdot z_n)} \quad . \tag{2.5}$$

Mathematically, the structure factor is the Fourier transform of the convolution between the real space lattice and a motif, which is in the case of X-ray diffraction the distribution of the electron density in the unit cell and in the case of neutron diffraction the distribution of the atomic nuclei in the unit cell. Owing to the fact that the structure factor is a Fourier transform, many properties of diffraction can be in general predicted, like the invariance of the diffracted pattern if the convoluted lattice with the motif is translated. This is an important statement as it implies that there is no need to define an artificial origin of the investigated crystal. Another important property of the Fourier transform is that the measured peak width is directly correlated with the number of unit cells which build the real space lattice. If the number of unit cells which contribute to the diffraction in three dimensions is very small, the Fourier transform will give a broader peak width. In contrast, if the number of unit cells in all three directions is high the experimental peak width is no longer dominated by size effects of the crystal and other effects come to the fore.

In order to calculate the intensity I of a h,k,l-dependent Bragg reflection, the square of the absolute value of the structure factor or equivalently the multiplication of the structure factor with its complex conjugate needs to be build. This product of the structure factor and its complex conjugate is proportional to the intensity:

$$I_{hkl} \propto F_{hkl} \cdot F^*_{hkl} = |F_{hkl}|^2 \quad . \tag{2.6}$$

In general, equations 2.5 and 2.6 are valid for crystal structures infinitely extended in three dimensions. Nevertheless, they are sufficient approximations for finite crystals and they are even applicable to nanocrystals which can have a spatial extent of only a few nanometers. But how can the diffracted intensity be calculated if the crystal is no longer built by regular building blocks? For example for amorphous compounds or even for liquids where the atoms or molecules can occupy all possible orientations? It is obvious that the deficit of regular building blocks with well-defined unit cells automatically leads to the loss of symmetry as without a unit cell no suitable coordinate system can be established and with this also no relative atomic coordinates for atoms or molecules can be given. This issue was addressed in 1915, when Peter Debye (1884-1966) published an article about the dispersion of X-rays [26]. In his work he considered an amorphous compound where a molecule or polyatomic ions can take all possible orientations in space. He realized that the diffracted intensity of such a compound depends only on the distance r_{mn} between two individual point scatterers m and n within or between the molecules and the scattering vector k[1]. Taking into account that all intra- and inter-molecular distances must be considered and that the electronic distribution of an individual point scatterer is given by the atomic form factor f, it is possible to modify the original double sum equation of Debye to obtain the commonly known Debye scattering equation:

$$I_{eu} = \sum_m \sum_n f_m \cdot f_n \cdot \frac{\sin k \cdot r_{mn}}{k \cdot r_{mn}} \quad . \tag{2.7}$$

In this representation of the Debye scattering equation the intensity is calculated in electronic units and it is possible to apply this equation to "gases, liquids, amorphous solids and crystalline powders" [27].

Looking at the scientific interests of Peter Debye and his particular interest into the scattering of X-rays from particles, it is quite obvious that he was also involved in one of the first powder diffraction experiment in 1916. Although as early as in 1913 Walter Friedrich in Germany [28] and Shoji Nishikawa (1884-1952) and S. Ono in Japan [29] carried out X-ray diffraction experiments with powders, they were not able to give the correct explanation for the diffraction rings which they saw because at that time they were not aware of the spectrum of their X-ray source [11]. As a consequence it took another three years, until Peter Debye and Paul Scherrer (1890-1969) could use the knowledge of characteristic X-rays in order to explain the occurrence of diffraction rings when they investigated lithium fluoride powder [30]. Astonishingly almost at the same time, on the other site of the Atlantic Ocean, Albert Wallace Hull (1880-1966) conducted a powder X-ray diffraction experiment with iron powder and he found the same explanations as Debye and Scherrer did before [31]. But in contrast to Debye and Scherrer the experimental setup of Hull was much more sophisticated as he was using one of the first monochromators with a zirconium filter in order to suppress the

1 The length k of the scattering vector $\vec{k}$ is defined as $k = \frac{4 \cdot \pi \cdot \sin\theta}{\lambda}$ [27].

characteristic K_β radiation and most of the unwanted Bremsstrahlung background of his molybdenum X-ray tube [31]. The diffraction patterns which Debye, Scherrer and Hull recorded were already looking very similar to the simulated powder diffraction patterns in figures 2.2c)+d).

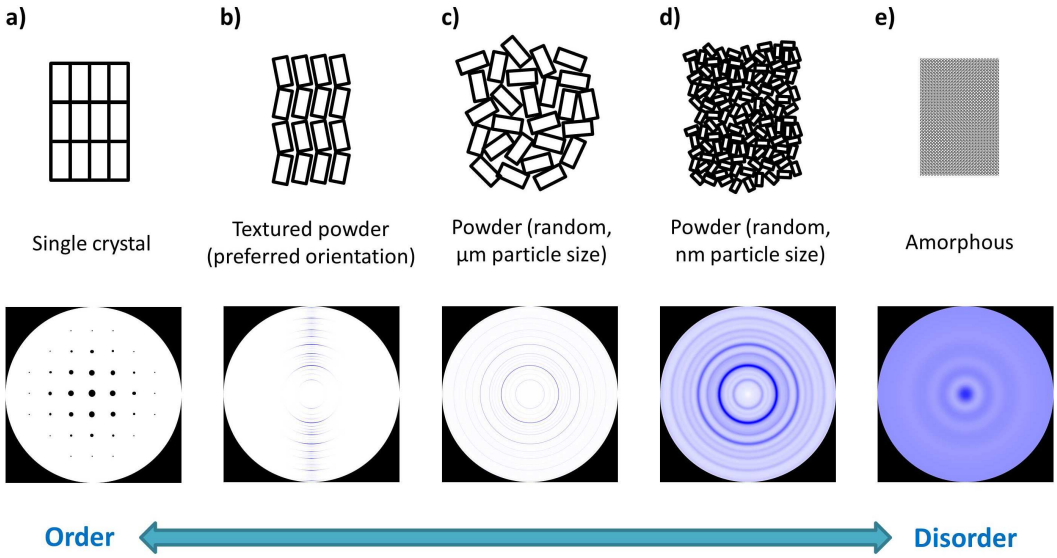

Figure 2.2: Simulated two-dimensional diffraction patterns of different types of crystalline materials. From left to right the evolution of these patterns is shown, when a single crystal is crushed and the disorder is increased. a) Diffraction pattern of a single crystal. b) Diffraction pattern of a textured powder with preferred orientation. c) Diffraction pattern of a powder with particles in micrometer size and d) in nanometer size. e) Diffraction pattern of an amorphous material (also valid for gases and liquids).

A descriptive interpretation of the Laue equations was given by Paul Peter Ewald (1888-1985) in 1913, when he introduced the concept of the Ewald sphere [32]. In this illustration of a reciprocal space lattice the diffraction condition can be easily graphically evaluated (see figure 2.3a)). In order to find the hkl values which fulfill the diffraction condition, the incident wave vector $\vec{s}_0$ has to be drawn in a reciprocal space lattice in that way, that the vector ends at the origin of the reciprocal space lattice. The direction of the incident wave vector is given by the experimental setup and the length of the vector is given by the reciprocal value of the wavelength. Subsequently the Ewald sphere is drawn by taking the value of the reciprocal wavelength as the radius with the starting point of the incident wave vector as the center of the sphere. The Laue conditions and therefore constructive interference are now fulfilled for all reciprocal lattice points hkl which lie on the surface of the Ewald sphere. To such a reciprocal lattice point it is possible to draw the outgoing wave vector $\vec{s}$ with the same length as for the incoming wave vector $\vec{s}_0$. The difference between the outgoing wave vector and the incoming wave vector gives the scattering vector $\vec{h}$.

$$\vec{h} = \vec{s} - \vec{s}_0 \quad . \tag{2.8}$$

However, the construction of the Ewald sphere does not solely provide information about physical values in reciprocal space like scattering vectors and reciprocal lattice points. If an equivalent description of the Bragg equation is taken, it is possible to give a geometrical interpretation of the angle between the incoming and the outgoing wave vector in real space. Such an equivalent description or variation of the Bragg equation is given by:

$$\frac{2 \cdot \sin\theta}{n \cdot \lambda} = \frac{1}{d} = |\vec{h}| \quad . \tag{2.9}$$

Without loss of generality, it can be shown that for constructive interference the scattering vector $\vec{h}$ must be equal to a reciprocal lattice vector $\vec{d^*_{hkl}}$ and that $|\vec{d^*_{hkl}}| = \frac{1}{|\vec{d}_{hkl}|}$ and $\vec{d} \parallel \vec{d^*}$. In the case of the Ewald construction, the multiple n of the wavelength can be set to 1, as the definition from above requires that the length of the incoming and outgoing wave vector is $\vec{s} = \vec{s}_0 = \frac{1}{\lambda}$. With this rewritten Bragg equation it is possible to derive a real space interpretation of the angle 2θ (see figure 2.3a)). This shows remarkably the power of the Ewald construction as it provides direct access to the real space diffraction angle 2θ which is required to position a detector in order to measure the diffracted intensity of a certain hkl reflection.

Although the explanation above seems to be only valid for the case of single crystal diffraction, it can be also used to explain the occurrence of diffraction rings in powder diffraction. In figure 2.3b) the effect is shown if a crystal is turned during the measurement or alternatively if a powder with all kind of orientations of the crystal structure is measured. In a static experiment it is only possible to measure the hkl reflections which lie directly on the surface of the Ewald sphere. If other hkl reflections shall be measured, the single crystal has to be turned until the corresponding reciprocal lattice points hits the surface of the Ewald sphere. A powder diffraction experiment is therefore comparable to a single crystal experiment at which the data integration is performed continuously while the single crystal is rotated in three dimensions. In such a dynamical diffraction experiment all reciprocal lattice points will hit the Ewald surface at a certain point in time. In contrast to that, the grains in a powder already have all possible orientations and therefore they contribute to the diffraction pattern at the same time giving the same smearing effect of the reciprocal lattice points onto the surface of a sphere as for a dynamic single crystal experiment. Consequently, this smearing of a reciprocal lattice point onto the surface of a sphere leads not only to the reduction in dimensionality (from three dimensions to one dimension; mathematically this is a projection: $\vec{d^*_{hkl}} \rightarrow |\vec{d^*_{hkl}}|$), but also to many other effects like systematic and accidental reflection overlaps which will be described later.

In figure 2.3 the evolution of a diffraction pattern of a single crystal which is split into smaller and smaller pieces is exemplary shown. In figure 2.2a) the diffraction of a single crystal gives sharp reflection spots, whereas in figure 2.2b) a crystal consisting

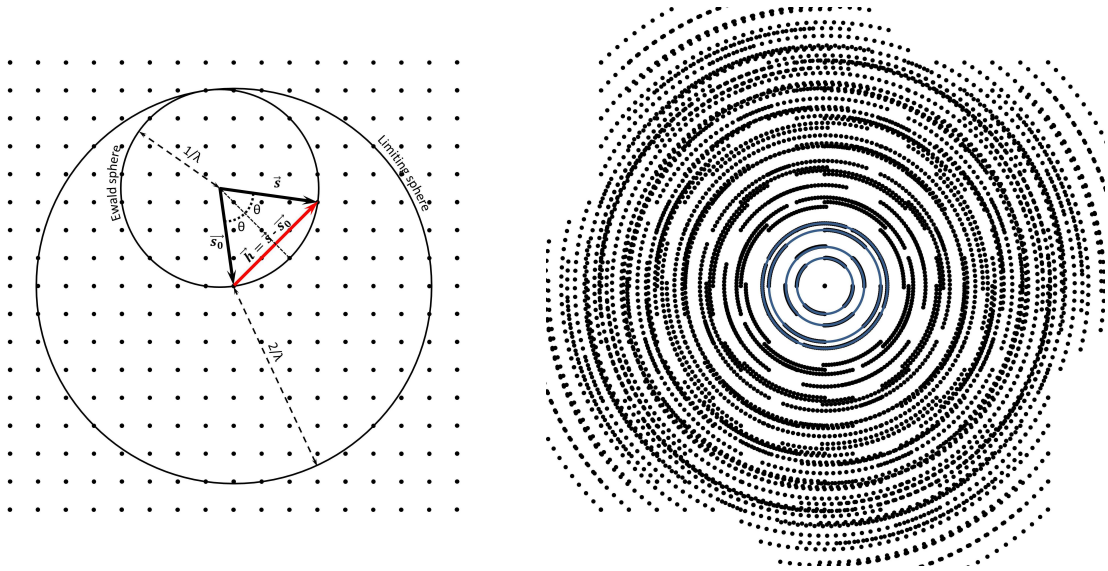

(a) Ewald construction: single crystal

(b) Ewald construction: powder

Figure 2.3: a) Two-dimensional projection of the reciprocal space lattice with the Ewald sphere and the limiting sphere (the limiting sphere determines the maximal reachable hkl values in a powder diffraction experiment). The radius of the limiting sphere is given by $\frac{2}{\lambda}$ (therefore the maximum reachable d_{hkl} value is given by $d_{hkl} = \frac{\lambda}{2}$). Please note that the incoming beam within the Ewald sphere does not necessarily start at a reciprocal lattice point. b) 24 single crystal diffraction patterns each rotated by an angle of 2°. It is obvious that in a powder where ideally all possible orientations of crystal grains exist, the single spots in 2 dimensions will merge into a continuous diffraction ring, which becomes a continuous diffraction sphere in 3 dimensions.

of different grains (=polycrystalline) with preferred orientation of these grains shows a smearing effect of the reciprocal lattice points. In the case of a powder (figure 2.2c)) where the grains are of micrometer size and where they ideally obtain all possible orientations a smearing of the reciprocal lattice points to a circle or diffraction ring can be observed. In general, these diffraction rings are cut projections of so called Debye-Scherrer cones (see figure 2.4 for a three-dimensional view of the optical path of the diffracted rays), which in turn are originating from cut projections through the above mentioned surface of the sphere which arises due to the smearing of the reciprocal lattice points. If the powder particles are further split into nanoparticles a severe broadening[1] of the diffraction rings can be observed (see figure 2.2d)). Finally the material becomes completely amorphous and the diffraction rings pass over to a halo effect (see figure 2.2e)).

1 The broadening due to the particle size can be modeled by the Scherrer equation: $\mathrm{FWHM}(2\theta) = \frac{K \cdot \lambda}{L \cdot \cos\theta}$, where $\mathrm{FWHM}(2\theta)$ is the full width half maximum for a given diffraction angle θ, K is the Scherrer constant which is almost equal to 1, λ is the used wavelength and L is the particle size [33].

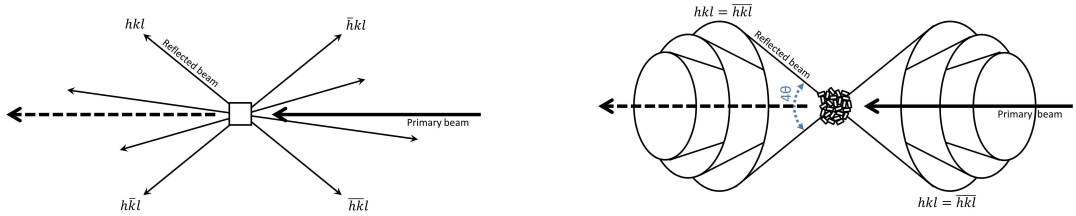

(a) Single crystal diffraction **(b)** Powder diffraction

Figure 2.4: Diffracted X-rays of a a) single crystal specimen and diffracted X-rays in b) Debye-Scherrer cones for a powder sample. The Debye-Scherrer rings result from a cut projection of the spheres which arise due to the smearing of reciprocal lattice points onto different spheres in reciprocal space. The cone shape is simply given by the propagation of the radiation.

Originating from the different appearances between the diffraction patterns of single crystals with single observable reciprocal lattice points and the diffraction patterns of powders with diffraction rings, the subsequent treatment of the acquired data is different. In both cases the possible hkl values have to be assigned to either the individual reciprocal lattice points or to the diffraction rings (normally the two-dimensional powder diffraction patterns are integrated along circles into a one-dimensional powder diffraction pattern as the intensity is a function of the radius and therefore no information will be lost during this integration. This argument becomes also clear by taking care of the above described reduction in dimensionality). From figure 2.5 it is obvious that this is a challenging task in the powder case, as the smearing of the reciprocal lattice points leads to different kinds of information losses. For instance, in the single crystal case the full three-dimensional measurement of reciprocal space provides the entire information about the kind of the reciprocal lattice and the individual intensities at the reciprocal lattice points from which the real space lattice and the Laue group can be deduced (because of the Fourier transform the single crystal diffraction pattern has always an inversion symmetry and therefore two reciprocal lattice points with the same intensity exist, the commonly known Friedel pairs). In contrast for the powder case, the information of the Laue group and also of the real space lattice is lost, as the intensities of radially symmetric equivalent reciprocal lattice points are merged into a single intensity and with this all orientation information is gone (e.g. reciprocal lattice points 100 and 001 in figure 2.5 are radially symmetric equivalent). The number of radially symmetric equivalent reciprocal lattice points which merge into a single reflection depends on the Laue group and is called reflection multiplicity (if the symmetry is known the reflection multiplicity as a systematic overlap can be easily treated, as it is just a multiple of the reflection intensity). Besides the reflection multiplicity a second systematic overlap of reflections can be observed. For example, if different independent hkl values lead to the same d_{hkl} value a systematic overlap occurs as can be seen e.g. for the (500) reflection and the (340) reflection for a cubic crystal structure in figure 2.5. The last possible overlap of reflections is occasional

or accidental. For instance if two reflections are very close in reciprocal space, broad peaks can merge into a single peak and cannot be any longer distinguished. This phenomenon can be often observed for high values of the measured 2θ range, where different reflections often come very close.

In addition to the reflection multiplicity and the systematic overlap, peak broadening and also the estimated standard deviation in each measurement of the angle 2θ is a severe problem which often makes it difficult to find the right indexing for a powder diffraction pattern. For instance the error (= estimated standard deviation) which arises in the determination of the correct d_{hkl} due to a shift of the 2θ value can be estimated by the curves in figure 2.6.

In order to find the correct indexing values for each Bragg reflection, the following indexing equation must be solved:

$$\frac{1}{d_{hkl}^2} = d_{hkl}^{*2} = h^2{\cdot}a^{*2}+k^2{\cdot}b^{*2}+l^2{\cdot}c^{*2}+2{\cdot}h{\cdot}k{\cdot}a^*{\cdot}b^*{\cdot}\cos\gamma^*+2{\cdot}h{\cdot}l{\cdot}a^*{\cdot}c^*{\cdot}\cos\beta^*+2{\cdot}k{\cdot}l{\cdot}b^*{\cdot}c^*{\cdot}\cos\alpha^* \quad . \tag{2.10}$$

This equation is the general equation for the triclinic case and simplifies in case of higher symmetries. This equation follows from equation 2.17 from table 2.1, if the relationships between direct and reciprocal lattice parameters from equations 2.18-2.24 of table 2.2 are used. In theory, the general triclinic case needs at least six independent observed d_{hkl} values in order to index the diffraction pattern and to find the correct reciprocal lattice parameters $a^*, b^*, c^*, \alpha^*, \beta^*, \gamma^*$. However, if there is a mentionable uncertainty of each of this six measured d_{hkl} values, it is almost impossible to find the correct reciprocal lattice parameters. Due to this reason, reliable indexing results of most of the computer algorithms used today can be obtained by providing more d_{hkl} values (usually between 20 and 30 values at all) than mathematically required. In the following, a short overview of different historic and modern algorithms is given.

In 1917, C. Runge proposed the first considerable approach for the systematic indexing of powder diffraction patterns [34]. Publications of T. Ito in 1949 [35] and of P.M. de Wolff in 1957 [36] enhanced this concept until in 1969 J.W. Visser published a computer program (nowadays known as "ITO" program) based on these concepts [37]. In general, the Runge-Ito-de Wolff method implemented by Visser is a zone[1] indexing algorithm which is very powerful for the indexing of powder diffraction patterns with lower symmetries [38, 39]. Another algorithm of that time is the one proposed by P.E. Werner in 1964 [40]. This method is a semi-exhaustive trial-and-error method where the Miller indices for the observed diffraction lines are permuted [39, 41]. The corresponding computer program is "TREOR". Another computer algorithm based on the successive dichotomy method was developed by D. Louër and M. Louër in 1972 [42]. Later the computer program was named "DICVOL" and was expanded to include

1 A crystallographic zone is a family of planes which have parallel cutting edges. The direction of the cutting edges is known as zone axis.

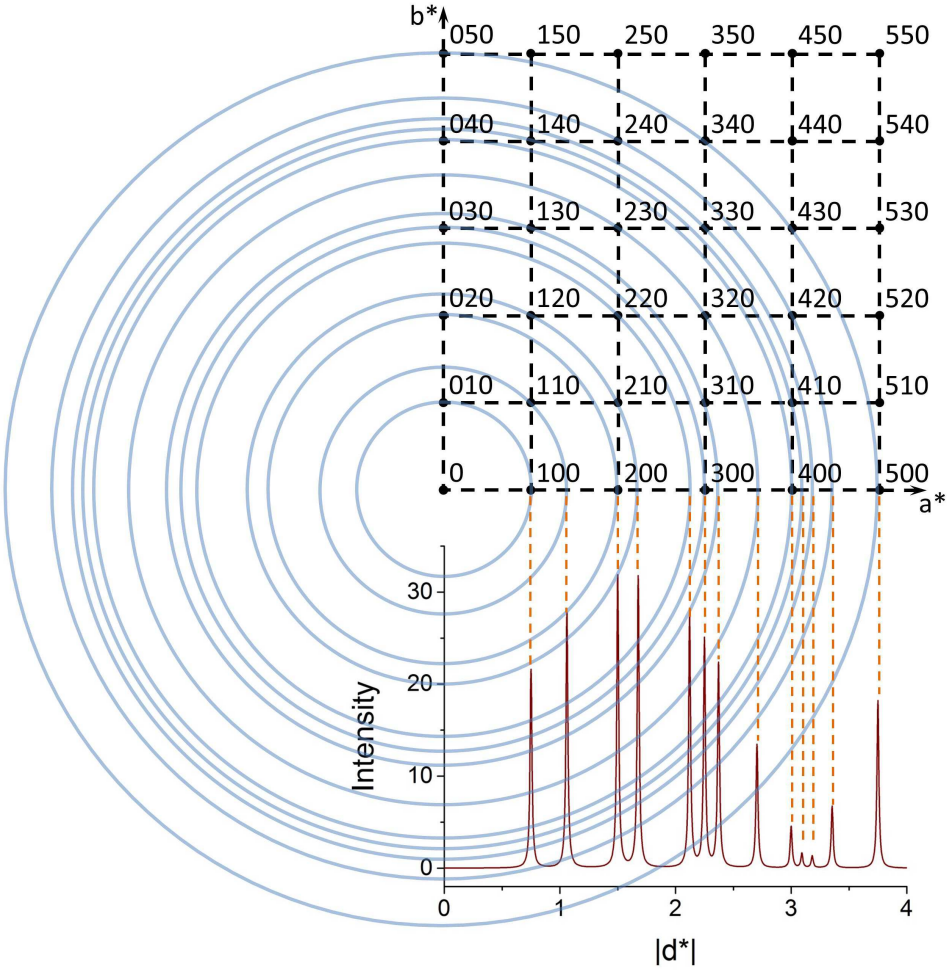

Figure 2.5: Cubic reciprocal lattice where the reciprocal lattice points are continuously smeared onto the surfaces of different spheres. If these spheres are arbitrarily cut through the center, continuous two-dimensional powder diffraction rings can be observed. Another cut projection through the center of the diffraction rings gives the one-dimensional powder diffraction pattern (In an experiment normally the one-dimensional powder diffraction pattern are obtained by the integration of the rings along a cut which is perpendicular to the rings). Indexing of the single peaks in this powder diffraction pattern can be done by following the orange dashed lines and then by following the corresponding lines of the circle to the reciprocal lattice points. Please note that for instance the reciprocal lattice points 100 and 001 merge into a single peak (this is the case of reflection multiplicity) as well as the reciprocal lattice points 500 and 340 merge into a single peak (this is the case of systematic overlap of reflections).

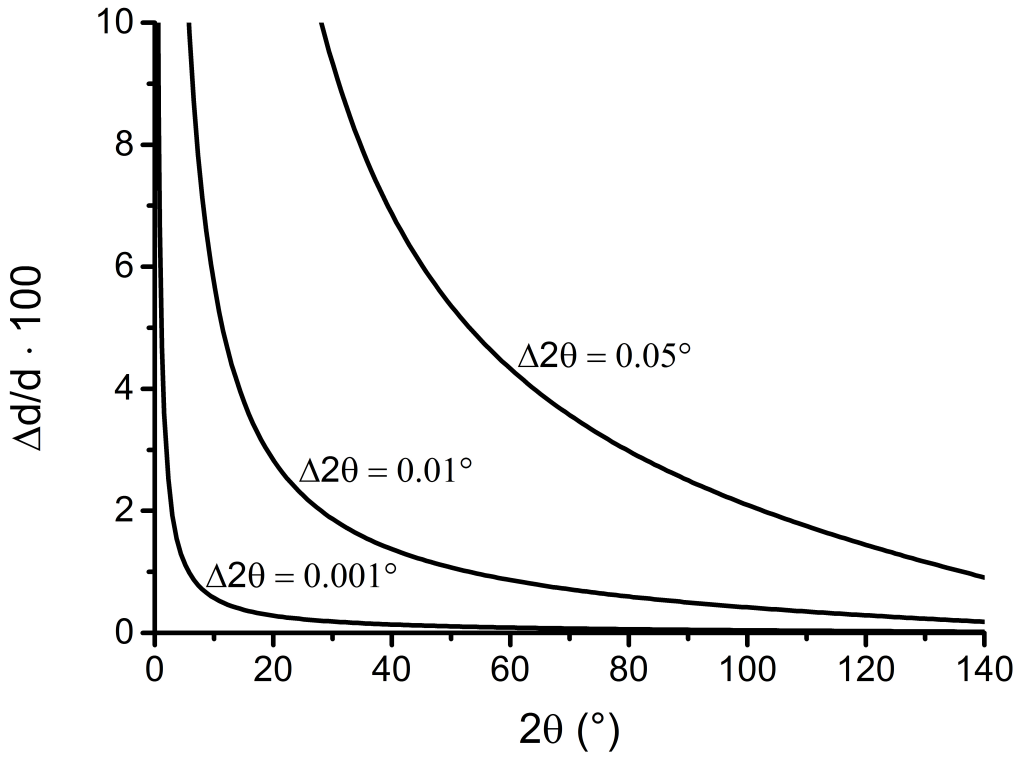

Figure 2.6: The deviation of the scattering angle by a constant angular misalignment leads to different percentage errors for the obtained $\frac{\Delta d}{d}$ values as can be seen by the different curves. For instance a misalignment of $\Delta 2\theta = 0.01°$ for a measured peak at $2\theta = 20°$ and at a wavelength of $\lambda = 1.54059$ Å leads to an error (= estimated standard deviation) in d of $\Delta d = 0.057$ Å. The curves can be calculated through the equation $\left|\frac{dd_{hkl}}{d_{hkl}}\right| \approx \frac{d\theta}{\tan\theta}$ which follows from the total differential of the Bragg equation [24].

monoclinic [43] and triclinic symmetries [44]. This method varies the cell parameters in direct space and tries to reduce the possible solution space [39, 41]. In addition to these algorithms meaningful figure of merits (FOM) were given by P.M. de Wolff in 1968 with the M_{20}-FOM [45] and by G.S. Smith and R.L. Snyder in 1979 with the F_N-FOM [46] which allowed the judgment of the quality of the calculated unit cell parameters.

Several other indexing programs were developed in recent time. Examples for indexing algorithms which use direct space approaches are for instance approaches with genetic algorithms [47] or Monte Carlo approaches like the indexing by singular value decomposition [48] or the McMaille approach [49].

Additionally, some of the indexing programs used nowadays also suggest probable

space groups by checking the pattern for systematically absent reflections (there is no possibility to determine all space groups unambiguously as some of them obey the same extinction rules).

Table 2.1: Equations for the calculation of the d_{hkl} values dependent on the real space unit cell parameters for the different crystal systems (from [39, 50]).

System	$1/d_{hkl}^2$
Cubic	$\frac{h^2+k^2+l^2}{a^2}$ (2.11)
Tetragonal	$\frac{h^2+k^2}{a^2}+\frac{l^2}{c^2}$ (2.12)
Orthorhombic	$\frac{h^2}{a^2}+\frac{k^2}{b^2}+\frac{l^2}{c^2}$ (2.13)
Hexagonal and trigonal (P)	$\frac{4}{3\cdot a^2}\cdot\left(h^2+k^2+h\cdot k\right)+\frac{l^2}{c^2}$ (2.14)
Trigonal (R)	$\frac{1}{a^2}\cdot\left(\frac{(h^2+k^2+l^2)\cdot\sin^2\alpha+2\cdot(h\cdot k+h\cdot l+k\cdot l)\cdot(\cos^2\alpha-\cos\alpha)}{1+2\cdot\cos^3\alpha-3\cdot\cos^2\alpha}\right)$ (2.15)
Monoclinic	$\frac{h^2}{a^2\cdot\sin^2\beta}+\frac{k^2}{b^2}+\frac{l^2}{c^2\cdot\sin^2\beta}-\frac{2\cdot h\cdot l\cdot\cos\beta}{a\cdot c\cdot\sin^2\beta}$ (2.16)
Triclinic	$\left[\frac{1}{1-\cos^2\alpha-\cos^2\beta-\cos^2\gamma+2\cdot\cos\alpha\cdot\cos\beta\cdot\cos\gamma}\right.$ $\cdot\left(\frac{h^2}{a^2}\cdot\sin^2\alpha+\frac{k^2}{b^2}\cdot\sin^2\beta+\frac{l^2}{c^2}\cdot\sin^2\gamma+\frac{2\cdot h\cdot k}{a\cdot b}\cdot(\cos\alpha\cdot\cos\beta-\cos\gamma)\right.$ (2.17) $\left.\left.+\frac{2\cdot h\cdot l}{a\cdot c}\cdot(\cos\alpha\cdot\cos\gamma-\cos\beta)+\frac{2\cdot k\cdot l}{b\cdot c}\cdot(\cos\beta\cdot\cos\gamma-\cos\alpha)\right)\right]$

Table 2.2: Relations between the real/direct space lattice parameters and the reciprocal space lattice parameters. Further relations can be found in [50].

$$a^* = \frac{1}{V} \cdot \mid \vec{b} \times \vec{c} \mid = \frac{b \cdot c \cdot \sin\gamma}{V} \tag{2.18}$$

$$b^* = \frac{1}{V} \cdot \mid \vec{a} \times \vec{c} \mid = \frac{a \cdot c \cdot \sin\beta}{V} \tag{2.19}$$

$$c^* = \frac{1}{V} \cdot \mid \vec{a} \times \vec{b} \mid = \frac{a \cdot b \cdot \sin\alpha}{V} \tag{2.20}$$

$$\cos\alpha^* = \frac{\cos\beta \cdot \cos\gamma - \cos\alpha}{\sin\beta \cdot \sin\gamma} \tag{2.21}$$

$$\cos\beta^* = \frac{\cos\alpha \cdot \cos\gamma - \cos\beta}{\sin\alpha \cdot \sin\gamma} \tag{2.22}$$

$$\cos\gamma^* = \frac{\cos\alpha \cdot \cos\beta - \cos\gamma}{\sin\alpha \cdot \sin\beta} \tag{2.23}$$

$$V = a \cdot b \cdot c \cdot \sqrt{1 - \cos^2\alpha - \cos^2\beta - \cos^2\gamma + 2 \cdot \cos\alpha \cdot \cos\beta \cdot \cos\gamma} \tag{2.24}$$

2.2 The Rietveld method

The method of choice in order to fit an entire one-dimensional powder diffraction pattern by the refinement of crystal structures is a structure based whole powder pattern fitting (WPPF) method developed by Hugo Rietveld in the late 1960s. This method, nowadays known as the Rietveld refinement method or just Rietveld method, uses a least-squares algorithm in order to refine a calculated powder diffraction pattern against an experimentally observed powder diffraction pattern.
In 1966, Hugo Rietveld made the first successful attempt to use a least-squares algorithm to refine directly the background corrected integrated intensities of X-ray and neutron powder patterns [51]. Although this first attempt was not well recognized by the crystallographic community, he continued his work and one year later he published the first WPPF analysis of tungsten trioxide, where he could show, that even a severe peak overlap of reflections can be treated by his refinement algorithm [52]. Finally in 1969, Hugo Rietveld published one of the most cited scientific articles in crystallography, where he demonstrated that with a powerful computer a WPPF can be performed with almost all important parameters which determine a crystal structure like lattice parameters, atomic positions, components of a magnetic vector, etc. [10] (for a full list see also [11]). However, within the first eight years, the Rietveld method was solely applied to neutron powder diffraction due to the simplicity of the obtained peak shapes (neutron powder diffraction peak shapes can be satisfactory modeled by the assumption of a simple Gaussian peak shape). After this period, in 1977, three different groups published nearly simultaneously Rietveld refined X-ray powder diffraction patterns by the application of more sophisticated peak shapes [53–55].

Although the basis of the Rietveld method was laid almost 50 years ago, the mathematical description remains unchanged. In general, a refinement of a crystal structure by a least-squares minimization between the calculated and observed powder diffraction pattern can be done by the following equation [10]:

$$Min = \sum_{2\theta_i} \left(Y_{obs}(2\theta_i) - Y_{calc}(2\theta_i)\right)^2 \quad , \tag{2.25}$$

where Min is the desired global minimum of the refinement, Y_{obs} is the experimentally observed powder diffraction pattern and Y_{calc} is the calculated diffraction pattern for which a detailed description is given below. Normally the 2θ space is a continuum, but due to the data collection procedure the 2θ space is discretized, which is denoted by the running index i whose integer value reflects the current data point.
Usually, equation 2.25 is modified with a weighting factor w in order to guarantee that peaks with a high intensity are not overestimated [10]:

$$Min = \sum_{2\theta_i} w(2\theta_i) \left(Y_{obs}(2\theta_i) - Y_{calc}(2\theta_i)\right)^2 \quad , \tag{2.26}$$

where the weighting w is e.g. given by $w(2\theta_i) = \frac{1}{Y_{obs}(2\theta_i)}$ assuming Poisson statistics [56].
Besides the weighting with the inverse observed intensity, other weighting schemes can be chosen. For instance in the TOPAS software [57] and in some textbooks [58], a weighting factor w with the inverse of the squared variance of the observed intensity is chosen (while it is assumed that all covariances between different observed intensities are zero [58]):

$$w(2\theta_i) = \frac{1}{\left(\sigma\left(Y_{obs}(2\theta_i)\right)\right)^2} \quad , \tag{2.27}$$

where $\sigma\left(Y_{obs}(2\theta_i)\right)$ denotes the variance (which is often simply the square-root of the estimated standard deviation/error of the measurement) of the experimentally observed intensity. Please note that Rietveld already stated in his publication from 1969, that if the variance of the observed intensity from counting statistics is equal to the observed intensity, then the weighting scheme becomes equal to the weighting with the inverse observed intensity (if not the squared variance is used as above in equation 2.27) [10].

The above described calculated intensity is given by the following equation:

$$Y_{calc}(2\theta_i) = \sum_p S_p \sum_{\{h,k,l\}_p} \left(\left|F_{calc}\left(\{h,k,l\}_p\right)\right|^2 \cdot \Phi_{\{h,k,l\}_p}\left(2\theta_i - 2\theta_{\{h,k,l\}_p}\right) \cdot Corr_{\{h,k,l\}_p}(2\theta_i) \right) + Bkg(2\theta_i) \tag{2.28}$$

where S_p is a phase p dependent scale factor, $\{h,k,l\}_p$ denotes a tupel of three Miller

indices which depend on the phase p, $F_{calc}\left(\{h,k,l\}_p\right)$ is the structure factor of a certain phase dependent Bragg reflection, $\Phi_{\{h,k,l\}_p}\left(2\theta_i - 2\theta_{\{h,k,l\}_p}\right)$ is the normalized peak profile at the peak position $2\theta_{\{h,k,l\}_p}$, $Corr_{\{h,k,l\}_p}(2\theta_i)$ is a product of different correction functions, which depend on the Bragg reflection and/or the discrete $2\theta_i$ value and finally $Bkg(2\theta_i)$ is the background which is normally fitted by point interpolation or polynomials.

In addition to the minimization equations 2.25 and 2.26 the least-squares algorithm requires residual values (R values) in order to judge the quality of the refinement. These R values also known as agreement factors are often defined differently:

$$R_p = \frac{\sum_{2\theta_i} |Y_{obs}(2\theta_i) - Y_{calc}(2\theta_i)|}{\sum_{2\theta_i} Y_{obs}(2\theta_i)} \quad , \tag{2.29}$$

$$R_{wp} = \sqrt{\frac{\sum_{2\theta_i} w(2\theta_i)(Y_{obs}(2\theta_i) - Y_{calc}(2\theta_i))^2}{\sum_{2\theta_i} w(2\theta_i)(Y_{obs}(2\theta_i))^2}} \quad , \tag{2.30}$$

$$R_{exp} = \sqrt{\frac{M-P}{\sum_{2\theta_i} w(2\theta_i)(Y_{obs}(2\theta_i))^2}} \quad , \tag{2.31}$$

$$GOF = \chi^2 = \frac{R_{wp}}{R_{exp}} = \sqrt{\frac{\sum_{2\theta_i} w(2\theta_i)(Y_{obs}(2\theta_i) - Y_{calc}(2\theta_i))^2}{M-P}} \quad , \tag{2.32}$$

$$R_B = \frac{\sum_{\{h,k,l\}_p} |I_{obs}(\{h,k,l\}_p) - I_{calc}(\{h,k,l\}_p)|}{\sum_{\{h,k,l\}_p} I_{obs}(\{h,k,l\}_p)} \quad . \tag{2.33}$$

Here R_p is the profile residual, R_{wp} is the weighted profile residual, R_{exp} is the expected residual with M as the number of data points and P as the number of the refined parameters, GOF is the goodness of fit (GOF) and R_B is the Bragg residual. Please note that the GOF given here is the one which is defined in the TOPAS software [57]. In textbooks [56, 59] and in the GSAS software [60] the GOF is defined as follows:

$$GOF = \chi^2 = \left(\frac{R_{wp}}{R_{exp}}\right)^2 = \frac{\sum_{2\theta_i} w(2\theta_i)\left(Y_{obs}(2\theta_i) - Y_{calc}(2\theta_i)\right)^2}{M-P} \quad . \tag{2.34}$$

In addition to the above given definitions for equations 2.29, 2.30 and 2.31, the R_p, R_{wp} and R_{exp} can be defined in a background corrected version if a low peak to background ratio makes such a definition necessary [58].

2.2.1 Sequential and parametric Rietveld refinements

The technical progress of today allows collecting huge amounts of data sets, especially when *in situ* powder diffraction experiments are carried out. In such cases the powder diffraction data sets depend on external variables like temperature, pressure, time, etc.. The subsequent treatment of these amounts of data sets by WPPF methods is often very time consuming, but in some cases the data handling can be simplified.

For instance, if the step width of the external variable is not too large, the refinement results of one diffraction pattern can be used as starting values for the next consecutive diffraction pattern, provided that no dramatic changes in the refined values will occur (which can happen if a phase transition sets in). This method, using the refinement results of a diffraction pattern for the next consecutive one is called sequential refinement or in the case of using the Rietveld method, sequential Rietveld refinement.

In 2007, Stinton and Evans published the first successful attempt of a parametric Rietveld refinement [61] (sometimes is also called surface refinement), where different powder diffraction patterns, which depend on common variables are treated simultaneously. In this approach, one or several parameters of different powder diffraction patterns are constrained by one or more equations where the independent variable is the external variable of the *in situ* measurement. It is obvious that any type of equation can be chosen, as long as the equation is physically or empirically connected with the information stored in a single or over a group of powder diffraction patterns. In numerous publications it could be shown that parametric Rietveld refinements have the potential to reduce the correlation between parameters, to reduce the final standard uncertainties, avoid false minima in individual powder diffraction pattern refinements and most importantly allow a direct modeling of parameters which are normally not part of the refinement as they are first introduced by the applied equations [61]. Another welcomed effect is the reduction of the total number of refined parameters which is believed to give a further stabilization of the refinement in a least-squares minimization process.

2.2.2 Whole powder pattern decomposition

Derived from the Rietveld method are the whole powder pattern decomposition (WPPD) methods according to Pawley [62] and to Le Bail *et al.* [63], which are WPPF methods that do not require the knowledge of a crystal structure. Instead of using the full information of the crystal structure as it is used in the Rietveld WPPF, the WPPD methods require only the approximate knowledge of the lattice parameters and the space group. Other parameters like the peak shape parameters or the zero shift can be obtained by the refinement and are independent from the crystal structure. The reason for that is, that only peak intensities are refined instead of refining the atomic positions of a structure factor which contributes to the peak intensity.
In the Pawley WPPD method the peak intensities are individually refined, which allows in general, for closely overlapping peaks, that one peak can become positive, whereas the other peak can become negative[1]. The correlation matrix can be used as a measure for the accuracy of individual reflection intensity.
In contrast to the Pawley WPPD method, the Le Bail WPPD method uses another

1 Nowadays, most of the refinement softwares used, disallow negative peak intensities in a Pawley as well as in a Le Bail refinement.

approach to obtain the intensities. Instead of performing a direct least-squares refinement of the intensities as the Pawley method does, the Le Bail method uses an iterative process to keep the intensities positive. After each least-squares refinement cycle, the obtained intensities from the Rietveld formula are used as squared structure factor amplitudes for the next refinement cycle. This process is continued iteratively, until the refinement converges. In general this is an adequate method to keep the intensities in most cases positive [56, 58].

2.3 The concept of symmetry modes

The concept of symmetry modes or also known as distortion modes is an intriguingly natural concept in order to describe structural, occupational or magnetic changes in a crystal structure, as it connects on a mathematical basis the higher symmetry (HS) of an undistorted crystal structure with the lower symmetry (LS) of the distorted version, as long as the space group of the distorted crystal structure with the lower symmetry is a subgroup of the parental space group of the undistorted crystal structure.

In crystallography, a group-subgroup relation between space groups always implies that a phase transition of a particular crystal structure between two of these groups can be in principal regarded as a quasi-continuous transformation, independent from the fact whether the real phase transition is of first or of second order. Due to this fact, such a quasi-continuous transformation can be described by a set of distortion vectors (or also known as polarization vectors) and corresponding amplitudes, which are responsible for the distortion of the entire crystal structure[1]. Although the description of a crystal structure change by distortion vectors sounds quite easy, the calculation of a specific distortion vector requires a profound knowledge of group theory and representation theory, therefore only a superficial explanation will be given here.

From diffraction experiments it is known, that each quasi-continuous phase transformation of a crystal structure to a lower symmetry and therefore to a subgroup will generate additional Bragg reflections, which are also sometimes called superstructure reflections. These superstructure reflections will appear at special k-points in the first Brillouin zone[2] of the parent crystal structure and are therefore connected with one or more propagation vectors $\vec{k}$ which point from the gamma point of the Brillouin zone

1 This explains also why phase transitions of first order can be equally described with this calculus, as the amplitude of a certain distortion, which shows first order behavior, will be simply discontinuous and makes a jump at the critical phase transition point, whereas the distortion vector will be not affected. This is also the reason why the author is calling this transformation as quasi-continuous, as a first order phase transition of a crystal structure which has a group-subgroup relationships can still be described with the same calculus.

2 The first Brillouin zone in physics is defined as the primitive Wigner-Seitz cell in reciprocal space.

to these k-points[1] [64]. For each propagation vector $\vec{k}$ it is possible to find a set of symmetry operations from the parental space group, for which the rotational part of these symmetry operators leave the propagation vector invariant. This set of symmetry operators is then called the group of the wave vector or the propagation vector group or simply the "little group" [65]. By mapping, these symmetry operations of the little group can be linked to a finite number of irreducible representations [66]. Interestingly, mathematically it can be shown, that each irreducible representation stands for a set of parental symmetry operations which can be broken[2] [66]. Furthermore, if a phase transitions breaks only symmetries of a specific irreducible representation then this irreducible representation is linked to an order parameter[3][4] [66]. Besides the connection with order parameters, each irreducible representation is also associated with basis vectors (mathematical term for the terms polarization vectors, distortion vectors, distortion modes or symmetry modes). If now a certain parameter is changed in the crystal structure upon crossing the phase transition, then this can be expressed as the sum of different basis or distortion vectors [70]:

$$r_{LS} = r_{HS} + \sum_m A_m \cdot \vec{\varepsilon}_m \quad , \tag{2.35}$$

where r_{LS} is the parameter value in the LS phase, r_{HS} is the parameter value in the HS phase and A_m is the amplitude of a certain polarization vector $\vec{\varepsilon}_m$.

Besides the simply explained concept of the symmetry modes, there are a lot of implications which arise from the mathematical basis, for instance that for a displacive/structural phase transition the number of distortion vectors is equal to the number of variable atomic-coordinate parameters [66]. Apart from that example lots of other implications as well as a rigorous calculus can be found in the literature given for instance by Miller and Love [71], Stokes *et al.* [72], Stokes and Hatch [73], Dove [69], Hatch and Stokes [74], Campbell *et al.* [64, 66], Orobengoa *et al.* [75] and Perez-Mato *et al.* [70].

Nowadays, for the exploration of the different possible crystal structures of a given parent structure, two very powerful tools, which are available online, can be used: ISODISTORT [64] and AMPLIMODES [75]. In ISODISTORT different modes can be used if the crystallographic information of a crystal structure is provided. This includes for instance a search of possible subgroups by a given propagation vector $\vec{k}$ or for

1 The simplest case is, that the superstructure reflections appear only at one k-point and are therefore connected only with a single propagation vector $\vec{k}$. This was the case for the determination of the magnetic propagation vector in chapter 3 and for the determination of the structural propagation vector in chapter 5.

2 In crystallographic terms, this means that each irreducible representation has the ability to lead to at least one or more different subgroups of the parental space group.

3 This implies that a phase transition that breaks multiple irreducible representation can have several order parameters.

4 The term "order parameter" refers to the order parameter from Landau theory [67–69].

instance the decomposition of a given crystal structure of the subgroup into symmetry modes. In contrast to ISODISTORT, AMPLIMODES provides only the possibility to perform the decomposition of given crystal structures of a group-subgroup pair into symmetry modes[1].

2.4 Magnetic neutron scattering and description of magnetic structures

The following sections describe the physical and mathematical properties of elastic magnetic neutron scattering as well as the crystallographic/mathematical description of the symmetry of magnetic structures in solids.

2.4.1 Magnetic neutron scattering and magnetic propagation vector

The standard method in order to determine magnetic structures in solids is to use unpolarized neutrons which are elastically scattered due to the dipole-dipole interaction between the neutron spin and the spin of unpaired electrons[2]. This includes that the neutrons are sensitive to both, the spin angular momentum and the orbital angular momentum contributions[3]. Besides the scattering from unpaired electrons, the neutrons are also scattered by the atomic nuclei, which results in a combined elastic scattering from the magnetic moments and the atomic nuclei of the solid. The intensity in neutron diffraction is therefore given by:

$$I_{hkl} \propto N_{hkl} \cdot N^*_{hkl} + M_{\perp,hkl} \cdot M^*_{\perp,hkl} = |N_{hkl}|^2 + |M_{\perp,hkl}|^2 \quad , \tag{2.36}$$

where the intensity I_{hkl} depends on the sum of the product of the nuclear structure factor N_{hkl} and its complex conjugate and the product of the magnetic structure factor $M_{\perp,hkl}$ and its complex conjugate. The form of the nuclear structure factor is the same as the structure factor F_{hkl} in equation 2.5. The magnetic structure factor $M_{\perp,hkl}$ is also known as magnetic interaction vector. The perpendicular sign $\perp$ next to the magnetic structure factor indicates that only the perpendicular component of the magnetic interaction vector contributes to the neutron scattering [65, 83, 84]. This is a crucial point as this allows the determination of the direction of the magnetic moments within the unit cell of the crystal structure.

For the following descriptions it is more convenient to substitute the Miller indices

1 For other modes like in ISODISTORT, one has to choose other tools from the Bilbao Crystallographic Server [76–78]

2 It is also possible to detect magnetic moments by X-ray diffraction, for instance if a wavelength close to an absorption edge is chosen and anomalous dispersion effects set in [79–82]

3 In the following the term spin means always the total angular momentum $\vec{J}$ of the system, which is given by the coupling of the spin angular momentum $\vec{S}$ and the orbital angular momentum $\vec{L}$.

h, k, l which are vector components of the scattering vector $\vec{h}$ by the scattering vector itself[1]. With this substitution the magnetic structure factor/magnetic interaction vector is given as:

$$M_\perp(\vec{h}) = \vec{h}_e \times M(\vec{h}) \times \vec{h}_e = M(\vec{h}) - \vec{h}_e \cdot (\vec{h}_e \cdot (\vec{h})) \quad , \tag{2.37}$$

where $\vec{h}_e$ is the unity vector $\vec{h}_e = \frac{\vec{h}}{|\vec{h}|}$ and $M(\vec{h})$ is the magnetic structure of the unit cell, which is given by:

$$M(\vec{h}) = \sum_{lj} p \cdot f_j(\vec{h}) \cdot \vec{m}_{lj} \cdot e^{2 \cdot \pi \cdot i \cdot \vec{h} \cdot \vec{r}_{lj}} \quad , \tag{2.38}$$

where the constant p is $p = \frac{1}{2} \cdot r_e \cdot \gamma$ with r_e as the classical electron radius ($r_e = \frac{e^2}{m_e \cdot c^2}$ with e the electron charge, m_e the mass of the electron and c the speed of light) and γ as the magnetic moment of the neutron in nuclear magnetons [65, 84]. This constant p is used in order to convert the magnetic moment configuration m_{lj}, which is given in Bohr magnetons to scattering lengths units [65]. $f_j(\vec{h})$ is the atomic magnetic form factor of atom j and $\vec{r}_{lj}$ is a lattice vector to atom j in the unit cell l of the crystal structure[2] [65, 83, 84].

If equations 2.38 and 2.37 are combined, then a complete expression of the magnetic interaction vector $M_\perp(\vec{h})$ is obtained:

$$M_\perp(\vec{h}) = \frac{1}{|\vec{h}|^2} \vec{h} \times \underbrace{\sum_{lj} p \cdot f_j(\vec{h}) \cdot \vec{m}_{lj} \cdot e^{2 \cdot \pi \cdot i \cdot \vec{h} \cdot \vec{r}_{lj}}}_{M(\vec{h})} \times \vec{h} \tag{2.39}$$

$$= \textstyle\sum_{lj} p \cdot f_j(\vec{h}) \vec{m}_{\perp,lj} \cdot e^{2 \cdot \pi \cdot i \cdot \vec{h} \cdot \vec{r}_{lj}} \quad . \tag{2.40}$$

In this equation, the magnetic moment configuration m_{lj} is given by the following Fourier series:

$$\vec{m}_{lj} = \sum_{\vec{k}} \vec{S}_{\vec{k}j} \cdot e^{-2 \cdot \pi \cdot i \cdot \vec{k} \cdot \vec{R}_l} \quad , \tag{2.41}$$

where $\vec{S}_{\vec{k}j}$ are complex Fourier coefficients in Bohr magnetons [65], which must fulfill the following relation $\vec{S}_{\vec{k}j} = \vec{S}^*_{-\vec{k}j}$ in order to keep the sum and therefore the magnetic moments as a real vector [65], $\vec{k}$ is the magnetic propagation vector which is restricted

1 In physics the scattering vector $\vec{h}$ is often denoted as $\vec{s}$ and the scattering vector $\vec{Q}$ is given as $\vec{Q} = 2 \cdot \pi \cdot \vec{h}$.

2 With the vector $\vec{R}_l$, which is a vector from the arbitrary origin of the crystal to the origin of the unit cell l of the crystal and a lattice vector $\vec{x}_j$ within the unit cell l, the lattice vector $\vec{r}_{lj}$ can be expressed as $\vec{r}_{lj} = \vec{R}_l + \vec{x}_j$.

to the first Brillouin zone [83] and $\vec{R}_l$ is a vector to the origin of the unit cell l of the crystal structure [65, 83, 84].

In general, the complex Fourier coefficients are given by the following relation:

$$\vec{S}_{\vec{k}j} = \vec{R}_{\vec{k}j} + i \cdot \vec{I}_{\vec{k}j} \cdot e^{-2 \cdot \pi \cdot i \cdot \Phi_{\vec{k}j}} \quad , \tag{2.42}$$

where $\vec{R}_{\vec{k}j}$ is the three component vector of the real part of $\vec{S}_{\vec{k}j}$, $\vec{I}_{\vec{k}j}$ is the three component vector of the imaginary part of $\vec{S}_{\vec{k}j}$ and the exponential function gives an additional phase factor with phase angle $\Phi_{\vec{k}j}$. The index $\vec{k}j$ at every variable denotes, that all these variables depend on a special vector $\vec{k}$ and a certain atom j in the crystallographic unit cell.

2.4.1.1 Examples of different Fourier coefficients and magnetic propagation vectors

In the following, different examples with increasing complexity will show, how the magnetic moment is affected by the choice of certain Fourier coefficients and magnetic propagation vectors and how the entire magnetic moment configuration for the crystal is established from equation 2.41. For this purpose, we assume a cubic crystal structure with space group $Pm\bar{3}m$ and that only one atom in the crystallographic unit cell is magnetic at position $(0.5, 0.5, 0.5)^T$. This reduces the index j from equation 2.41 to 1 and therefore it can be neglected.

1. $\vec{S}_{\vec{k}} = (0, 0, w)^T$ (w = real) and $\vec{k} = (0, 0, 0)^T$

Since a zero magnetic propagation vector leads always to a zero phase in the exponent, therefore the Fourier coefficient $\vec{S}_{\vec{k}} = (0, 0, w)$ (w only real and without the assumption of an additional phase factor $\Phi_{\vec{k}j}$) is not influenced and all magnetic moments point along the same direction, along the z-direction (see figure 2.7). In this case the magnetic unit cell coincides with the crystallographic unit cell and the ferromagnetic Bragg peaks in a diffraction pattern lie on top of the nuclear Bragg peaks, as the magnetic reflections appear at the nodes of the nuclear reciprocal lattice and their intensities are therefore added.

2. $\vec{S}_{\vec{k}} = (0, 0, w)^T$ (w = real) and $\vec{k} = (0, 0, 0.5)^T$

In this example the vector $\vec{k}$ gives rise to a regular sign modulation of the Fourier coefficient $\vec{S}_{\vec{k}} = (0, 0, w)$ (w only real and without the assumption of an additional phase factor $\Phi_{\vec{k}j}$). For the first cell at $R_1 = (0, 0, 0)^T$ the magnetic moment points along the positive z-direction, whereas for the second cell at $R_2 = (0, 0, 1)^T$ the magnetic moment points along the negative z-direction. In this case, the description of the magnetic unit cell needs a doubling of the crystallographic unit cell, as the configuration is clearly antiferromagnetic (see figure 2.7).

3. Cycloid configuration with $\vec{S}_{\vec{k}}$ complex and $\vec{k} = (1/3, 1/3, 0)^T$

For this example the Fourier coefficient has complex entries and therefore equation 2.41 must be rewritten in order to keep the sum and therefore the magnetic moments real:

$$\begin{aligned}\vec{m}_{lj} &= \sum_{\vec{k}} \frac{1}{2} \cdot \left(\vec{S}_{\vec{k}j} + \vec{S}^*_{-\vec{k}j}\right) \cdot e^{-2\cdot\pi\cdot i\cdot\vec{k}_\pm\cdot\vec{R}_l} \\ &= \sum_{\vec{k}} \left(\vec{R}_{\vec{k}j} \cdot \cos\left(2\cdot\pi\cdot\left(\vec{k}\cdot\vec{R}_l + \Phi_{\vec{k}j}\right)\right) + \vec{I}_{\vec{k}j} \cdot \sin\left(2\cdot\pi\cdot\left(\vec{k}\cdot\vec{R}_l + \Phi_{\vec{k}j}\right)\right)\right) \quad (2.43)\end{aligned}$$

where the condition $\vec{S}_{\vec{k}j} = \vec{S}^*_{-\vec{k}j}$ was used (the full calculation can be found in appendix A).
If the phase angle $\Phi_{\vec{k}j}$ is neglected and it is assumed that $\vec{R}_{\vec{k}j} = (0, 0, w_1)^T$ and $\vec{I}_{\vec{k}j} = (w_1, w_1, 0)^T$, then a cycloid in the xy-plane can be created (see figure 2.7).

2.4.2 Crystallographic description of magnetic structures: magnetic space groups and representation theory

In the following subsections, two state-of-the-art concepts will be presented in order to give a mathematical description of magnetic structures.

2.4.2.1 Magnetic space groups (Shubnikov groups)

The description of the magnetic space groups is almost equal to the description of the colored space groups (black and white space groups). In both space group classes, an additional symmetry operation, often called time reversal operation, is needed in order to change the color or the spin direction of a given object after the ordinary spatial symmetry operation[1]. For instance in the case of the colored space groups, the time reversal operation changes the color "black" into the color "white"[2]. If the time reversal operation is then combined with an ordinary spatial symmetry operation, then a point in space of color "black" can be transformed to another point in space of color "white". In general, this concept can be also used for the change of a spin direction (magnetic moment direction). In contrast to the colored space groups one

1 The term "ordinary spatial symmetry operations" is used here in order to denote, that these are the symmetry operations which are known from the 230 crystallographic space groups, which transform one point in space to another point in space.

2 If the author considers a time reversal operation in the present thesis, it always means that something is changed. In the literature this corresponds often to a multiplication with -1 in order to denote that something is changed (in theses cases the change is denoted by a sign change).

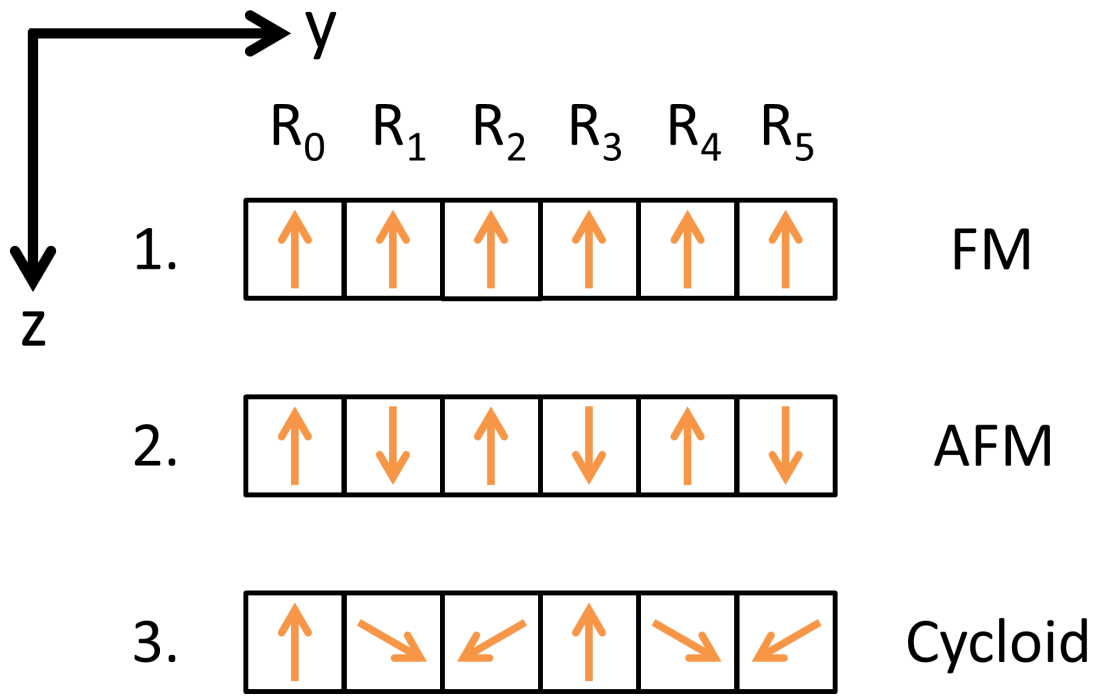

Figure 2.7: Examples for magnetic structures for different magnetic propagation vectors and different real and complex Fourier coefficients. a) ferromagnetic (FM) configuration with $\vec{S}_{\vec{k}} = (0,0,w)^T$ (w = real) and $\vec{k} = (0,0,0)^T$, b) antiferromagnetic (AFM) configuration with $\vec{S}_{\vec{k}} = (0,0,w)^T$ (w = real) and $\vec{k} = (0,0,0.5)^T$ and c) cycloid configuration with $\vec{S}_{\vec{k}}$ complex and $\vec{k} = (1/3,1/3,0)^T$. The unit cells which are shown by the black squares are given by the lattice vector $R_l = (0,l,0)^T$ with l as integer.

has to bear in mind, that a color is a scalar quantity, whereas a spin is an axial vector[1].

If the concept of an additional symmetry operation/time reversal operation is applied to the 230 crystallographic space groups, then the 1651 magnetic space groups or also known as Shubnikov groups can be derived [65]. These 1651 Shubnikov groups consist of 3 different classes of space groups. The first class is the class of the 230 crystallographic space groups or also known as monochrome groups or Fedorov groups.

1 The reason why it must be an axial vector is obvious. From the definition, an axial vector transforms under an inversion in that way, that its direction is not changed, whereas a polar vector changes its direction by 180°. If a polar vector would be used in conjunction with an ordinary spatial symmetry operation and a time reversal operation, than the direction of the polar vector would be changed after the spatial symmetry operation and again after the time reversal operation. Although it is also possible to use polar vectors for the description of spins/magnetic moments, it is logically more convenient to use axial vectors, as there direction is invariant under the application of an ordinary spatial symmetry operation.

The second class is the class of the 230 gray groups or also known as paramagnetic space groups[1]. The third and biggest class is the class of the 1191 black and white space groups, which can be divided into 674 equi-translation subgroups ("translationsgleiche Untergruppen") and 517 equi-class subgroups ("klassengleiche Untergruppen").

In order to catalogue the different 1651 Shubnikov groups two different notations can be used. The first notation is the BNS setting (named after Belov, Neronova, Smirnova [85, 86]) and the second notation is the OG setting (named after Opechowski and Guccione [87–91]). The notations of both settings are identical except for the the equi-class subgroups [65].

From the definition of the Shubnikov groups by the addition of a time reversal operation to the ordinary spatial symmetry operations it is obvious that this mathematical description accounts exclusively for commensurate magnetic structures. In order to describe commensurate and incommensurate magnetic structures a description of the magnetic structures by the representation theory is necessary.

2.4.2.2 Representation theory for magnetic structures

In representation theory for magnetic structure it is possible to determine the complex Fourier coefficients $\vec{S}_{\vec{k}j}$ from equation 2.41 by the sum over free parameters $C^{\nu}_{n\lambda}$ and complex constant vectors $\vec{S}^{\vec{k}\nu}_{n\lambda}(j_s)$ [65]:

$$\vec{S}_{\vec{k}j_s} = \sum_{n\lambda} C^{\nu}_{n\lambda} \cdot \vec{S}^{\vec{k}\nu}_{n\lambda}(j_s) \qquad , \tag{2.44}$$

where j is no longer a single atom as in equations 2.38-2.42, but stands for a complete Wyckoff site[2], the subindex s is a single atom for a given Wyckoff position j, $C^{\nu}_{n\lambda}$ is a free parameter[3] for the active irreducible representation Γ_ν from the little group G_k with component λ, which labels the component corresponding to the dimension of Γ_ν, n gives the number, how often an irreducible representation Γ_ν is contained in the entire magnetic representation and $\vec{S}^{\vec{k}\nu}_{n\lambda}(j_s)$ are complex constant vectors which can be calculated from the irreducible representations Γ_ν [65]. In general, this complex constant vectors are obtained in a similar way like the basis vectors for the symmetry mode approach described before, except for the fact that they are axial vectors [65]. In the approach of representation theory for magnetic structures as described above, there is no limitation to commensurate magnetic propagation vectors $\vec{k}$ as it was the case for the description with Shubnikov groups. Therefore the representation theory

1 An example of a gray group can be given by considering that a point in space has simultaneously both colors black and white (therefore the name gray). If this point is now transformed, than it will be again black and white (=gray), no matter if a time reversal operator is applied or not.)
2 Sometimes this index for the Wyckoff site is also called "orbit".
3 This parameter corresponds to an order parameter according to Landau theory [65] and is therefore responsible for the amplitude of the magnetic moment.

is the more general approach in order to describe magnetic structures.

2.5 Phase transitions and phenomenological Landau theory

In the following, a short overview of the concepts of phase transitions and phenomenological Landau theory, as they are used in the present thesis, is given.

2.5.1 Phase transitions

In order to characterize and to classify the different phenomena which can be observed if one phase is transformed to another, different classification schemes have been developed. In the following the most prominent classification schemes are presented, which consist of the Ehrenfest classification and the modern classification.

2.5.1.1 Ehrenfest classification

The oldest classification scheme for phase transitions was given by Paul Ehrenfest in 1933, who defined the order n of a phase transition according to the number of the first non-continuous derivative of a particular thermodynamic potential, the Gibbs energy (also known as Gibbs free energy or free enthalpy) [92–94]. This means that, for a given Gibbs energy $G(T,p)$, a first order phase transition is characterized by a jump at critical values of T and p of the first partial derivatives $S(T,p) = -\left(\frac{\partial G}{\partial T}\right)_p$ and $V(T,p) = -\left(\frac{\partial G}{\partial p}\right)_T$, where S is the entropy, T is the temperature, p is the pressure and V is the volume (the subscript denotes that this variable is constant). In case of a second order phase transition the first partial derivatives of $G(T,p)$ are continuous, whereas the second partial derivatives exhibit a discontinuity. This means that for a given Gibbs energy $G(T,p)$ the heat capacity $C_p = -T \cdot \frac{\partial^2 G}{\partial T^2}$ and the compressibility $\kappa_T = -V \cdot \frac{\partial^2 G}{\partial p^2}$ are discontinuous at critical values of T and p. Interestingly, although this definition allows for higher order phase transitions, they have not been observed so far [94].

2.5.1.2 Modern classification

Although the Ehrenfest classification is valid for many phase transitions, it is too strict in order to describe all observed phase transition phenomena[1] [94]. For instance, one point of criticism regarding the Ehrenfest classification is, that the observed behaviors for the heat capacity and compressibility are rather asymptotic with a singularity at the critical phase transition point for a second order phase transition, which is in contrast to the proposed analytical discontinuity [94].

1 From the later described phenomenological Landau theory, which is a classical non-quantum mechanical theory, the Ehrenfest classification is strictly confirmed [94].

Therefore the modern classification, defines only two types of phase transitions, a discontinuous phase transition which corresponds to a first order phase transition and a continuous phase transition which corresponds to a second order phase transition [94]. For a first order phase transition the definition is almost equal to the definition from the Ehrenfest classification, although it is extended to a discontinuity of the first derivative of an arbitrary thermodynamic potential[1] [94]. In contrast to the first order phase transitions, the second order phase transitions are defined slightly different. According to the textbook of Nolting [94], a second order phase transition is given, if at least one second partial derivative of an arbitrary thermodynamic potential shows a non-analytical behavior[2].

In the present thesis, the modern classification for the phase transitions will be used, although for the given experimental examples, the Ehrenfest classification scheme would be also applicable.

2.5.2 Phenomenological Landau theory

The Landau theory is a classical (= non-quantum mechanical) theory, which was developed in order to describe phenomenologically the observed thermodynamic behavior of an order parameter in the vicinity of a phase transition [7, 67, 94, 95]. In principle, the Landau theory considers a phase as homogeneous, which means that interactions on a microscopic scale are not incorporated, which classifies this theory as a mean-field theory [94, 95]. Moreover, the negligence of local fluctuations on the microscope scale leads also to one of the points of criticism of the theory, as in the immediate vicinity of the critical phase transition point, the fluctuations become too large to disregard them[3] [94–96]. Despite this deficiency, Landau theory provides an insight into the symmetry breaking process during a phase transition by an order parameter, which is zero above and non-zero below the critical phase transition point[4] [68].

The assumption which Landau made was, that in the vicinity of a critical point, a phase transition can be modeled by a Taylor series of the Gibbs free energy G, which depends on an order parameter Q and one or more intensive variables, for instance a temperature T [7, 67, 94, 95]:

1 In his publication from 1933, Ehrenfest used only the thermodynamic potential of the Gibbs energy for his considerations [92–94].

2 The mathematical definition of an analytical function is given by a function which can be locally described by a convergent power series.

3 In addition to large fluctuations, Landau theory is also not applicable in cases where the interactions are of short range and not of long range [95].

4 An order parameter can usually be identified with a macroscopic physical quantity like polarization or magnetization but also with collective motions of atoms as it will be shown in sections 4.4.4 and 4.4.5.

$$G(Q,T) = G_0 + a(T)\cdot Q + \frac{1}{2}\cdot b(T)\cdot Q^2 + \frac{1}{3}\cdot c(T)\cdot Q^3 + \frac{1}{4}\cdot d(T)\cdot Q^4 + \ldots \quad (2.45)$$

here G_0 is the thermodynamic potential in the phase where $Q = 0$ and a, b, c and d are functions of the temperature T.
If only a finite number of orders of such a Taylor series is considered, then a necessary condition for such an approximation of the Gibbs free energy is, that the values of Q are small [7, 67, 94, 95]. For the investigation of, for instance, the special case of a simple continuous phase transition without any couplings to other parameters[1], it is sufficient to consider only even terms up to the 4th order [7, 67, 94, 95]:

$$G(Q,T) = G_0 + \frac{1}{2}\cdot b(T)\cdot Q^2 + \frac{1}{4}\cdot d(T)\cdot Q^4 \quad . \quad (2.46)$$

The so obtained Gibbs potential is known as the 2-4 Landau potential, due to the present terms of second and fourth order [68].

In order to gain some information about the nature of the two coefficients b and d above and below the critical phase transition point, the energy minimum of the 2-4 Landau potential can be investigated. For this purpose, the first and second pressure derivative of equation 2.46 must be generated and the necessary and sufficient conditions of a minimum must be applied [7, 67, 94, 95]:

$$\frac{\partial G(Q,T)}{\partial Q} = b(T)\cdot Q + d(T)\cdot Q^3 \stackrel{!}{=} 0 \quad , \quad (2.47)$$

$$\frac{\partial^2 G(Q,T)}{\partial Q^2} = b(T) + 3\cdot d(T)\cdot Q^2 \stackrel{!}{>} 0 \quad . \quad (2.48)$$

For the phase, where $Q = 0$ and therefore $T > T_c$ or $T = T_c$, it is evident from the conditions in equations 2.47 and 2.48, that the coefficient b must have a positive value, whereas for $Q > 0$ and therefore $T < T_c$, it follows that b must have a negative value. The simplest assumption which can be made to model such a behavior of $b(T)$ is the following:

$$b(T) = k\cdot(T - T_c) \quad , \quad (2.49)$$

where k is a positive constant and T_c is the critical phase transition temperature.

1 For a coupling to for instance spontaneous strain see Salje [68].

The behavior of the order parameter Q in the region $T < T_c$ can be modeled if equation 2.47 is solved for Q and if it is combined with the result from equation 2.49:

$$Q = \pm \underbrace{\sqrt{\frac{k \cdot T_c}{d(T)}}}_{A} \cdot \sqrt{\frac{T_c - T}{T_c}} = \pm A \cdot \left(\frac{T_c - T}{T_c}\right)^{\frac{1}{2}} \quad . \tag{2.50}$$

From this equation it can be deduced that $d(t)$ must be positive (otherwise the square root would result in a complex value) and that the critical exponent is $\beta = \frac{1}{2}$. Therefore, from all the assumptions which were made, it can be stated that for a simple continuous phase transition without any couplings to other parameters, the Landau theory will result in an exact critical exponent.
An illustration of the energy landscape in dependence on the temperature T and the order parameter Q is given in figure 2.8a). In this figure the typical bifurcation (marked by the solid red line in the energy minimum of the Gibbs free energy potential) of an order parameter can be seen, which corresponds to an reversal of the sign for a physical macroscopic property, like the magnetization or the polarization in a bulk material. Furthermore, in figure 2.8b) it is also shown what happens, if a 2-3-4 Landau potential is chosen. In this case, there exists only one energy minimum and the order parameter Q jumps, which indicates a first order phase transition.

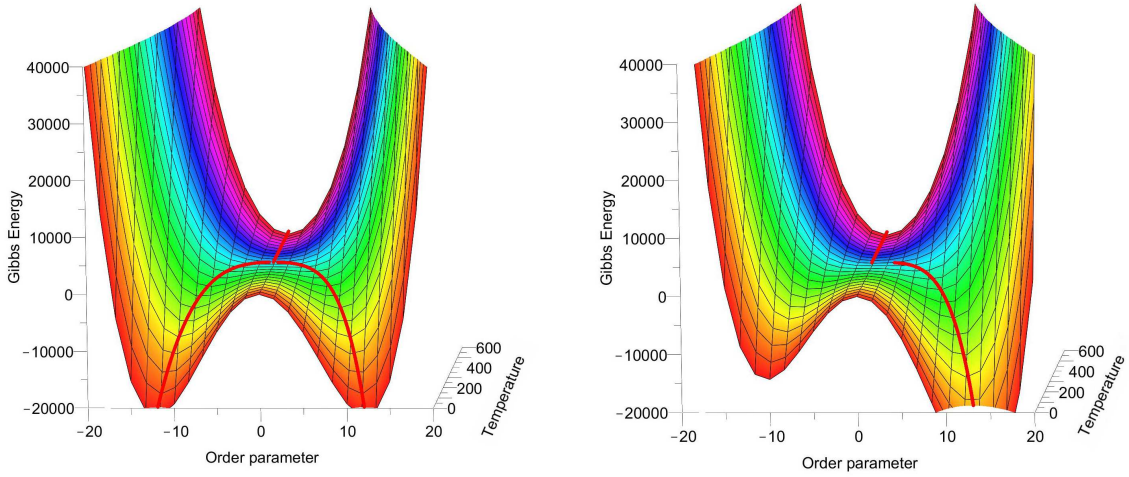

(a) 2-4 potential **(b)** 2-3-4 potential

Figure 2.8: Temperature and order parameter dependent energy landscape for a a) 2-4 Landau potential and for a b) 2-3-4 Landau potential. The red solid line marks the path of the lowest Gibbs energy.

2.6 Ferroic and multiferroic phenomena

The symmetry of a crystal structure can not solely be broken by the displacive motion of atoms or atomic groups, but also by other long-range ordering effects like macroscopic spontaneous magnetization, macroscopic spontaneous electrical polarization or macroscopic spontaneous deformation of the crystal, which occur if a intensive property like temperature is changed. Similar to the case of a continuous displacive phase transition, such a continuous phase transition and therefore the symmetry breaking of a crystal structure by a long-range ordering effect is also connected with an order parameter, which is zero in the high symmetry phase and finite in the low symmetry phase.
Depending on the observable physical macroscopic properties which arise spontaneously in the low symmetry phase, the different ferroic orders can be categorized. The onset of a macroscopic spontaneous magnetization leads for instance to a(n) (anti-)ferromagnetic order, whereas a macroscopic spontaneous electrical polarization leads to a(n) (anti-)ferroelectric order. If a crystal structure exhibits macroscopic spontaneous deformation then this can be described as ferroelastic order.

The following subsections give an overview of the different ferroic orders[1], which can be observed either individually in single ferroic materials or simultaneously in multiferroic materials.

2.6.1 (Anti-)Ferroelectricity

A ferroelectric phase is characterized by a non-vanishing spontaneous electric polarization $\vec{P}$ below, for instance, a critical temperature $T_{c,FE}$ without the application of an external electric field $\vec{E}$. However, as the spontaneous polarization $\vec{P}$ is a vector quantity, it can be switched by 180° by an external electrical field $\vec{E}$. This means that an ferroelectric phase in a solid with a non-vanishing spontaneous polarization must possess a dielectric hysteresis curve in a $\vec{P}(\vec{E})$ diagram[2].

The physical microscopic reasons for the occurrence of the non-vanishing spontaneous polarization $\vec{P}$ in a crystal structure is manifold, but in general a classification into proper ferroelectric effects and improper ferroelectric effects can be done.

1 The ferrotoroidic order will be neglected in this work, as there is an ongoing discussion about the unambiguous observation of this ferroic order [3].

2 This statement is correct for ferroelectricity. In the case of antiferroelectricity there exist two sublattices with opposite spontaneous polarization and therefore a net spontaneous polarization is normally canceled, which means that no dielectric hysteresis can be observed. In the case of ferrielectricity, a dielectric hysteresis curve can be observed, as the absolute value of the two different spontaneous polarization vectors is not equal and therefore a net spontaneous polarization is left over.

2.6.1.1 Proper ferroelectricity

If the primary order parameter, which is connected with the continuous ferroic phase transition from a paraelectric to a ferroelectric phase, is given by the spontaneous polarization, then this kind of ferroelectricity is called proper ferroelectricity [7].

Proper ferroelectricity occurs in materials, where the spontaneous polarization arises due to structural effects, like for instance hybridization effects of filled oxygen p orbitals and empty d orbitals of transition metals (e.g. in $BaTiO_3$) [97, 98] or for instance polarizable lone pairs which move away from their centrosymmetric position in a oxygen surrounding (e.g. in $BiFeO_3$) [97]. In addition, such a structural effect must break the spatial inversion symmetry of the crystal structure, as otherwise the spontaneous polarization will be canceled out. Therefore proper ferroelectricity cannot occur in all space groups or point groups, respectively. An overview of all three dimensional point groups is given in table 2.3. Only the polar point groups where all symmetry operations leave at least two points invariant are capable of producing pyroelectricity and eventually proper ferroelectricity[1].

Table 2.3: All 32 crystallographic point groups in 3 dimensions. All of the non-centrosymmetric point groups are capable of being piezoelectric, except for point group 432. All 10 polar point groups, which are a subgroup of the non-centrosymmetric point groups, are capable of being pyroelectric. Proper ferroelectricity can only occur in the polar and therefore pyroelectric point groups [7].

Crystal system	Centrosymmetric point groups		Non-centrosymmetric point groups				
			Polar		Non-polar		
Cubic	$m\bar{3}$	$m\bar{3}m$	-		432	$4\bar{3}m$	23
Tetragonal	$4/m$	$4/mmm$	4	$4mm$	$\bar{4}$	$\bar{4}2m$	422
Orthorhombic	mmm		$mm2$		222		
Hexagonal	$6/m$	$6/mmm$	6	$6mm$	$\bar{6}$	$\bar{6}m2$	622
Trigonal	$\bar{3}$	$\bar{3}m$	3	$3m$	32		
Monoclinic	$2/m$		2	m	-		
Triclinic	$\bar{1}$		1		-		
Total number	11 groups		10 groups		11 groups		

1 This is a convenient feature, as materials with a centrosymmetric point group/space group exhibit certainly not proper ferroelectricity.

2.6.1.2 Improper ferroelectricity

In contrast to proper ferroelectricity, the spontaneous polarization of improper ferroelectricity is not connected with a primary order parameter, as the observable spontaneous polarization arises as a secondary effect due to a coupling to another ordering phenomenon [97]. In general, there exist different possibilities how ordering can induce improper ferroelectricity. For instance, improper ferroelectricity can occur if a structural phase transition leads to a special kind of lattice distortions, therefore this ferroelectricity effect is also known as geometric ferroelectricity (e.g. in hexagonal manganites $RMnO_3$ (R=Ho-Lu, Y)) [4, 97]. Another possible origin for improper ferroelectricity is charge ordering, where ions of different valence states must order non-symmetrically in order to give a net spontaneous electric polarization (e.g. in $LuFe_2O_4$) [4, 97]. Besides geometric ferroelectricity and charge ordering induced ferroelectricity, improper ferroelectricity can also arise due to an ordering of magnetic moments, which breaks the inversion symmetry of a crystal structure (e.g. $TbMnO_3$) [4, 97].

2.6.2 (Anti-)Ferromagnetism

Similar to (anti-)ferroelectricity, the (anti-)ferromagnetism can be characterized by a non-vanishing spontaneous magnetization $\vec{M}$ below, for instance, a critical temperature $T_{c,FM}$ without the application of an external magnetic field $\vec{H}$. An external magnetic field $\vec{H}$ can switch the direction of the spontaneous magnetization by 180°, which is also similar to the switching of the spontaneous polarization in ferroelectricity by an electric field $\vec{E}$. This means that a ferromagnetic compound will show, analogue to a ferroelectric compound, a magnetic hysteresis curve $\vec{M}(\vec{H})$ with a non-vanishing spontaneous magnetization, whereas an antiferromagnetic compound will not show such a behavior, as the microscopic magnetic moments sitting on two different sublattices cancel each other out[1].

The microscopic mechanisms, which lead to the formation of magnetic structures with ferromagnetic, antiferromagnetic and ferrimagnetic ordering is given by different coupling mechanisms between the magnetic moments. One of these mechanism is for instance the direct exchange mechanism, where the magnetic moments couple directly, if the wave functions have a sufficient overlap [7]. This direct coupling can be described in the Heisenberg model by the following Hamiltonian H:

$$H = -J \sum_{i,j} \vec{S}_i \cdot \vec{S}_j \quad , \tag{2.51}$$

where J is the exchange constant between the two spins $\vec{S}$ of the atoms i and j [99].

1 In a ferrimagnetic compound a net spontaneous magnetization and therefore a magnetic hysteresis curve can be observed, as the magnetic moments on the two sublattices do not cancel themselves completely out.

Another exchange mechanism is the superexchange, where the exchange interaction between two magnetic ions is mediated by a nonmagnetic ion and commonly an antiferromagnetic ordering of the magnetic moments is established [99]. A similar but not equal exchange mechanism is given by the double exchange, where the exchange interaction between two magnetic ions is also mediated by a nonmagnetic ion, but usually a ferromagnetic ordering of the magnetic moments is established [99]. A further exchange mechanism is given by the Ruderman-Kittel-Kasuya-Yosida exchange, where the exchange interaction between two magnetic moments is mediated by the polarization of the conduction electrons [99].

2.6.3 Ferroelasticity

A ferroelastic compound exhibits a macroscopic spontaneous strain ε below, for instance, a critical temperature $T_{c,FELA}$ without the application of an external stress σ. Similar to the hysteresis effects in ferroelectric and/or ferromagnetic compounds an elastic hysteresis $\sigma(\varepsilon)$ can be observed, if an external stress σ is applied. Above a critical temperature $T_{c,FELA}$ the macroscopic spontaneous strain vanishes and the occurring phase is called a paraelastic phase [7, 68].

2.6.4 Multiferroics

According to the definition given by Schmid in his publication in 1994 [100], a multiferroic material is a material which exhibits two or more ferroic properties simultaneously in the same phase. This definition is nowadays extended, as most of the multiferroic materials show a coupling between at least two of these ferroic orders, why the term "multiferroics" is now often used for materials exhibiting not only different ferroic orders but also a full or partial coupling between them [3, 98].

As already explained in the introduction (see chapter 1), of special interests are multiferroic materials which exhibit a magnetoelectric coupling, as these materials are potential candidates for new magnetoelectronic devices. Therefore a short overview of the basics of magnetoelectric coupling mechanisms will be given.

2.6.4.1 Magnetoelectric coupling

The magnetoelectric coupling mechansims in multiferroics can be explained, if either the Helmholtz free energy F [3, 101] or the Gibbs free energy G [7, 102] is given as an expansion in dependence on the electrical field $\vec{E}$ and on the magnetic field strength $\vec{H}$. Using the Einstein summation convention, the expansion for the Gibbs free energy is given by:

$$\begin{aligned} G(\vec{E},\vec{H}) &= G_0 - P_i^S E_i - \mu_0 M_i^S H_i \\ &\quad -\frac{1}{2}\varepsilon_0\varepsilon_{ij}E_iE_j - \frac{1}{2}\mu_0\mu_{ij}H_iH_j - \alpha_{ij}E_iH_j \\ &\quad -\frac{1}{2}\beta_{ijk}E_iH_iH_k - \frac{1}{2}\gamma_{ijk}H_iE_jE_k - \dots \quad , \end{aligned} \tag{2.52}$$

where G_0 is the Gibbs free energy in the phase without spontaneous polarization or spontaneous magnetization, P_I^S is the i-th component of the spontaneous polarization, M_i^S is the i-th component of the spontaneous magnetization, E_i, E_j, E_k are components of the electrical field $\vec{E}$, H_i, H_j, H_k are components of the magnetic field strength $\vec{H}$, ε_0 is the vacuum permittivity, μ_0 is the vacuum permeability, ε_{ij} is the relative permittivity, which is related to the electric susceptibility χ_e by $\chi_e = \varepsilon_{ij} - 1$, μ_{ij} is the relative permeability, which is related to the magnetic susceptibility χ_m by $\chi_m = \mu_{ij} - 1$, α_{ij} is a tensor, which describes a linear magnetoelectric coupling, β_{ijk} is a third-rank tensor, which describes a electrobimagnetic coupling and γ_{ijk} is a third-rank tensor, which describes a magnetobielectric coupling.

The influence of the magnetoelectric coupling on either the polarization or the magnetization becomes obvious, if the derivatives of the expansion of the Gibbs free energy with respect to the electric field vector or the magnetic field strength vector are built. For the polarization this gives

$$\begin{aligned} P(\vec{E},\vec{H}) &= -\frac{\partial G}{\partial E_i} \\ &= P_i^S + \varepsilon_0\varepsilon_{ij}E_j + \alpha_{ij}H_j + \frac{1}{2}\beta_{ijk}H_iH_k + \gamma_{ijk}H_iE_j + \dots \quad , \end{aligned} \tag{2.53}$$

whereas for the magnetization the following equation can be obtained

$$\begin{aligned} M(\vec{E},\vec{H}) &= -\frac{\partial G}{\partial H_i} \\ &= M_i^S + \mu_0\mu_{ij}H_j + \alpha_{ij}E_i + \beta_{ijk}E_iH_j + \frac{1}{2}\gamma_{ijk}E_iE_k + \dots \quad . \end{aligned} \tag{2.54}$$

From both equations it is evident, that a magnetic field can influence the polarization and that a electric field can influence the magnetization.

CHAPTER 3

Temperature dependent *in situ* investigations of $Bi_{1-x}Sr_xFeO_{3-\delta}$

3.1 Motivation

Among the multiferroic materials the bismuth ferrite ($BiFeO_3$) perovskite is one of the most important ones, as it exhibits a magnetoelectric coupling between two ferroic properties, which is present at room temperature and is therefore interesting for the integration in new electronic devices [9]. The crystal structure of the $BiFeO_3$ perovskite at room temperature is trigonal (more specific rhombohedral) with the non-centrosymmetric space group $R3c$ [103], which allows for proper ferroelectricity[1]. The ferroelectric properties of $BiFeO_3$ were discovered in 1970 by Teague *et al.* [104], who reported a dielectric hysteresis in a single crystal of $BiFeO_3$. In a detailed theoretical study by Ravindran *et al.* it could be confirmed that the driving force for the ferroelectricity is the stereochemically active Bi $6s^2$ "lone pair", which is responsible for the shift of the Bi^{3+} cation away from a centrosymmetric position to a non-centrosymmetric one[2] [9, 106, 107].
At 825°C (corresponds to 1098 K) the crystal structure of α-$BiFeO_3$ changes to β-$BiFeO_3$, which is believed to have a centrosymmetric most probable orthorhombic space group [9, 108], therefore this structural phase transition is also connected with the ferroelectric Curie temperature, as this marks the ferroelectric to paraelectric phase transition [9].
Besides the ferroelectricity, $BiFeO_3$ has also antiferromagnetic properties with a quite high Néel temperature of 380°C (corresponds to 653 K) [109, 110]. On a local scale by considering only one crystallographic unit cell the magnetic moments show a typical G-type antiferromagnetic arrangement [9, 103, 110, 111]. This picture changes dramatically if several hundred crystallographic unit cells are considered. By careful neutron time-of-flight measurements, Sosnowska *et al.* were able to demonstrate that the actual magnetic structure consists of a spin cycloid which propagates along the [110]

1 In this work solely the hexagonal setting and not the rhombohedral setting will be used in order to describe the trigonal/rhombhohedral crystals structure of $BiFeO_3$

2 The shift of the cations is along the hexagonal [001] direction, therefore the spontaneous polarization does also occur in this direction [9, 105].

direction of the rhombohedral crystal structure in the hexagonal setting [9, 112, 113]. The magnetic propagation vector which they found is $\vec{k} = (0.0045, 0.0045, 0)^T$, which leads to a huge spin cycloid length of approximately 620 Å [9, 112–114]. Although there were many attempts to look for additional magnetic phase transitions (e.g. [115]), it seems that the magnetic structure of the spin cycloid is preserved from low temperatures of 2 K up to the Néel temperature[1] [9, 117–119].
In 2008, Lebeugle *et al.* [120] and Lee *et al.* [121] were able to show that the change of the polarization direction by applying a voltage on a single crystal of $BiFeO_3$ also changes the magnetic planes, which is a direct evidence for the magnetoelectric coupling in this material [9, 107]. Nowadays it is known that the magnetoelectric coupling is not a linear but rather a quadratic coupling, which arises due to the "lone pair" induced polarization, which breaks the inversion symmetry and which therefore induces a small canting of the spins which can be described using a Dzyaloshinskii-Moriya interaction [9, 122].
Already in 2003, Wang *et al.* published an article in which they could show that they can achieve an enhanced polarization and an enhanced magnetization in a thin film of $BiFeO_3$ compared to the polarization value reported for the bulk system [123]. Although it was later shown from a single crystal study that the large polarization is intrinsic, the research on $BiFeO_3$ thin films and heterostructures became more and more important [9].

In order to tune the amazing phenomena observed in the $BiFeO_3$ perovskite, doping with other chemical elements is an appropriate way to change the ferroic properties. Different studies showed that a high doping of the A-site of the $BiFeO_3$ perovskite can lead to an enhancement of the magnetic properties, which is mainly explained by the formation of a collinear antiferromagnetic structure of the magnetic moments of the Fe^{3+} cations and the resulting suppression of the spin cycloid (see for instance [105, 124, 125]). Another possibility in order to influence the spin cycloid was given in 2002 by Sosnowska *et al.*, who demonstrated, that also a doping of the perovskite B-site by manganese can lead to a suppression of the spin cycloid[2] [126].
Among numerous studies, which investigated the doping of the A-site of the $BiFeO_3$ perovskite, the doping with diamagnetic strontium cations gained special attention, as many contradictory results regarding the doping dependent crystal structures and multiferroic properties were reported. One of the first studies from 1966, concerning the solid solution series between $BiFeO_3$ and $SrFeO_3$ was performed by MacChesney *et al.* [127], who reported from X-ray powder diffraction data that the $Bi_{1-x}Sr_xFeO_{3-\delta}$ perovskites have rhombohedral symmetry for $x = 0 - 0.1$, cubic symmetry for $x = 0.2 - 0.6$, tetragonal symmetry for $x = 0.7$ and again cubic symmetry for $x = 0.8 - 1$.

1 An overview of different obtained Néel temperatures for $BiFeO_3$ was already given in 1980 in the publication of Fischer *et al.* [116].
2 In general, there are numerous publications on doping either the A-site or the B-site or both in order to influence the spin cycloid, the ferroelectricity or the strength of the magnetoelectric coupling.

In addition, they observed from measurements of a $Bi_{0.4}Sr_{0.6}FeO_{2.83}$ perovskite with a magnetometer weak ferromagnetism from which they concluded, that it must originate from an antiferromagnetic ordering with additionally canted magnetic moments.
Another X-ray powder diffraction study was performed by Li *et al.* in 2001, who reported in agreement with the study of MacChesney *et al.* [127], that the crystal structures of the $Bi_{1-x}Sr_xFeO_{3-\delta}$ perovskites between x = 0.2 and x = 0.67 exhibit cubic symmetry [128]. However more importantly, they performed also detailed Mössbauer spectroscopy measurements for the entire investigated doping range from which they could show that no intermediate valence state between Fe^{3+} and Fe^{4+} cations can be found, although the oxygen deficiency suggests one [128]. Instead of a certain amount of Fe^{4+} cations due to the oxygen deficiency, they found solely Fe^{3+} cations which possess two different coordination environments, an octahedral one and a tetrahedral one [128]. Furthermore they could also demonstrate from the Mössbauer spectroscopy measurements that the amount of tetrahedral coordinated Fe^{3+} cations increases with the doping concentration of diamagnetic Sr^{2+} cations [128]. Besides the decrease of the octahedrally coordinated Fe^{3+} cations with increasing strontium dopant, they could also prove that an increase of the strontium dopant leads additionally to a decrease of the observed spontaneous magnetization [128].
Regarding Mössbauer spectroscopy studies, Lepoittevin *et al.* reported for the $Bi_{1/3}Sr_{2/3}FeO_{2.67}$ perovskite that the Fe^{3+} cation has three different coordination environments, namely an octahedral one, a pyramidal one and a distorted pyramidal one [129]. Similar findings were made for $Bi_{0.5}Sr_{0.5}FeO_{3-\delta}$ by V.V. Pokatilov *et al.*, who found octahedral, tetrahedral and square-pyramidal coordinations for the Fe^{3+} cation [130], whereas V.S. Pokatilov *et al.* found octahedral and square-pyramidal coordinations for the Fe^{3+} cation in the $Bi_{0.75}Sr_{0.25}FeO_{3-\delta}$ perovskite [131]. In 2012, Gippius *et al.* showed from Mössbauer spectroscopy measurements that the spin cycloid of the solid solution end member $BiFeO_3$ is destroyed upon a strontium doping concentration of 7% [132].
Further structural studies were given by V.S. Pokatilov *et al.*, who reported from X-ray powder diffraction rhombohedral symmetry up to a composition of x = 0.1, a mixed rhombohedral and cubic phase for x = 0.1 to x = 0.15 and cubic symmetry up to a composition of x = 0.67 [133], which is in agreement with the studies of MacChesney *et al.* [127] and Li *et al.* [128]. Similar findings from X-ray powder diffraction data by Anokhin *et al.*, additionally stated that for x = 0.7 to x = 0.9 a mixed cubic and tetragonal phase must be assumed and that for x = 1 a tetragonal symmetry occurs[1] [138]. Likewise to these authors, Brinkman *et al.* and Zheng-Zheng *et al.* reported also cubic symmeties for the $Bi_{1-x}Sr_xFeO_{3-\delta}$ perovskites with x = 0.3 to x = 0.8 [139] and x = 0.4 to x = 0.6 [140].
Although many authors reported cubic symmetry, some authors claimed also other

1 Depending on the oxygen deficiency δ, the $SrFeO_{3-\delta}$ can possess different crystal structures ranging from cubic symmetries to orthorhombic incommensurate symmetries (see for instance Takeda *et al.* [134], Hodges *et al.* [135], Schmidt and Campbell [136] and Reehuis *et al.* [137]).

symmetries like Lepoittevin *et al.*, who reported an orthorhombic symmetry found by electron diffraction for the $Bi_{1/3}Sr_{2/3}FeO_{2.67}$ perovskite [129]. Also rhombohedral symmetries were reported, for instance by Khomchenko *et al.*, who used the $BiFeO_3$ space group *R*3*c* in order to model the $Bi_{1-x}Sr_xFeO_{3-\delta}$ perovskites with x = 0.2 and 0.3 [105, 141–143]. Interestingly, Withers *et al.* reported cubic symmetry by X-ray powder diffraction investigations for the $Bi_{0.54}Sr_{0.46}FeO_{2.77}$ perovskite, although they found by transmission electron microscopy investigations that the crystal structure must be described by a complicated superspace symmetry [144, 145].

However, the most important study with respect to neutron powder diffraction, (which is more sensitive to oxygen positions than X-ray powder diffraction), was carried out by Troyanchuk *et al.* [146, 147], who reported that the best refinement results for a composition above x = 0.2 could be achieved assuming a tetragonal symmetry with G-type antiferromagnetic moments. For a $Bi_{1-x}Sr_xFeO_{3-\delta}$ perovskite with x = 0.5, they stated that the (200) reflection with respect to the cubic system is significantly broadened compared to the (111) reflection and therefore they explained this observation by a tetragonal distortion [146, 147]. Furthermore they observed also a transition region for the composition of x = 0.07 to x = 0.14, were they assumed a rhombohedral and a tetragonal phase [147]. Interestingly, these results are partially in contradiction to a study performed by Pachoud *et al.*, who showed from synchrotron X-ray powder diffraction and neutron powder diffraction that the $Bi_{1-x}Sr_xFeO_{3-\delta}$ perovskite with x = 0.75 can be described in a cubic symmetry[1] [148].

Concerning the multiferroic properties there were also different results reported. Khomchenko *et al.* reported that they could confirm spontaneous electric polarization by piezoresponse force microscopy for the $Bi_{1-x}Sr_xFeO_{3-\delta}$ perovskites with x = 0.2 and x = 0.3 [105, 141–143]. From their measurements they concluded that a doping by Sr^{2+} cations leads to a suppression of the displacement of the Bi^{3+} cation and therefore to a suppression of the ferroelectricity [105]. In addition, for the same compositions, they carried out measurements of the spontaneous magnetization (similar to MacChesney *et al.* [127] and Li *et al.* [128]) from which they found weak ferromagnetism in the $Bi_{0.7}Sr_{0.3}FeO_3$ perovskite [105, 142] and no spontaneous magnetization for the $Bi_{0.8}Sr_{0.2}FeO_3$ perovskite [141, 143]. Similar to Khomchenko *et al.*, Wang *et al.* found the highest spontaneous magnetization for a composition with x = 0.3, although they also observed spontaneous magnetization for a composition of x = 0.2 [149] and no spontaneous magnetization for x = 0.1, which in turn is in contradiction to results from Zheng-Zheng *et al.* [140], who reported the highest value for the spontaneous magnetization at a composition level of x = 0.1. However, Zheng-Zheng *et al.* agreed on the ferroelectric behavior of the $Bi_{1-x}Sr_xFeO_{3-\delta}$ perovskites found by Khomchenko *et al.* [105, 141–143] and they stated that it can be observed within a compositional range of x = 0 to x = 0.4 [140].

A possible explanation for the contradictory results regarding the weak ferromagnetism

1 The modeling of the cubic symmetry by Pachoud *et al.* was done either by using a disorder model within the cubic symmetry or by using anisotropic displacement parameters [148].

was given by Troyanchuk *et al.*, who observed that the spontaneous magnetization is probably affected by the synthesis conditions [146]. In addition, they assumed that the spontaneous magnetization above a composition of x = 0.2 is caused by impurities [147]. Further, they explained that it is very likely that a small number of oxygen vacancies leads to the destruction of the spin cycloid and to a canting of the antiferromagnetically aligned magnetic moments [147]. In addition, they believed that the lowering of the octahedral distortions due to the loss of the rhombohedral $R3c$ symmetry at x = 0.15 also leads to the loss of ferroelectricity [146], which in turn would stand in contradiction to the findings of Khomchenko *et al.* [105, 141–143] and Zheng-Zheng *et al.* [140].

From this extended overview, it can be stated that the amount of oxygen vacancies and the actual crystal structure symmetries play a crucial role for the ferroelectric and magnetic behavior in the $Bi_{1-x}Sr_xFeO_{3-\delta}$ perovskite system. Therefore, in this work, an accurate symmetry determination at room temperature for the $Bi_{1-x}Sr_xFeO_{3-\delta}$ perovskites with a compositional range of x = 0 to x = 0.5 was carried out, using synchrotron X-ray and neutron powder diffraction. In addition, using neutron powder diffraction, high temperature experiments were performed in order to determine the behavior of the oxygen stoichiometry and therefore the oxygen vacancies using a special gas environment which possibly allows for fast oxygen exchange kinetics within the powder. As some authors reported a weak ferromagnetic behavior above a composition of x = 0.1 (which suggest a spin canting of the G-type antiferromagnetically aligned magnetic moments), detailed reinvestigations of the magnetic structure were undertaken in order to search for peak asymmetries which probably can indicate such canting behaviors. Furthermore the critical Néel temperatures for the $Bi_{1-x}Sr_xFeO_{3-\delta}$ perovskites are determined from neutron powder diffraction and differential scanning calorimetry, as the literature values seems also to be ambiguous[1].

3.2 Synthesis

The synthesis of the $Bi_{1-x}Sr_xFeO_{3-\delta}$ perovskites (with x = 0, 0.1, 0.2, 0.3, 0.4 and 0.5) was carried out at the Max Planck Institute for Solid State Research by Dr. Anja Wedig. The synthesis of the reddish-brown colored $Bi_{1-x}Sr_xFeO_{3-\delta}$ powders with x = 0.1, 0.2, 0.3, 0.4 and 0.5 was performed by solid state reactions of Bi_2O_3, $SrCO_3$ and Fe_2O_3 powders, which were first ground in a mortar and then calcined for 2 hours at 770°C in an oven. After the first calcination process, the powders were ball-milled for 1 hour in a zirconia ball mill (Fritsch, Germany) and then calcinated again for 8 hours at the corresponding temperature given in table 3.1 below, followed by another

1 For instance V.S. Pokatilov *et al.* reported a value of T_N = 670(3) K [131] for the $Bi_{0.75}Sr_{0.25}FeO_{3-\delta}$ perovskite from Mössbauer spectroscopy measurements , whereas Pachoud *et al.* reported a value of T_N = 643 K for the same composition from neutron powder diffraction measurements [148].

ball-milling of the powders for 1 hour. The last step with 8 hours heating and 1 hour ball-milling was repeated for a second time until the final synthesized $Bi_{1-x}Sr_xFeO_{3-\delta}$ powders (with x = 0.1, 0.2, 0.3, 0.4 and 0.5) were obtained. Further details of the above described solid state reactions can be found in the doctoral thesis of Dr. Anja Wedig [150].
For the synthesis of the $BiFeO_{3-\delta}$ perovskite powders a different synthesis route was used. The glycine-nitrate process [151] requires two solutions of Bi_2O_3 in a 3:2 volume mixture of double-distilled water and 65% nitric acid and $Fe(NO_3)_3$ in double-distilled water. Combustion of a mixture of both solutions together with glycine yielded a solid residue, which was ground in a mortar and then heated for 2 hours at 700°C in an oven. As final step the $BiFeO_{3-\delta}$ powder was ball-milled for 1 hour. Further details of the used glycine-nitrate process for the synthesis of the $BiFeO_{3-\delta}$ perovskite powder can be found in the doctoral thesis of Dr. Anja Wedig [150].

Table 3.1: Oven temperatures for the synthesis of the $Bi_{1-x}Sr_xFeO_{3-\delta}$ perovskite powders. The heating rate of the oven was 10 K/min and the cooling rate was 20 K/min.

Compound	Oven temperature
$Bi_{0.5}Sr_{0.5}FeO_{3-\delta}$	1050°C
$Bi_{0.6}Sr_{0.4}FeO_{3-\delta}$	1050°C
$Bi_{0.7}Sr_{0.3}FeO_{3-\delta}$	950°C
$Bi_{0.8}Sr_{0.2}FeO_{3-\delta}$	950°C
$Bi_{0.9}Sr_{0.1}FeO_{3-\delta}$	950°C
$BiFeO_{3-\delta}$	700°C

3.3 Experimental setup

Room temperature synchrotron X-ray powder diffraction measurements of the $Bi_{0.5}Sr_{0.5}FeO_{3-\delta}$ sample in a capillary were performed by Dr. Andy Fitch at the European Synchrotron Radiation Facility (ESRF), Grenoble at the former beamline ID31. The collection of the diffraction patterns was done in Debye-Scherrer mode using a wavelength of $\lambda = 0.30646(1)$ Å (≈ 40.46 keV) with a channel cut Si(111) monochromator. Diffracted X-rays were detected using scintillation counters integrated in a 9-channel Si(111) multianalyzer stage.

Further room temperature synchrotron X-ray powder diffraction measurements of the $Bi_{1-x}Sr_xFeO_{3-\delta}$ perovskites (with x = 0, 0.2 and 0.5) in capillaries were carried out by Dr. Oksana Magdysyuk, Frank Adams, Dr. Tomce Runcevski and Prof. Dr. Robert E. Dinnebier at the PETRAIII Deutsche Elektronensynchrotron (DESY), Hamburg at beamline P02.1. The collection of the diffraction patterns was done in Debye-Scherrer mode using a wavelength of $\lambda = 0.206834(1)$ Å (≈ 59.94 keV) obtained by a double crystal Laue monochromator of diamond(111) and Si(111) crystals. Diffracted X-rays

were detected using a fast area Perkin Elmer image plate detector.
The integration of the collected two-dimensional Debye-Scherrer rings to one-dimensional powder diffraction patterns was subsequently performed using the computer program FIT2D [152]. The parameters which were required for this integration were determined from a LaB_6 reference sample.

Temperature dependent neutron powder diffraction measurements of the $Bi_{1-x}Sr_xFeO_{3-\delta}$ samples (with x = 0, 0.1, 0.2, 0.3 and 0.5) were performed by the author and collaborators (Dr. Anatoliy Senyshyn, Dr. Dominik Samuelis, Dr. Anja Wedig, Nils Ohmer) at the neutron research reactor Heinz Maier-Leibnitz (FRM II), Garching at the SPODI high resolution neutron powder diffractometer. During neutron irradiation, the samples were stored in niobium containers, which had a diameter of 12 mm, a wall thickness of 50 µm and a fill height of the powders of approximately 30 mm. The collection of the neutron diffraction patterns was done in Debye-Scherrer geometry using two different wavelengths (see table 3.2). Monochromatic neutrons at these wavelengths were obtained using Ge(551) crystals. Diffracted neutrons were detected by 80 position sensitive 3He counting tubes with a height of 30 cm which covered a 2θ range of 0° to 160°. Each counting tube covers an angle range of 0.05° which requires 40 steps in order to measure the full 2° range which corresponds to the measurable range of one counting tube. Further details of the SPODI diffractometer can be found in the publication of Hoelzel *et al.* [153].
The integration of the collected cuts of two-dimensional Debye-Scherrer rings to one-dimensional powder diffraction patterns was subsequently performed by a non-commercial beamline scientist written program. The resulting usable range of the so obtained powder diffraction patterns is 0.95° 2θ to 151.9° 2θ. In order to obtain a sufficient counting statistic for the measured diffractograms, each diffractogram was integrated for half an hour and five diffractograms were collected at each temperature step and subsequently added to a single diffractogram.

Table 3.2: Wavelengths for the high resolution neutron powder diffraction measurements of $Bi_{1-x}Sr_xFeO_{3-\delta}$ perovskite powders.

Compound	Neutron wavelength
$Bi_{0.5}Sr_{0.5}FeO_{3-\delta}$	1.548140(20) Å
$Bi_{0.7}Sr_{0.3}FeO_{3-\delta}$	1.548296(20) Å
$Bi_{0.8}Sr_{0.2}FeO_{3-\delta}$	1.548140(20) Å
$Bi_{0.9}Sr_{0.1}FeO_{3-\delta}$	1.548296(20) Å
$BiFeO_{3-\delta}$	1.548140(20) Å

In order to perform temperature dependent neutron powder diffraction measurements, the niobium containers were put into a high temperature furnace [153], which can be used either evacuated or with gases at small pressures.
Due to the fact that the temperature dependent neutron powder diffraction experiment should also reveal the oxygen kinetics of the $Bi_{1-x}Sr_xFeO_{3-\delta}$ perovskite powders, a special gas environment and special heating procedures were required. For the room

temperature measurements the furnace was evacuated until a high vacuum of 10^{-4} – 10^{-5} mbar was reached. For all elevated temperature measurements the furnace was filled with a special argon-oxygen gas mixture with a partial oxygen pressure of pO_2 = 49.27 ppm. For the temperature dependent measurements below 300 °C, approximately 20 mbar of this special gas was filled into the furnace, whereas for temperature measurements of 300 °C and above a gas pressure of approximately 50 mbar was chosen. Before changing the gas pressure at a temperature of 300 °C, the samples were equilibrated for 20-30 min at 300 °C and a gas pressure of approximately 20 mbar. The heating rate for all temperature steps was 0.5 $\frac{^{\circ}C}{s}$ and the neutron powder diffraction measurements were at the earliest started, when the temperature fluctuation was below 0.1 °C at a particular temperature step.
The reason for this special gas-filling and heating procedure as described above is the following: Below temperatures of 300 °C it can be expected that only oxygen from the surface is exchanged with the gas environment, therefore a smaller defined partial oxygen pressure can be used as the amount of exchanged oxygen is lower than for the exchange of oxygen from the bulk [154, 155]. The annealing step at a temperature of 300 °C is performed in order to activate the bulk diffusion of the oxygen in the $Bi_{1-x}Sr_xFeO_{3-\delta}$ perovskites [154, 155]. The elevated pressure at 300 °C and above is used in order to have a defined oxygen environment [154, 155]. Such a defined oxygen partial pressure ensures that the oxygen in the powders is in balance with the environment and that the maximum of the diffusion coefficient can be reached[1] [154–156]. With respect to the temperature dependent neutron powder diffraction measurements, this entire procedure is crucial, as it ensures that not only the loss of oxygen in these perovskites can be studied, but also the incorporation kinetics of oxygen into the $Bi_{1-x}Sr_xFeO_{3-\delta}$ compounds. General informations about the oxygen kinetics in perovskites (especially $SrTiO_3$) can be found in the publication of Merkle and Maier [154, 155] and detailed informations about the oxygen kinetics in $Bi_{1-x}Sr_xFeO_{3-\delta}$ perovskites can be found in the doctoral thesis of Dr. Anja Wedig [150].

The measurement of the heat flow was done using a commercial differential scanning calorimeter Pyris 1 of the PerkinElmer corporation. The measured temperature range was 50 K to 600 K and the heating rate was 10 K/min. Measurements were kindly carried out by Ewald Schmitt, who provided for the author the measured raw data.

1 For $SrTiO_3$ the maximum of the chemical diffusion coefficient for oxygen at elevated temperatures is reached at a partial oxygen pressure of approximately 10^{-8} bar [154–156]. If it is assumed that the $Bi_{1-x}Sr_xFeO_{3-\delta}$ perovskites have the maximum chemical diffusion coefficient for oxygen at elevated temperatures at a similar level of the partial oxygen pressure, then the required gas pressure of an Ar/O_2 gas mixture with a partial oxygen pressure of $pO_2 \approx 50$ ppm can be calculated. Taking Dalton's law for partial pressures and roughly the estimation that the number of parts in a gas are equivalent to the partial pressure, then a value of 50 mbar Ar/O_2 ($pO_2 \approx 50$ ppm) corresponds to a partial oxygen pressure of $250 \cdot 10^{-8}$ bar. Please note that this value is much higher then the desired value of 10^{-8} bar, which leads to a lower chemical diffusion coefficient for oxygen at these temperatures.

3.4 Determination of crystal structures at room temperature from powder diffraction data

The investigation of the $Bi_{1-x}Sr_xFeO_{3-\delta}$ perovskites (with x $\geq$ 0.14) by different authors showed (see section 3.1), that these compounds can be in general described with a cubic crystal structure in space group $Pm\bar{3}m$ or with a tetragonal crystal structure in space group $P4/mmm$[1][2] [146, 147, 157]. In order to unveil the most probable symmetry and therefore the most probable crystal structure for the $Bi_{1-x}Sr_xFeO_{3-\delta}$ perovskites (with x = 0.1, 0.2, 0.3 and 0.5) different synchrotron X-ray powder diffraction measurements and high resolution neutron powder diffraction measurements at room temperature were performed[3].

All measured synchrotron X-ray powder diffractograms were treated with Rietveld analysis which was performed using a commercial version of the TOPAS 4.2 program [57] offered by the Bruker AXS Corporation. Rietveld refinements of neutron powder diffractograms were done using a test version of the TOPAS 5 program, as this new version is able to carry out Rietveld refinements of commensurate magnetic structures. The refinement of the high resolution neutron powder diffraction data of $BiFeO_3$ was performed with the FullProf program suite [83], due to the presence of an incommensurate magnetic structure. For all data sets, independent from the particle type (photon or neutron), the diffraction background was modeled by refineable Chebyshev polynomials and the peak shape modeling of the Bragg reflections was done using the fundamental parameter approach[4] [159, 160]. The zero shift was individually determined for each room temperature powder diffraction pattern. Peak broadening of all crystalline phases due to sample dependent effects was modeled by the integrated crystallite size and phenomenological strain macros (a detailed explanation of these macros can be found in the TOPAS 4.2 manual [57] and partially in section 4.4). The synchrotron as well as the neutron radiation was assumed to be 100% horizontally polarized.

Due to the influence of the different radiation types and the different diffractometer setups on the physical observable peak shape, different peak shape corrections were required for a successful Rietveld refinement. For the synchrotron X-ray powder diffraction measurements carried out at beamline ID31, the peak asymmetry due to

1 The usage of a tetragonal space group by some authors is owed to the fact that they claim that a slight tetragonal distortion can be present in the crystal structure, which means that the tetragonal lattice parameter c is almost equal to the tetragonal lattice parameter a

2 There exist also approaches to describe the $Bi_{0.7}Sr_{0.3}FeO_{3-\delta}$ perovskite with the trigonal crystal structure of the undoped $BiFeO_3$ compound [105].

3 The crystal structure of the $BiFeO_3$ perovskite in space group $R3c$ is well known from extensive powder and single crystal studies, therefore this compound will be not treated within this section

4 Except for the refinement of the $BiFeO_3$ perovskite, where for the refinement in FullProf refineable Chebyshev polynomials for the background and a pseudo Voigt peak shape with a modeling of the full width half maximum (FWHM) by the phenomenlogical Caglioti formula $FWHM^2 = W + V \cdot \tan\theta + U \cdot \tan^2\theta$ [158] was used.

axial divergence was corrected by a model developed by Finger *et al.* [161]. For the synchrotron X-ray powder diffraction measurements carried out at beamline P02.1, no obvious peak asymmetry in the diffraction patterns could be observed, therefore no additional correction was necessary. For the high resolution neutron powder diffraction measurements several corrections had to be applied. These corrections were determined by carrying out careful Rietveld refinements of silicon reference samples. The first applied correction is a simple axial model which corrects for the peak asymmetry due to axial divergence. A second more phenomenological correction had to be applied for the aperture of the detector slit and a third also more phenomenological correction had to be applied for the variable beam divergence[1].
In addition to the observable $Bi_{1-x}Sr_xFeO_{3-\delta}$ perovskite phase another phase can be seen throughout all neutron powder diffraction patterns. This phase belongs to the niobium containers, which were used as sample holders and therefore this phase was modeled as an additional Rietveld phase.

In order to determine whether the $Bi_{1-x}Sr_xFeO_{3-\delta}$ perovskites (with x = 0.1, 0.2, 0.3 and 0.5) possess a cubic or tetragonal crystal structure at room temperature, careful Rietveld refinements in both space groups were carried out. For all Rietveld refinements, the occupancy between the Bi cation and the Sr cation was constrained in such a way, so that the real composition can be directly obtained by the refinement. Contrary, the occupancy of the Fe cation was fixed to full occupation, whereas the occupancies of the oxygen anions are refined. Symmetry dependent anisotropic displacement parameters (ADP) were used for all atomic positions, as these parameters can be very sensitive to false space groups. In the neutron powder diffraction measurements, magnetic Bragg reflections were incorporated using the results from section 3.5. The results of all these refinements are given representatively by the corresponding R_{wp} values in table 3.3.

Although the R_{wp} values of the tetragonal crystal structure in table 3.3 are always lower than those of the corresponding cubic crystal structure, it is very unlikely that the $Bi_{1-x}Sr_xFeO_{3-\delta}$ perovskites (with x = 0.2, 0.3 and 0.5) posses a tetragonal symmetry. This can be explained by the fact, that in general the difference between the corresponding R_{wp} values for the synchrotron X-ray powder diffraction measurements is always smaller than 0.1 %, which is a too small difference in order to give a clear indication of a symmetry change. In addition, the refined ADPs in the tetragonal crystal structure gave unreasonably large values for the oxygen anions, whereas the ADPs for the cubic crystal structure are all in a physical acceptable range (e.g. for the refinement of $Bi_{0.5}Sr_{0.5}FeO_{3-\delta}$ measured at ID31: Bi/Sr: u11 = u22 = u33 = 0.05268(18), u12 = u13 = u23 = 0; Fe: u11 = u22 = u33 = 0.01569(23), u12 = u13

1 These corrections are in principle phenomenological, but the mathematical calculus accounts for the way, how the neutron intensity is detected by the horizontally aligned detectors and how the cuts of the two-dimensional Debye-Scherrer rings are integrated into one-dimensional powder diffraction patterns. For the refinement of the $BiFeO_3$ perovskite, the integrated asymmetry corrections in FullProf were used.

Table 3.3: Space group dependent R_{wp} values determined for the refined $Bi_{1-x}Sr_xFeO_{3-\delta}$ perovskite powder patterns measured at different synchrotron X-ray powder diffractometers (ID31, P02.1) and a neutron powder diffractometer (SPODI). For the diffraction pattern of $Bi_{0.9}Sr_{0.1}FeO_{3-\delta}$ a clear determination of the space group could not be carried out.

Compound	Beamline	$Pm\bar{3}m$ R_{wp} (%)	$P4/mmm$ R_{wp} (%)
$Bi_{0.5}Sr_{0.5}FeO_{3-\delta}$	ID31	10.144	10.116
$Bi_{0.5}Sr_{0.5}FeO_{3-\delta}$	P02.1	6.296	6.200
$Bi_{0.5}Sr_{0.5}FeO_{3-\delta}$	SPODI	8.117	7.919
$Bi_{0.7}Sr_{0.3}FeO_{3-\delta}$	SPODI	7.427	7.334
$Bi_{0.8}Sr_{0.2}FeO_{3-\delta}$	P02.1	8.181	8.144
$Bi_{0.8}Sr_{0.2}FeO_{3-\delta}$	SPODI	8.148	8.063
$Bi_{0.9}Sr_{0.1}FeO_{3-\delta}$	SPODI	-	-

= u23 = 0 and O: u11 = 0.02630(195), u22 = u33 = 0.06835(198), u12 = u13 = u23 = 0)[1]. The same effect can be observed for the high resolution neutron powder diffraction measurements, where the difference in the R_{wp} values is a bit higher (≤ 0.2 %): The cubic crystal structures have reasonable ADPs, whereas the tetragonal crystal structures posses ADP values, which imply too large anisotropic displacements of the corresponding atomic positions at room temperature.
Interestingly, for the $Bi_{0.9}Sr_{0.1}FeO_{3-\delta}$ sample the symmetry could not be determined unambiguously. The majority of the room temperature neutron powder diffraction pattern can be refined with a trigonal phase (space group $R3c$), which is almost isostructural to the crystal structure of the $BiFeO_3$ perovskite at room temperature, except for the shared atomic position of the Bi and Sr cation. Unfortunately the Rietveld refinement of this phase does not cover the entire observable intensity, although the corresponding magnetic Bragg reflections are accounted. Troyanchuk *et al.* reported the same phenomenon, namely, that they could not synthesize a phase pure $Bi_{0.9}Sr_{0.1}FeO_{3-\delta}$ perovskite which consists of only one crystalline phase[147]. In detail, they were not able to synthesize phase pure compounds in a range of $0.07 \leq x \leq 0.14$ and they concluded that these compounds must be a mixture of two phases of rhombohedral/trigonal and pseudo-tetragonal (or in the present case cubic) character [147]. Although it is very likely that this assumption is correct, it was not possible to carry out a two-phase mixture Rietveld refinement of the powder diffraction pattern of $Bi_{0.9}Sr_{0.1}FeO_{3-\delta}$ which is precise enough to use it for further investigations of the temperature dependent magnetic behavior or for the clear determination of the oxygen stoichiometry. Therefore this sample will be neglected in the following discussions.

Although many authors claim that the $Bi_{1-x}Sr_xFeO_{3-\delta}$ perovskites with $0.2 \leq x \leq 0.5$

1 The reported values of the anisotropic displacement parameters are of the same order as reported by Pachoud *et al.* [148].

have a tetragonal distortion [146, 147, 157], the present study cannot find any clear evidence for that. Certainly it cannot be ruled out that special synthesis conditions favor a tetragonal rather than a cubic symmetry, but in the present case under the synthesis conditions described in section 3.2, the $Bi_{1-x}Sr_xFeO_{3-\delta}$ perovskites with $0.2 \leq x \leq 0.5$ have most probable a cubic crystal structure. Therefore these compounds will be treated as cubic perovskites in the subsequent sections.

3.4.1 Investigation of the diffraction background

In all (temperature dependent) powder diffraction patterns of the $Bi_{1-x}Sr_xFeO_{3-\delta}$ perovskites (with x = 0.1, 0.2, 0.4 and 0.5) the background shows a very corrugated behavior, which especially can be seen if the intensity is plotted in a logarithmic scale. In figure 3.1 the background of the powder diffraction experiments of the $Bi_{0.5}Sr_{0.5}FeO_{3-\delta}$ perovskite with different radiation types is exemplarily shown.

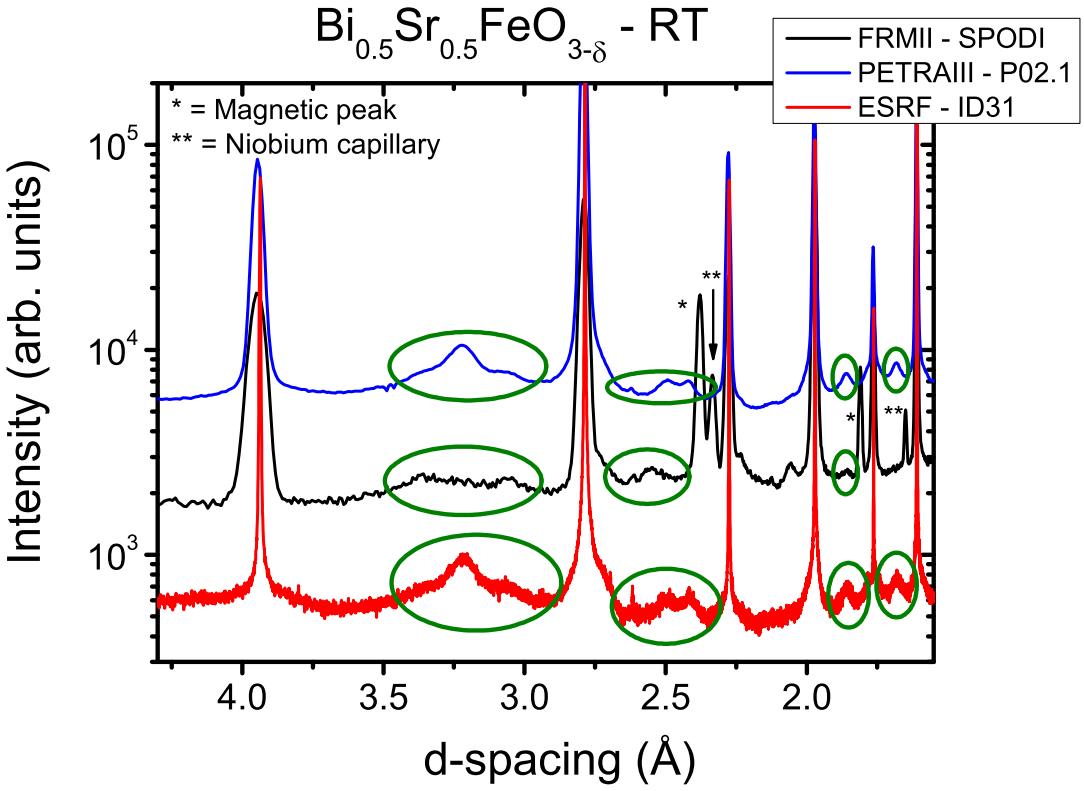

Figure 3.1: Corrugated background in the room temperature powder diffraction measurements of the $Bi_{0.5}Sr_{0.5}FeO_{3-\delta}$ perovskite. Peak like observations are marked with green circles.

Some parts of the corrugated background have almost peak like character of very broadened peaks, therefore it was tried to find superstructure models, which are able to fit the observed broadened peaks. In doing so, cubic and tetragonal crystal structures where probed with a maximal unit cell volume of 64 times the primitive perovskite

unit cell volume. Although it was partially possible to model some of these broadened peaks, no unit cell could be found which was able to model all observed peak like corrugations. Even the assumption of two phases, one which is a crystalline phase without superstructure and one which is a crystalline phase with superstructure, failed.
A possible explanation for the observed corrugated background in a most likely pure phase can be given, if the assumption is made that the powder grains contain stacking faults. In general, there are different options how stacking faults become noticeable in a powder diffraction pattern. In many cases, if stacking faults are present, the Bragg reflection gets unnatural broadened at the base of the peak [162]. This broadening is often very asymmetric giving rise to a hump on one side of the base of the peak. Besides this option how stacking faults can become visible, there exist also cases where the stacking faults can produce sharp or almost sharp peaks. The reason for that is quite simple. If the stacking faults exhibit a more or less regular packing, than something like a crystal structure with a larger unit cell is created. This larger unit cell can be often described as superstructure of the basic crystal structure and therefore sharp Bragg reflections are expected. If the packing of the stacking faults is no longer regular, than no distinct superstructure can be assumed and this gives rise to very broadened nearly amorphous like peaks.
In the special case of the $Bi_{1-x}Sr_xFeO_{3-\delta}$ perovskites it seems to be possible to find an approximate structure, perhaps with a lower symmetry than probed with the first trials above. However, it is a challenging task to find an appropriate superstructure model which is able to model the observed background behavior, as computer programs, which allow a direct modeling of stacking faults from a powder diffraction pattern, are still under development[1]. Therefore the investigation of the stacking faults in the $Bi_{1-x}Sr_xFeO_{3-\delta}$ perovskites is a subject of future investigations[2].
In order to handle the present corrugated background, especially for the neutron powder diffraction data refinements, Chebyshev polynomials of very high order (up to 14th order) must be applied.

3.5 Sequential Rietveld refinement of high-temperature neutron powder diffraction data

In this section, detailed investigations of the high resolution neutron powder diffraction data of the $Bi_{1-x}Sr_xFeO_{3-\delta}$ perovskites are presented, in order to reveal the behavior of the intrinsic oxygen stoichiometry under heating and the given environmental conditions by the application of a special gas environment. Another aspect of this investigation is a detailed temperature dependent analysis of the magnetic structure,

1 A promising approach for the modeling of stacking faults in TOPAS is given by Bette *et al.*, who used global optimization methods in order to model different stacking fault types in NiCl(OH) [163].
2 Different attempts to find the superstructure lattice parameters with the program K_Search [83] from the FullProf program suite [83] failed.

which will be compared to the results given in the literature. Furthermore the Néel temperature of these compounds will be, to the knowledge of the author, for the first time accurately determined by a power-law fit of the Rietveld refined components of the magnetic moments.

3.5.1 Determination of the magnetic propagation vectors

In general, the determination of the magnetic propagation vectors $\vec{k}$ is similarly done as the determination of the propagation vector of a crystallographic superstructure. First the positions of the magnetic Bragg peaks in a neutron powder diffraction have to be identified, which then, together with the information of the basic crystal structure, are subjected to a program like K_Search [83] from the FullProf program suite [83]. With K_Search, it is possible to search either for commensurate or incommensurate magnetic or crystallographic superstructures. The result after a run of the K_Search program is a list with probable propagation vectors, which are judged by the following R-factor:

$$R_{factor} = \sum_{Given\ observations} \frac{|S_{obs} - S_{calc,closest}|}{S_{obs}} \quad , \tag{3.1}$$

where S_{obs} is an observed reciprocal d-spacing $\frac{1}{d}$ and $S_{calc,closest}$ is the closest calculated reciprocal d-spacing.

For all $Bi_{1-x}Sr_xFeO_{3-\delta}$ perovskites (with x = 0, 0.2, 0.3 and 0.5) the magnetic Bragg peaks were identified and the individual magnetic propagation vectors $\vec{k}$ were determined by K_Search. The results for the cubic and as well as for the tetragonal crystal structures can be found in table 3.4, where the determined $\vec{k}$ vector and the corresponding R_{factor} are given. Please note that the results for the tetragonal crystal structures were only determined in order to perform Rietveld refinements for the symmetry determination in section 3.4. Please note further that for the diffraction pattern of the $Bi_{0.9}Sr_{0.1}FeO_{3-\delta}$ perovskite no clear determination of the space group of the crystal structure could be carried out and therefore no magnetic propagation vector could be determined. Interestingly, for all cubic $Bi_{1-x}Sr_xFeO_{3-\delta}$ perovskites with x = 0.2, 0.3 and 0.5 the same commensurate magnetic propagation vector of $\vec{k} = (0.5, 0.5, 0.5)^T$ is found. This magnetic propagation vector with a value of 0.5 for each component suggests a doubling of the crystallographic unit cell in each direction, which would lead to a magnetic unit cell volume of 8 times the crystallographic unit cell volume. Later in section 3.5.2 we will see that with an appropriate choice of the crystallographic unit cell a magnetic unit cell with a volume of 4 times the crystallographic unit cell volume can give a sufficient description of the observed ordering of the magnetic moments. A commensurate magnetic propagation vector of $\vec{k} = (0.5, 0.5, 0.5)^T$ was also determined for the $Bi_{1-x}Sr_xFeO_{3-\delta}$ perovskites (with x $\geq$ 0.14) by Troyanchuk *et al.* [146, 147] and Pachoud *et al.* [148].

In contrast to the determination of the magnetic propagation vectors for the

Table 3.4: Commensurate magnetic propagation vectors $\vec{k}$ determined for the $Bi_{1-x}Sr_xFeO_{3-\delta}$ perovskites. For the diffraction pattern of $Bi_{0.9}Sr_{0.1}FeO_{3-\delta}$ a clear determination of the space group of the crystal structure could not be carried out and therefore no magnetic propagation vector could be determined. The values for the space group $P4/mmm$ were determined in order to perform a refinement of the magnetic Bragg reflections in section 3.4 in order to determine the most probable symmetry of the $Bi_{1-x}Sr_xFeO_{3-\delta}$ perovskites with $0.2 \leq x \leq 0.5$.

Compound	$Pm\bar{3}m$		$P4/mmm$	
	$\vec{k}$	R-factor (%)	$\vec{k}$	R-factor (%)
$Bi_{0.5}Sr_{0.5}FeO_{3-\delta}$	$(0.5, 0.5, 0.5)^T$	0.0477	$(0.5, 0.5, 0.5)^T$	0.0442
$Bi_{0.7}Sr_{0.3}FeO_{3-\delta}$	$(0.5, 0.5, 0.5)^T$	0.0483	$(0.5, 0.5, 0.5)^T$	0.0460
$Bi_{0.8}Sr_{0.2}FeO_{3-\delta}$	$(0.5, 0.5, 0.5)^T$	0.0855	$(0.5, 0.5, 0.5)^T$	0.0791
$Bi_{0.9}Sr_{0.1}FeO_{3-\delta}$	-	-	-	-

$Bi_{1-x}Sr_xFeO_{3-\delta}$ perovskites (with x = 0.2, 0.3 and 0.5), the determination of the magnetic propagation vector of $BiFeO_3$ is far more challenging. From the literature it is known that for the $BiFeO_3$ perovskite the local description of the alignment of the magnetic moments can be given by a G-type antiferromagnetic model of the magnetic moments parallel to the crystallographic *c*-axis with a magnetic propagation vector of $\vec{k} = (0, 0, 0)^T$ [109–111]. Such a magnetic propagation vector with only zero components means that the magnetic unit cell coincidences with the crystallographic unit cell [111]. Amazingly, this model is not correct on a larger scale as it could be shown by Sosnowska *et al.* in 1982 from time-of-flight neutron measurements of a polycrystalline sample of $BiFeO_3$ [112, 113]. With the much higher resolution from the neutron time-of-flight diffractometer it was possible to show, that the first magnetic Bragg peak, consists of four different peaks[1], which led to the determination of a new incommensurate magnetic propagation vector of $\vec{k} = (0.0045, 0.0045, 0)^T$ [112, 113]. Therefore, the model of the magnetic structure of the $BiFeO_3$ perovskite had to be revised. The new model of the alignment of the magnetic moments gave a spin cylcoid in the *a*-*b* plane of the crystal structure with a huge period of the cycloid of approximately 620 Å [112].

Unfortunately, the resolution of the high resolution neutron powder diffractometer SPODI was not sufficient to see the splitting of the first magnetic Bragg peak, although a hint on a non-zero magnetic propagation vector was given by the asymmetry of the observed peak shape. Investigations with K_Search revealed that the correct incommensurate magnetic propagation vector could not be determined. A determination of a possible commensurate solution with K_Search suggested a magnetic propagation vector with $\vec{k} = (2/3, 0, 2/3)^T$ ($R_{factor} = 0.3673$) which is even more incorrect than

1 In particular, the first magnetic Bragg peak is build by two reflections, (003) and (101), of a simple G-type antiferromagnetic model. In the time-of-flight measurements, these two reflections are clearly distinguishable and in addition, the (101) has two satellite reflections. which results in a total number of 4 magnetic Bragg reflections at the observed position.

the local picture with a magnetic propagation vector of $\vec{k} = (0, 0, 0)^T$ (the R_{factor} for this solution determined by K_Search is $R_{factor} = 0.507707$).
In order to determine which magnetic model is suited to model the observed magnetic Bragg peaks, different Rietveld refinements with different magnetic models were carried out. Finally, it turned out that the best fit could be achieved, if the description with a magnetic propagation vector of approximately $\vec{k} = (0.0045, 0.0045, 0)^T$ as determined by Sosnowska *et al.* [112] is applied, because this accounts best for the observed asymmetry of the peak shape.

3.5.2 Determination of the magnetic structure using symmetry modes

With the knowledge of the magnetic propagation vector $\vec{k} = (0.5, 0.5, 0.5)^T$ and the basic crystal structure in space group $Pm\bar{3}m$ it is possible to explore probable commensurate magnetic structures for the $Bi_{1-x}Sr_xFeO_{3-\delta}$ perovskites (with x = 0.2, 0.3 and 0.5). For the exploration of probable magnetic structures two very powerful tools, which are available online, can be used: "ISODISTORT" developed by Campbell *et al.* [64] and "MAXMAGN" developed by Perez-Mato *et al.* [164] which is part of the "Bilbao Crystallographic Server" [76–78]. With this tools it is possible to derive different probable magnetic structures using group theoretical methods and representation theory, which can then be subsequently tested by a Rietveld refinement on the experimentally observed powder diffraction pattern.

Similar to the description of a crystal structures, it is always mandatory to find the highest possible symmetry with the lowest unit cell volume which is able to give a full description of the magnetic structure. Therefore, in the first instance two solutions with tetragonal symmetry given by ISODISTORT were considered[1]. The first solution has a Shubnikov group label of I_c4/mcm (140.550) in the BNS setting and a label of $P_I4/mm'm'$ (123.19.1017) in the OG setting. The volume of this magnetic unit cell is four times the volume of the crystallographic unit cell with lattice parameters $a = \sqrt{2} \cdot a_p$, $b = \sqrt{2} \cdot a_p$ and $c = 2 \cdot a_p$ (a_p is the simple cubic lattice parameter of the $Bi_{1-x}Sr_xFeO_{3-\delta}$ perovskites). In this model, the magnetic moments are aligned along the *c*-axis of the cubic perovskite with a G-type antiferromagnetic arrangement. The second solution has also tetragonal symmetry and it seems to be a crystallographically equal solution to the first one[2]. The Shubnikov label for this symmetry is I_bmma (74.562) in the BNS setting and $C_Im'mm$ (65.18.562) in the OG setting. The volume of this magnetic unit cell is equivalently also four times the crystallographic unit cell with another choice of the lattice parameters $a = \sqrt{2} \cdot a_p$, $b = 2 \cdot a_p$ and $c = \sqrt{2} \cdot a_p$
In this model, the magnetic moments are aligned along the face diagonal of the *a*-*c*

1 For both solutions the primary order parameter, which allows for a continuous phase transition [64], is given by the irreducible representation mR5-.

2 In 1959, Gen Shirane showed that for a collinear magnetic structure with tetragonal symmetry only the angle between the magnetic moments and the unique crystallographic axis can be determined unambiguously in a neutron powder diffraction experiment [65, 84, 165].

plane of the cubic perovskite with a G-type antiferromagnetic arrangement. Individual Rietveld refinements with both models in TOPAS 5 using magnetic symmetry modes determined from ISODISTORT revealed, that both solutions resulted in the same values of the residual factors, which was expected due to the equivalence of both models. Although both models can be chosen in order to describe the correct G-type antiferromagnetic structure, it is better to use the first one, as the index i of the isotropy subgroup relative to the cubic parent space group is lower and the alignment of the magnetic moments along the c-axis is more convenient for visualization (see figure 3.2).

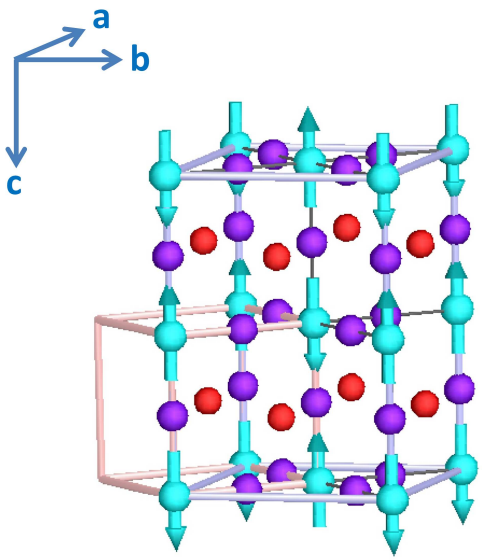

Figure 3.2: Tetragonal magnetic unit cell and magnetic moments of the $Bi_{1-x}Sr_xFeO_{3-\delta}$ perovskite (with x = 0.2, 0.3 and 0.5) for Shubnikov group I_c4/mcm (140.550) in the BNS setting. The cubic parent structure is indicated by the pink cube edges. The drawn axes correspond to the larger tetragonal cell.

Due to the fact, that the tetragonal solutions gave almost a perfect Rietveld refinement of the magnetic Bragg reflections, other solutions given by ISODISTORT with lower symmetries (trigonal, monoclinic, triclinic) were not considered[1].
Besides the solution of ISODISTORT, the solutions from the program MAXMAGN can be also evaluated. As expected MAXMAGN found the same tetragonal solutions as ISODISTORT. However, as MAXMAGN is calculating the maximal magnetic space groups for a given propagation vector, it gives the same symmetries with the same

1 Interestingly, a weak ferromagnetism would suggest, that the magnetic propagation vector $\vec{k}$ has a small deviation from the ideal value of $\vec{k} = (0.5, 0.5, 0.5)^T$, which would be observable as a slight peak asymmetry of a magnetic Bragg peak. Such peak asymmetries for the magnetic Bragg reflections cannot be observed in the present Rietveld refinements, therefore it is concluded, that either the resolution of the neutron powder diffractometer is too low or that no weak ferromagnetism occurs above a composition of x = 0.2.

Shubnikov groups but with larger unit cell lattice parameters of $a = 2 \cdot a_p$, $b = 2 \cdot a_p$ and $c = 2 \cdot a_p$. As it is possible to model the magnetic structure of the $Bi_{1-x}Sr_xFeO_{3-\delta}$ perovskites (with x = 0.2, 0.3 and 0.5) correctly by the same Shubnikov groups with a lower unit cell volume, the solutions given by MAXMAGN were neglected.

As already stated in the last subsection, the magnetic structure of the $BiFeO_3$ perovskite on a long range scale is incommensurate, if not a local environment is considered. Therefore it is not possible to find a Shubnikov group with high symmetry and small unit cell volume, which allows for the modeling of the spin cycloid in $BiFeO_3$. The magnetic structure of $BiFeO_3$ in the local environment as well as the magnetic structure on a larger scale are shown in figure 3.3. Locally a clear G-type antiferromagnetic spin structure is established, whereas at a larger scale, parts of the spin cycloid can be intriguingly seen.
A Rietveld refinement of the room temperature neutron powder diffraction of $BiFeO_3$ with the FullProf program [83] revealed that the physical correct spin model must be applied in order to account for the obvious peak asymmetry of the (101)/(003) magnetic reflection. This application is done by a direct refinement of three of the six components of the complex Fourier coefficients. Interestingly, the result of the Rietveld refined magnetic propagation vector of the spin cycloid at room temperature differs from the value given by Sosnowska *et al.* [112, 113]. Sosnowska *et al.* gave a value of the magnetic propagation vector of $\vec{k} = (0.0045, 0.0045, 0)^T$ [112, 113], whereas the Rietveld refinement of the high resolution neuton powder diffraction pattern of $BiFeO_3$ resulted in a magnetic propagation vector of $\vec{k} = (0.0034(3), 0.0034(3), 0)^T$, which corresponds to a spin cycloid length of approximately 820 Å. The reason for that difference can be explained if the different resolutions of the used neutron diffractometers are considered. The resolution of the used time-of-flight neutron diffractometer by Sosnowska *et al.* in 1982 was $\frac{\Delta d}{d} = 7 \cdot 10^4$ at $d_{hkl} = 4.5$ Å [112], whereas the resolution of SPODI is much lower with $\Delta 2\theta = 0.05°$ [153], which corresponds to a $\frac{\Delta d}{d}$ of $\frac{\Delta d}{d} \approx 2.5 \cdot 10^3$ at the same d_{hkl} value as above. Therefore the ambiguity for a measurement of a small magnetic propagation vector is much higher for SPODI.

3.5.3 Results of the sequential Rietveld refinement

The temperature dependent (pseudo-)cubic lattice parameter a for the $Bi_{1-x}Sr_xFeO_{3-\delta}$ perovskites (with x = 0, 0.2, 0.3 and 0.5) can be found in figure 3.4.

From this figure several findings can be confirmed, which were also observed by other authors [127, 128, 138, 139, 147]. Depending on the Sr^{2+} cation doping level and the amount of oxygen vacancies, which can be derived from the oxygen non-stoichiometry

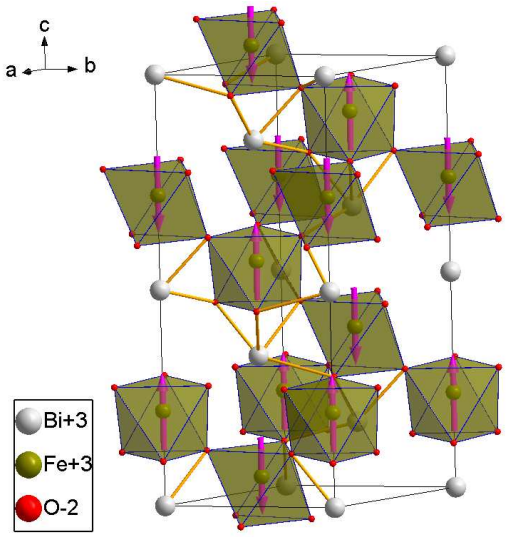

(a) $BiFeO_3$ (local)

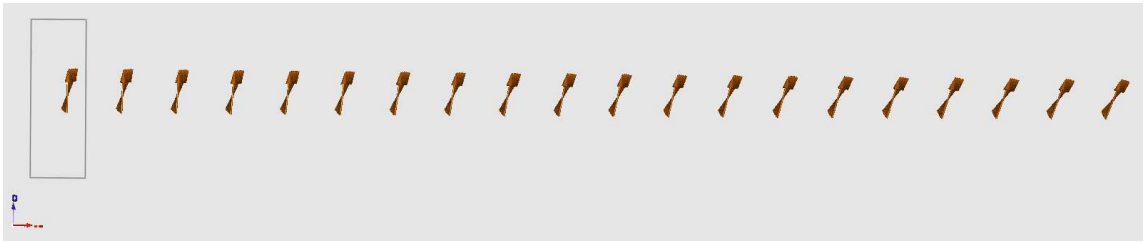

(b) $BiFeO_3$ (long range). View along *b*-axis.

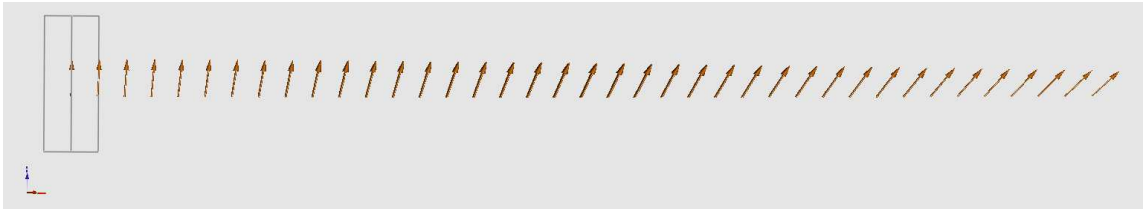

(c) $BiFeO_3$ (long range). View along [$\bar{1}$10]-direction

Figure 3.3: a) Local view of the magnetic structure of the $BiFeO_3$ perovskite. The local alignment of the magnetic moments seems to be G-type antiferromagnetic. Choosing one layer of magnetic moments and enlarging the unit cell to 20×20, a part of the spin cycloid can be seen: b) view along the *b*-axis and c) view along the [$\bar{1}$10] face diagonal (in order to see the propagation of the spin cyloid in the [110]-direction).

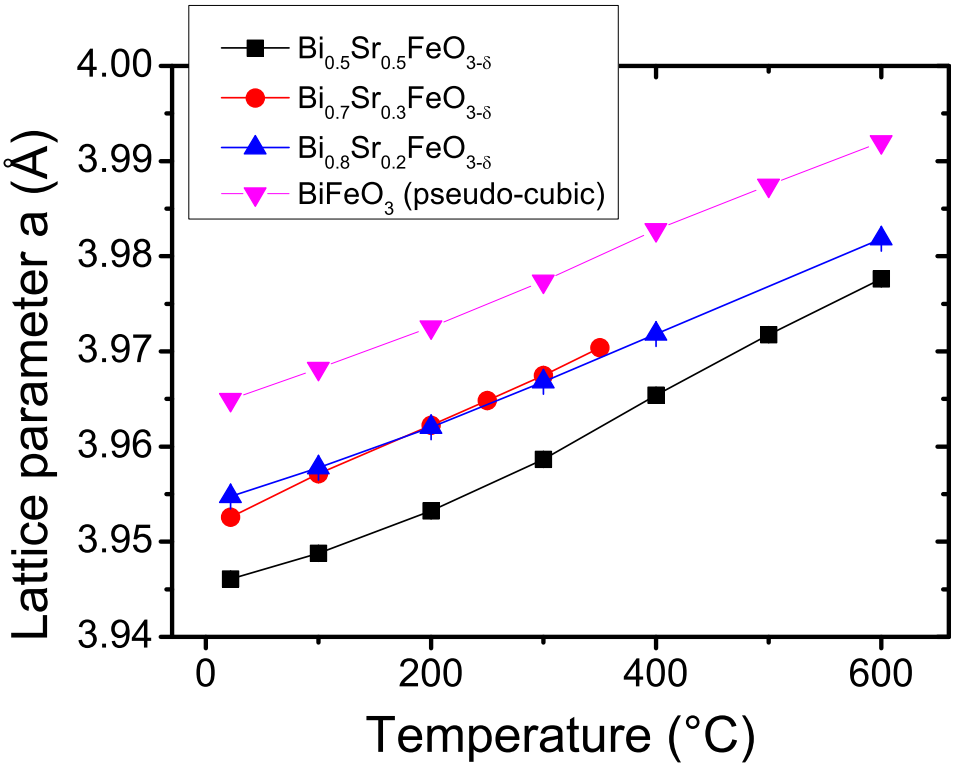

Figure 3.4: Temperature dependent (pseudo-)cubic lattice parameter a for the $Bi_{1-x}Sr_xFeO_{3-\delta}$ perovskites obtained by Rietveld refinements of neutron powder diffraction data. The trigonal lattice parameters of the $BiFeO_3$ perovskite are transformed to pseudo-cubic lattice parameters (transformation matrix is given in appendix C). The lines are guides to the eye.

in figure 3.5, the lattice parameters of the cubic $Bi_{1-x}Sr_xFeO_{3-\delta}$ perovskites shrink[1][2]. The temperature dependent investigations of the lattice parameter reveal that the $Bi_{1-x}Sr_xFeO_{3-\delta}$ perovskites are at least stable up to 600°C ($\approx$ 873 K) and that no phase transitions can be observed in the investigated temperature range[3]. Interestingly for the $Bi_{0.5}Sr_{0.5}FeO_{3-\delta}$ perovskite, a non-linear thermal expansion behavior can be observed, whereas for the $Bi_{1-x}Sr_xFeO_{3-\delta}$ perovskites with x = 0.2 and x = 0.3 an al-

1 Interestingly, this phenomenon was also observed by several other studies [127, 128, 138, 139, 147], whereas Zheng-Zheng *et al.* reported an increase in the lattice parameters of the $Bi_{1-x}Sr_xFeO_{3-\delta}$ perovskites with an increase of the Sr^{2+} cation concentration [140].

2 Previously it was assumed that the lattice parameters of $Bi_{1-x}Sr_xFeO_{3-\delta}$ perovskites are also affected by the lower Shannon radii of the Fe^{4+} cations in contrast to the Fe^{3+} cations [127, 166], but this could be disproved by the Mössbauer spectroscopy investigations which revealed that only Fe^{3+} cations are present [128–131].

3 It can be expected, that this holds also true for the $Bi_{0.7}Sr_{0.3}FeO_{3-\delta}$ perovskite, where not enough data points could be collected due to the limited measurement time at the neutron powder diffractometer SPODI.

most linear thermal expansion of the lattice parameters as for the $BiFeO_3$ perovskite can be found. Unfortunately, this non-linear behavior cannot be explained by the amount of oxygen vacancies as the oxygen non-stoichiometry of the $Bi_{0.5}Sr_{0.5}FeO_{3-\delta}$ perovskite follows an approximately linear trend. Furthermore, this phenomenon cannot be coupled to the behavior of other crystallographic parameters obtained by the sequential Rietveld refinement, as they all show almost linear temperature-dependent behaviors.
Another noticeable observation is the similarity of the lattice parameters between the $Bi_{1-x}Sr_xFeO_{3-\delta}$ perovskites with x = 0.2 and x = 0.3. Although they possess a different oxygen stoichiometry[1], the temperature-dependent lattice parameters are nearly identical, which is unusual as the synthesis conditions for both compounds were formally the same[2].

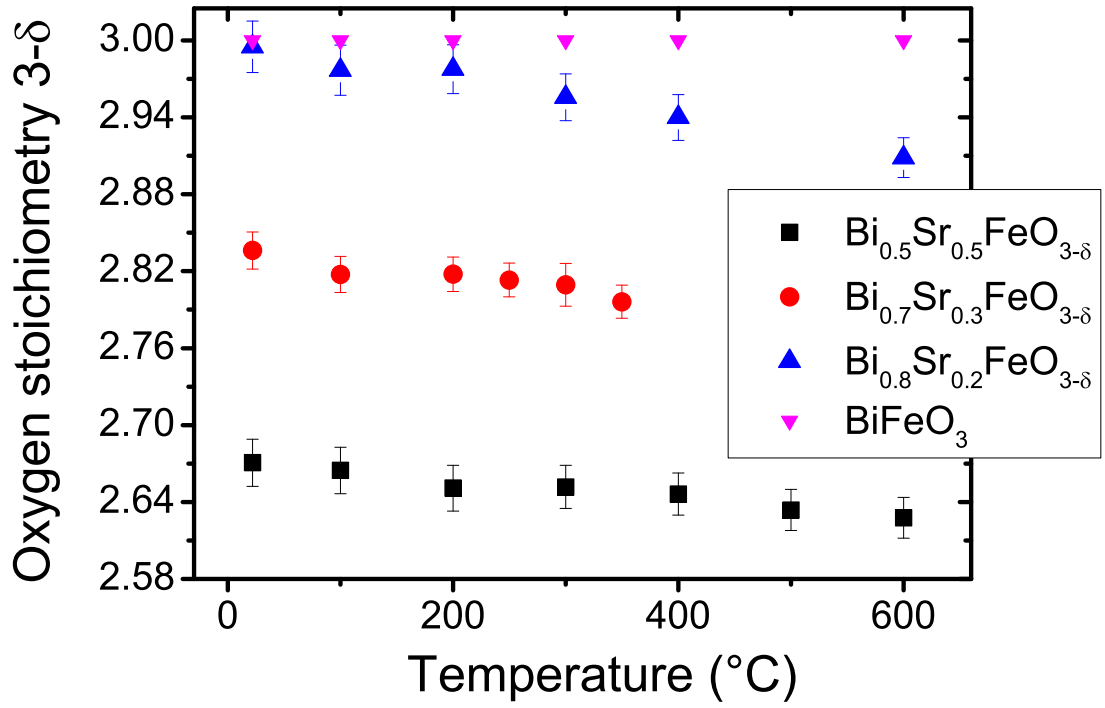

Figure 3.5: Temperature dependent oxygen stoichiometry $3 - \delta$ for the $Bi_{1-x}Sr_xFeO_{3-\delta}$ perovskites obtained by Rietveld refinements of neutron powder diffraction data.

The temperature dependent oxygen stoichiometry in figure 3.5 shows that there is a small linear decrease in the amount of oxygen within the $Bi_{1-x}Sr_xFeO_{3-\delta}$ perovskites

1 At room temperature the chemical formulas are given as $Bi_{0.7}Sr_{0.3}FeO_{2.84}$ and $Bi_{0.8}Sr_{0.2}FeO_{2.99}$.
2 This effect was also observed by Li *et al.* [128], who assumed that this phenomenon can be ascribed to the synthesis conditions as the they used different temperatures for the synthesis process.

with x = 0.3 and x = 0.5. This is in contrast to the $Bi_{1-x}Sr_xFeO_{3-\delta}$ perovskite with x = 0.2, where the slope of the decrease is much more pronounced. Interestingly, this behavior of the $Bi_{1-x}Sr_xFeO_{3-\delta}$ perovskite with x = 0.2 coincides with the observance of the corresponding lattice parameter behavior, which probably suggests that the real synthesis conditions for the compound with the composition with x = 0.2 were different from that given in section 3.2[1].

For all temperature dependent high resolution neutron powder diffraction patterns the magnetic Bragg reflections were fitted by the given magnetic structure models from subsection 3.5.2. For the $Bi_{1-x}Sr_xFeO_{3-\delta}$ perovskites with x = 0.2, 0.3 and 0.5, this means, that sequential Rietveld refinements of the magnetic Bragg reflections could be performed using a single amplitude of a magnetic symmetry mode (mR5-, see also subsection 3.5.2), which in turn is directly connected with the value of the magnetic moment at that temperature[2]. The obtained refined results of the temperature dependent magnetic moments can be found in figures 3.6a)-c).

In contrast to the $Bi_{1-x}Sr_xFeO_{3-\delta}$ perovskites with x = 0.2, 0.3 and 0.5 which are refined using the program TOPAS 5, the magnetic moments of the temperature dependent measurement series of the $BiFeO_3$ perovskite can be directly obtained from the Fourier components which are refined using the FullProf program (see also subsection 3.5.2). The resulting magnetic moments of the $BiFeO_3$ perovskite can be found in figure 3.6d).

Careful inspections of all neutron powder diffraction patterns in the temperature range of 350 °C to 400 °C (≈ 623 K to 673 K) revealed, that the magnetic Bragg peaks (which show only a moderate intensity at such high temperatures) are significantly broadened at their base[3]. The reason for this phenomenon is, that with the increase of the temperature and the gradual approach to the critical Néel temperature, the long-range ordering of the magnetic moments becomes perturbed by temperature-dependent fluctuations and therefore a short-range ordering character of the magnetic moments becomes apparent. This means that with increasing temperature, the magnetic domain sizes become smaller and smaller due to increasing fluctuations, which have the same broadening effect on the magnetic Bragg peaks, as small powder particles have a broadening effect on the nuclear Bragg peaks of the crystal structure.
For a Rietveld refinement of the magnetic Bragg peaks this implies that two contributions must be modeled, from the long-range and the short-range ordering, as the sharp long-range ordering magnetic peaks can be normally seen on top of the broadened

1 At the present moment, there is no obvious reason why the oxygen kinetics in the $Bi_{1-x}Sr_xFeO_{3-\delta}$ perovskite with x = 0.2 should differ from that of the $Bi_{1-x}Sr_xFeO_{3-\delta}$ perovskite with x = 0.3. Therefore it is more likely that the formal synthesis conditions were not exactly reached.

2 All other parameters which are required for a Rietveld refinement of the magnetic Bragg reflections are constrained to corresponding values of the nuclear crystal structure phase.

3 This behavior can be best seen for the first magnetic reflection of a given compound, as this reflection usually shows the highest intensity.

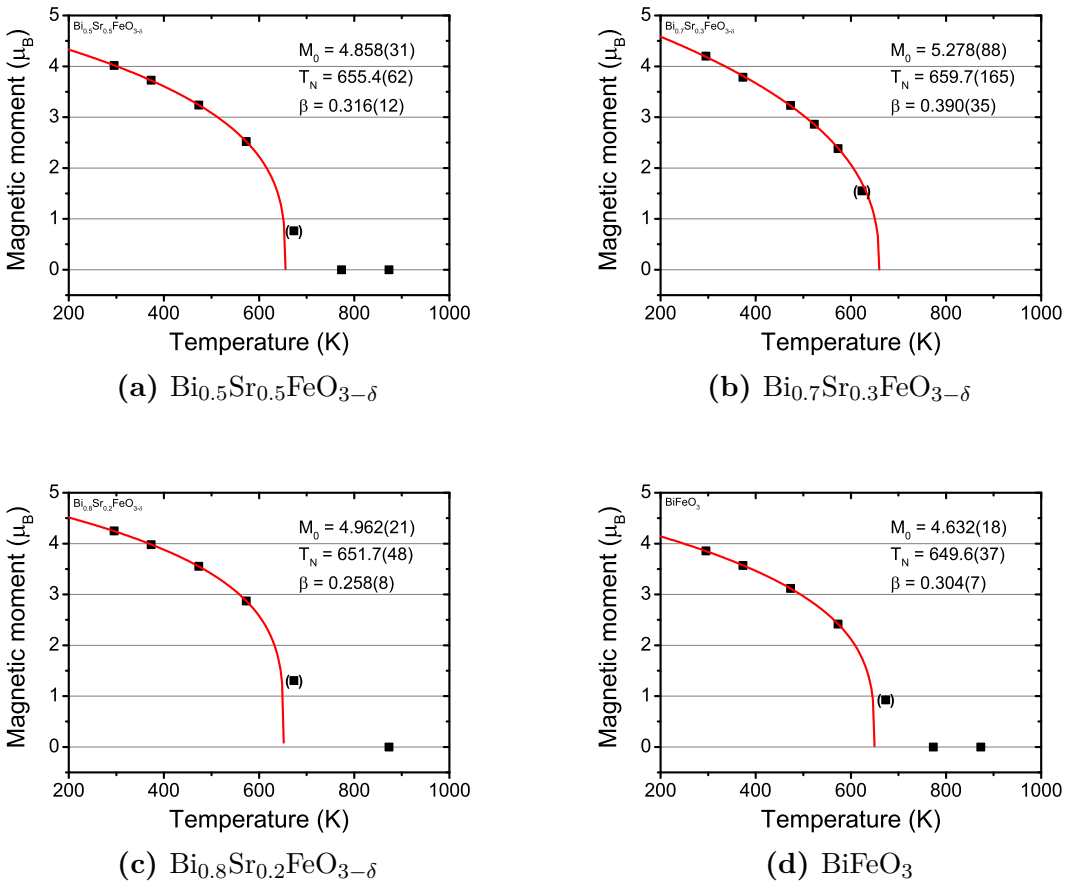

(a) $Bi_{0.5}Sr_{0.5}FeO_{3-\delta}$ **(b)** $Bi_{0.7}Sr_{0.3}FeO_{3-\delta}$

(c) $Bi_{0.8}Sr_{0.2}FeO_{3-\delta}$ **(d)** $BiFeO_3$

Figure 3.6: Temperature dependent magnetic moments for the $Bi_{1-x}Sr_xFeO_{3-\delta}$ perovskites obtained by Rietveld refinements of neutron powder diffraction data. The values in brackets were not considered in the fitting with the shown power-law behavior (see also explanations given in the text).

short-range ordering magnetic peaks. Unfortunately, for none of the $Bi_{1-x}Sr_xFeO_{3-\delta}$ perovskites it was possible to obtain a stable refinement with both contributions, therefore only the long-range ordering contribution was taken for the modeling of the magnetic Bragg reflections. Therefore, the values for the magnetic moments in a temperature range of 350 °C to 400 °C in figures 3.6a)-d) are given in brackets, as the refined values are certainly not consistent with the real magnetic moments at the corresponding temperatures.

The antiferromagnetic to paramagnetic phase transition of the $Bi_{1-x}Sr_xFeO_{3-\delta}$ perovskites can be modeled by a power-law behavior, for instance one, which can be derived from Landau theory [67–69]:

$$M(T) = M(0) \cdot \left(\frac{T_{crit} - T}{T_{crit}}\right)^{\beta} \quad , \tag{3.2}$$

where $M(T)$ is the value of the magnetic moment at a certain temperature T, $M(0)$ is the magnetic moment at zero temperature, the critical temperature T_{crit} is identical to the Néel temperature T_N, at which the magnetic moment approaches zero and β is the critical exponent, whose value depends on the type of the observed thermodynamic system[1].
In the modeling of the corresponding given Néel temperatures and critical exponents in figure 3.6a)-d), the values in brackets were left out in order to ensure that short-range ordering effects do not affect the determined critical values.

The determined critical Néel temperature of $T_N = 650(4)$ K for the $BiFeO_3$ perovskite is in quite good agreement with the values, which are given in the literature (e.g. Kiselev *et al.* reported a value of 653 K [109, 110]. Other values can be found in the publication of Fischer *et al.* [116]). Interestingly, the determined critical temperatures of the $Bi_{1-x}Sr_xFeO_{3-\delta}$ perovskites (with x = 0.2, 0.3 and 0.5) from neutron powder diffraction have similar Néel temperatures, although quite different values were reported in literature. For instance V.V. Pokatilov *et al.* reported from Mössbauer spectroscopy measurements a value of $T_N = 637(3)$ K for the $Bi_{0.5}Sr_{0.5}FeO_{3-\delta}$ perovskite [130], V.S. Pokatilov *et al.* reported from Mössbauer spectroscopy measurements a value of $T_N = 670(3)$ K for the $Bi_{0.75}Sr_{0.25}FeO_{3-\delta}$ perovskite [131] and for the same $Bi_{0.75}Sr_{0.25}FeO_{3-\delta}$ perovskite, Pachoud *et al.* reported a value of $T_N = 643$ K from neutron powder diffraction measurements. Concerning the present critical Néel temperatures determined from temperature dependent high resolution neutron powder diffraction data, it can be stated that an A-site doping by Sr^{2+} cations up to 50% certainly destroys the spin cycloid, whereas it seems that the critical temperatures for the antiferromagnetic to paramagnetic phase transitions are unaffected.

3.6 Thermal analysis by differential scanning calorimetry

In addition to the determination of the Curie or Néel temperature by neutron diffraction, it is also possible to observe magnetic phase transitions by thermal analysis using differential scanning calorimetry (DSC) [167]. The reason for that is that the heat capacity C_p at constant pressure, which is sensitive to first and second order (magnetic) phase transitions, is proportional to the measured heat flow in a DSC experiment:

1 The experimental value for the critical exponent, which is typically determined for a(n) (anti)ferromagnetic to paramagnetic phase transitions is in the range of $\beta = 0.34$ - 0.37 [94].

$$C_p := \frac{dQ}{dT} \tag{3.3}$$

$$C_p = \frac{dH}{dt} \cdot \frac{dt}{dT} \tag{3.4}$$

$$\propto \frac{dH}{dt} \tag{3.5}$$

where Q is the heat, T is the temperature, H is the enthalpy which is equal to the heat Q in this case and t is the time. Equation 3.3 gives the definition of the heat capacity. The term $\frac{dH}{dt}$ in equation 3.4 is the measured heat flow and the term $\frac{dt}{dT}$ is the inverse heating rate.
The explanation of the sensitivity of the heat capacity with respect to first and second order phase transitions results from the definition of the order of a phase transition. For a first order phase transition the first derivative of the Gibbs free energy is discontinuous, whereas for a second order phase transition the first derivative of the Gibbs free energy is continuous and the second derivative is discontinuous[1]. In thermodynamics, it is possible to relate the second derivative of the Gibbs free energy with the heat capacity, therefore the DSC measurements can be used to investigate the onset of (magnetic) phase transitions (a detailed calculation of the derivatives and all relations can be found in appendix D).

Although the second derivative of the Gibbs free energy and therefore the heat capacity must be discontinuous at the occurrence of a second order phase transition, it is often difficult to determine accurately the endothermic peak of a magnetic phase transition[2] in a DSC curve. According to Williams and Chamberland, the endothermic peak of a magnetic phase transition "can be weak or strong depending upon the sample weight, rate of heating, the magnetic interactions involved, and the purity of the sample" [167]. Due to this reason a sensitive DSC apparatus with an appropriate heating rate and a sufficient calibration is required[3].

The raw data of the heat flow for the $Bi_{1-x}Sr_xFeO_{3-\delta}$ perovskites (with x = 0, 0.1, 0.2, 0.3, 0.4 and 0.5) from the DSC experiment can be found in figure 3.7a). For all obtained datasets the baselines (definition see [170]) were determined by using 25-30 points of the corresponding data curve which were interpolated with a spline curve. The so obtained baseline was then subsequently subtracted from the heat flow curves

1 This classification is also known as the Ehrenfest classification [92] (see also section 2.5.1).
2 In principle it is possible to measure first and second order magnetic phase transition as in both cases the second derivative of the Gibbs free energy is discontinuous. Please note, that in general magnetic phase transitions are of second order as long as they are not coupled with other effects, like structural phase transitions [168].
3 The visibility of the endothermic peak of a magnetic phase transition can be enhanced by an external magnetic field [169], however this method was not used in the present work.

(see figure 3.7b)). Although the noise in the baseline subtracted DSC curves is quite high, the endothermic peaks of the magnetic phase transitions are clearly visible for the $Bi_{1-x}Sr_xFeO_{3-\delta}$ perovskites samples with x = 0, 0.2, 0.3 and 0.4. In contrast to that the endothermic peak of the $Bi_{1-x}Sr_xFeO_{3-\delta}$ sample with x = 0.5 shows a strange splitting which can be possibly accounted to the noise in the DSC curve. For the sample with x = 0.9, the endothermic peak is too small, so that it was simply not possible to determine its position.

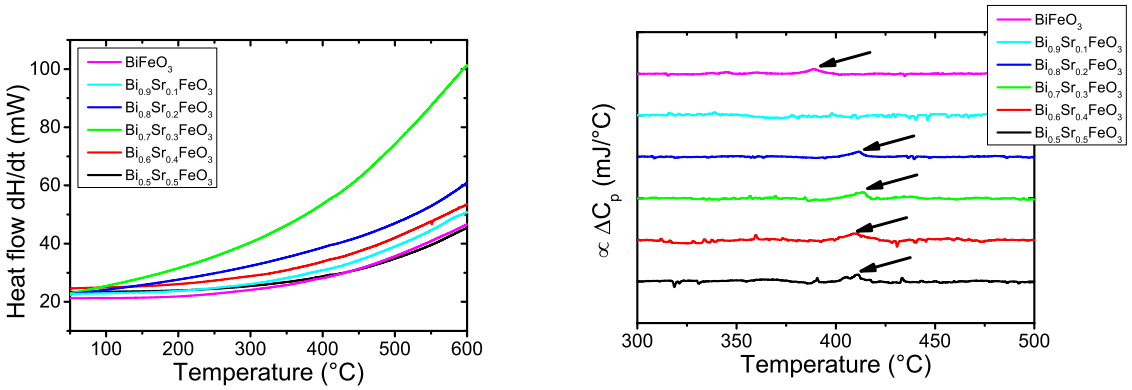

(a) DSC raw data **(b)** DSC data with subtracted baseline

Figure 3.7: Temperature dependent heat flow of the $Bi_{1-x}Sr_xFeO_{3-\delta}$ perovskites (x = 0, 0.1, 0.2, 0.3, 0.4 and 0.5) measured by DSC. Picture a) shows the raw data and picture b) shows the heat flow with subtracted baseline.

In general, the enthalpy of the transition can be determined by a simple integration of the heat flow over temperature, but in this work the focus lies more on the determination of the critical Néel temperature of the antiferromagnetic phase transition. Williams and Chamberland showed that the top of the endothermic peak can be approximately used as the critical temperature [167] (see also [171]), therefore the top of the peak was used for the determination of the Néel temperature, whereas the largest assumed error bar can be given by the base width of the peak. The result of these determinations is summarized in the phase diagram in figure 3.8.

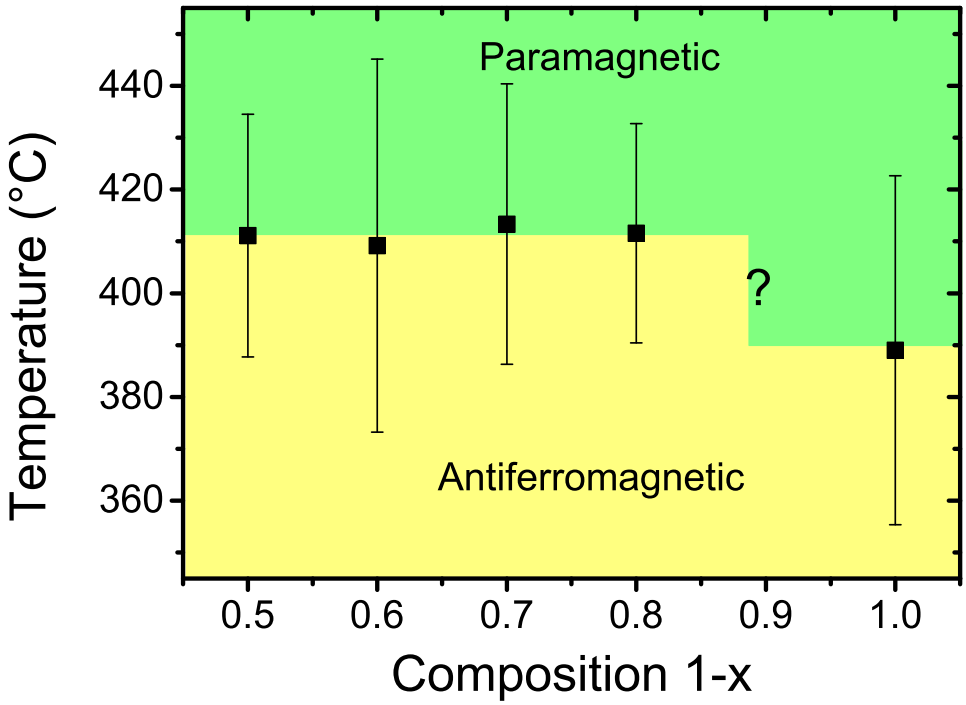

Figure 3.8: Néel temperature of the antiferromagnetic to paramagnetic phase transition determined from the top position of the endothermic peaks of the corresponding DSC measurements of the $Bi_{1-x}Sr_xFeO_{3-\delta}$ perovskites.

3.7 Conclusion

Investigations of the room temperature synchrotron X-ray and neutron powder diffraction measurements of the $Bi_{1-x}Sr_xFeO_{3-\delta}$ perovskites (x = 0 to x = 0.5) revealed that the crystal structure of the undoped $BiFeO_3$ perovskite can be described using space group $R3c$, whereas it was not possible to determine accurately the crystal structure of the $Bi_{0.9}Sr_{0.1}FeO_{3-\delta}$ perovskite, as this compound consists most likey of a rhombohedral and a cubic phase [133, 147]. For the other investigated $Bi_{1-x}Sr_xFeO_{3-\delta}$ perovskites (x = 0.2, 0.3 and 0.5), it could be shown that the best description of these crystal structures is rather given by the cubic space group $Pm\bar{3}m$ than by the tetragonal space group $P4/mmm$.

High resolution neutron powder diffraction measurements at room temperature revealed that for all investigated $Bi_{1-x}Sr_xFeO_{3-\delta}$ perovskites magnetic Bragg reflections are present. From these magnetic Bragg reflections a magnetic propagation vector of $\vec{k} = (0.5, 0.5, 0.5)^T$ could be determined for the $Bi_{1-x}Sr_xFeO_{3-\delta}$ perovskites with x = 0.2, 0.3 and 0.5, whereas it was not possible to determine the incommensurate magnetic propagation vector for the undoped $BiFeO_3$ perovskite, due to the limited resolution of the used neutron powder diffractometer. The magnetic propagation vec-

tor of the $Bi_{1-x}Sr_xFeO_{3-\delta}$ perovskites with x = 0.2, 0.3 and 0.5 led to a G-type antiferromagnetic unit cell, which is 4 times larger than the crystallographic unit cell and can be best described by the Shubnikov group with label I_c4/mcm (140.550) in the BNS setting and a label of $P_I4/mm'm'$ (123.19.1017) in the OG setting.
Sequential Rietveld refinements of the temperature dependent neutron powder diffraction data of the $BiFeO_3$ perovskite showed, that a clear peak asymmetry of the magnetic (101)/(003) reflection can be observed. Therefore Rietveld refinements were carried out using the full description of the magnetic structure by the spin cycloid. In contrast to the $BiFeO_3$ perovskite, no peak asymmetries could be observed for the magnetic reflections of the $Bi_{1-x}Sr_xFeO_{3-\delta}$ perovskites with x = 0.2, 0.3 and 0.5, which indicates that either no weak ferromagnetism due to spin canting for these perovskites is present or that the resolution of the neutron powder diffractometer is simply too low.

Regarding the ferroelectric properties of the doped $Bi_{1-x}Sr_xFeO_{3-\delta}$ perovskites, it can be stated that the transition to a cubic crystal structure with space group $Pm\bar{3}m$ prohibits the occurrence of proper ferroelectricity, as this space group is a non-polar space group. However, it is still possible that improper ferroelectricity due to the magnetoelectric coupling occurs, although no magnetic structure which breaks the inversion symmetry was observed and therefore it is very unlikely that ferroelectricity is present above a composition level of x = 0.2. Perhaps a spin canting, which could not be observed due to the limited resolution of the neutron powder diffractometer, is present and this would lead to a break of the inversion symmetry and therefore would allow for improper ferroelectricity due to magnetoelectric coupling.
Besides the determination of the magnetic and crystal structure symmetries, the temperature dependent behavior of the oxygen stoichiometry was investigated, as it is believed that the present oxygen vacancies have a crucial influence on the magnetic and ferroelectric properties of the $Bi_{1-x}Sr_xFeO_{3-\delta}$ perovskite system. For this reason the temperature dependent neutron powder diffraction experiments were performed in a special gas environment, which ensures defined conditions for the oxygen exchange rates. As it was expected from the chosen environmental conditions for all doped $Bi_{1-x}Sr_xFeO_{3-\delta}$ perovskites a decrease in the oxygen stoichiometry can be found and therefore an increase in the number of oxygen vacancies.

The critical Néel temperatures for the antiferromagnetic to paramagnetic phase transitions of the $Bi_{1-x}Sr_xFeO_{3-\delta}$ perovskites were determined by neutron powder diffraction as well as by differential scanning calorimetry measurements. The results of these measurements are summarized in the magnetic phase diagram in figure 3.9.

From this phase diagram it is clear, that a discrepancy between the Néel temperatures determined from neutron powder diffraction and the Néel temperatures determined from differential scanning calorimetry measurements exists. A possible explanation of this discrepancy would be, that in the differential scanning calorimetry measurements no defined gas environment was used, in contrast to the neutron powder diffraction measurements. Perhaps this led to a different amount of oxygen vacancies in the $Bi_{1-x}Sr_xFeO_{3-\delta}$ perovskites, which, as already mentioned, has certainly an effect

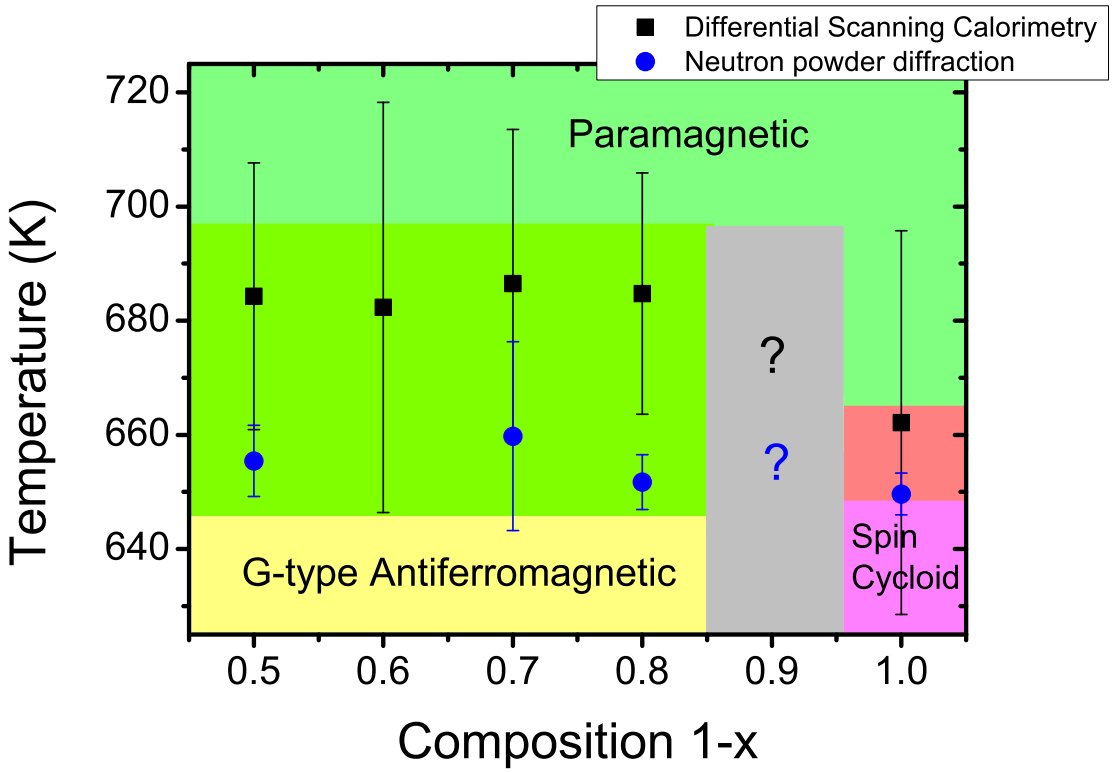

Figure 3.9: Néel temperature of the antiferromagnetic to paramagnetic phase transition determined for the $Bi_{1-x}Sr_xFeO_{3-\delta}$ perovskites. Blue points are obtained from Rietveld refinements of neutron powder diffraction data, whereas black points are obtained by the top position of the endothermic peaks of the corresponding DSC measurements.

on the magnetic properties of these perovskites[1]. Although, this is still a speculation at the moment, it shows intriguingly that the role of the oxygen vacancies on the magnetic properties of the $Bi_{1-x}Sr_xFeO_{3-\delta}$ perovskites must certainly be investigated in more detail[2].

1 In a theoretical study of Borisov *et al.* [172], it was shown that the critical Néel temperature decreases with an increasing oxygen vacancy level in the $ATcO_3$ (A = Ca, Sr, Ba) perovskites.

2 Please note that for the full stoichiometric $BiFeO_3$ where no oxygen exchange takes place, the agreement between the critical Néel temperature determined from neutron powder diffraction and from differential scanning calorimetry measurements is much better.

CHAPTER 4

High pressure *in situ* investigations of $LaFeO_3$

The results of this chapter are already published in three different publications: "*M. Etter, M. Müller, M. Hanfland, R.E. Dinnebier - High-pressure phase transitions in the rare-earth orthoferrite $LaFeO_3$*" [173], "*M. Etter, M. Müller, M. Hanfland, R.E. Dinnebier - Possibilities and limitations of parametric Rietveld refinement on high pressure data: The case study of $LaFeO_3$*" [174] and "*M. Etter & R.E. Dinnebier - Direct parameterization of the pressure-dependent volume by using an inverted approximate Vinet equation of state*" [175].

4.1 Motivation

The investigation of perovskites under high pressure has nowadays became a standard method in order to tune the fascinating properties of this material class. For instance in 1994, Gao *et al.* [176] were able to shift the critical superconducting temperature of cuprate perovskites to higher values. However, this is only one aspect why the investigation of perovskites under high pressure can be very intriguing. Often the simple investigation of the change of the perovskite crystal structure under high pressure is decisive. For instance, the structural investigation of the $MgSiO_3$ perovskite is very important since this material is the most common material in the earth mantle and the understanding of this material can give rise to a better understanding of the earth's interior. Although both examples are very extreme cases of the high pressure research of perovskites, they show remarkably how important high pressure investigations of perovskites can be.
A fascinating perovskite, which is a typical representative of the rare-earth orthoferrites is the lanthanum ferrite ($LaFeO_3$) perovskite with space group *Pbnm* (space group number 62). This perovskite has interesting characteristics as it exhibits three different ferroic properties. At ambient conditions[1] the insulating $LaFeO_3$ possess a G-type like antiferromagnetic behavior, where the magnetic moments are roughly aligned along the orthorhombic *a*-axis [177]. Detailed investigations showed that the magnetic mo-

1 The author denotes with ambient conditions an air pressure of 1 atm and a temperature of 20°C.

ments are slightly canted [178, 179], which leads to a weak ferromagnetic component parallel to the *c*-axis [180]. The magnetic interaction in this compound results from a Dzyaloshinskii-Moriya interaction with an angle of approximately 157° between Fe-O-Fe atoms at room temperature and ambient conditions [179–181]. In addition to the antiferromagnetic ordering, Abrahams *et al.* [182] reported that $LaFeO_3$ possess also ferroelastic order (see also Fossdal *et al.* [183]) and Acharya *et al.* [184] reported that they observed ferroelectric order, due to magnetoelectric coupling[1]. Therefore $LaFeO_3$ exhibits three ferroic phenomena, making it an interesting multiferroic compound[2].
A high temperature X-ray powder diffraction study of the $LaFeO_3$ perovskite revealed that the orthorhombic unit cell becomes less distorted with increasing temperature, until a distortion minimum at the Néel temperature T_N of approximately 735 K is reached [185–187]. Above this temperature an increase of the unit cell distortion can be observed until at a temperature of approximately 1228 K a first order phase transition to the trigonal space group $R\bar{3}c$ occurs. At this transition point the Glazer tilt system [188] changes from $a^-a^-b^+$ to $a^-a^-a^-$ [185, 189]. In the study of Selbach *et al.* [185], they observed also that, while the unit cell distortion reaches its minimum, the distortion of the corner-sharing FeO_6 octahedra becomes larger in the temperature range of $500\ K \leq T \leq 850\ K$. An explanation for this behavior can be given by looking at the size mismatch between the Fe^{3+} and La^{3+} cations which leads to a Goldschmidt tolerance factor [190] which is too low [185].
Since already thermal energy is able to influence the distortion phenomena occurring in $LaFeO_3$, it is worthwhile to investigate the behavior of the distortions in this perovskite by directly applying high pressure. A Mössbauer spectroscopy study of Xu *et al.* [191] at the room temperature isotherm revealed that in the pressure range of $30\ GPa \leq p \leq 50\ GPa$ a partial high-spin ($S = \frac{5}{2}$) to low-spin ($S = \frac{1}{2}$) transition of the Fe^{3+} cation takes place and therefore two different magnetic sublattices are established. At higher pressure values of approximately 60 GPa a complete spin-crossover to the low-spin state occurs [191]. This experimentally observed spin-crossover is in agreement with recent density functional theory (DFT) calculations performed by Javaid *et al.* [192, 193]. They found that the pressure dependent spin-crossover can be explained by the increase of the crystal-field splitting energy, which increases with the distortion level of the FeO_6 octahedra and the shortening of the bondings within the FeO_6 coordination polyhedra due to the increase of the applied pressure [181, 192].

Although Xu *et al.* [191] performed synchrotron X-ray powder diffraction measurements of $LaFeO_3$ in order to support their Mössbauer results, they did not carry out a full crystallographic treatment of their data with Rietveld refinements, which is essential in order to understand the structural evolution and the behavior of $LaFeO_3$

1 Proper ferroelectricity is not allowed in this compound, as the structural investigations clearly state that this compound has a centrosysmmetric structure with a non-polar space group. Therefore magnetoelectric coupling is required in order to develop improper ferroelectricity.
2 To the knowledge of the author, there exists no study about investigations of a possible coupling between ferroelastic properties and the other ferroic properties.

under high pressure. Therefore, the high pressure behavior of $LaFeO_3$ powder samples were investigated by synchrotron X-ray powder diffraction measurements up to pressures of 48 GPa employing different pressure media (nitrogen, argon and a mixture of methanol-ethanol in a ratio of 4:1).
This investigation focused on three different aspects. The first aspect was the full investigation by Rietveld refinements of the crystal structure at every pressure value and the modeling of the volume and lattice parameters by equations of state (EoS) in order to determine the bulk modulus, its pressure derivative and the lattice parameters at zero pressure. The second aspect was the investigation of the measured data sets by different alternative crystallographic approaches (see sections 4.4.2, 4.4.3, 4.4.4 and 4.4.5), in particular the application of different models for the refinement of the atomic positions in the atomic configuration space, in order to investigate which model is the most suitable one to investigate multiferroics like the $LaFeO_3$ perovskite under high pressure. The third and last aspect is to perform parametric Rietveld refinements of the measured data sets in order to investigate the ability of this approach with respect to high pressure synchrotron X-ray powder diffraction data sets.

4.2 Synthesis

The synthesis of the $LaFeO_3$ perovskite was performed by a solid state reaction of a stoichiometric mixture of La_2O_3 and Fe_2O_3 powders as described by Peterlin-Neumaier and Steichele [178] and by Selbach *et al.* [185].

4.3 Experimental setup

High pressure synchrotron X-ray powder diffraction measurements were performed by Dr. Michael Hanfland at the European Synchrotron Radiation Facility (ESRF), Grenoble at beamline ID09 in 1996. Four samples of the $LaFeO_3$ powder were loaded into membrane driven diamond-anvil cells (DAC) together with either nitrogen or argon or a mixture of methanol-ethanol in a ratio of 4:1 as pressure media. A single X-ray powder diffraction measurement of the $LaFeO_3$ powder in a capillary at ambient conditions at a wavelength of 0.45555 Å was made, in order to guarantee that there are no impurities of other phases present. The first high pressure measurement series was carried out for $LaFeO_3$ with nitrogen as pressure medium using 300 µm diameter culet diamonds and a maximum pressure of 40.5 GPa. In a second run the DAC was equipped with 600 µm diameter culet diamonds and with a mixture of methanol-ethanol in ratio of 4:1. In this run the pressure was successively increased up to 13.3 GPa. In a third run, 350 µm diameter culet diamonds together with argon were used and the pressure was successively increased up to 47.9 GPa. In the fourth and last run, again a mixture of methanol-ethanol in a ratio of 4:1 was used, together with 350 µm diameter culet diamonds and this time the pressure was successively increased up to 46.9 GPa. All high pressure measurements were done at the room temperature

isotherm. For the determination of the pressure, the ruby fluorescence method was used by applying a non-linear hydrostatic pressure scale given by Mao *et al.* [194]. The collection of the diffraction patterns was done in Debye-Scherrer mode with monochromatic radiation at wavelengths of 0.45555 Å (first run (nitrogen)), 0.45587 Å (second run (meth.-eth. 4:1)), 0.45582 Å (third run (argon)) and 0.45584 Å (fourth run (meth.-eth. 4:1)). The monochromatic radiation was obtained by irradiating a water-cooled Si-(111) monochromator with a standard undulator with a 46 mm period. A beam size of 30 x 30 μm^2 was obtained by using horizontal slits, whereas the vertical focusing was achieved by using a Pt-coated silicon mirror. Diffracted X-rays were detected by using A3 format image plates with an offline Molecular Dynamics image plate scanner with a pixel size of 100 μm^2.

The integration of the collected two-dimensional Debye-Scherrer rings to one-dimensional powder diffraction patterns was subsequently performed by using the computer program FIT2D [152]. The parameters which were required for this integration were determined from a Si reference sample.
Simulated two-dimensional Guinier patterns of these high pressure synchrotron X-ray powder diffraction measurements can be found in figure 4.1a)-d).

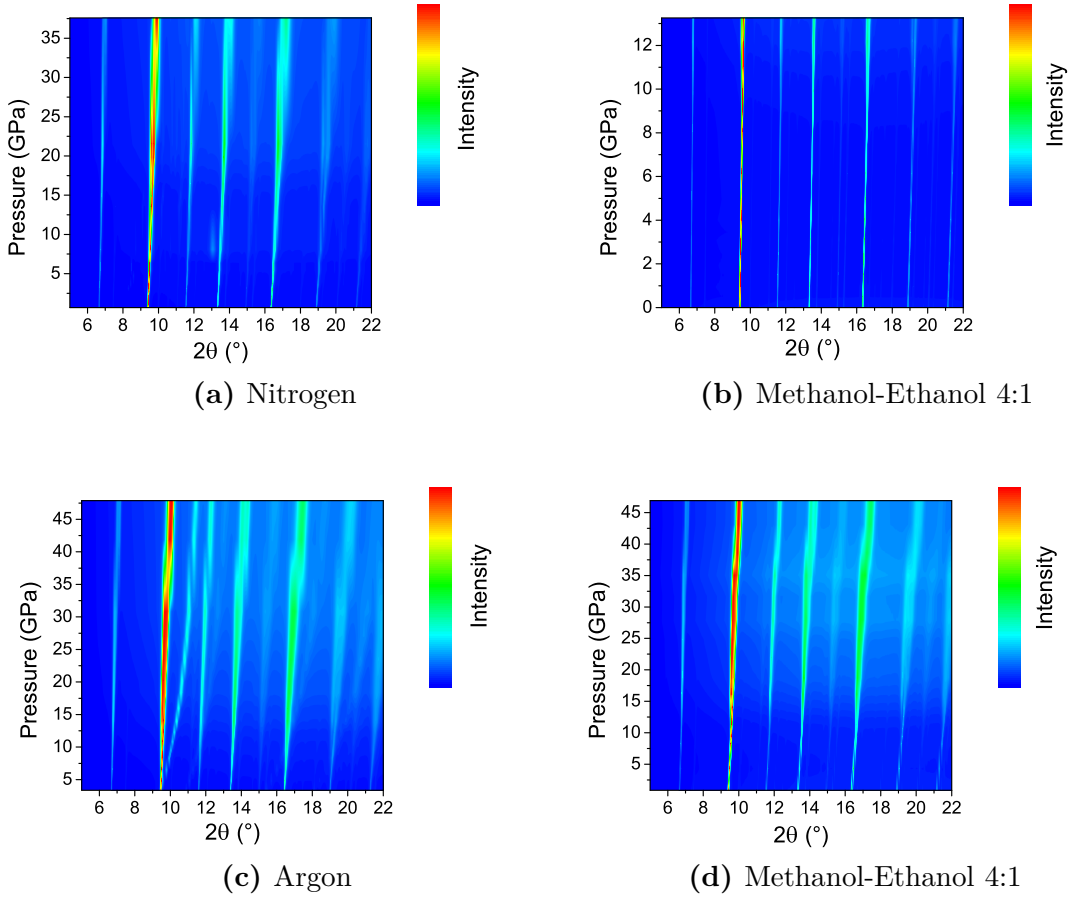

(a) Nitrogen **(b)** Methanol-Ethanol 4:1

(c) Argon **(d)** Methanol-Ethanol 4:1

Figure 4.1: Simulated two-dimensional Guinier patterns of the pressure dependent *in situ* synchrotron X-ray powder diffraction measurements of $LaFeO_3$ at room temperature for different pressure media: a) nitrogen, c) argon and b)+d) methanol-ethanol in a mixture of 4:1. In the investigated 2θ range ($5° \leq 2\theta \leq 20.8°$) 71 reflections of the *Pbnm* phase are present.

4.4 Sequential and parametric Rietveld refinements of pressure dependent synchrotron X-ray powder diffraction data with different approaches

Sequential and parametric Rietveld refinements for all high pressure synchrotron X-ray powder diffraction data sets were performed by using the commercial version of the TOPAS 4.2 program [57] offered by the Bruker AXS Corporation. Due to geometric restrictions for the synchrotron X-ray beam passing through the DAC, the refined 2θ range of every diffraction pattern was limited to 5° to 20.8° 2θ, except for the diffractogram of the capillary measurement, where the fitted range was from 5° to 37.4° 2θ. For all data sets and each pattern the diffraction background was

modeled by refineable Chebyshev polynomials and the peak shape modeling of the Bragg reflections was performed using the fundamental parameter approach [159, 160]. The synchrotron radiation was assumed to be 100% horizontally polarized and the zero shift of a particular data set was determined for the first measurement and then kept fixed throughout the corresponding data set (the values of the zero shifts can be found in table 4.1).

Table 4.1: Zero shifts which were determined for the first pattern of a data set and then fixed throughout the corresponding data sets.

Data set	Zero shift (° 2θ)
Capillary	0.00163(10)
Nitrogen (1. run)	0.00120(9)
Meth.-Eth. 4:1 (2. run)	-0.00004(6)
Argon (3. run)	-0.00026(19)
Meth.-Eth. 4:1 (4. run)	-0.00062(6)

Peak broadening of all crystalline phases due to sample dependent effects were modeled by the integrated crystallite size and phenomenological strain macros[1]. During the refinements it turned out, that a greater stabilization of the refinement can be achieved, when the phenomenological Gaussian and Lorentzian strain parameters are constrained to the same value. For the modeling of the crystallite size it became apparent, that at lower pressures the Gaussian as well as the Lorentzian crystallite size can be determined by the macros, whereas at higher pressures the crystallite size cannot be any longer correctly modeled by these macros. Therefore the Gaussian and Lorentzian crystallite size contribution to the peak width modeling was neglected at higher pressure values.
Although for $LaFeO_3$, a modeling with anisotropic displacement parameters (ADP) of the individual atoms at room temperature and ambient conditions is possible, it is more convenient to use an overall isotropic atomic displacement parameter for each diffraction pattern when pressure is applied as such a parameter is not that sensitive and therefore more stable compared to the ADPs, especially when the diffraction peaks start to broaden due to increased pressure.
At higher pressure values symmetry-adapted spherical harmonics of 4th or even 6th

1 In TOPAS the sample dependent peak broadening is modeled by macros which influence the full width half maximum (FWHM) of a peak at a given point 2θ. As the sample dependent peak shape is normally a convolution between a Gaussian and a Lorentzian peak shape there are macros which influence the peak shape of the Gaussian FWHM and the Lorentzian FWHM individually. The broadening of the FWHM due to the finite crystallite size is given by the Scherrer formula: $\mathrm{FWHM}_{L/G}(2\theta) = \frac{K \cdot \lambda}{L_{L/G} \cdot \cos\theta}$, where K is the Scherrer constant which is equal to 1, λ is the used wavelength and L is the refineable crystallite size parameter. The subscripts L and G denote the Lorentzian and Gaussian contribution, respectively. The broadening of the FWHM due to strain phenomena is given by the following phenomenological equation: $\mathrm{FWHM}_{L/G}(2\theta) = strainparameter_{L/G} \cdot \tan\theta$. A more detailed explanation of these macros can be found in the TOPAS 4.2 manual [57].

order were used, in order to describe phenomenologically the severe anisotropic peak broadening caused by the visible loss of hydrostatic conditions of the used pressure media[1][2].

Pre-investigations of the raw data of the nitrogen and argon measurement series revealed, that some additional peaks can be observed in these data sets. These additional peaks can be ascribed to solid phases of argon and nitrogen, respectively. Argon crystallizes at room temperature and a pressure of ≈ 1.3 GPa [196–198] and nitrogen crystallizes at room temperature (300 K) and a pressure of ≈ 2.44 GPa [199–201]. To account for these phases, an additional structureless whole powder pattern decomposition (WPPD method, in particular a WPPD according to Le Bail *et al.* [63] (also known as Le Bail method), was used.
The argon phase could be modeled in space group $Fm\bar{3}m$ over the entire pressure range [197, 202], whereas the nitrogen phase required 4 different space groups $P63/mmc$ (β-nitrogen), $Pm\bar{3}n$ (δ-nitrogen), $P42/ncm$ (δ^*-nitrogen) and $R\bar{3}c$ (ε-nitrogen), due to the fact that nitrogen undergoes 4 different phase transitions in the measured pressure range [199, 203].

4.4.1 Crystal structure at room temperature and ambient conditions

Although the room temperature crystal structure of $LaFeO_3$ at ambient conditions is known since it was determined by Geller and Wood in 1956 [204], a synchrotron X-ray powder diffraction measurement of the sample in a capillary and a detailed Rietveld refinement in space group $Pbnm$ (space group no. 62) was performed in order to ensure the phase purity of the used sample. With the Rietveld refinement shown in figure 4.2 it could be proved that the sample does not contain any impurities.

The refined lattice parameters are $a = 5.5549(1)$ Å, $b = 5.5663(1)$ Å and $c = 7.8549(2)$ Å, resulting in a volume of $V = 242.876(9)$ Å^3. These values are in good agreement with the values which were given by Geller and Wood [204] and Marezio and Dernier [205] (see also table 4.2). The calculated density and the calculated linear absorption coefficient as well as the residual values of the refinement are listed in table 4.2.

In table 4.3 the refined atomic positions and the refined overall atomic isotropic displacement parameter can be found. All atomic positions are fully occupied. Al-

1 It was also tried to model the anisotropic broadened peak shapes by a multi-dimensional distribution of lattice metrics within a powder sample [195], however, the application of spherical harmonics seems to give better refinement results.
2 The author wants to note, that independent from the individual onsets of the non-hydrostatic regimes, which depend on the used pressure media, the spherical harmonics were necessary above pressure values of 9.5 GPa
3 As defined in Topas 4.2: GOF = R_{wp} / R_{exp}.
4 For image plate data a GOF < 1 can occur if a pixel-splitting algorithm is used [206].

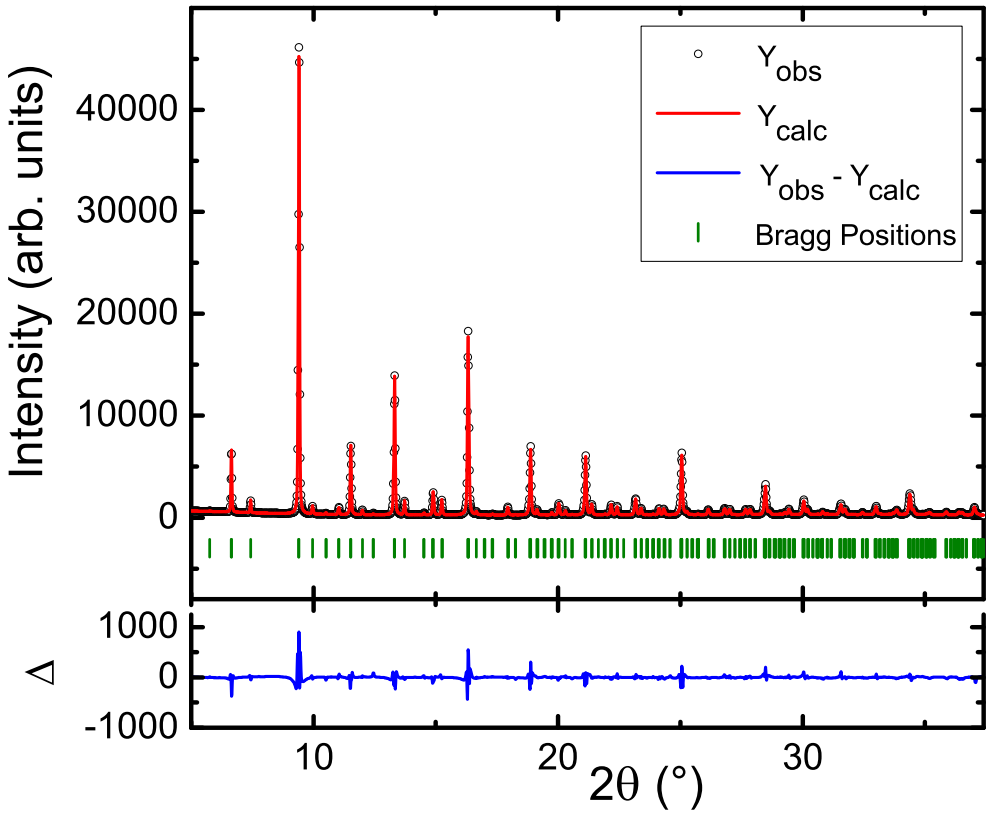

Figure 4.2: Rietveld refinement of $LaFeO_3$ at ambient conditions. The measurement of the sample was done in a capillary in Debye-Scherrer geometry.

Table 4.2: Lattice parameters, volume, density, linear absorption coefficients and residual values obtained from the Rietveld refinement of $LaFeO_3$ in *Pbnm* at ambient conditions. For reasons of comparison the literature values of Geller and Wood [204] and Marezio and Dernier [205] are also shown.

	This work	Geller and Wood [204]	Marezio and Dernier [205]
a (Å)	5.5549(1)	5.556	5.553(2)
b (Å)	5.5663(1)	5.565	5.563(2)
c (Å)	7.8549(2)	7.862	7.867(3)
Volume (Å^3)	242.876(9)	243.09	243.02
Density ρ ($\frac{g}{cm^3}$)	6.6387(2)	-	-
Linear absorption coefficient ($\frac{1}{cm}$)	82.423(3)	-	-
R_{exp}	3.843	-	-
R_{wp}	3.761	-	-
R_p	2.634	-	-
$\frac{R_{wp}(Rietveld)}{R_{wp}(Pawley)}$	1.224	-	-
GOF[3]	0.979[4]	-	-

though a refinement of the capillary measurement of $LaFeO_3$ with ADPs might be possible, these parameters were not applied, as a comparison with the high pressure results is much easier using solely an overall isotropic atomic displacement parameter. A presentation of the crystal structure of $LaFeO_3$ at room temperature and ambient conditions can be found in figures 4.9a)+c).

Table 4.3: Wyckoff positions, oxidation states, Cartesian coordinates and overall isotropic atomic displacement parameter obtained from the Rietveld refinement of $LaFeO_3$ in space group *Pbnm* at ambient conditions.

Atom	Wyckoff-position	Oxidation state	x	y	z	B_{iso} (Å^2)
La	4c	+3	-0.0064(2)	0.0293(1)	0.25	0.318(8)
Fe	4b	+3	0	0.5	0	
O1	4c	-2	0.0765(19)	0.4875(9)	0.25	
O2	8d	-2	-0.2817(13)	0.2853(12)	0.0366(10)	

Taking the values of the refined atomic coordinates it is possible to investigate the octahedral environment of the Fe^{3+} cation by calculating the bond lengths and the bond angles within the FeO_6 octahedron (due to symmetry reasons all octahedra within the crystal structure are equivalent). Exemplary, such an octahedron is shown in figure 4.3. By calculating the corresponding bond lengths between iron and oxygen atoms in the FeO_6 octahedron, it is obvious that this coordination polyhedron is not regular but rather distorted. Due to symmetry reasons the octahedron exhibits two different bond lengths between the iron atom and the oxygen O2 anion on the Wyckoff position 8*d* in the equatorial plane. The first bond length Fe-O2 is 1.99(1) Å (labeled with O21), whereas the second bond length Fe-O2 is 2.0185(8) Å (labeled with O22). The bond lengths between the apical O1 anion in Wyckoff position 4*c* and the Fe cation is 2.0104(22) Å. The other three bond lengths within the FeO_6 octahedron are given by inversion symmetry where the center of inversion lies at the position of the iron atom. The bond angle given by O21, Fe and O22 is 88.83(8)°, whereas the adjacent bond angle given by O22, Fe and O21 is 91.17(8)°. The other two bond angles in the equatorial plane are again given by inversion symmetry. The bond angle given by O1, Fe and O21 is 89.76(33)°, whereas the bond angle given by O1, Fe and O22 is 89.13(30)°. All other angles are either given as adjacent angles (for instance 180° - angle "O1-Fe-O21") or by inversion symmetry.
From these investigations it is clear, that although the Fe^{3+} cation is not Jahn-Teller active, its corresponding coordination octahedron is rather distorted at ambient conditions.

4.4.2 Approach A: Free Rietveld refinement

In this section the first Rietveld refinements of the high pressure synchrotron X-ray powder diffraction data are carried out in order to investigate all structural changes which occur in the $LaFeO_3$ perovskite if the applied pressure is successively increased.

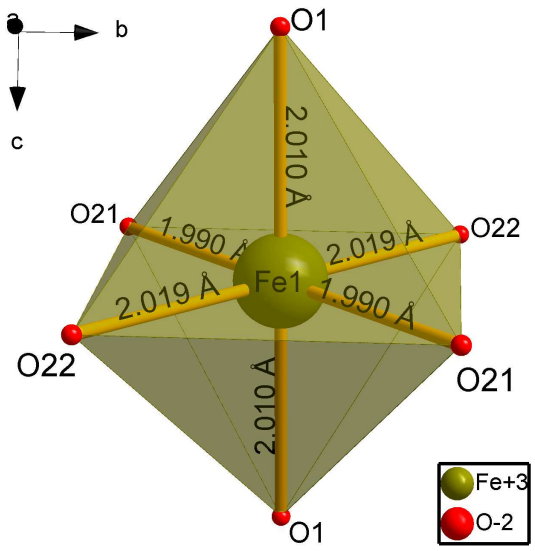

Figure 4.3: Coordination spheres of the FeO_6 octahedron at ambient conditions in the $LaFeO_3$ perovskite. Please note that due to the symmetry two different bond lengths between the central iron cation and the oxygen O2 anion exist.

The term "free" in the "free Rietveld refinement" denotes that a traditional atomic coordinate refinement is used, where all atomic coordinates on general positions can be freely refined. The results of the sequential free Rietveld refinement will also be used to judge the quality of the results of the other approaches carried out in sections 4.4.3-4.4.5.

4.4.2.1 Sequential Rietveld refinement

The sequential Rietveld refinements of the high pressure synchrotron X-ray powder diffraction measurements were carried out individually for each pressure media dependent data set, as the changes of the crystalline properties of the $LaFeO_3$ perovskite are not necessarily pressure media independent. Therefore, in this section, all figures contain the results of all 4 different data sets in order to exhibit the pressure media dependent effects.
In figure 4.4 the pressure dependent orthorhombic lattice parameters and the pressure dependent unit cell volume are presented. Due to the increasing pressure all three crystalline lattice vectors as well as the volume are decreasing, until at approximately 38 GPa a volume cell drop of around 3% can be observed. By following the lattice parameter b, this drop is obviously pronounced, whereas the lattice parameters a and c give only a small indication for such a drop. This findings already indicate a first order phase transition of the $LaFeO_3$ perovskite, for which the crystallographic and physical details will be given later.

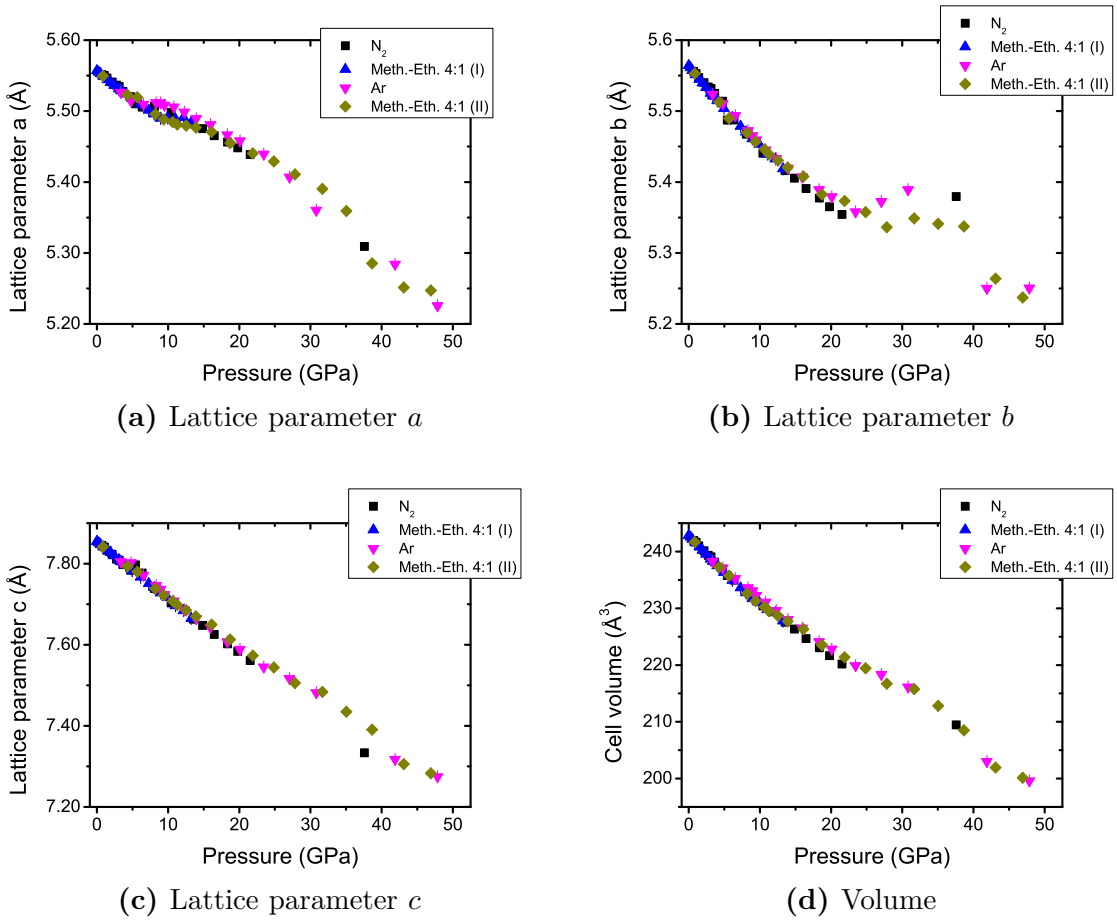

(a) Lattice parameter a **(b)** Lattice parameter b

(c) Lattice parameter c **(d)** Volume

Figure 4.4: Pressure dependent orthorhombic a)-c) lattice parameters and d) unit cell volume of $LaFeO_3$. For the lattice parameter b, a jump, indicating a structural first order phase transition, at approximately 38 GPa is visible.

If the lattice parameters a and b are plotted within one figure (see figure E.1 in appendix E), a crossing of these parameters at approximately 2.1 GPa can be observed. Such a crossing of lattice parameters allows a crystallographic description with a tetragonal unit cell, although the crossing of the lattice parameters is not necessarily connected with a phase transition to a tetragonal crystal structure. Therefore, the description of the lattice parameters at this point were kept in the orthorhombic crystal system framework. Interestingly a similar crossing of the lattice parameters a and b can be observed, if the $LaFeO_3$ perovskite is heated to a temperature of 675 K at ambient conditions [185]. However, such a crossing of the pressure dependent lattice parameters could not be observed below 8 GPa for the structurally similar $GdFeO_3$ perovskite [207].

Detailed investigations of the pressure dependent changes in the atomic coordinates revealed, that the atomic La y-coordinate exhibits a typical power-law behavior, as it shows a continuous shift with increasing pressure towards a special position which

indicates that the crystal structure probably adopts a higher symmetry. In order to model a probable phase transition, a fit of the pressure dependent La y-atomic coordinate by a suitable power-law behavior according to Landau theory was done by applying the following equation [67–69]:

$$La_y(P) = La_y(0) \cdot \left(\frac{P_{crit} - P}{P_{crit}}\right)^{\beta} + La_{HS} \quad , \tag{4.1}$$

where $La_y(P)$ is the value of the lanthanum y-coordinate at a certain pressure P, P_{crit} is the critical pressure, where the phase transition to the higher symmetry takes place, La_{HS} is a constant which accounts for non-zero values of the atomic coordinates in the high symmetry phase[1] and β is the critical exponent, whose value depends on the type of the observed thermodynamic system[2].
The resulting fit of the refined data of the La y-coordinate with the power-law behavior according to equation 4.1 can be seen in figure 4.5b)[3].

The determined critical pressure value by the La y-coordinate is $P_{crit} = 20.5(6)$ GPa and the corresponding critical exponent was determined to $\beta = 0.48(5)$. As the value of the critical exponent is very close to the expected value of $\beta = \frac{1}{2}$ for a displacive second order phase transition without any coupling to strain, etc. [69], it can be assumed that the $LaFeO_3$ perovskite undergoes a structural second order phase transition to a higher symmetry at the determined critical pressure value. A similar behavior as for the La y-coordinate can be observed for some oxygen coordinates, in particular the O1 y-, O2 x- and O2 y-coordinate, although the determination of the oxygen positions is not as precise as for the lanthanum coordinates[4]. For these oxygen coordinates also a trend to a special position can be found (see figures 4.5 and 4.6).
Assuming that the structural phase transition is of second order, a group-subgroup relationship can be established, whereas the crystal structure at ambient conditions with space group *Pbnm* must be regarded as the subgroup in this relationship. Different Rietveld refinements of the data sets between 21 and 30 GPa with probable super-

1 In the case of the La y-coordinate, the constant La_{HS} is equal to zero.
2 For displacive phase transitions of second order without any coupling to strain, etc., the value of the critical exponent can be expected to be $\frac{1}{2}$, which can be found experimentally as well as it can be determined theoretically by mean-field theory [69].
3 In this graph, the atomic coordinates are fixed to their special positions after reaching the critical phase transition point. However, the fit was done by using the non-fixed values of the La y-coordinate above the phase transition.
4 The reason for the vague determination of the oxygen coordinates lies in the usage of X-rays, because X-rays are not that sensitive to oxygen as compared to lanthanum, as the scattering power of an oxygen anion is much smaller than the scattering powder of a lanthanum cation. In addition, the applied pressure has also an influence on the intensity of the phase peaks, as the peaks become unnaturally broadened above the hydrostatic limit of the used pressure medium and this makes an unambiguous determination of the oxygen positions also rather complicated.

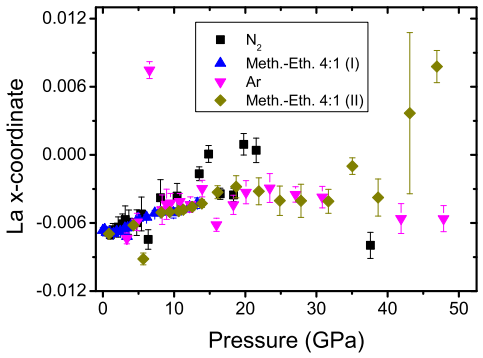

(a) La x-coordinate

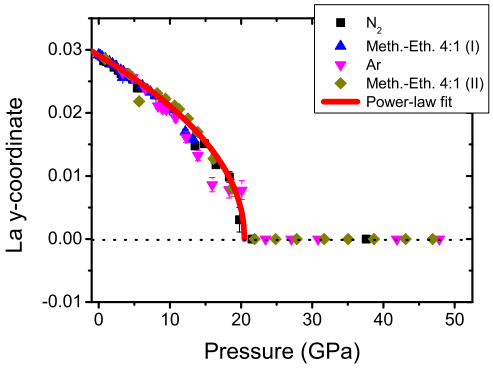

(b) La y-coordinate

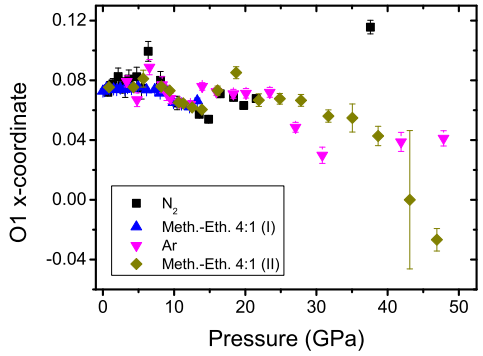

(c) O1 x-coordinate

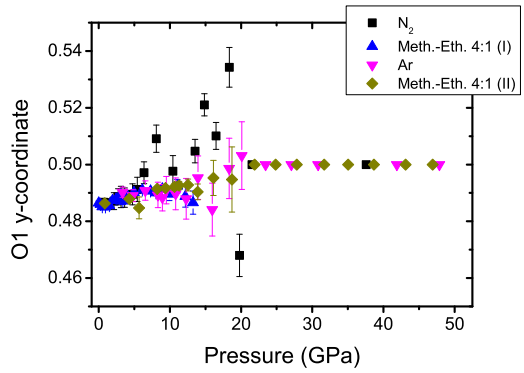

(d) O1 y-coordinate

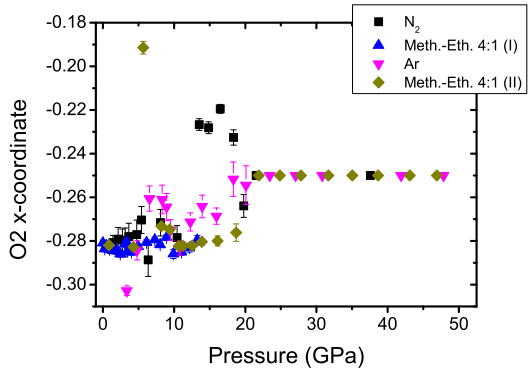

(e) O2 x-coordinate

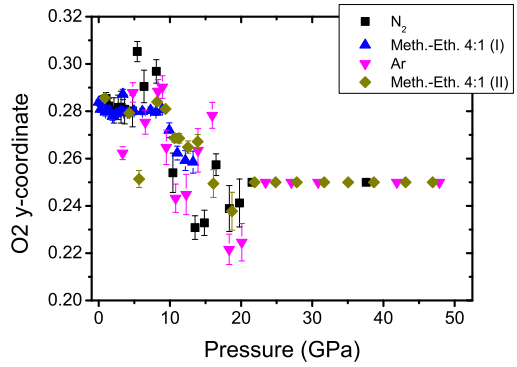

(f) O2 y-coordinate

Figure 4.5: Pressure dependent atomic coordinates of the $LaFeO_3$ perovskite. The lanthanum y-coordinate in b) gives a clear indication of a second order phase transition. A subsequent power-law fit for this coordinate resulted in a critical exponent of $\beta = 0.48(2)$ and a critical pressure of $P_{crit} = 20.5(6)$ GPa. (The figures of the atomic coordinates are continued in figure 4.6).

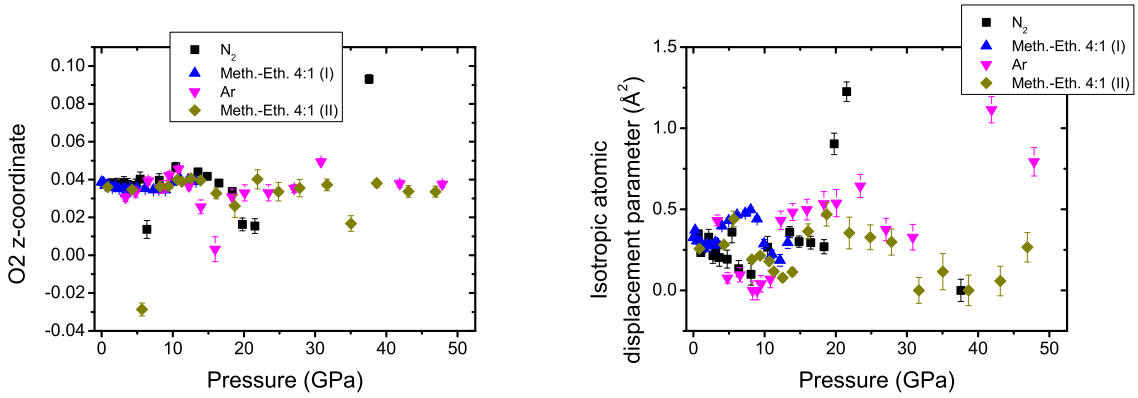

(a) O2 z-coordinate

(b) Overall isotropic atomic displacement parameters

Figure 4.6: a) Continued pressure dependent atomic coordinates of the $LaFeO_3$ perovskite from figure 4.5. b) Pressure dependent overall isotropic atomic displacement parameter for all datasets.

groups of the space group *Pbnm*[1] revealed that the best refinement can be achieved with the minimal non-isomorphic supergroup *Ibmm*. A plot of the Rietveld refinement of the high pressure synchrotron X-ray powder diffraction pattern of the fourth run at approximately 24.8 GPa with methanol-ethanol as pressure medium can be found in figure 4.7. The crystallographic details of this second order phase transition as well as the refined atomic coordinates in space group *Ibmm* can be found in the Bärnighausen tree [208] in figure 4.8.

The crystal structure of the $LaFeO_3$ perovskite at room temperature and ambient conditions in space group *Pbnm* as well as the crystal structure at room temperature and at a pressure of 24.8 GPa in space group *Ibmm* are displayed in figure 4.9. It is obvious, by looking at figures 4.9c) and d), which give a viewing direction along the crystallographic *c*-axis, that the FeO_6 octahedra must rotate respectively tilt continuously until a higher symmetry and therefore a higher structural ordering is reached in the high pressure phase[2].

For the determination of the crystal structure above 38 GPa the high pressure synchrotron X-ray powder diffraction pattern of the fourth run at approximately 43.1 GPa with methanol-ethanol as pressure medium was used. An indexing of this powder pattern revealed that tetragonal and orthorhombic crystal structures have comparable

1 The space group *Pbnm* is a non-standard setting of the space group *Pnma*, therefore supergroups in the standard setting as well as in the non-standard setting were used in order to preform the Rietveld refinements

2 The rotation/tilting of the FeO_6 octahedra must be continuously due to the assumption of a second order phase transition of the entire crystal structure of the $LaFeO_3$ perovskite. An evidence for this behavior will be also given in subsection 4.4.5, where the rotation/tilting is modeled by rotational symmetry modes of a rigid body

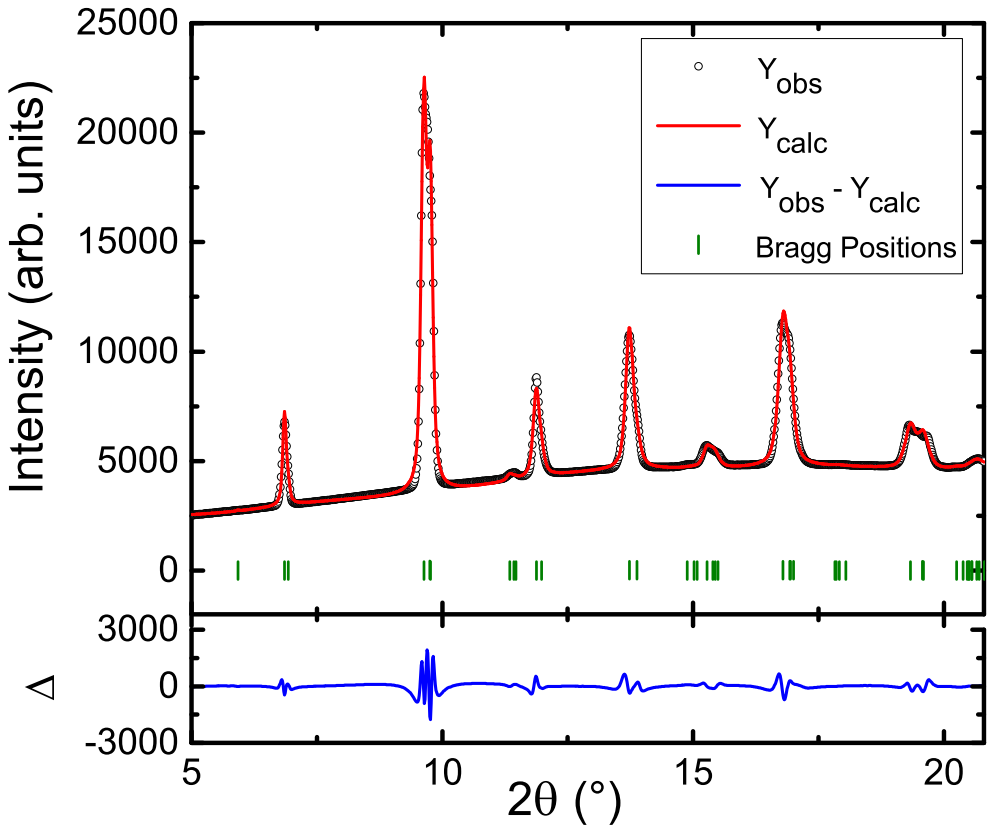

Figure 4.7: Rietveld plot of the $LaFeO_3$ perovskite at 24.8 GPa using methanol-ethanol as pressure medium (fourth run). The limited 2θ range is due to the geometric restriction by the DAC.

figure of merits[1]. In order to determine the most probable crystal structure and corresponding space group, different whole powder pattern fittings (WPPF) according to the Le Bail method [63] were performed. These WPPFs showed, that orthorhombic crystal structure solutions have considerably lower R_{wp} values (e.g. R_{wp} of $Cmmm$ is 1.766 % with 70 reflections in the investigated range) in contrast to tetragonal crystal structure solutions which have significantly enhanced R_{wp} values (e.g. R_{wp} of $P4$ is 2.228 % with 108 reflections in the investigated range)[2]. Subsequent Rietveld refinements of different possible orthorhombic crystal structure showed, that the best refinement can still be achieved in space group $Ibmm$, which characterizes this phase transition as an isostructural or isosymmetric first order phase transition (for details of this isostructural phase transition see also the Bärnighausen tree in figure 4.8).

1 The figure of merit in TOPAS 4.2 [57] is defined according to the de Wolff figure of merit [45].

2 The author would like to mention, that at such high pressure values in the non-hydrostatic regime, the obvious peak broadening can hamper the determination of the real crystal structure. Although, due to this reason such an indexing can be sometimes doubtful, the difference of almost 0.5 % is believed to be high enough in order to state that the orthorhombic crystal structure has a higher probability.

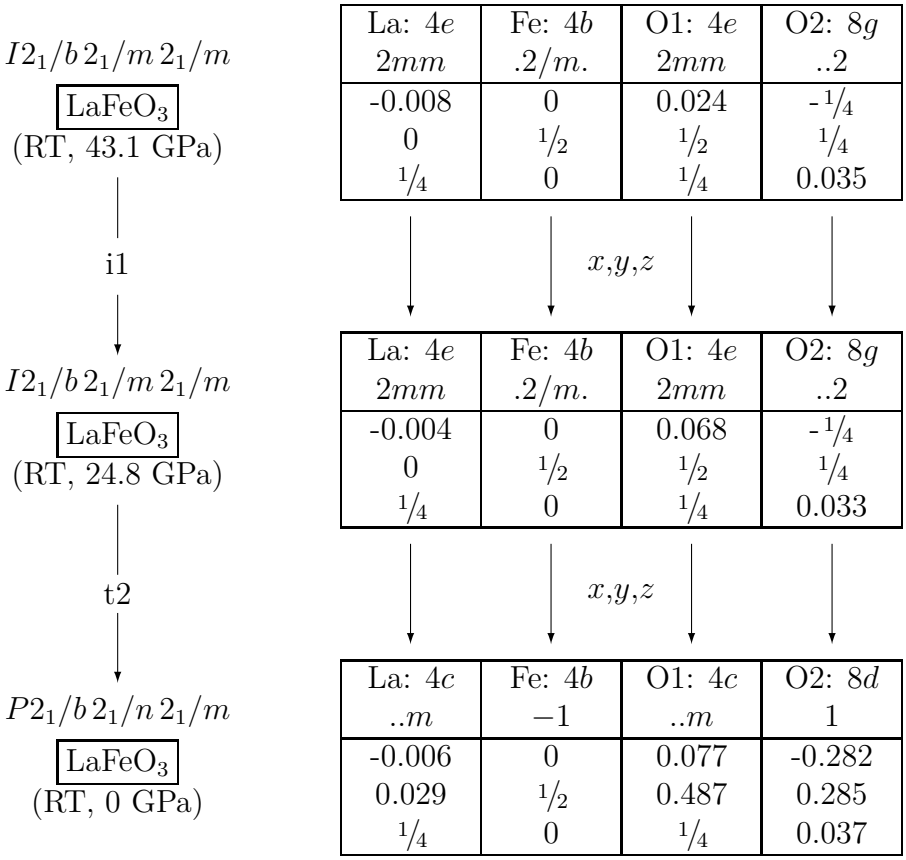

Figure 4.8: Bärnighausen tree [208] for the first and second order phase transitions in $LaFeO_3$ at the room temperature isobar and at pressures below 45 GPa. Lattice parameters for the *Ibmm* phase at 24.8 GPa are $a = 5.429(1)$ Å, $b = 5.357(1)$ Å and $c = 7.543(3)$ Å. Lattice parameters for the *Ibmm* phase at 43.1 GPa are $a = 5.262(2)$ Å, $b = 5.253(2)$ Å and $c = 7.306(2)$ Å.

The finding of an isostructural first order phase transition is in agreement with other high pressure studies of the $LaFeO_3$ perovskite (and also some other orthoferrites), where Mössbauer spectroscopy, X-ray powder diffraction and density functional theory (DFT) calculations revealed that in the pressure range of 30 GPa $\leq$ p $\leq$ 50 GPa a high-spin (S = $\frac{5}{2}$) to low-spin (S = $\frac{1}{2}$) transition of the Fe^{3+} cation takes place [181, 191–193, 209]. Although Xu *et al.* attributed the phase transition with a volume drop of approximately 3% to a first order phase transition from an orthorhombic crystal structure to a tetragonal one [191], it could be clearly shown by Rietveld refinements that this is not the case, as the phase transition is isosymmetric and therefore the crystal structure maintains the orthorhombic symmetry. This result is also in accordance with the study of Rozenberg *et al.* [209], who showed that other $RFeO_3$ orthoferrites (with R = Pr, Eu, Lu) also possess an isostructural first order phase

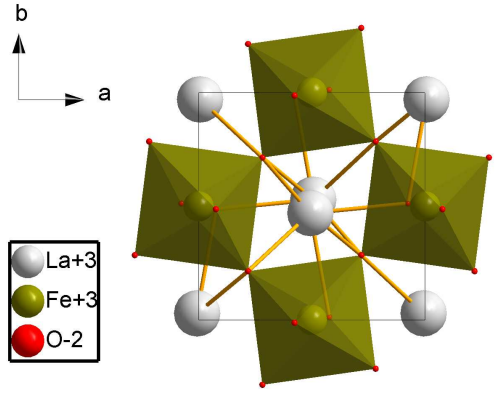

(a) 0 GPa, view along c

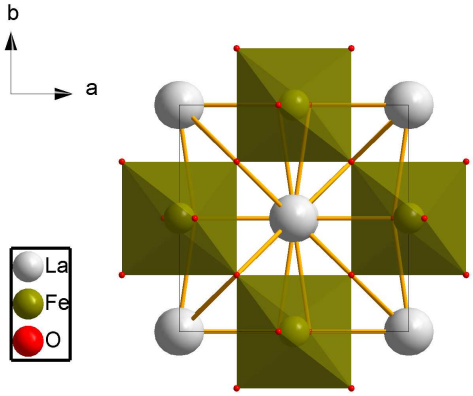

(b) 24.8 GPa, view along c

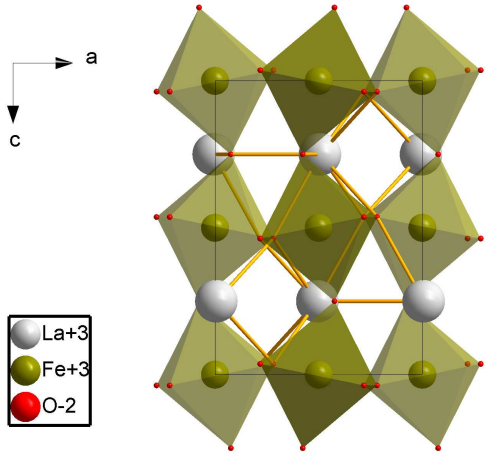

(c) 0 GPa, view along b

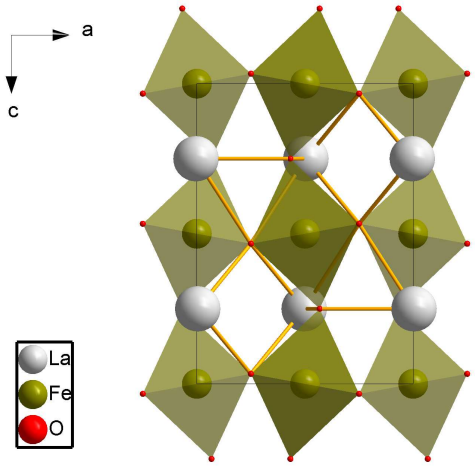

(d) 24.8 GPa, view along b

Figure 4.9: Crystal structure of the $LaFeO_3$ perovskites at different pressures. Ambient crystal structure in space group *Pbnm*, a) view along *c* and c) view along *b*. Crystal structure at 24.8 GPa in space group *Ibmm*, b) view along *c* and d) view along *b*.

transition within approximately the same pressure range[1]. Despite the fact, that the $LaFeO_3$ perovskite does not show a first order phase transition to a tetragonal crystal structure, Xu *et al.* reported from X-ray powder diffraction that the phase transition seems to be very "sluggish" [191]. This finding can be confirmed by the inspection of the lattice parameters and the volume in figure 4.4. The reason for this behavior is, that the region around the approximate critical phase transition value of 38 GPa can be regarded as a coexistence region of two different phases, for which an evidence is given by the Mössbauer study of Xu *et al.*, which demonstrated that at the room temperature isotherm in the pressure range of 30 GPa $\leq$ p $\leq$ 50 GPa the high-spin to low-spin transition takes only partially place, which therefore leads to two different magnetic sublattices and to two different crystal structures with different lattice parameters and volumes[2] [191]. Interestingly for a similar orthoferrite, namely $PrFeO_3$, this coexistence region can be much better observed by synchrotron X-ray powder diffraction, in contrast to $LaFeO_3$, as it was shown by Xu *et al.* [191] and Rozenberg *et al.* [209].

The DFT calculations by Javaid *et al.* proofed that the pressure dependent spin-crossover can be explained by the pressure dependent increase of the crystal-field splitting energy, which increases due to the change of the distortion level of the FeO_6 octahedron, which in turn results from the shortening of the Fe-O bondings within the FeO_6 octahedron [181, 192, 193]. Therefore the high-spin to low-spin transition is not only connected to the shrinkage of the entire unit cell volume of the crystal structure, but also to the shrinkage of the octahedral volume of the FeO_6 coordination polyhedron. In figure 4.10 the volume of the FeO_6 octahedron is plotted.

In this figure the three pressure dependent crystal structure phases can clearly be observed by the evolution of the octahedral volume. Until the occurrence of the second order phase transition at the critical pressure value of approximately 20.5 GPa, the octahedral volume decreases almost linearly. Above that value, there is also an almost linear decrease of the octahedral volume, although the slope of that linear decrease has changed. At higher pressure values an abrupt decrease of the octahedral volume at an approximate critical phase transition value of 38 GPa can be observed. This volume drop indicates the reduction of the Fe-O bond lengths due to the high-spin to low-spin transition.

Transitions to the non-hydrostatic regime and determination of the equation of state parameters

For the determination of reliable equation of state (EoS) parameters, special atten-

1 For these orthoferrites an isostructural first order phase transition in space group *Pbnm* was observed [209].

2 Unfortunately, in the literature no discussion was found, if the partial high-spin to low-spin transition is attributed to an intra-domain or inter-domain phenomenon.

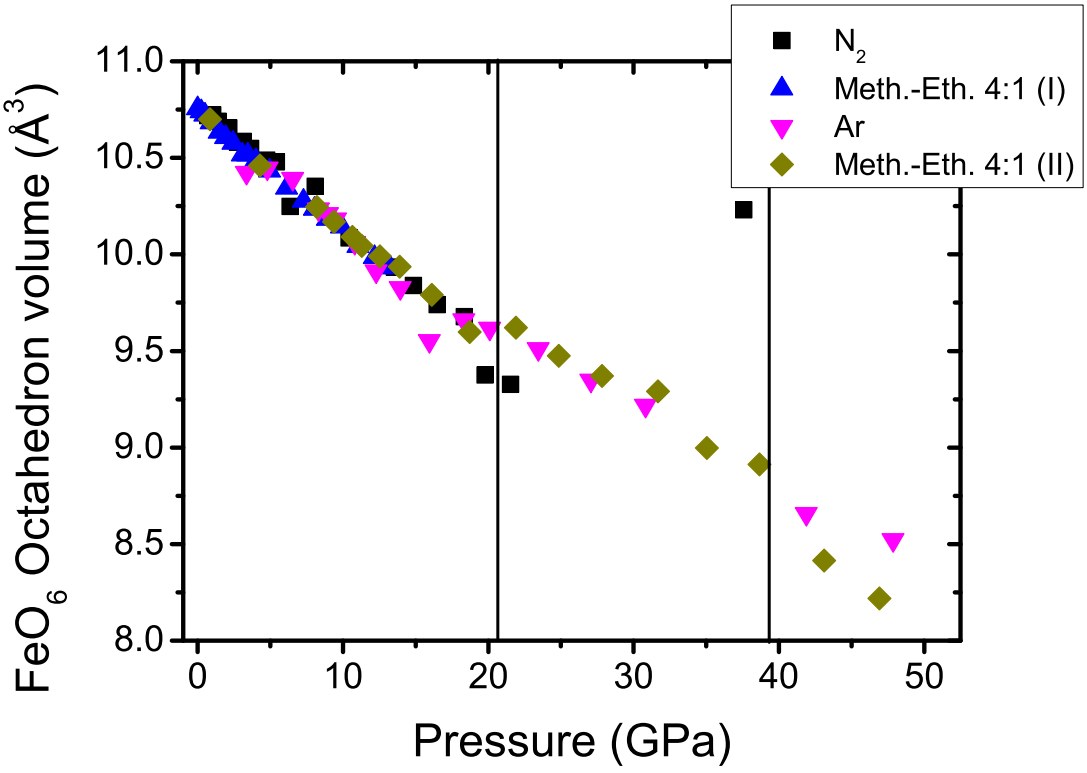

Figure 4.10: Pressure dependent volume of the FeO_6 octahedron in the $LaFeO_3$ perovskite. Three different regions (separation by black solids lines) can be distinguished, which correspond to the three crystal structure phases.

tion has to be paid on to the onset of non-hydrostatic conditions, which will be shown later. In the hydrostatic regime the pressure on the sample and therefore the compression of the sample is mediated by the used pressure medium, which acts as an isotropic quantity, whereas in the non-hydrostatic regime, the pressure on the sample cannot be any longer regarded as being isotropic. The reason for that behavior of the pressure medium depends mainly on two effects, firstly the pressure dependent intermolecular forces within the gas or liquid which is used as pressure medium and secondly on the geometry of the high pressure experiment, which is given by the DAC. As in most experiments the DAC cannot be modified due to the geometry of the performed experiments (e.g. powder diffraction experiments), the limiting factor is given by the type of the used pressure medium.
In order to determine the corresponding hydrostatic limits, at which the non-hydrostatic conditions set in, single crystal as well as powder diffraction experiments with standard samples like silicon (Si), lanthanum hexaboride (LaB_6) or quartz (SiO_2) can be carried out, as the measured peak width of these samples is highly sensitive to the onset of non-hydrostatic conditions [210]. Using this method, Angel *et al.* determined the following hydrostatic limits for the used pressure media performing X-ray diffraction experiments with quartz single crystals: ≈1.9 GPa for argon, ≈3 GPa for

nitrogen and ≈ 9.8 GPa for a mixture of methanol and ethanol (ratio 4:1) [210]. In contrast, if these hydrostatic limits are determined by another method like the ruby fluorescence method, then different values for the onset of non-hydrostatic conditions can be determined [211]. Nevertheless, in this work, the hydrostatic limits determined by Angel *et al.* [210] will be used, as these values agree with the observed pressure dependent phenomena which occur for the refined $LaFeO_3$ parameters.

As it was already explained at the beginning of section 4.4, a constrained phenomenological Gaussian and Lorentzian strain parameter together with Gaussian and Lorentzian crystallite size parameters were used in order to model the peak broadening due to sample dependent effects. During the pressure dependent Rietveld refinements it turned out, that especially the constrained phenomenological Gaussian and Lorentzian strain parameter is very sensitive to the onset of non-hydrostatic conditions as can be seen in figure 4.11b).

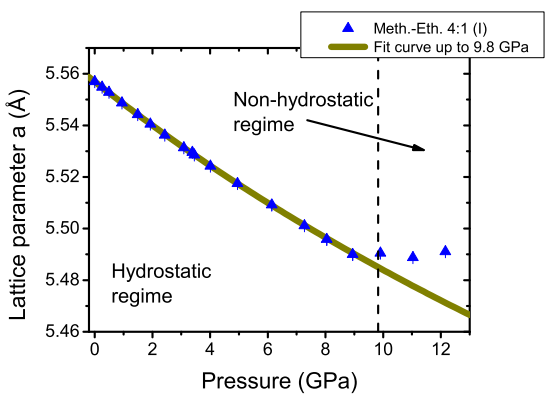

(a) Lattice parameter a for the first methanol-ethanol measurement series

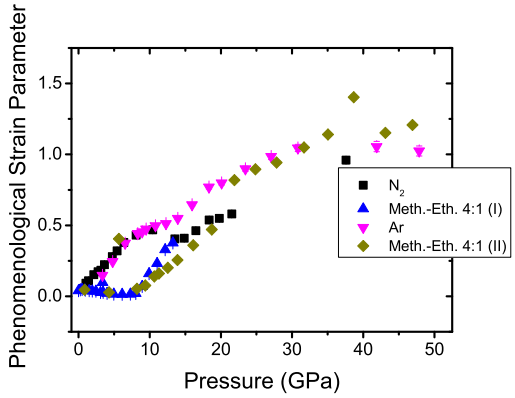

(b) Phenomenological strain parameter

Figure 4.11: a) Pressure dependent lattice parameter a of $LaFeO_3$ obtained for the first methanol-ethanol measurement series. The onset of the non-hydrostatic regime of the used pressure media is obvious, as there is clear kink at approximately 9.8 GPa observable in the sequential refined data sets. b) Pressure dependent phenomenological strain parameters for the different pressure media dependent data sets. From this figure the onset of the non-hydrostatic regime for the different pressure media can be estimated (the definition of the phenomenological strain parameter is given in a footnote earlier in this chapter).

The reason for the increase of the value of the phenomenological strain parameter at the hydrostatic limit is rather simple, as it is directly connected to the FWHM of the diffraction peaks and therefore it is the same phenomenon as it was used in the method of the determination of the hydrostatic limit by Angel *et al.* [210]. From figure 4.11b) it is also obvious that the onset of the non-hydrostatic regime is at low pressures for the pressure media argon and nitrogen and at much higher pressures for the methanol-ethanol mixture in a ratio of 4:1. This means, that the measured and refined data sets below the hydrostatic limit of the methanol-ethanol measurement

series are in fact more reliable than the values determined for the argon and nitrogen measurement series.
Interestingly, the onset of the non-hydrostatic conditions can also be observed in the behavior of the lattice parameters. If, for instance, the pressure dependent lattice parameter a of the methanol-ethanol measurement series of the second run is displayed in detail, then a kink in the trend of this parameter can be observed (see figure 4.11a)). This shows remarkably, that the fit of the lattice parameters and of the volume of the $LaFeO_3$ perovskite by EoS will be only reliable up to the hydrostatic limit.
Due to this reason, the determination of EoS parameters from the results of the sequential Rietveld refinements of the $LaFeO_3$ perovskite will be only carried out for the methanol-ethanol measurement series.

In order to determine the bulk modulus, the first pressure derivative of the bulk modulus and the volume at ambient pressure of the $LaFeO_3$ perovskite, different semi-empirical EoS can be used. Although today many authors prefer the usage of the Birch-Murnaghan EoS [212, 213], the focus in this work was laid on the Murnaghan EoS [214] and the Vinet EoS [215], as the Murnaghan EoS is an analytical invertible equation and for the Vinet EoS a suitable approximation, which makes this EoS invertible, can be found[1].

In general, EoS are presented as a pressure equation which depends on the volume, the bulk modulus, the first or higher pressure derivatives of the bulk modulus and the volume at zero pressure. Most of these EoS are valid on the room temperature isotherm although they do not possess a special term which accounts for the temperature. Among the many proposed isothermal EoS, the Murnaghan EoS is well known:

$$P(V) = \frac{B_0}{B_0'} \cdot \left[\left(\frac{V_0}{V} \right)^{B_0'} - 1 \right] \quad , \tag{4.2}$$

where $P(V)$ is the pressure, which depends on the volume V, V_0 is the volume at zero pressure[2], B_0 is the bulk modulus and B_0' is the first pressure derivative of the bulk modulus.
The benefit of this equation for parametric Rietveld refinements is, that it is analytically invertible, and the inversion is given by the following equation:

$$V(P) = V_0 \left(1 + \frac{B_0' P}{B_0} \right)^{-\frac{1}{B_0'}} \quad . \tag{4.3}$$

As the Murnaghan EoS is a semi-empirical equation, it is only valid over a certain range of volume compression. In the case of the Murnaghan EoS a validity up to

1 The possible invertibility of the EoS is of great importance for e.g. parametric Rietveld refinements (see subsection 4.4.2.2).
2 The difference between the volume in vacuum/at zero pressure and ambient conditions is that small, so that we can assume that both volumes are approximately equal.

a volume compression of 10% can be assumed [216, 217]. For the determination of the EoS parameters for the $LaFeO_3$ perovskite this means, that a volume compression of 10% is first reached at approximately 25 GPa, which is far beyond the hydrostatic limit of the used methanol-ethanol 4:1 pressure medium. Therefore it can be assumed, that the Murnaghan EoS will provide reliable values below 9.8 GPa in the case of the $LaFeO_3$ perovskite.

Although the inverted Murnaghan EoS is now a volume equation, it is still not a suitable equation for a parametric Rietveld refinement, as the volume of the unit cell is in general a quantity, which can be derived from the results of the refinement of a powder diffraction pattern, but not refined itself. In order to have a refineable quantity the inverted Murnaghan EoS must be transformed from a bulk equation to a linear equation. A suitable transformation for such a "linearized" Murnaghan EoS is given by Angel [217], which results in the following "linearized" inverted Murnaghan EoS:

$$a(P) = a_0 \cdot \left(1 + \frac{B'_{0_a} P}{B_{0_a}}\right)^{-\frac{1}{3 \cdot B'_{0_a}}} \quad , \tag{4.4}$$

where $a(P)$ is the value of the lattice parameter at a certain pressure, a_0 is the lattice parameter at ambient conditions, B_{0_a} is the linear modulus and B'_{0_a} is the first pressure derivative of the linear modulus.
In order to derive this "linearized" equation, simply the cube root of both volumes from equation 4.3 is taken and the bulk modulus parameters are replaced by pseudo-linear modulus parameters. The validity of this approach for cubic, tetragonal and orthorhombic crystal systems was also demonstrated by Angel, as he stated that the second-order strain tensor and the second-order bulk tensor are diagonal matrices and that the entries on the diagonal represent the main axis of the corresponding crystal system [217].

In table 4.4 the Murnaghan EoS parameters for the bulk modulus, the first pressure derivative of the bulk modulus as well as all linear parameters belonging to the corresponding crystal axis for the $LaFeO_3$ perovskite can be found.

In addition, in this table also the theoretical values of the bulk modulus, of the first pressure derivative of the bulk modulus and of the volume at ambient conditions for a cubic $LaFeO_3$ crystal structure with ferromagnetic (FM) or G-type antiferromagnetic (AFM) moment configuration are listed [219]. Shein *et al.* calculated these theoretical values using an *ab initio* pseudo-potential method with the inclusion of single-site Coulomb correlations [219]. The employed EoS in these calculations was the Birch EoS [220].

In contrast to the Murnaghan EoS, the Vinet EoS is believed to be more "universal", as it is applicable to a wide range of solids, including metals, ionic solids and simple organic compounds [218]. In addition, the range of validity for the Vinet EoS is much higher compared to the Murnaghan EoS, as it is applicable even at high com-

Table 4.4: Bulk modulus, its pressure derivative and the volume at ambient conditions of the $LaFeO_3$ perovskite determined by an inverted Murnaghan EoS [214] from sequential Rietveld refinement of the first and second 4:1 methanol-ethanol measurement series (second and fourth run) up to the hydrostatic limit (approximately 9.8 GPa [210]). Below the bulk values, the corresponding values of the "linearized" inverted Murnaghan EoS [216, 217] are given, namely the linear modulus, the first pressure derivative of the linear modulus and the lattice parameter at ambient conditions for all orthorhombic lattice parameters a, b and c. In addition, the corresponding bulk and linear values determined for the Vinet EoS are given. The values were determined by the program EOSFIT 5.2 [218]. Theoretical values from the literature are taken by Shein *et al.* [219] and are calculated for a cubic crystal structure of $LaFeO_3$ with either ferromagnetic (FM) or G-type antiferromagnetic (AFM) moment configuration using for both the Birch EoS [220]. Furthermore the corresponding literature values for the isostructural $GdFeO_3$ perovskite derived from single crystal X-ray diffraction measurements are given for reasons of comparison [221].

	Vinet EoS	Murnaghan EoS	Birch EoS [220] Cubic $LaFeO_3$ (FM)	Birch EoS [220] Cubic $LaFeO_3$ (AFM)	Birch-Murnaghan EoS (3rd order) [221] $GdFeO_3$
V_0 (Å^3)	242.87(1)	242.87(1)	57.16	56.67	230.384(10)
$B_0(GPa)$	172(1)	172(2)	197.9	198.4	182(1)
B'_0	4.3(2)	4.3(3)	5.4	5.4	6.3(3)
a_0 (Å)	5.557(1)	5.556(1)	3.852	3.841	5.35105(23)
B_{0_a} (GPa)	212(2)	209(3)			188(3)
B'_{0_a}	8.3(5)	9.2(7)			5.2(7)
b_0 (Å)	5.564(1)	5.564(1)			5.61249(10)
B_{0_b} (GPa)	141(1)	142(1)			181(1)
B'_{0_b}	4.4(2)	4.2(3)			5.7(4)
c_0 (Å)	7.855(1)	7.86(1)			7.67106(11)
B_{0_c} (GPa)	176(1)	176(1)			172(2)
B'_{0_c}	1.6(3)	1.5(3)			8.2(5)

pression ratios up to volume compressions of $\frac{V}{V_0} > 0.6$ [218]. Different studies showed also, that the accuracy of the Vinet EoS is quite good, therefore it is believed that this equation, which is based on an empirical potential [215], is among the most accurate EoS [222, 223].
The Vinet EoS is given by the following equation [215]:

$$P(V) = 3 \cdot B_0 \cdot \left(\frac{1-f}{f^2}\right) \cdot \exp\left[\frac{3}{2} \cdot (B'_0 - 1) \cdot (1-f)\right] \quad , \tag{4.5}$$

where f is given as $\left(\frac{V}{V_0}\right)^{\frac{1}{3}}$.
Although the equation of the Vinet EoS looks quite simple, it is not possible to find

an analytical inversion $V(P)$ for this equation. However, as already explained above, for a parametric Rietveld refinement it is mandatory to have an inverted version of this equation and furthermore it must be also possible to find a "linearized" form of this equation. A suitable possibility to overcome this challenge is to expand the exponential part of the Vinet EoS by a Taylor series up to third order and to invert the resulting approximation [175]. This will result in four extensive equations of which two are physically meaningful, as they cover the experimental accessible range of the bulk modulus and the first pressure derivative of the bulk modulus [175]. Following the approach of Angel [217], it is also possibe to create a "linearized" version of this inverted third-order Vinet EoS approximation [175], which can be used in a parametric Rietveld refinement (see appendix F).

With the program EOSFIT 5.2 [218] it is possible to fit a bulk and a "linearized" version of the Vinet EoS to a set of data points[1], which in turn are retrieved by the sequential Rietveld refinements of the powder diffraction patterns of the $LaFeO_3$ perovskite (for the results see table 4.4).

The comparison between corresponding values in table 4.4 shows, that both equations give almost the same result for an individual parameter, therefore both EoS seem to be suitable in order to model the pressure dependent behavior of the unit cell volume and lattice parameters of the $LaFeO_3$ perovskite.

4.4.2.2 Parametric Rietveld refinement

As it was already stated in section 2.2.1, parametric Rietveld refinements can be very useful in many regards, as the application of constraints in form of equations will lead to a reduction of parameters and therefore the smaller number of parameters can lead to a stabilization of the least-square iteration process. Furthermore, the application of such equations can even sharpen the global refinement minimum, as long as the chosen equations are inherent to the investigated powder diffraction patterns.

This statement already shows, that is not possible to perform a parametric Rietveld refinement with all four measurement series of the $LaFeO_3$ perovskite, as the onset of the non-hydrostatic regimes is different for the different used pressure media and therefore the parameterization with a single EoS would certainly lead to wrong physical results. In addition, it cannot be fully excluded that wrong results will be obtained, if two different measurement series with the same pressure medium are constrained[2].

1 These data points must be given as P(V) table, therefore it is directly possible to use the Vinet EoS in order to determine the corresponding bulk and linear EoS parameters.

2 To the knowledge of the author, it exists no study where, for instance, the dependence of the hydrostatic limit on the particle size is investigated. If it is now assumed, that such a dependency exists, then two differently ground samples of $LaFeO_3$ are no longer comparable, even if the same pressure medium is used.

In order to apply an EoS to the widest possible pressure range, only the methanol-ethanol measurement series can be taken, as the hydrostatic regimes for argon and nitrogen cover only a limited pressure range (see section 4.4.2.1).
Besides the parameterization of the lattice parameters of $LaFeO_3$ with EoS, also a parameterization of some of the atomic coordinates can be done, as some of them obey the power-law behavior given by equation 4.1. However, in order to speed up the computational process of the parametric Rietveld refinement, the unnormalized version of equation 4.1 was used, which is given by:

$$La_y(P) = A \cdot (P_{crit} - P)^{\beta} + La_{HS} \quad , \tag{4.6}$$

where the amplitude A can be analytical converted to the physical amplitude $La_y(0)$ by $A = La_y(0) \cdot P_{crit}^{\beta}$.

To carry out a parametric Rietveld refinement with both parameterization approaches, the EoS parameterization for the lattice parameters and the power-law behavior parameterization for the atomic coordinates, a suitable measurement series must be used, in order to fulfill all of the above mentioned requirements for a parametric Rietveld refinement. This suitable measurement series is only given by the methanol-ethanol measurement series of the fourth run, as this series has a wide hydrostatic regime and there are enough data points in order to model the behavior of the atomic coordinates even up to high pressures of 46.9 GPa.

The results of the parameterization of the lattice parameters by a "linearized" inverted Murnaghan EoS[1] can be found in figure 4.12 and in table 4.5. An overview of the differences between the parameters in the sequential and in the parametric Rietveld refinement is given in table 4.6. From this table it can be seen, that up to the hydrostatic limit of 9.8 GPa, the lattice parameters are modeled by the Murnaghan EoS, whereas the lattice parameters above can be either refined individually or they can be fixed to the values determined by the sequential Rietveld refinement[2].

Unfortunately, in the hydrostatic regime of this measurement series only 4 data points are present, which explains the observed differences between the values of the parametrically determined EoS parameters and the corresponding EoS parameters which were determined from the sequentially refined data sets[3].

The parameterization of the atomic coordinates with equation 4.6 is shown in figure

1 The results of the parameterization of the lattice parameters by a "linearized" inverted third order Vinet EoS approximation are within one estimated standard deviation in agreement with the results of the "linearized" inverted Murnaghan EoS and therefore they are not shown here.

2 In the particular case of the parametric Rietveld refinement of $LaFeO_3$, these values were fixed to the results from the sequential Rietveld refinement, in order to reduce the number of refineable parameters, which leads to a better stabilization of the refinement.

3 Please note, that the difference is only 3 times the estimated standard deviation, which is surprisingly small, considering the amount of data points and the number of equation variables.

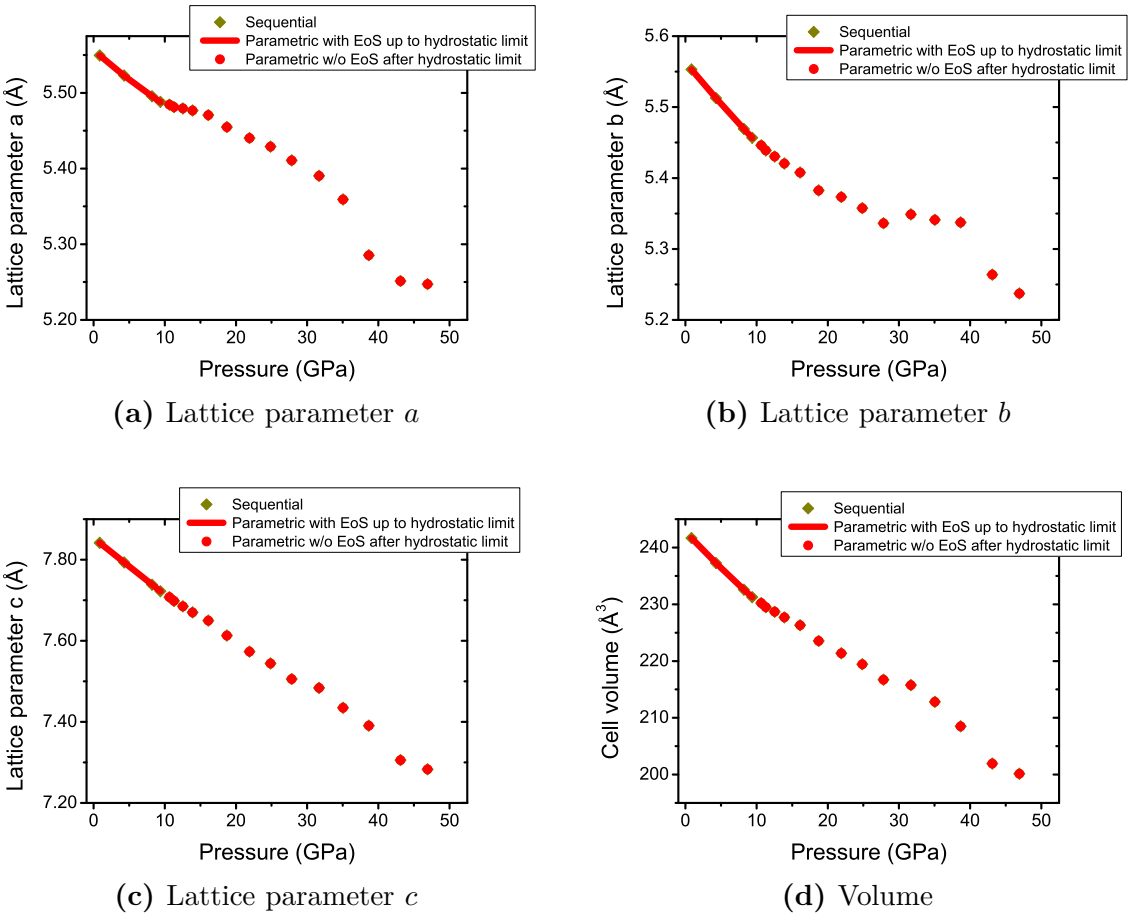

(a) Lattice parameter a **(b)** Lattice parameter b

(c) Lattice parameter c **(d)** Volume

Figure 4.12: Pressure dependent orthorhombic a)-c) lattice parameters and d) unit cell volume of $LaFeO_3$ from sequential as well as from parametric Rietveld refinement. For the parametric Rietveld refinement, the red lines denote that these parts were parameterized with the "linearized" inverted Murnaghan EoS, whereas the red points denote that these values were refined individually. The red line for the volume is calculated by the parameterized values of the lattice parameters.

4.13. Although four atomic coordinates, namely the La y-, the O1 y-, the O2 x- and the O2 y-coordinate take part in the structural second order phase transition and therefore they should obey a power-law behavior with a common critical exponent[1], it was only possible to parameterize the La y- and O1 y-coordinates with this model, as the modeling of the other coordinates by a power-law behavior either with individual critical exponents or a common critical exponent led always to unphysical values. Probably this phenomenon can be attributed to the uncertainty of the determination of the atomic O2 positions at higher pressure values (see also the comment about the determination of the oxygen positions in subsection 4.4.2.1). Due to this reasons, the

1 The reason for the common critical exponent is given by the collective motion of all atoms, which in sum lead to the structural second order phase transition of the $LaFeO_3$ perovskite.

Table 4.5: Linear moduli, corresponding pressure derivatives and the lattice parameters at ambient conditions of the $LaFeO_3$ perovskite determined by an inverted Murnaghan EoS [214] from parametric Rietveld refinement of the second 4:1 methanol-ethanol measurement series (fourth run) up to the hydrostatic limit (approximately 9.8 GPa [210]). Please note that in the parameterized region, only 4 data points were present.

	Murnaghan EoS
a_0 (Å)	5.557(1)
B_{0_a} (GPa)	215(7)
B'_{0_a}	8.1(11)
b_0 (Å)	5.564(1)
B_{0_b} (GPa)	150(3)
B'_{0_b}	2.4(5)
c_0 (Å)	7.854(1)
B_{0_c} (GPa)	186(3)
B'_{0_c}	-0.1(6)

O2 x- and O2 y-coordinates were refined individually.

The critical pressure value for the structural second order phase transition is automatically determined by the parametric Rietveld refinement out of the power-law behavior for the La y- and O1 y-coordinate and is given as $P_{crit} = 20.6(10)$ GPa. This value is in almost perfect agreement with the value of $P_{crit} = 20.5(6)$ GPa, which was determined using the La y-coordinate of the sequential Rietveld refinements of all measurement series. The same agreement can be seen for the critical exponent, which is determined to the same value of $\beta = 0.48(5)$ for the sequential as well as for the parametric Rietveld refinement.

In order to judge the reliability of the determined parameter values by the parametric Rietveld refinement, a comparison between the R_{wp} values of the sequential Rietveld refinement and the R_{wp} values of the parametric Rietveld refinement was carried out (see figure 4.14).

As can be seen from figure 4.14 the R_{wp} values are almost identical, which indicates that the parametric Rietveld refinement has reached the same quality as the sequential Rietveld refinements[1].

1 In cases where wrong equations or constraints are applied in the parametric Rietveld refinement, the R_{wp} values of the parametric Rietveld refinement usually show a significant enhancement compared to the R_{wp} values of the sequential Rietveld refinement. However, the deviation between the EoS parameters states clearly, that, although the same refinement quality is reached, both refinement types must not be necessarily 100% identical.

Table 4.6: Incomplete overview of used parameters in the sequential and parametric Rietveld refinement of approach A. The term "refined" in the column of the parametric Rietveld refinements denotes that a parameter was individually refined for each diffraction pattern.

	Sequential	Parametric
Background	refined	refined
Lattice parameters a, b, c	refined	Murnaghan EoS up to the hydrostatic limit of 9.8 GPa, above fixed to sequential results
Atomic coordinates:		
La_z, Fe_x, Fe_y, Fe_z, $O1_z$	fixed	fixed
La_x, $O1_x$, $O2_x$, $O2_y$, $O2_z$	refined	refined
La_y, $O1_y$	refined up to 20.5 GPa, above fixed	power-law equations with common critical exponent up to the parametrically determined P_{crit}, above automatically fixed
Phenomenological strain parameter	refined	refined
Overall isotropic atomic displacement parameter	refined	refined
Scale factor	refined	refined
Zero shift	fixed	fixed
Spherical harmonics for anisotropic peak broadening (if required)	refined	refined

4.4.3 Approach B: Rigid body refinement

Modeling atomic groups by rigid bodies is nowadays a common method in order to refine single crystal and powder diffraction data, as the number of free atomic coordinates can be strongly reduced. With this reduction, the degrees of freedom or in other words the dimension of the parameter space of the Rietveld refinement (in case of powder diffraction) will be also reduced, which usually gives rise to a greater stabilization of the refinement and in addition, if the right constraints are applied, it will sharpen the global minimum [59, 224].
In general, rigid bodies are defined by fixed bond lengths and fixed bond angles between atoms within the rigid body, although in modern Rietveld refinement programs (e. g. Topas 4.2 [57]) it is possible to set up rigid bodies which are rather deformable, as internal bond lengths and bond angles can be also a subject of a refinement. Therefore these rigid bodies are no longer rigid, which is why they should be denoted as deformable body or much better, as it is related to the refinement, they should be called constrainable atomic group.

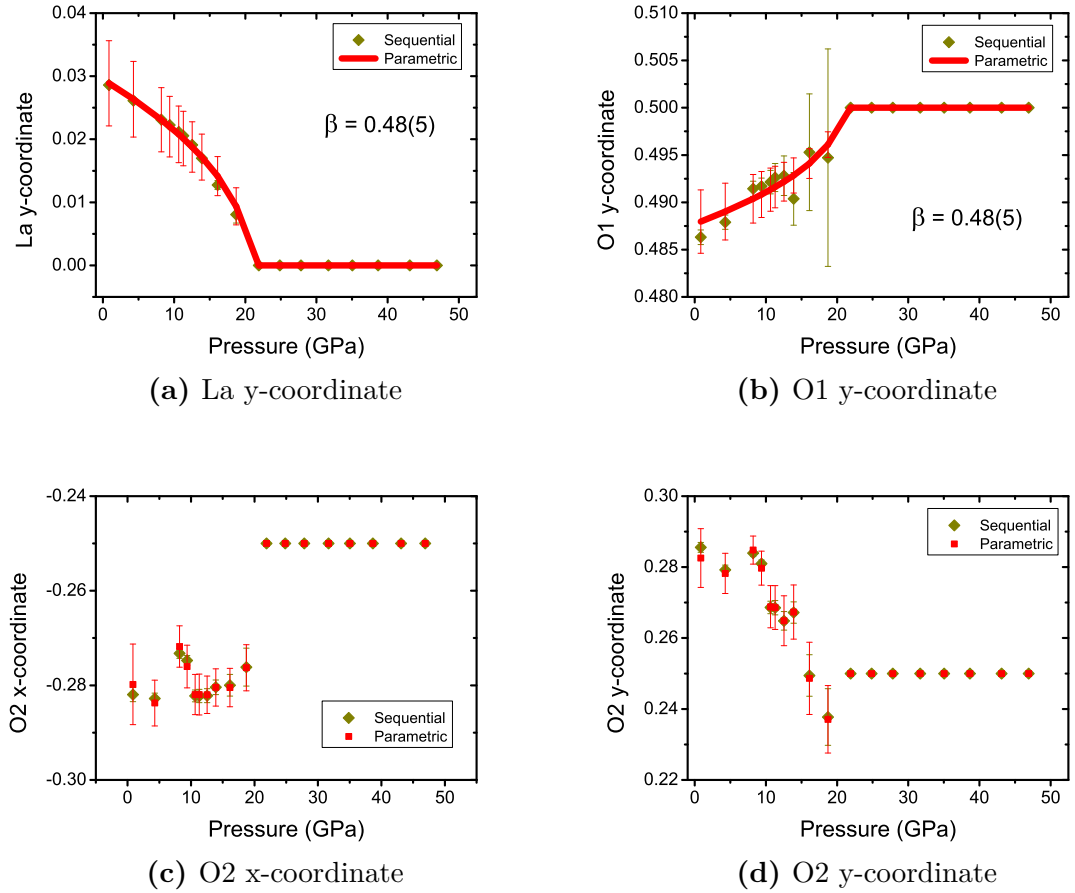

(a) La y-coordinate **(b)** O1 y-coordinate

(c) O2 x-coordinate **(d)** O2 y-coordinate

Figure 4.13: Pressure dependent sequentially and parametrically refined atomic coordinates of the $LaFeO_3$ perovskite. The lanthanum y-coordinate and the O1 y-coordinate are parametrically modeled with a power-law behavior and a common critical exponent.

In the case of the $LaFeO_3$ it is quite clear from the sequential refinements by traditional atomic coordinates (see subsection 4.4.2.1), that a rigid body will be not applicable, as the internal bond lengths and bond angles will certainly change under the applied pressure (see as an indicator also the change of the volume of the FeO_6 octahedron in figure 4.10). In figure 4.15 a schematic picture of the applied constrainable atomic group is given, which highlights the three internal degrees of freedom, which are required in order to model the FeO_6 octahedron under pressure correctly.

From this picture, it can be seen that the bond lengths r_3 and r_2 between the central Fe^{3+} cation and the anion ligands O1 and $O2_1$ will be refineable parameters. The bond length between the central Fe^{3+} cation and the ligand $O2_2$ anion will be automatically calculated by the refinement software due to the given symmetry operations of the

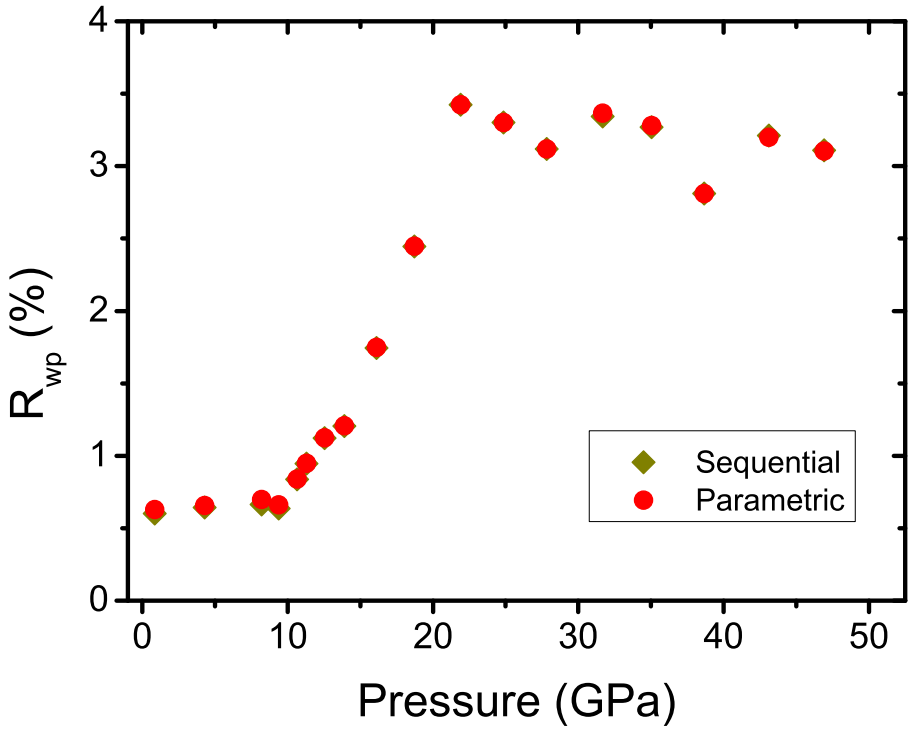

Figure 4.14: Comparison between the R_{wp} values of the sequential and parametric Rietveld refinement of approach A.The congruence of the R_{wp} values indicates the correctness of the applied physical constraints.

space group $Pbnm$[1]. The last necessary refineable internal parameter of the FeO_6 octahedron is the angle a_{12} between the O1, Fe and $O2_1$ ions.
Besides the three internal degrees of freedom r_3, r_2 and a_{12} three outer degrees of freedom must be employed, in order to rotate the FeO_6 octahedron around three axes which are in this case collinear to the three crystallographic axes[2]. In the following, these rotation angles will be denoted as *cva*, *cvb* and *cvc*.

A comparison with the number of degrees of freedom with the traditional atomic coordinate refinement shows, that the above given description of the atomic con-

1 Although the $LaFeO_3$ perovskite exhibits at approximately 20.5 GPa a structural second order phase transition to a space group of higher symmetry, it is still possible to model the observed data by a lower symmetry, as a powder diffraction pattern can always be modeled by a subgroup of the actual space group.

2 There will be no degrees of freedom for the translation of the FeO_6 octahedron, as the Fe^{3+} cation lies on a special position and therefore the translational degrees of freedom are fixed.

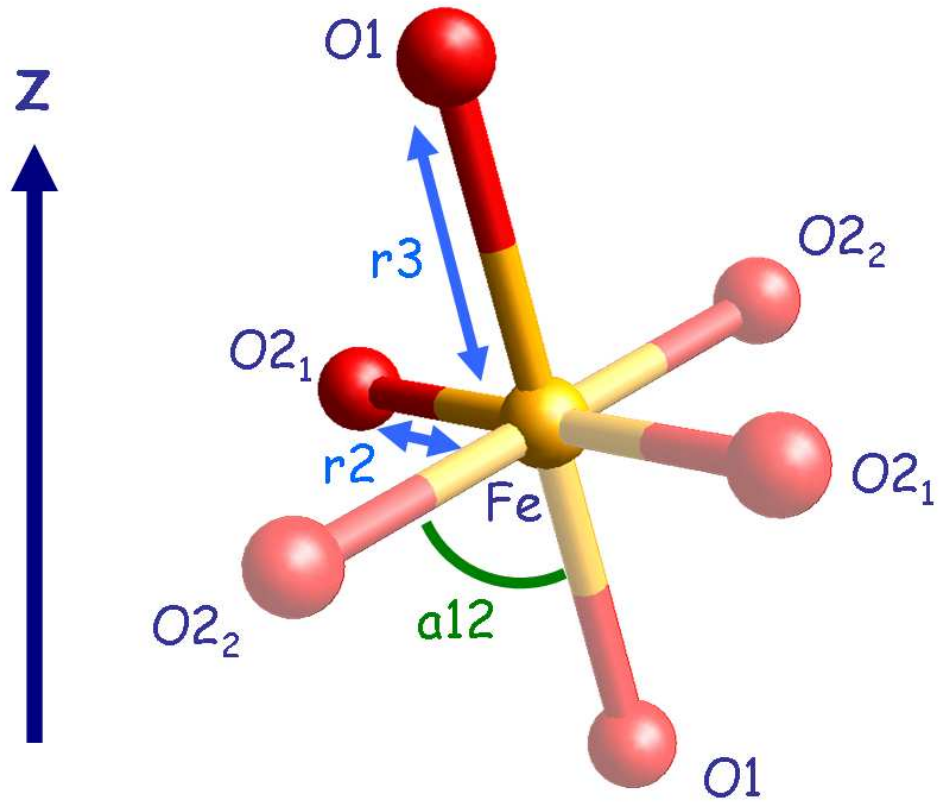

Figure 4.15: Schematic picture for the applied constrainable atomic group for the pressure dependent Rietveld refinement of the $LaFeO_3$ perovskite. The constrainable atomic group is build by the Fe^{3+} cation in the middle of the picture and the oxygen anions O1 and $O2_1$. The full octahedron which is received by symmetry operations of space group *Pbnm* is shown in semi-transparent.

strainable group has one additional degree of freedom too much[1]. In order to prevent an overdeterminacy of the applied model, one parameter must be constrained to another parameter either within the modeling of the FeO_6 octahedron or by a parameter which also takes part in the Rietveld refinement. Fortunately, the bond length r_3 has a dependency on the lattice parameter c and on the rotation angles cva and cvb, which is given by the following equation:

$$r3 = \frac{c}{4} \cdot \frac{1}{\cos(cva) \cdot \cos(cvb)} \quad . \tag{4.7}$$

This equation can be obtained, if the allowed movements of the O1 anion are ana-

1 In the traditional atomic coordinate refinement, the oxygen anions have in sum five refineable parameters for their coordinates, whereas the constrainable atomic group model up to now has six refineable parameters.

lyzed. From the traditional atomic coordinate refinement it is known, that a single O1 anion can only move in a given xy-plane of the $LaFeO_3$ crystal structure. This means that rotations around the three rotation axes have to leave this plane invariant and therefore the position of this plane relative to any other xy-plane can only be affected by the lattice parameter c, as the distance between two of such xy-planes will shrink with the lattice parameter c. By checking the symmetry operations acting on the O1 atom it is obvious, that the distance between two of these planes must always be $\frac{c}{4}$[1]. As the rotation around the rotation axis which is collinear with the crystallographic c-axis does not affect the length of r_3, it can be disregarded. The length r_3 is only affected by the rotation axis which is collinear with the crystallographic a-axis as this rotation will produce a shift of the O1 atom in the y-direction and by the rotation axis which is collinear with the crystallographic b-axis as this rotation will produces a shift of the O1 atom in the x-direction. From trigonometric considerations it can be shown that the projection of the bond length r_3 onto the crystallographic c-axis is then exactly given by the above defined equation 4.7.

Although the constrainable atomic group model does not comprise a reduction of the number of refineable parameters, it will give a new perspective on collective movements of atomic groups within $LaFeO_3$ perovskite under high pressure, as the modeled parameters are directly connected with these movements.

4.4.3.1 Sequential Rietveld refinement

As expected, the sequential Rietveld refinements with the constrainable FeO_6 atomic group using rigid body techniques provided the same refinement results as they were obtained from approach A, which is confirmed by the comparison of the R_{wp} values of both approaches in figures 4.16a)-d).

The exact results for the lattice parameters, the unit cell volume, the atomic coordinates, the overall isotropic atomic displacement parameter and the constrained phenomenological Gaussian and Lorentzian strain parameter can be found in appendix G.

The behavior of the bond lengths r_3 and r_2 as well as the behavior of the bond angle a_{12} is displayed in figures 4.17a)-c), whereas the behavior of the three rotation angles cva, cvb and cvc is displayed in figures 4.17d)-f).

For all parameters the shown behavior can be expected, except for the fact, that the Rietveld refinements at high pressure gave very small estimated standard deviations, although in reality these values are certainly much larger at such pressures. Sole exception is given for the rotation angle cvc of the argon measurements series, where the refinement was not able to determine the correct parameter value, which can be attributed to the insufficient data quality. This is also the reason, why the R_{wp} value of approach B is higher in figure 4.16c) compared to the R_{wp} value of approach A in

1 Simply said, this is the distance between two O1 anions in the c-direction.

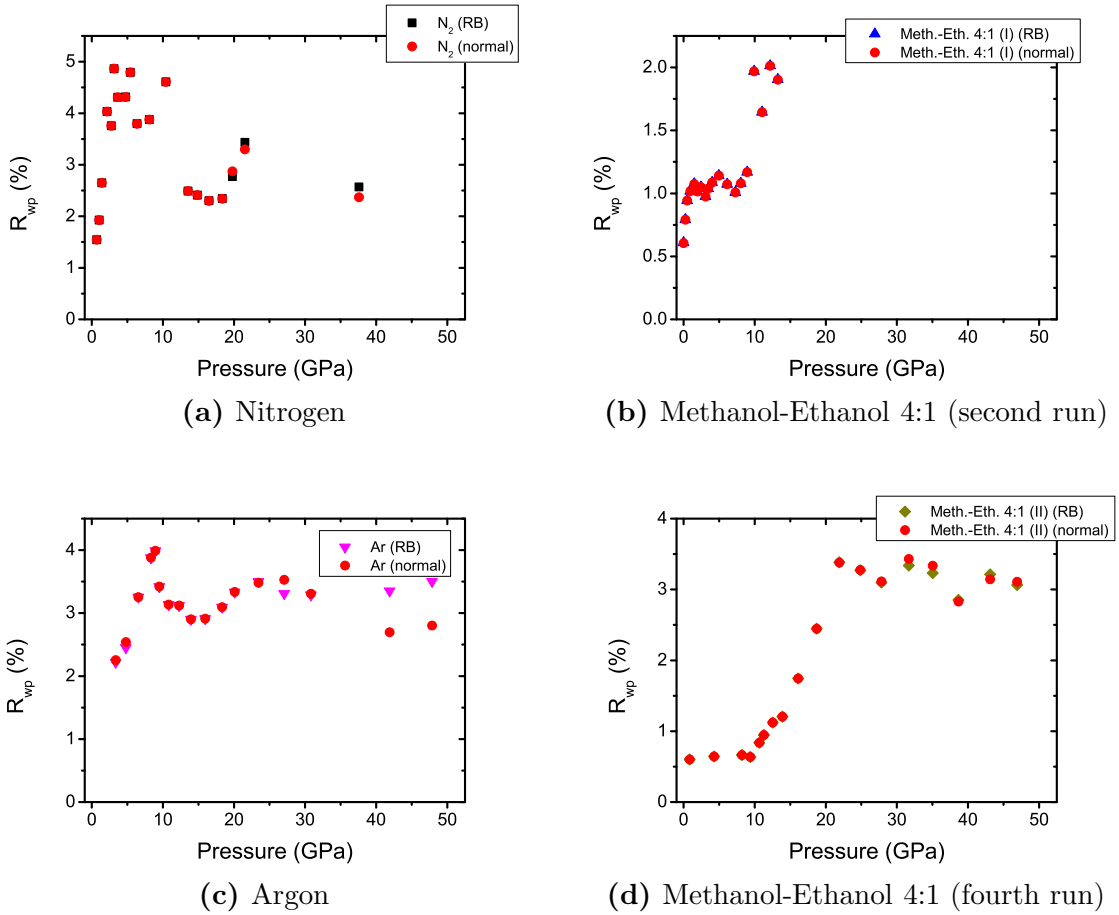

(a) Nitrogen **(b)** Methanol-Ethanol 4:1 (second run)

(c) Argon **(d)** Methanol-Ethanol 4:1 (fourth run)

Figure 4.16: Pressure dependent weighted residual values (R_{wp}) for the a) nitrogen (first run), b) 4:1 methanol-ethanol (second run), c) argon (third run) and d) 4:1 methanol-ethanol (fourth run) measurement series of the high pressure synchrotron X-ray powder diffraction measurements of the $LaFeO_3$ perovskite.

the same figure.

4.4.3.2 Parametric Rietveld refinement

As already explained in subsection 4.4.2.2, soley the methanol-ethanol measurement series of the fourth run will be used in order to perform a parametric Rietveld refinement of approach B.

Similar to approach A, the lattice parameters up to the hydrostatic limit can be parameterized with the "linearized" inverted Murnaghan EoS. Likewise as in approach A, the lanthanum y-coordinate was modeled by the power-law behavior from equation 4.6 in order to determine the critical transition pressure P_{crit} of the structural second order phase transition.
In addition to the lattice parameters and the lanthanum y-coordinate, all three ro-

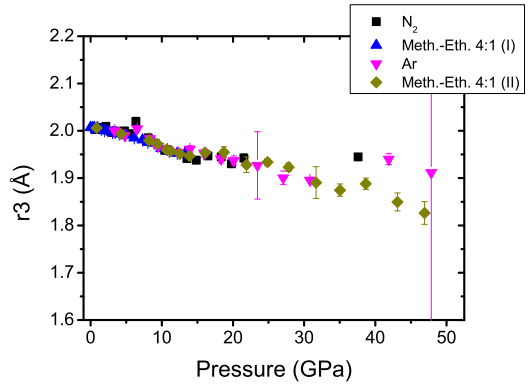

(a) Bond length $r3$

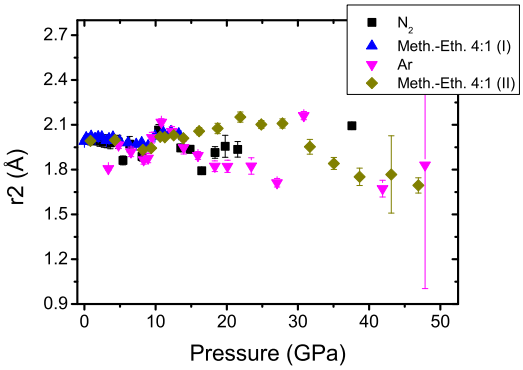

(b) Bond length $r2$

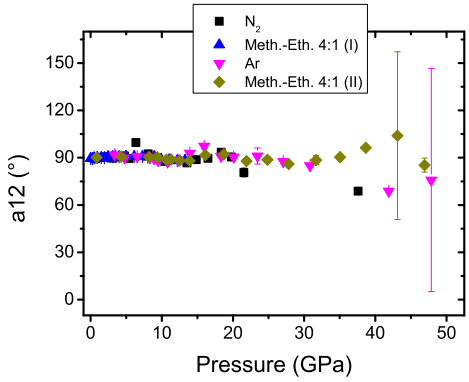

(c) Bond angle a_{12}

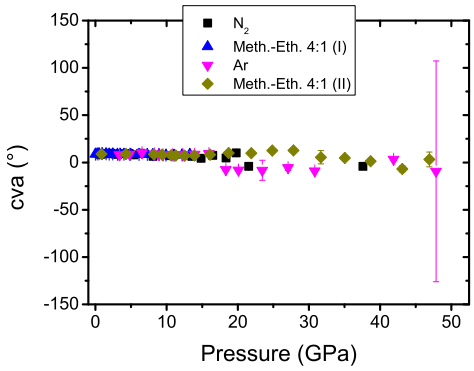

(d) Rotation angle *cva*

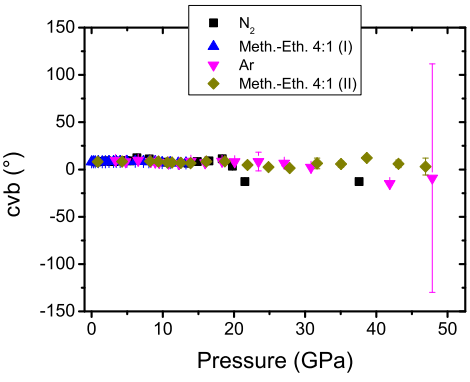

(e) Rotation angle *cvb*

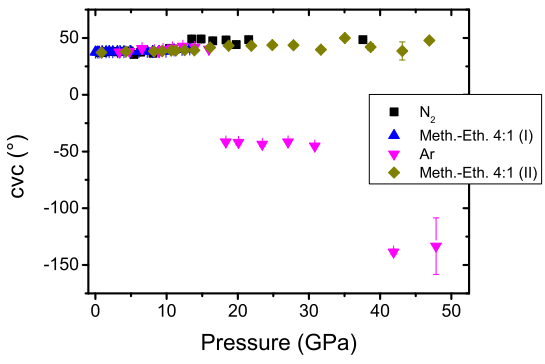

(f) Rotation angle *cvc*

Figure 4.17: Pressure dependent a)-b) bond lengths, c) bond angles and d)-f) rotation angles of the FeO_6 octahedron in the $LaFeO_3$ perovskite. Please note that the bond length $r3$ is calculated from the lattice parameter c and the two rotation angles *cva* and *cvb* via equation 4.7.

tation angles of the FeO_6 octahedron were parameterized. Although it is hard to determine from figures 4.17d)-f), it can be roughly assumed, that the rotation angles *cva* and *cvb* can be fixed to their corresponding arithmetic mean value, whereas the rotation angle *cvc* follows the same power-law behavior as the lanthanum y-coordinate. From different attempts to perform a parametric Rietveld refinement of approach B, it became apparent by comparing the different R_{wp} values, that this assumptions can be made, as long as the overall critical exponent is fixed to $\beta = \frac{1}{2}$. A similar restriction must be given for the last parameter which can be parameterized, as the modeling of the bond length r_3 by an empirical linear equation over the entire investigated pressure range requires a fixing of the slope and the constant of that linear equation[1].

The parameterization of the lattice parameters as well as the parameterized lanthanum y-coordinate looks similar to figures 4.12a)-c) and figure 4.13a), respectively, for approach A. The behavior of the parameterization of the three rotation angles and the bond length r_3 is shown in figures 4.18a)-d).

From these figures it is obvious that the rotation angle *cva* can be fixed to a value of 9° and that the rotation angle *cvb* can be fixed to a value of 8°, whereas the rotation angle *cvc* in combination with the lanthanum y-coordinate can be regarded as primary order parameter of the system, which drives the structural second order phase transition.
The behavior of the bond length r_3 is in so far interesting, as no onset of the non-hydrostatic regime can be seen, which is also suggested by the possible modeling of this parameter over the entire pressure range by a simple empirical linear equation. Interestingly, this effect can be always seen for all parameters which depend on the atomic coordinates and for all approaches[2].

The quality of the parametric Rietveld refinement is again given by the comparison of the R_{wp} values of the sequential Rietveld refinement and the parametric Rietveld refinement of approach B (see figure 4.19).

The critical pressure value of $P_{crit} = 20.8(5)$ GPa which is parametrically determined for the structural second order phase transition is within one estimated standard deviation identical to the one determined sequentially and parametrically from approach A.

An overview of the differences between the parameters in the sequential and in the parametric Rietveld refinement of the rigid body approach is given in table 4.7 and the parametrically determined EoS parameters are given in table 4.8. The deviation of the EoS parameters from the EoS parameters determined for the sequential Rietveld refinement of approach B are similarly explained as in subsection 4.4.2.2.

1 The values for the slope and the constant are determined by a linear fit of the sequential Rietveld refined values.

2 Perhaps, this behavior can be best explained as a deconvolution of the absolute atomic coordinates (which are in fact affected by the hydrostatic limit) into relative atomic coordinates x, y and z and hydrostatic limit affected lattice parameters.

Table 4.7: Incomplete overview of used parameters in the sequential and parametric Rietveld refinement of approach B. The term "refined" in the column of the parametric Rietveld refinements denotes that a parameter was individually refined for each diffraction pattern.

	Sequential	Parametric
Background	refined	refined
Lattice parameters a, b, c	refined	Murnaghan EoS up to the hydrostatic limit of 9.8 GPa, above fixed to sequential results
Atomic coordinates:		
La_z	fixed	fixed
La_x	refined	refined
La_y	refined up to 20.5 GPa, above fixed	power-law equation up to the parametrically determined P_{crit}, above automatically fixed
"Rigid body" coordinates:		
$r2$ (Fe-$O2_1$)	refined	refined
$r3$ (Fe-O1)	calculated by eq. 4.7	straight line with fixed slope and intercept
a_{12} ($O2_1$-Fe-O1)	refined	refined
cva (rotation around a)	refined	fixed
cvb (rotation around b)	refined	fixed
cvc (rotation around c)	refined	power-law equation up to the parametrically determined P_{crit}, above automatically fixed
Phenomenological strain parameter	refined	refined
Overall isotropic atomic displacement parameter	refined	refined
Scale factor	refined	refined
Zero shift	fixed	fixed
Spherical harmonics for anisotropic peak broadening (if required)	refined	refined

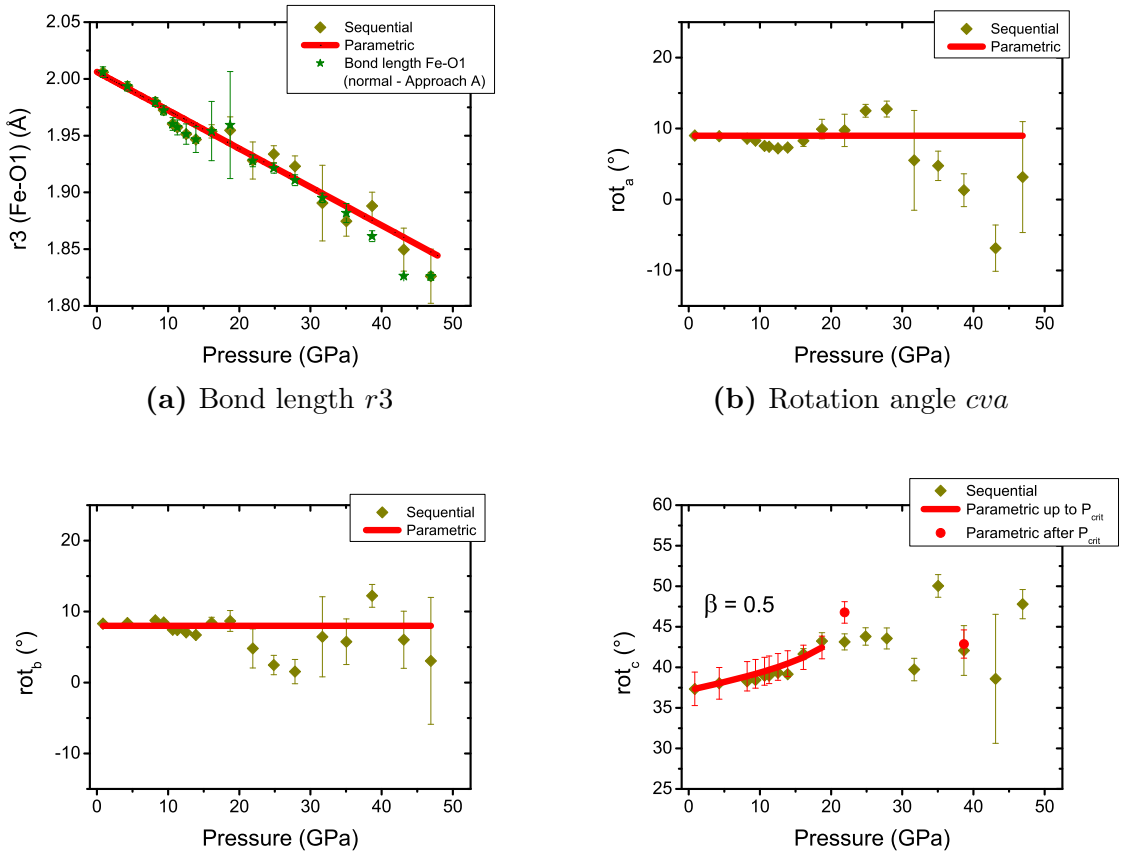

(a) Bond length $r3$

(b) Rotation angle cva

(c) Rotation angle cvb

(d) Rotation angle cvc

Figure 4.18: Pressure dependent a)-b) bond lengths, c) bond angles and d)-f) rotation angles of the FeO_6 octahedron in the $LaFeO_3$ perovskite. Please note that the bond length $r3$ is calculated from the lattice parameter c and the two rotation angles cva and cvb via equation 4.7.

4.4.4 Approach C: Symmetry mode refinement

Perovskites as a material class with general formula ABO_3 are particularly suited for the investigation by symmetry modes, as the observed tilting phenomena of the BO_6 octahedra usual obeys group-subgroup relationships[1] [188, 225–230]. Such a group-subgroup relationship is naturally given for the $LaFeO_3$ perovskite as the pressure induced structural second order phase transition can be described by a tilting of the FeO_6 octahedra, as it was shown by the parameterization of the rotation angles of the

1 The basic tilting of the octahedra depends on the chemical composition of the A- and B-site and additionally on variables like temperature, pressure, etc. if, in the case for temperature as variable, between 0 K and the decomposition temperature one or more phase transitions occur. Even for structural phase transitions of first order, often a group-subgroup relationship can be established due to the possibility to describe the orientation of the BO_6 octahedron as tilting phenomenon.

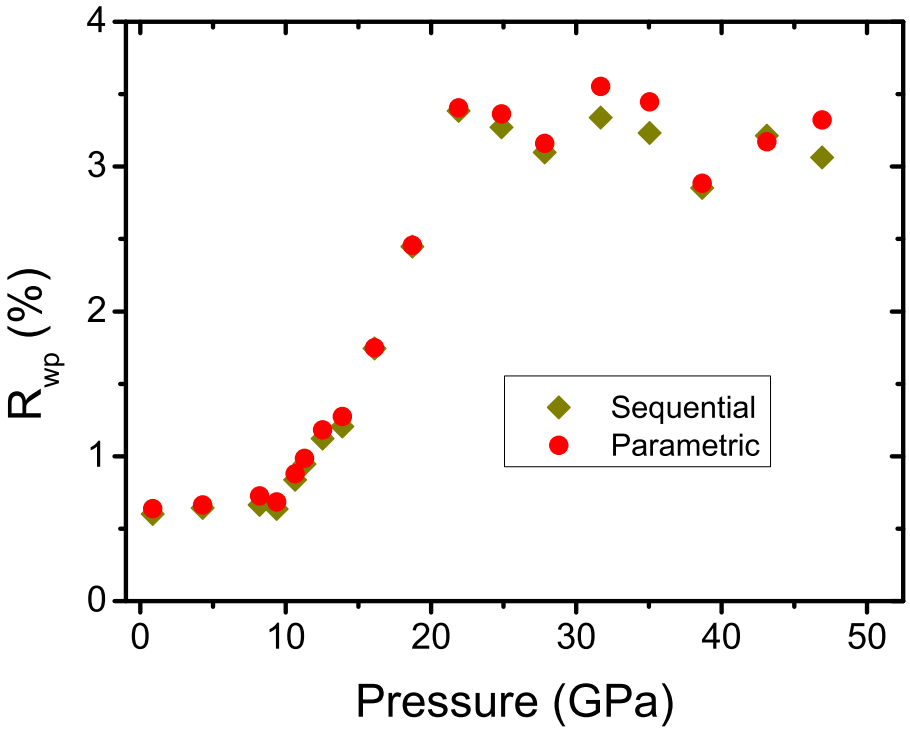

Figure 4.19: Comparison between the R_{wp} values of the sequential and parametric Rietveld refinement of approach B. The congruence of the R_{wp} values indicates the correctness of the applied physical constraints.

Table 4.8: Linear moduli, corresponding pressure derivatives and lattice parameters at ambient conditions of the $LaFeO_3$ perovskite determined by an inverted Murnaghan EoS [214] from parametric Rietveld refinement of the second 4:1 methanol-ethanol measurement series (fourth run) up to the hydrostatic limit (approximately 9.8 GPa [210]). Please note that in the parameterized region, only 4 data points were present.

	Murnaghan EoS
a_0 (Å)	5.557(1)
B_{0_a} (GPa)	207(7)
B'_{0_a}	9.5(11)
b_0 (Å)	5.564(1)
B_{0_b} (GPa)	150(3)
B'_{0_b}	2.6(5)
c_0 (Å)	7.853(1)
B_{0_c} (GPa)	192(3)
B'_{0_c}	-1.2(6)

FeO_6 constrainable atomic group in subsection 4.4.3.2.

This opens up two different possibilities in order to describe the pressure dependent $LaFeO_3$ perovskite crystal structure by symmetry modes. The first option would be to use the natural occurring higher symmetric space group $Ibmm$ in order to describe the lower symmetric space group $Pbnm$ as a distortion of the parent/higher symmetric space group. Although this looks like a rational option, it is not commonly accepted, as the tilting of perovskites is normally described by the second option using the perovskite aristotype space group $Pm\bar{3}m$ [188, 225–230]. Therefore, symmetry mode investigations with ISODISTORT [64] will be done using a virtual cubic crystal structure of the $LaFeO_3$ perovskite[1].

The investigations of the distorted cubic parent crystal structure of the $LaFeO_3$ perovskite revealed, that there are two primary order parameters, the R4+ and the M3+ modes[2], which correspond to modes which allow the FeO_6 octahedra to tilt. Besides the primary order parameters, there exist three secondary modes, namely the modes R5+, X5+ and M2+, which can be either attributed to shifts of the lanthanum cation or to distortions of the FeO_6 octahedron. A full overview of all symmetry modes and their influence on different atomic positions is given in table 4.9.

For a possible continuous structural phase transition of the crystal structure from space group $Pm\bar{3}m$ to space group $Ibmm$ the primary order parameter R4+ is required in order to tilt the FeO_6 octahedra into the corresponding position. Further the secondary parameter R5+ is required in order to induce a slight distortion of the FeO_6 octahedron and to shift the lanthanum cation along the crystallographic a-direction. For a further continuous structural phase transition of the crystal structure from space group $Ibmm$ to space group $Pbnm$ the primary order parameter M3+ must be activated, which is responsible for a rotation of the FeO_6 octahedron around the crystallographic c-axis. In addition the secondary modes M2+ and X5+ are required in order to distort the FeO_6 octahedron further. The X5+ mode is also responsible for a shift of the lanthanum cation along the crystallographic b-direction. As a result, the pressure dependent structural second order phase transition in the $LaFeO_3$ perovskite from space group $Ibmm$ to the subgroup $Pbnm$ can be described by the

1 For the description of a simple ABO_3 perovskite in space group $Pm\bar{3}m$, there exist two different possibilities. The first possibility is to place the A cation in the cube corner and therefore on Wyckoff site 1a (B cation on Wyckoff site 1b and the oxygen anion on Wyckoff site 3c) and the second possibility is to place the A cation in the cube center on Wyckoff position 1b (B cation on Wyckoff site 1a and the oxygen anion on Wyckoff site 3d). As the labeling of the irreducible representations and therefore the labeling of the symmetry modes are highly dependent on the given parent structure, one has to choose a standard setting in order to make different tilting descriptions with symmetry modes comparable. The commonly accepted standard setting is given by placing the A cation to Wyckoff site 1b (as can be seen by the mode labeling given in the literature [228–230]).

2 The labeling of the irreducible representations and therefore the mode description follows the notation of Miller and Love [71].

Table 4.9: Symmetry modes (denoted with a∗) and strain modes (denoted with s∗) as determined from ISODISTORT [64] for the group-subgroup relationships in the $LaFeO_3$ perovskite using a cubic parent structure with space group $Pm\bar{3}m$. The mode description follows the notation of Miller and Love [71].

Name	Mode description	Influence on
a1	$Pm\bar{3}m$[1/2,1/2,1/2]R5+(0,a,a)[La1:b]T1u(a)	La_x
a2	$Pm\bar{3}m$[0,1/2,0]X5+(0,0,0,0,a,a)[La1:b]T1u(a)	La_y
a3	$Pm\bar{3}m$[1/2,1/2,1/2]R4+(0,a,-a)[O1:d]Eu(a)	$O1_x$, $O2_z$
a4	$Pm\bar{3}m$[1/2,1/2,1/2]R5+(0,a,a)[O1:d]Eu(a)	$O1_x$, $O2_z$
a5	$Pm\bar{3}m$[0,1/2,0]X5+(0,0,0,0,a,a)[O1:d]Eu(a)	$O1_y$
a6	$Pm\bar{3}m$[1/2,1/2,0]M2+(a,0,0)[O1:d]A2u(a)	$O2_x$, $O2_y$
a7	$Pm\bar{3}m$[1/2,1/2,0]M3+(a,0,0)[O1:d]Eu(a)	$O2_x$, $O2_y$
s1	$Pm\bar{3}m$[0,0,0]GM1+(a)strain(a)	Lattice parameter
s2	$Pm\bar{3}m$[0,0,0]GM3+(a,0)strain(a)	Lattice parameter
s3	$Pm\bar{3}m$[0,0,0]GM5+(a,0,0)strain(a)	Lattice parameter

three symmetry breaking parameters M3+, M2+ and X5+, where the M3+ mode can be regarded as primary order parameter and the M2+ and the X5+ mode can be regarded as secondary modes.

4.4.4.1 Sequential Rietveld refinement

The power of the symmetry mode concept becomes evident in the case of the $LaFeO_3$ perovskite under high pressure. As the secondary mode M2+ has an amplitude which is 25 times lower compared to the M3+ tilting mode, it can be safely set to zero even in the low-symmetric *Pbnm* phase. Due to this fixing of the M2+ mode it can be expected that the refinement is more stable compared to the sequential Rietveld refinements in approach A and B. That this is intriguingly the case can be seen by the comparison of the R_{wp} values of the sequential refinements between the traditional atomic coordinate approach (A) and the symmetry mode approach (C) in figures 4.20a)-d).

For all measurement series with all pressure media it can be seen that an enhancement of the refinement quality, especially at higher pressure values, can be achieved. This enhancement at higher pressure values can be attributed to the way how the different atomic coordinates are constrained by the same symmetry modes[1].
The refined pressure dependent amplitudes of all symmetry and strain modes are shown in figures 4.21 and 4.22, whereas the results of the lattice parameters, the unit cell volume, the atomic coordinates as calculated from the amplitudes of the symmetry modes, the overall isotropic atomic displacement parameter and the constrained phenomenological Gaussian and Lorentzian strain parameter can be found in appendix H.

1 For instance the O1 x- and O2 z-coordinate are crosswise constrained by the R4+ and R5+ symmetry modes.

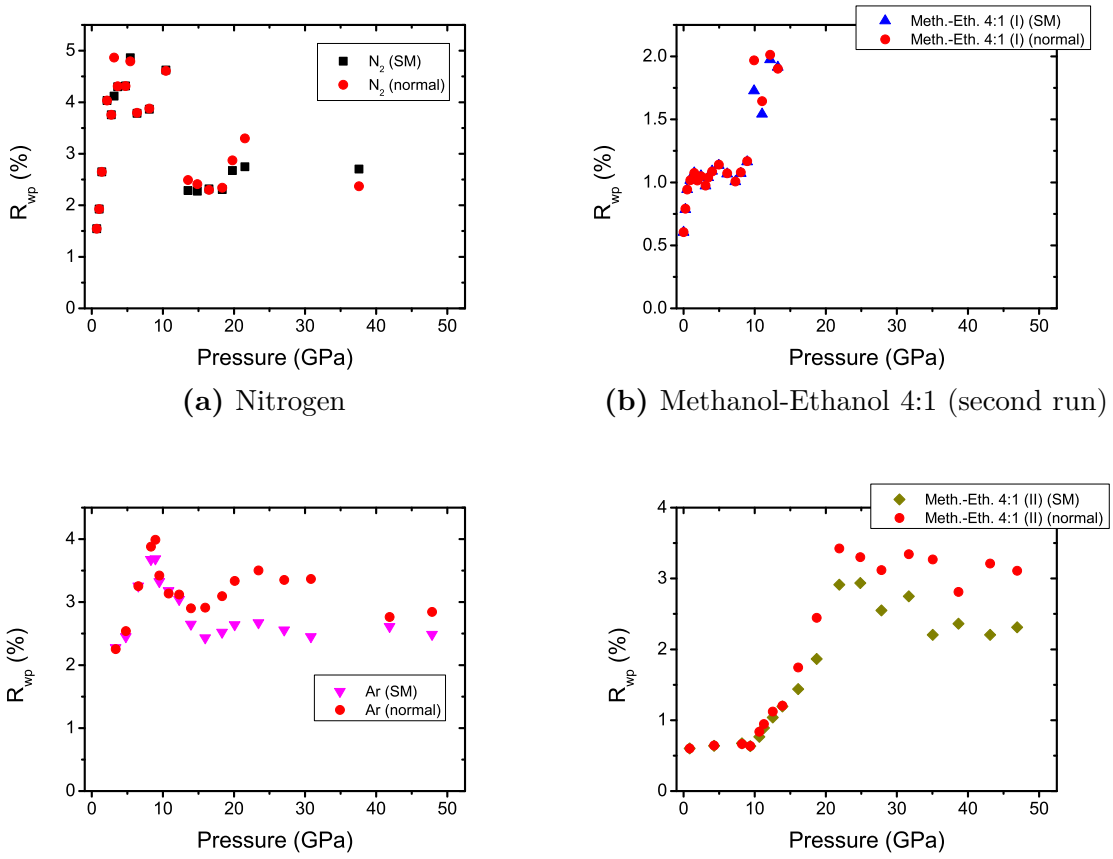

(a) Nitrogen **(b)** Methanol-Ethanol 4:1 (second run)

(c) Argon **(d)** Methanol-Ethanol 4:1 (fourth run)

Figure 4.20: Pressure dependent weighted residual values (R_{wp}) for the a) nitrogen (first run), b) 4:1 methanol-ethanol (second run), c) argon (third run) and d) 4:1 methanol-ethanol (fourth run) measurement series of the high pressure synchrotron X-ray powder diffraction measurements of the $LaFeO_3$ perovskite.

In general, the application of strain modes[1] is not a necessary requirement in order to model pressure dependent lattice parameters, however, it is an exemplary case in order to show, that they are also applicable for the $LaFeO_3$ perovskite.

4.4.4.2 Parametric Rietveld refinement

Similar to the parametric Rietveld refinement in approach A and B, only the methanol-ethanol measurement series of the fourth run will be used in order to perform a para-

1 Strain modes are a possibility how ISODISTORT [64] can treat the changes in the lattice parameters, if the lattice parameters of the subgroup are not simply derived by the multiplication of integer transformation matrices to the parent space group. According to the ISODISTORT manual each strain mode consists of a linear combination of the six strain components, exx, eyy, ezz, eyz, exz, exy [64].

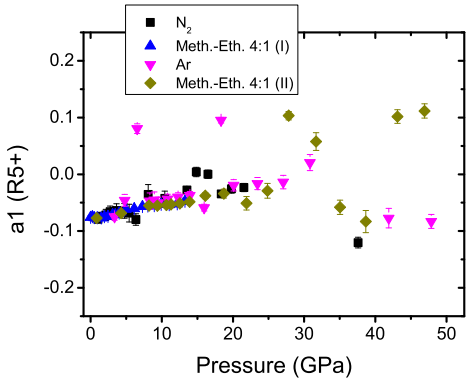

(a) a1 (R5+)

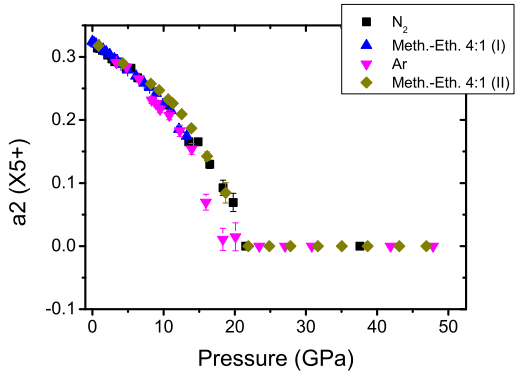

(b) a2 (X5+)

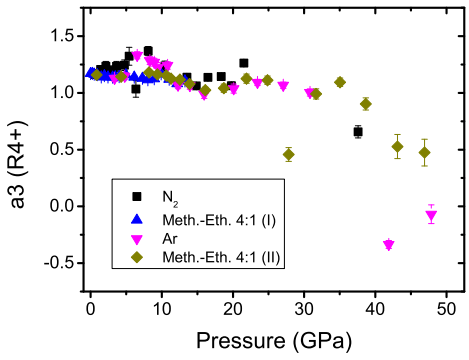

(c) a3 (R4+)

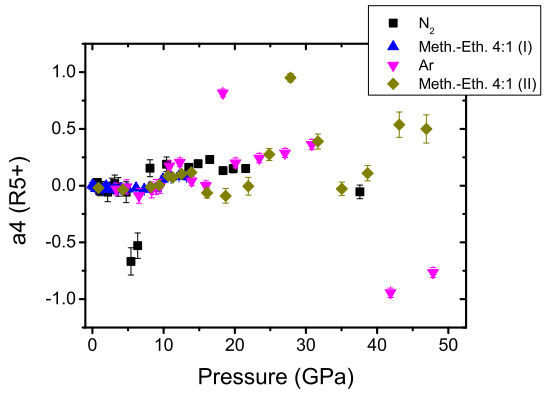

(d) a4 (R5+)

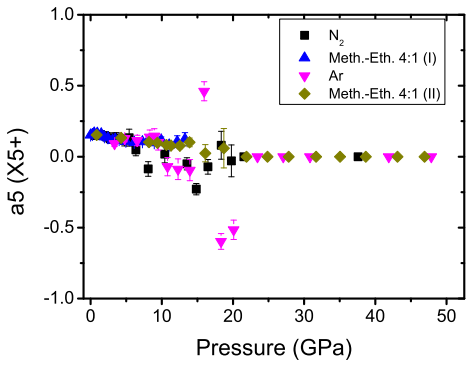

(e) a5 (X5+)

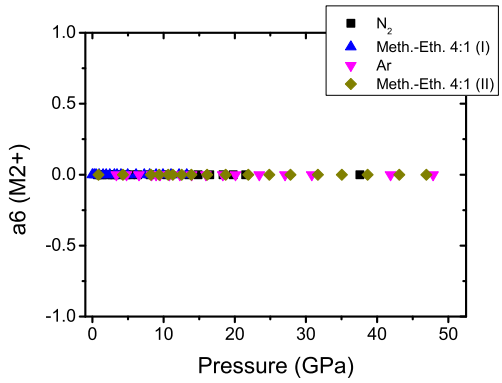

(f) a6 (M2+)

Figure 4.21: Pressure dependent amplitudes of the symmetry modes for the $LaFeO_3$ perovskite (continued in figure 4.22).

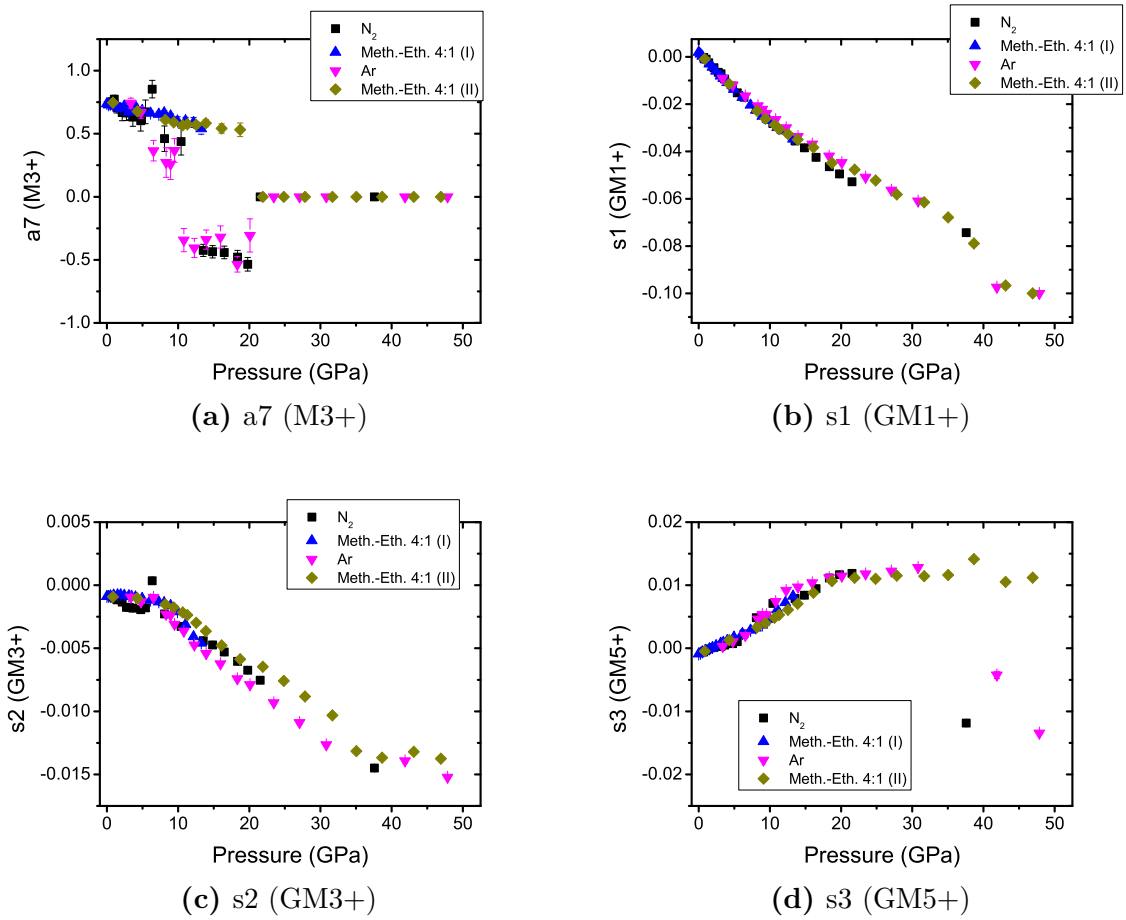

(a) a7 (M3+) **(b)** s1 (GM1+)

(c) s2 (GM3+) **(d)** s3 (GM5+)

Figure 4.22: a) Continued pressure dependent amplitudes of the symmetry modes of the $LaFeO_3$ perovskite from figure 4.21. b)-d) pressure dependent amplitudes of the strain modes.

metric Rietveld refinement of approach C.

In contrast to the lattice parameters, it is in general not possible to model the strain modes by equations of state as a single lattice parameters has not necessarily a linear relationship with a single strain mode[1]. Therefore, the strain modes in the parametric Rietveld refinement were replaced by ordinary lattice parameters, which can be modeled with a Murnaghan EoS as in approach A and B. An overview of the parametrically determined EoS parameters is given in table 4.10. The deviation of the EoS parameters from the EoS parameters determined for the sequential Rietveld refinement of approach A are similarly explained as in subsection 4.4.2.2.

1 In general, the lattice parameters are calculated by a linear transformation of a linear combination of strain modes. Therefore there is no mathematical necessity, why a single strain mode should show a behavior which can be modeled by an EoS.

Table 4.10: Linear moduli, corresponding pressure derivatives and lattice parameters at ambient conditions of the $LaFeO_3$ perovskite determined by an inverted Murnaghan EoS [214] from parametric Rietveld refinement of the second 4:1 methanol-ethanol measurement series (fourth run) up to the hydrostatic limit (approximately 9.8 GPa [210]). Please note that in the parameterized region, only 4 data points are present.

	Murnaghan EoS
a_0 (Å)	5.557(1)
B_{0_a} (GPa)	216(6)
B'_{0_a}	7.8(9)
b_0 (Å)	5.563(1)
B_{0_b} (GPa)	153(3)
B'_{0_b}	1.9(4)
c_0 (Å)	7.854(1)
B_{0_c} (GPa)	182(3)
B'_{0_c}	0.6(5)

From the investigation of the behavior of the amplitudes of the different symmetry modes in the sequential Rietveld refinement it is obvious, that only the X5+ mode with the amplitudes $a2$ and $a5$ can be modeled by the former used power-law behavior. The reason for that is simply, that these modes are individually connected with the La y- and O1 y-coordinates. All other atomic coordinates are given as linear combinations of different symmetry modes and therefore there exists no mathematical necessity, why a single symmetry mode must obey a power-law behavior, as was already stated above for the case of the strain modes and EoS. The only exception is given by the amplitude $a6$ of the M2+ symmetry mode, as the amplitude was almost zero in the sequential Rietveld refinement and was therefore fixed to zero in the parametric Rietveld refinement.

The behavior of the parameterized symmetry modes in the parametric Rietveld refinement together with the corresponding values of the sequential Rietveld refinement are shown in figures 4.23a)-c).

As the $a2$ and $a5$ amplitude belong to the same irreducible representation, they must be modeled by a common critical exponent. This procedure is identical to the procedures of the common critical exponent in approach A and B and can be attributed to the collective atomic motion, which must occur in order to result in a structural second order phase transition. From the parametric Rietveld refinement of the mode amplitudes, the critical pressure value can be determined to $P_{crit} = 21.0(12)$ GPa, which agrees also within one estimated standard deviation with the value determined from sequential and parametric refinements using approach A.

Finally, an overview of the differences between the parameters in the sequential and in the parametric Rietveld refinement of the symmetry mode approach is given in table 4.11 and the quality comparison of the R_{wp} values of the parametric Rietveld refine-

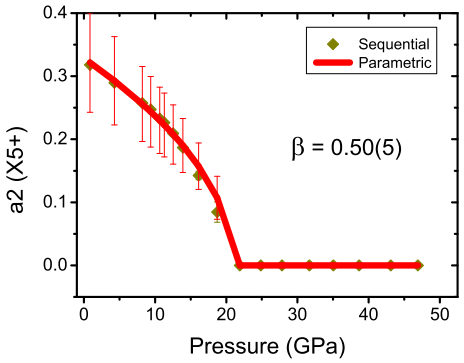

(a) a2 (X5+)

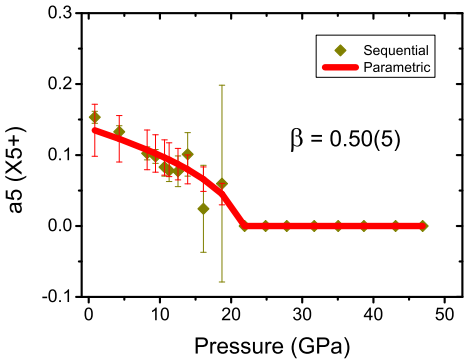

(b) a5 (X5+)

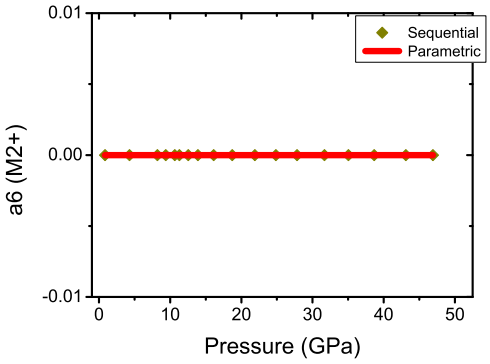

(c) a6 (M2+)

Figure 4.23: Parameterized pressure dependent amplitudes of the symmetry modes X5+ and M5+ of the $LaFeO_3$ perovskite. The modeling of the amplitudes of the X5+ mode was done using a common critical exponent.

ment against the R_{wp} values of the sequential Rietveld refinement is given in figure 4.24).

4.4.5 Approach D: Refinement with rotational symmetry modes of a rigid body

Structural variations within a crystal structure can normally be regarded as a collective motion of atoms. Therefore, in order to get a deeper understanding of such collective atomic motions, it is advisable to find a model which describes the collective atomic motion as a whole. The usage of rigid bodies and/or constrainable atomic groups in Rietveld refinements is a first step towards to such a holistic approach. Besides the intuitive rigid body approach, also the symmetry mode concept gives in parts such a holistic approach, as the different atomic shifts can be sometimes constrained by a single irreducible representation. Although both approaches have their strengths,

Table 4.11: Incomplete overview of used parameters in the sequential and parametric Rietveld refinement of approach C. The term "refined" in the column of the parametric Rietveld refinements denotes that the parameter was individually refined for each diffraction pattern.

	Sequential	Parametric
Background	refined	refined
Lattice parameters a, b, c	calculated from three refineable strain modes	Murnaghan EoS up to the hydrostatic limit of 9.8 GPa, above fixed to sequential results
Atomic coordinates: La_z, Fe_x, Fe_y, Fe_z, $O1_z$	fixed	fixed
Symmetry modes:		
a1	refined	refined
a2	refined up to P_{crit} above fixed	power-law equation up to the parametrically determined P_{crit}, above automatically fixed
a3	refined	refined
a4	refined	refined
a5	refined up to P_{crit} above fixed	power-law equation up to the parametrically determined P_{crit}, above automatically fixed
a6	fixed to zero	fixed to zero
a7	refined up to P_{crit}, above fixed	refined up to P_{crit}, above fixed
Phenomenological strain parameter	refined	refined
Overall isotropic atomic displacement parameter	refined	refined
Scale factor	refined	refined
Zero shift	fixed	fixed
Spherical harmonics for anisotropic peak broadening (if required)	refined	refined

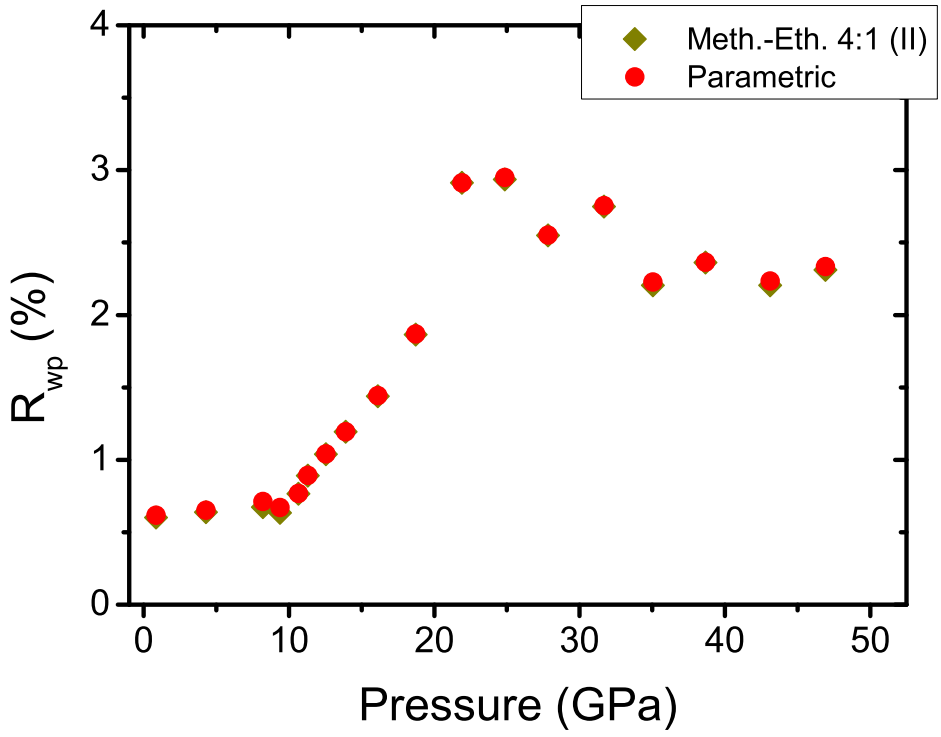

Figure 4.24: Comparison between the R_{wp} values of the sequential and parametric Rietveld refinement of approach C.The congruence of the R_{wp} values indicates the correctness of the applied physical constraints.

they have also some weaknesses. For instance if in the rigid body/constrainable atomic group approach, too many internal degrees of freedom must be used or if in the symmetry mode approach too many irreducible representations are required in order to give an easy description of the collective atomic motions.
Recently a new approach came up, where both methods, rigid bodies and symmetry modes, are naturally combined [231]. This new approach uses rotational symmetry modes, which are able to rotate a rigid body or a constrainable atomic group in a crystal structure, therefore these rotational symmetry modes give direct access to the polyhedral tiltings in crystal structures for instance to octahedral tiltings in perovskites. In detail, the rigid body or constrainable atomic group is rotated around an unique rotation axis, which is given by a vector, whose components are in turn given by the rotational symmetry modes. Due to this reason the length of the vector is defined by the three rotational symmetry modes. Furthermore, the degree of rotation of the rigid body or the constrainable atomic group is given by the length of this vector, which ensures a natural connection between the rotation of the rigid body or

the constrainable atomic group and the unique rotation axis[1].

In the case of the Rietveld refinement of the high pressure synchrotron X-ray powder diffraction data of the $LaFeO_3$ perovskite, the three rotational symmetry modes can be determined by the ISODISTORT software [64], using as parental space group the space group $Ibmm$ instead of the perovskite aristotype space group $Pm\bar{3}m$[2]. Unfortunately, the constrainable atomic group from approach B cannot be maintained, as the bond length $r3$ was calculated from two rotation angles, which do not exist in the approach of rotational symmetry modes of a rigid body. Therefore a new constrainable atomic group had to be constructed, which is similar but not equal to the constrainable atomic group in approach B (see figure 4.25).

Likewise to the constrainable atomic group in approach B, the bond length $r3$ is defined between the central Fe^{3+} cation and the O1 anion, the bond length $r2$ is defined between the central Fe^{3+} cation and the $O2_1$ anion and the bond angle $a12$ is defined between the O1-Fe-$O2_1$ atoms. Due to the total number of degrees of freedom, which amounts to 5 for the traditional atomic coordinates in approach A, one degree of freedom must be constrained to another parameter of the refinement. From approach B, it is known, that such a suitable constraint can be found for the pressure dependent bond length $r3$, which could be calculated by the lattice parameter c and two rotation angles. As the degrees of freedom of all three rotation angles are replaced by the rotational symmetry modes, another constraint than in approach B had to be found. Such a constraint can be given by the definition of another angle $a11$ between the O1 anion and a dummy atom X1 which has zero occupancy and therefore does not influence the refinement. The position of the dummy atom is defined in such a way, that the distance between the dummy atom and the Fe^{3+} cation is always parallel to the crystallographic c-axis. The reason for the introduction of such a dummy atom is simply a technical one, as the TOPAS program [57] does not allow the calculation of the angle $a11$ between the O1 anion and the crystallographic c-axis. With this introduction of the dummy atom, TOPAS is able to calculate intrinsically the angle $a11$, therefore the angle $a11$ is not an additional refineable parameter. Knowing the angle between O1, Fe and X1 it is then possible to modify equation 4.7 to a new form, as the bond length $r3$ can still be expressed as a projection onto the c-axis:

$$r3 = \frac{c}{4} \cdot \frac{1}{\cos(a11)} \quad . \tag{4.8}$$

With this definition, only the pressure dependent bond length $r2$ and the pressure dependent bond angle $a12$ are refineable parameters. Therefore, the total number of

1 Mathematically it can be shown, that rotations around three coordinate axes can be combined into a rotation around a unique axis, as the successive multiplication of a vector by three rotational matrices can be converted into a single rotational matrix.

2 The reason for the adoption of the lower symmetric space group is simply, that this new crystallographic approach can be investigated having fewer dependencies in contrast to the higher symmetric aristotype space group.

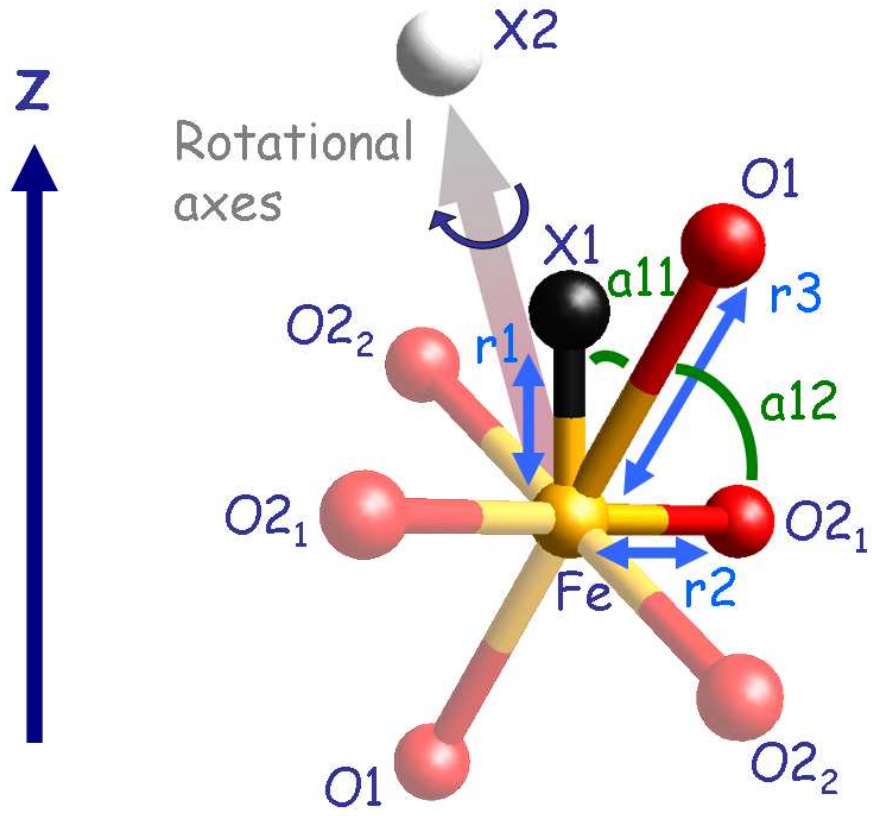

Figure 4.25: Schematic picture for the applied constrainable atomic group for the pressure dependent Rietveld refinement of the $LaFeO_3$ perovskite. The constrainable atomic group is build by the Fe^{3+} cation in the middle of the picture and the oxygen anions O1 and $O2_1$. The full octahedron which is received by symmetry operations of space group *Pbnm* is shown in semi-transparent. The unique rotation axis is build by the Fe^{3+} cation and a dummy atom X2 with zero occupancy. Further explanations of this constrainable atomic group are given in the text.

degrees of freedom for the FeO_6 octahedron is the same as in approach A and B. In addition to the degrees of freedom for the FeO_6 octahedron, the La x- and y-coordinates must be modeled by ordinary symmetry modes[1] and the lattice parameters are treated by strain modes as integrated in ISODISTORT. An overview of the different symmetry modes, strain modes and rotational symmetry modes is given in table 4.12.

4.4.5.1 Sequential Rietveld refinement

That the new approach of the rotational symmetry modes of a rigid body (abbreviated in the following as RBSM) is competitive to the other approaches can be clearly seen

1 Another possibility would be to treat these coordinates by the traditional atomic coordinate approach, as different approaches can be combined within the same Rietveld refinement.

Table 4.12: Symmetry modes (denoted with a∗), rotational symmetry modes (denoted with mm∗) and strain modes (denoted with s∗) determined from ISODISTORT [64] for the group-subgroup relationships in the $LaFeO_3$ perovskite using the higher symmetric space group *Ibmm* as parent structure. The mode description follows the notation of Miller and Love [71].

Name	Mode description	Influence on
a1	*Ibmm*[0,0,0]GM1+(a)[La1:e]A1(a)	La_x
a2	*Ibmm*[1,1,1]X4+(a)[La1:e]B1(a)	La_y
mm1	*Ibmm*[0,0,0]mGM1+(a)[Fe1:b]Ag(a)	"RB" rotation
mm2	*Ibmm*[1,1,1]mX4+(a)[Fe1:b]Bg_1(a)	"RB" rotation
mm3	*Ibmm*[1,1,1]mX4+(a)[Fe1:b]Bg_2(a)	"RB" rotation
s1	*Ibmm*[0,0,0]GM1+(a)strain_1(a)	a
s2	*Ibmm*[0,0,0]GM1+(a)strain_2(a)	b
s3	*Ibmm*[0,0,0]GM1+(a)strain_3(a)	c

if the pressure dependent R_{wp} values are compared to the R_{wp} values of the traditional atomic coordinate approach (see figure 4.26a)-d))

The quality of the different refinements given by the R_{wp} is comparable, although at higher pressure values, the R_{wp} values of the RBSM approach are slightly enhanced. The sequentially refined pressure dependent values of the bond lengths and the bond angles are presented in figures 4.27a)-d)[1], whereas the results of the refinement of the amplitudes of the symmetry modes and the rotational symmetry modes are shown in figures 4.28a)-e). The rotation angle given in figure 4.28f) is calculated from the three rotational symmetry modes.

The pressure dependent values of the atomic coordinates of the $LaFeO_3$ perovskite, which are calculated from the symmetry modes and the constrainable atomic group in cooperation with the rotational symmetry modes can be found in appendix I. In appendix H, also the pressure dependent results of the the overall isotropic atomic displacement parameter and the constrained phenomenological Gaussian and Lorentzian strain parameter are given, as well as the unit cell volume and the lattice parameters, whereas the latter mentioned lattice parameters are calculated by the pressure dependent amplitudes of the strain modes, which are presented in figure 4.29.

In contrast to the strain modes of approach C, fortunately the strain modes in approach D are not a set of linear equations, as a single strain mode can be directly

1 Interestingly, the TOPAS refinement program calculated quite unreasonable estimated standard deviations. Such unreasonable high estimated standard deviations can occur, if the correlation between the parameters becomes too high, which seems to be the case for this set of parameters, as the correlation matrix of the refined and calculated parameters $r3$, $r2$, $a12$, $a11$, $mm1$, $mm2$ and $mm3$ gives a 100% correlation between each pair of the mentioned parameters.

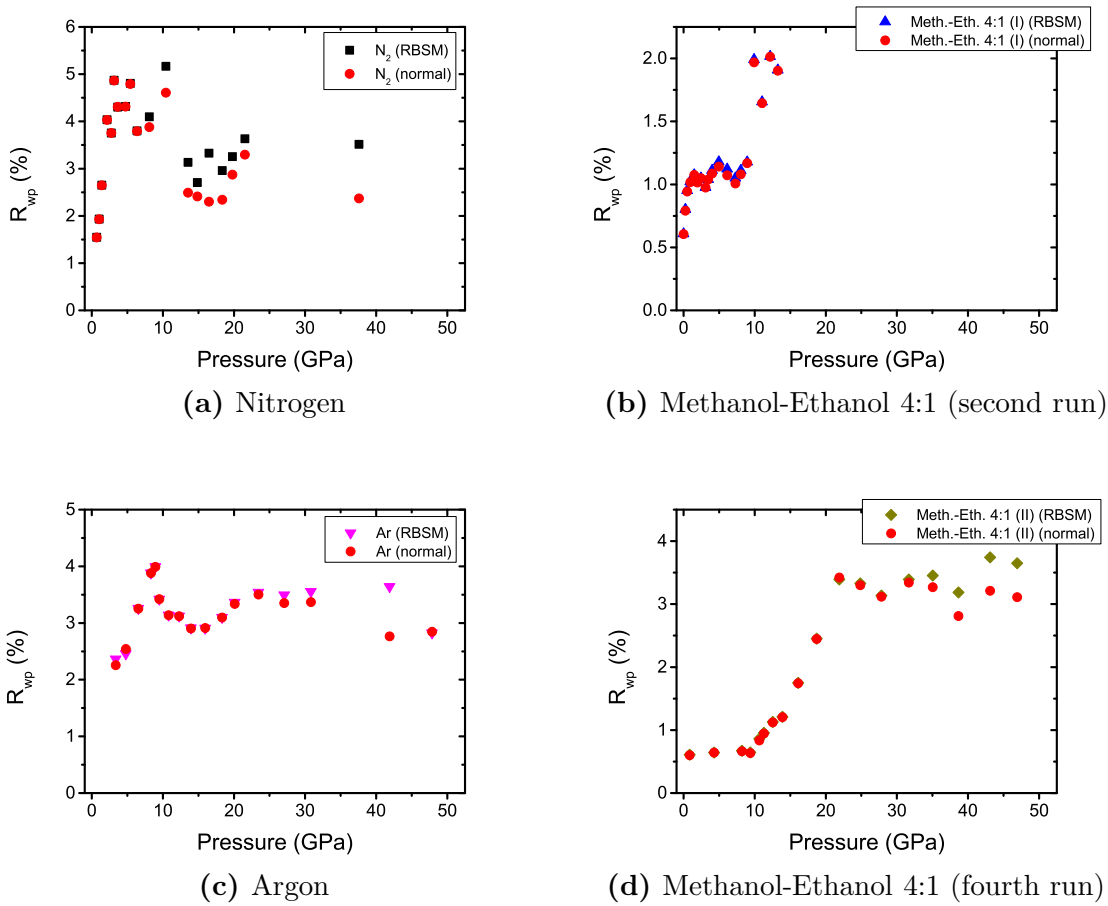

(a) Nitrogen **(b)** Methanol-Ethanol 4:1 (second run)

(c) Argon **(d)** Methanol-Ethanol 4:1 (fourth run)

Figure 4.26: Pressure dependent weighted residual values (R_{wp}) for the a) nitrogen (first run), b) 4:1 methanol-ethanol (second run), c) argon (third run) and d) 4:1 methanol-ethanol (fourth run) measurement series of the high pressure synchrotron X-ray powder diffraction measurements of the $LaFeO_3$ perovskite.

transformed via a linear transformation to its corresponding lattice parameter[1]. The straightforward proportionality between strain modes and lattice parameters opens up the possibility to model phenomenologically the strain modes by "linearized" and inverted EoS (which was done in the parametric Rietveld refinement), which are normally only used for the modeling of the pressure dependent lattice parameters.

4.4.5.2 Parametric Rietveld refinement

Similar to the parametric Rietveld refinement in approach A, B and C only the methanol-ethanol measurement series of the fourth run was used in order to perform

1 The reason for that is, that the group-subgroup relation is chosen within the same crystal system and that both space groups have the same setting, therefore the transformation matrix between the lattice parameters of both orthorhombic phases is given by the unit matrix.

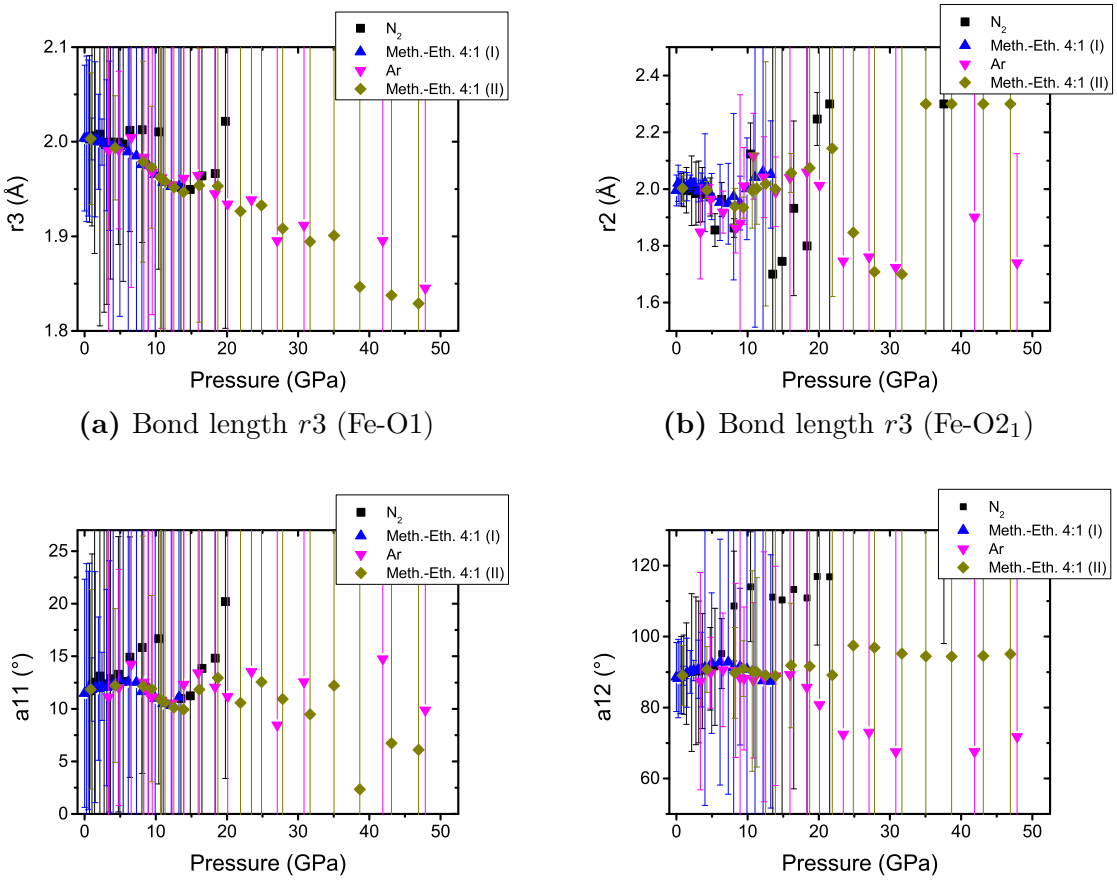

(a) Bond length $r3$ (Fe-O1)

(b) Bond length $r3$ (Fe-$O2_1$)

(c) Bond angle $a11$

(d) Bond angle $a12$

Figure 4.27: Pressure dependent a)-b) bond lengths and c)-d) bond angles of the FeO_6 octahedron in the $LaFeO_3$ perovskite. Please note that the bond length $r3$ is calculated from the lattice parameter c and the bond angle $a11$ via equation 4.8 and that the bond angle $a11$ is calculated intrinsically by the refinement program.

a parametric Rietveld refinement using approach D.

As already stated in the last subsection, it is possible to model phenomenologically the amplitudes of the strain modes by "linearized" and inverted EoS. Such a phenomenological parameterization of the amplitudes of the strain modes can be for instance done with the Murnaghan EoS up to the hydrostatic limit of 9.8 GPa, which is shown in figures 4.30b)-d)[1].

In figure 4.30a) also the modeling of the amplitude of the X4+ mode, which is responsible for the y-coordinate shift of the lanthanum cation, by a power-law behavior according to equation 4.6 is shown. The critical exponent of this symmetry

1 Unfortunately, this modeling implies that no physical values of the linear moduli, etc. can be given, as no transformation rule between the linear moduli of the amplitudes of the strain modes and the linear moduli of the lattice parameters could be found.

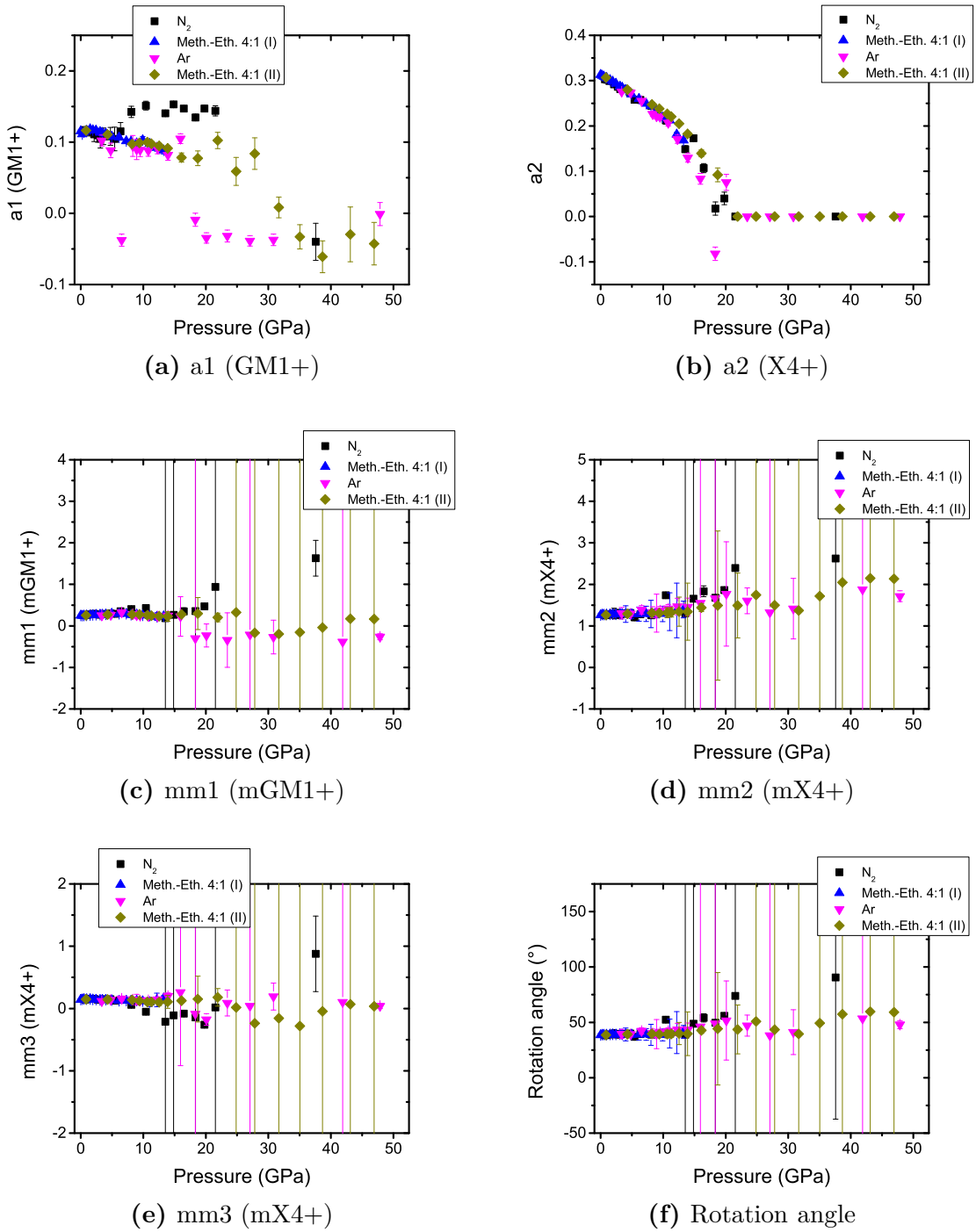

(a) a1 (GM1+) **(b)** a2 (X4+)

(c) mm1 (mGM1+) **(d)** mm2 (mX4+)

(e) mm3 (mX4+) **(f)** Rotation angle

Figure 4.28: Pressure dependent a)-b) symmetry modes and c)-e) rotational symmetry modes in the $LaFeO_3$ perovskite. The rotation angle shown in f) is calculated from the rotational symmetry modes and is responsible for the tilting of the FeO_6 octahedron.

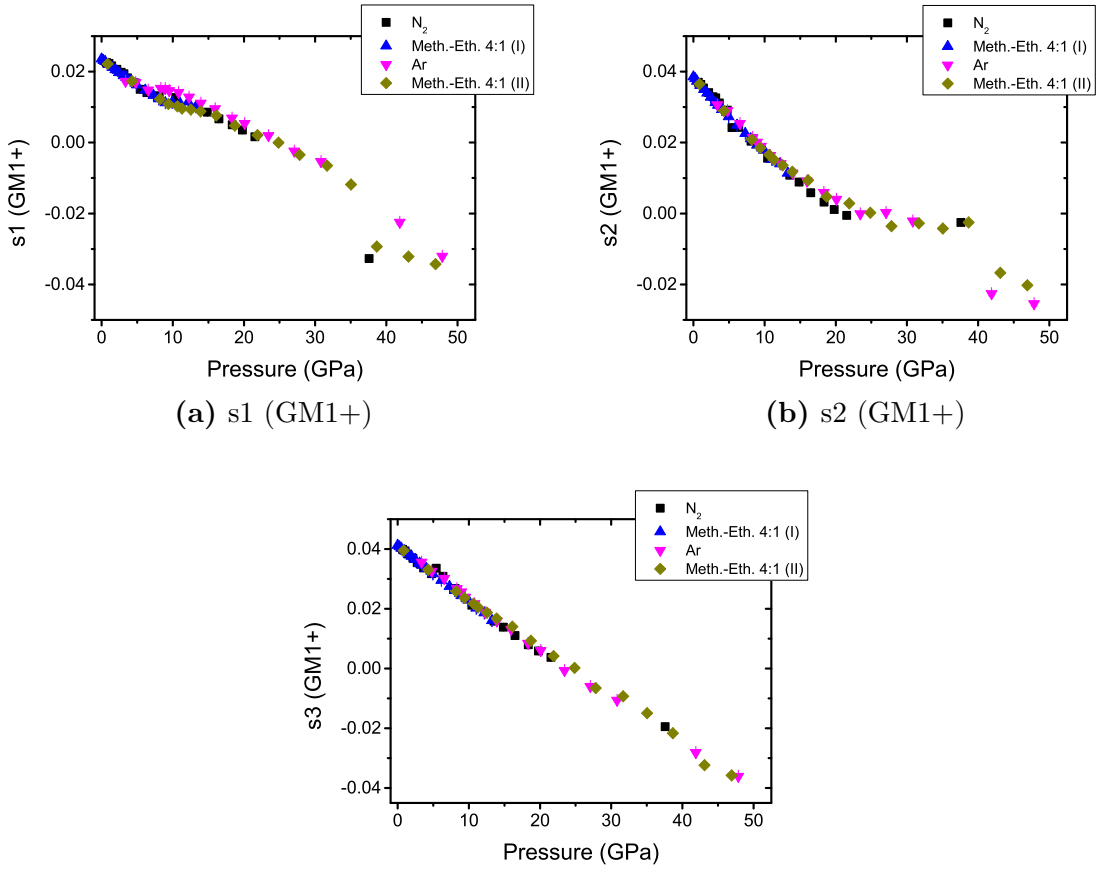

(a) s1 (GM1+)

(b) s2 (GM1+)

(c) s3 (GM1+)

Figure 4.29: Pressure dependent amplitudes of the strain modes in the $LaFeO_3$ perovskite.

mode parameterization is constrained to the same value of the critical exponent of the power-law modeling of the rotational symmetry mode $mm2$ in figure 4.31b). The parametrically determined critical pressure from the power-law behaviors for the structural second order phase transition in the $LaFeO_3$ perovskite is $P_{crit} = 20.8(35)$ GPa, which is within one estimated standard deviation in agreement with the values determined sequentially and parametrically from approach A. The other two rotational symmetry modes $mm1$ and $mm3$ had no significant influence on the behavior of the rotation angle as it could be seen from the sequential Rietveld refinements, therefore the values of these rotational modes were kept fixed to their arithmetic mean (see figures 4.31a) and 4.31c)).

A general overview of the differences between the parameters in the sequential and in the parametric Rietveld refinement of the rotational symmetry modes of a rigid body approach is given in table 4.13.

By comparing the R_{wp} values of the parametric Rietveld refinement with the R_{wp} values of the sequential Rietveld refinements (see figure 4.32), it can be clearly stated that the new approach of rotational symmetry modes of a rigid body is quite compre-

Table 4.13: Incomplete overview of used parameters in the sequential and parametric Rietveld refinement of approach D. The term "refined" in the column of the parametric Rietveld refinements denotes that the parameter was individually refined for each diffraction pattern.

	Sequential	Parametric
Background	refined	refined
Lattice parameters a, b, c	calculated from three refineable strain modes	Murnaghan EoS for strain modes up to the hydrostatic limit of 9.8 GPa, above fixed to sequential results
Atomic coordinates:		
La_z, dummy atom X1	fixed	fixed
Symmetry modes:		
a1	refined	refined
a2	refined up to P_{crit} above fixed	power-law equation up to the parametrically determined P_{crit}, above automatically fixed
Rotational modes:		
mm1	refined	fixed
mm2	refined	power-law equation up to the parametrically determined P_{crit}, above automatically fixed
mm3	refined	fixed
"Rigid body" coordinates:		
$r2$ (Fe-$O2_1$)	refined	refined
$r3$ (Fe-O1)	calculated by eq. 4.8	straight line with fixed slope and intercept
a_{11} (angle O1-Fe-X1)	dependent on rotational modes and automatically determined	dependent on rotational modes and automatically determined
a_{12} (angle $O2_1$-Fe-O1)	refined	refined
Phenomenological strain parameter	refined	refined
Overall isotropic atomic displacement parameter	refined	refined
Scale factor	refined	refined
Zero shift	fixed	fixed
Spherical harmonics for anisotropic peak broadening (if required)	refined	refined

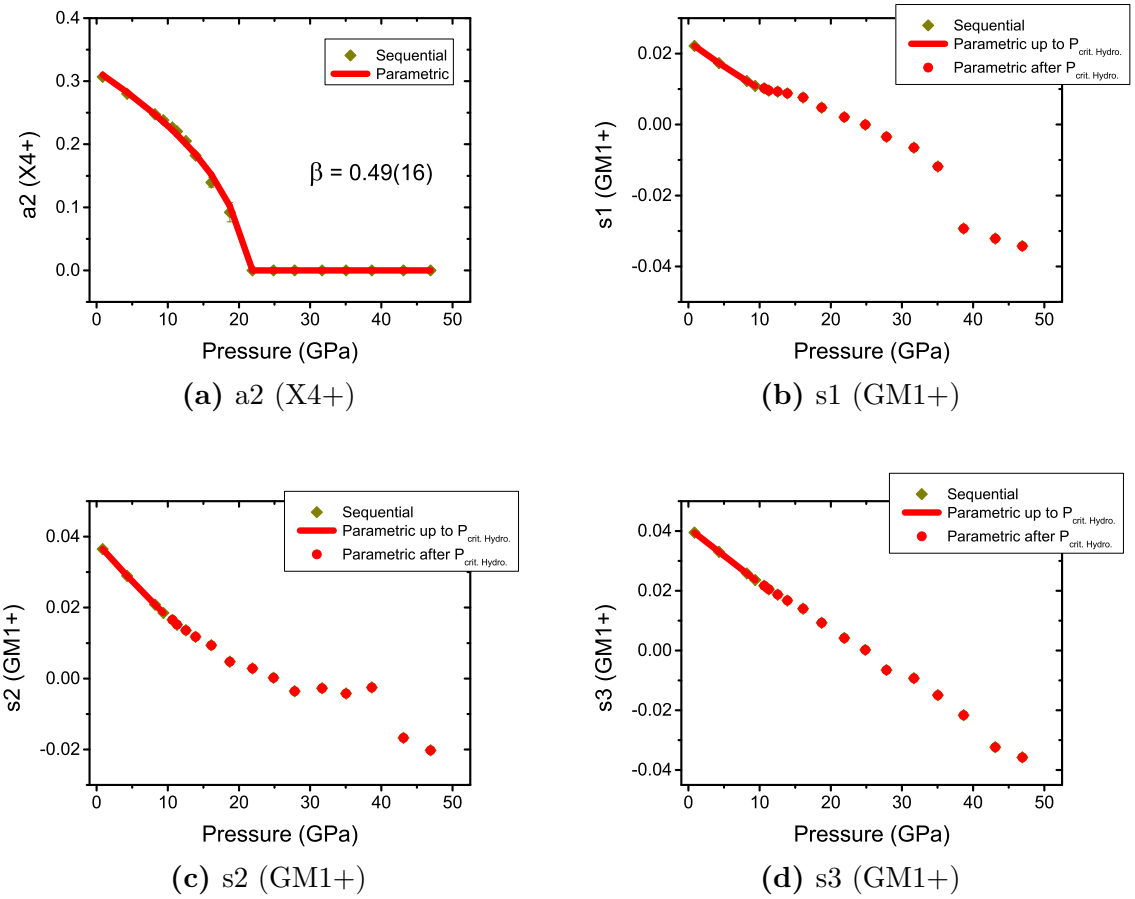

(a) a2 (X4+) **(b)** s1 (GM1+)

(c) s2 (GM1+) **(d)** s3 (GM1+)

Figure 4.30: Parameterized pressure dependent a) amplitudes of the symmetry mode X4+ and b)-d) phenomenological parameterized amplitudes of the strain modes of the $LaFeO_3$ perovskite. The modeling of the amplitudes of the X4+ mode was done using a power-law behavior with the same critical exponent as for the modeling of the amplitude of the mm2 (mX4+) mode (see figure 4.31b)).

hensive and can be regarded as being competitive compared to the well-established approaches A-C.

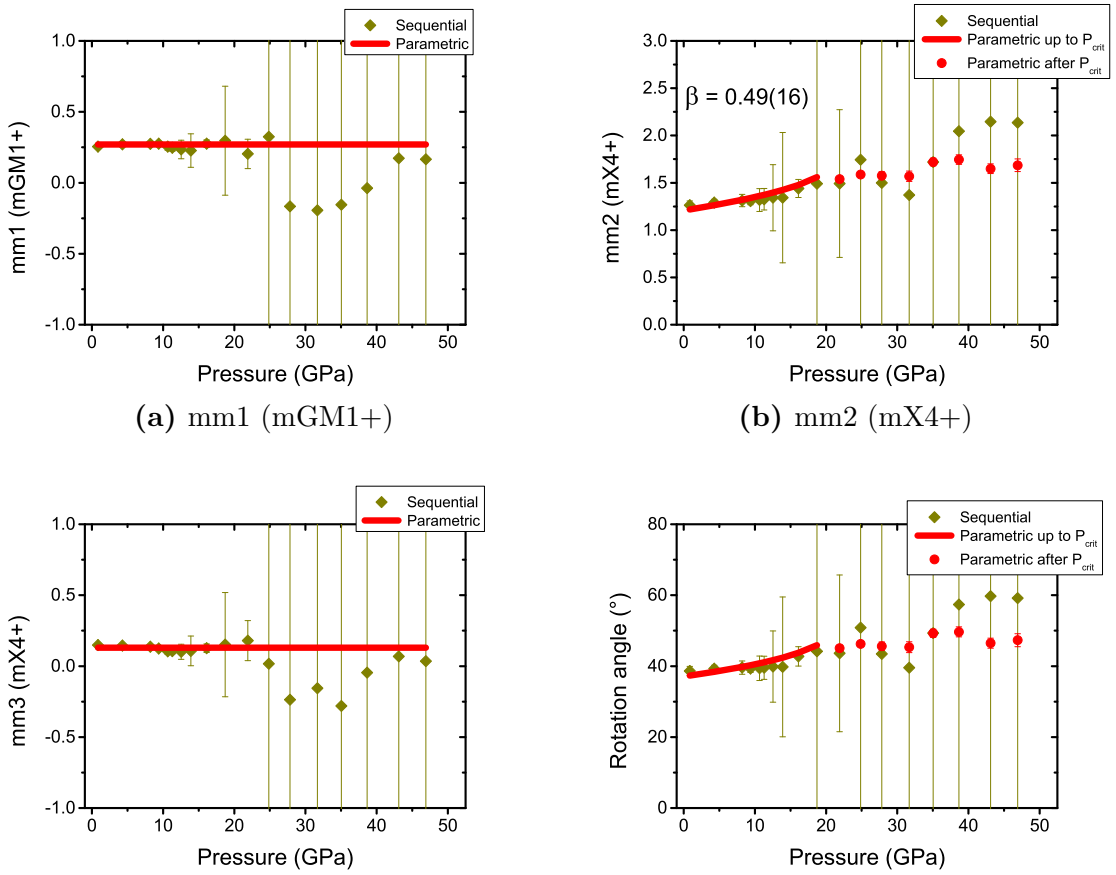

(a) mm1 (mGM1+) **(b)** mm2 (mX4+)

(c) mm3 (mX4+) **(d)** Rotation angle

Figure 4.31: Parameterized pressure dependent a)-c) rotational symmetry modes of the $LaFeO_3$ perovskite, which are responsible for the tilting of the FeO_6 octahedron. The rotation angle in d) of the FeO_6 octahedron is calculated by the three rotational symmetry modes.

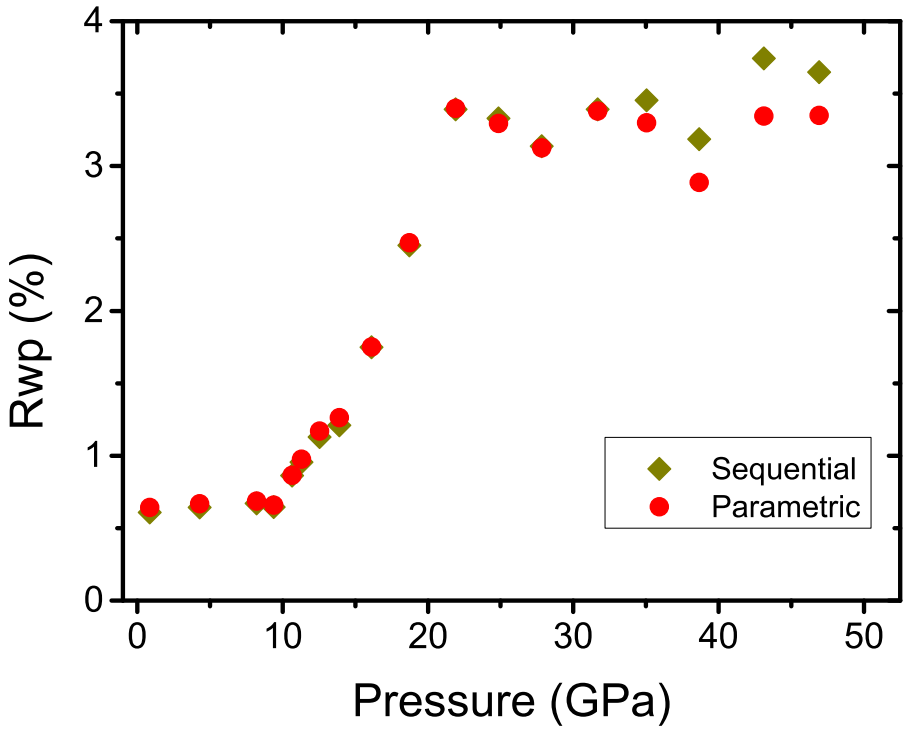

Figure 4.32: Comparison between the R_{wp} values of the sequential and parametric Rietveld refinement of approach D. The congruence of the R_{wp} values indicates the correctness of the applied physical constraints.

4.5 Conclusion

Investigations of the high pressure synchrotron X-ray powder diffraction measurements of the $LaFeO_3$ perovskite using different pressure media along the room temperature isotherm revealed, that this perovskite can be describes by an orthorhombic crystal structure with space group *Pbnm* up to a critical pressure value of approximately 20.5(6) GPa, where a structural second order phase transition to another orthorhombic crystal structure with higher symmetry and therefore with higher structural order occurs (see figure 4.33).

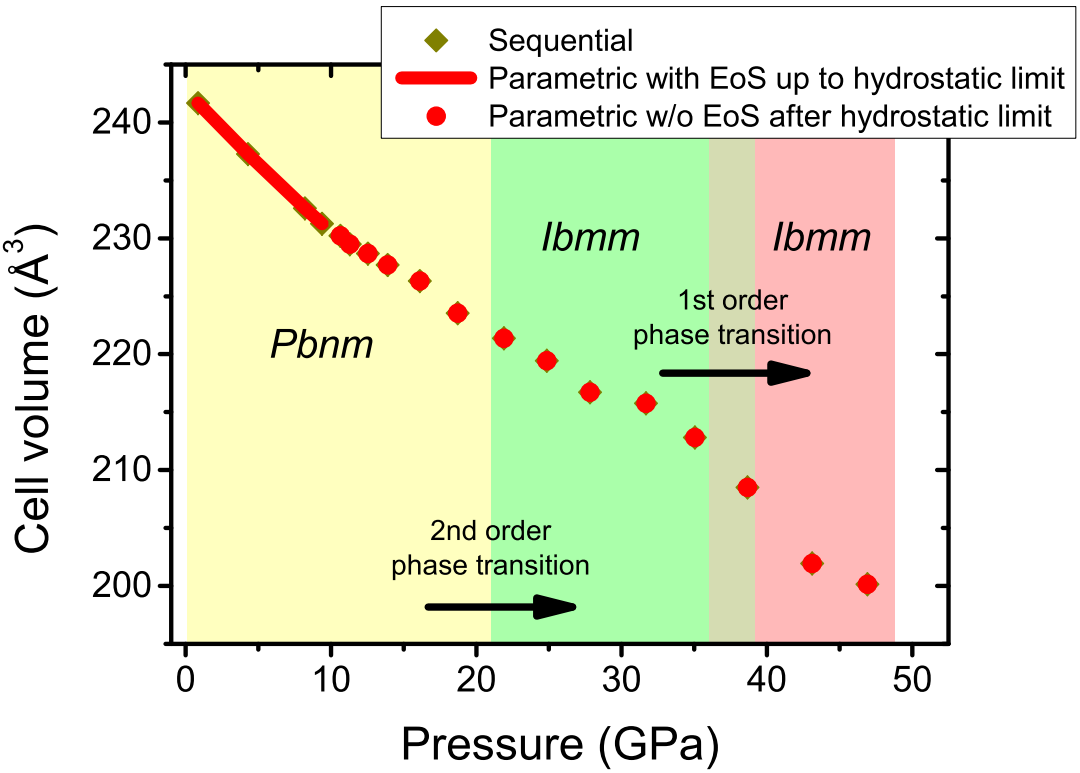

Figure 4.33: Pressure dependent structural phase diagram of the $LaFeO_3$ perovskite along the room temperature isotherm.

The observed orthorhombic high pressure crystal structure of the $LaFeO_3$ perovskite in the pressure range of approximately 20.5 GPa to approximately 38 GPa could be best described using the space group *Ibmm*. At approximately 38 GPa a "sluggish" isostructural first order phase transition with a volume drop of approximately 3% is observed, which is in agreement with previous synchrotron X-ray powder diffraction measurements of the orthorhombic lattice parameters and the unit cell volume performed by Xu *et al.* [191]. In the present work, due to intensive sequential and parametric Rietveld refinements, it could be clearly shown, that the first order phase transition is isosymmetric/isostructural and therefore a transition to a tetragonal crystal structure can be excluded, which is in contrast to the assumptions of Xu *et al.* [191].

As was shown by high pressure Mössbauer studies carried out by Xu *et al.* [191] at the room temperature isotherm, this first order phase transition can be attributed to a pressure induced high-spin ($S = \frac{5}{2}$) to low-spin ($S = \frac{1}{2}$) transition of the Fe^{3+} cation, which was recently underlined by density functional theory (DFT) studies of Javaid *et al.* [192, 193].

Besides the structure determinations, the influence of different pressure media onto the $LaFeO_3$ perovskite was investigated in detail. It could be shown that a pressure medium with a mixture of methanol-ethanol in a ratio of 4:1 is the most suitable one, in order to determine the parameters for different equations of state (EoS). Using a Murnaghan EoS the bulk modulus for the $LaFeO_3$ perovskite could be determined to $B_0 = 172(2)$ GPa, the first pressure derivative of the bulk modulus could be determined to $B_0' = 4.3(3)$ and the volume at ambient conditions could be determined to $V_0 = 242.87(1)$ Å^3.
Furthermore, the application of "linearized" and inverted EoS in parametric Rietveld refinements was investigated and proved to be stable and accurate enough in order to determine linear moduli directly from refinements of X-ray powder diffraction data.

Different approaches to describe the behavior of the atomic coordinates during a Rietveld refinement by rigid bodies/constrainable atomic groups and symmetry modes were tested and it was found that from each of these approaches fundamental information about the collective motion of atoms can be obtained. Using the symmetry mode approach it could be shown that primary order parameters in conjunction with secondary modes are responsible for the structural second order phase transition, whereas the rigid body/constrainable atomic group approaches were able to give a more direct picture, as the pressure dependent tilting of a single FeO_6 octahedron within the $LaFeO_3$ perovskite can be described as rotation around a unique axis in the case of the approach of rotational symmetry modes of a rigid body or it can be described by rotations around the crystallographic axes in the case of the rigid body/constrainable atomic group approach.

Concerning the multiferroic properties of the $LaFeO_3$ perovskite, it could be shown that the pressure dependent structural second order phase transitions is a transition between centrosymmetric / non-polar space groups and therefore no proper ferroelectricity can be expected in the high pressure phase of the $LaFeO_3$ perovskite. If ferroelectricity is maintained at higher pressure values, it can be expected that it is also induced by a magnetoelectric coupling, as it is the case for the present ferroelectricity at ambient conditions [184]. However, many questions regarding the pressure dependent ferroic properties and the pressure dependent coupling between them, could not be resolved by the present study and give rise to future studies.

CHAPTER 5

Temperature dependent *in situ* investigations of $BiCu_3Cr_4O_{12}$

5.1 Motivation

A-site ordered quadruple perovskites[1] with general chemical formula $AA'_3B_4O_{12}$ (with A, A', B = metallic cations) exhibt a rich field of temperature- or pressure-dependent electronic phenomena like inter-site charge transfer (ISCT) between the A' and B cations [233–246] as well as charge disproportionation (CD) of the B cations [233–237, 242, 247–254], where the CD often leads also to charge ordering (CO) effects on the B-site. In addition to the temperature or pressure dependent electronic transitions, magnetic (antiferromagnetic (AFM), ferromagnetic (FM) or ferrimagnetic (FiM)) and/or structural phase transition occur conjointly at the same critical temperature/-pressure. Simultaneously the conductivity/resistivity is often changing so that the quadruple perovskites cover the entire range from insulators up to metallic behavior. An overview of the particular properties of different quadruple perovskites is given in table 5.1. Common to nearly all of these quadruple perovskites is the paramagnetic behavior and the structural description in space group $Im\bar{3}$ in the high-symmetry/high-temperature phase (a description of the cubic crystal structure is given in section 5.4.1).

Except for the interesting ISCT and CD phenomena in quadruple perovskites even multiferroic properties were recently discovered. For instance, in $CaMn_3Mn_4O_{12}$, which shows antiferromagnetic behavior below $T_{c,1} = 90$ K, magnetically induced ferroelectric polarization was found [255, 256]. In outstanding studies of Zhang *et al.* [255] and Johnson *et al.* [256] it could be shown that the electric polarization occurs simultaneously with the first antiferromagnetic transition and that the electric polarization is perpendicular to the in-plane rotation of the magnetic moments. Therefore $CaMn_3Mn_4O_{12}$ is an interesting example for an improper ferroelectric behavior. An-

1 The term "quadruple perovskite" is chosen as the formula sum is four times the formula sum of a normal perovskite with general formula ABO_3. The term "quadruple perovskite" follows also the terminology of Howard *et al.* [232], who gave a definition for the term "double perovskites". Following this terminology by considering the ratio of 1:3 of the cations on the A-site, it is logical to name these perovskites quadruple perovskites.

other example for combined antiferromagnetic and proper ferroelectric phenomena is the quadruple perovskite $BiMn_3Mn_4O_{12}$ [257]. Small deviations of the anisotropic displacement parameters (ADP) of the Bi cation showed that the symmetry must be lowered from the centrosymmetric space group $I2/m$ to the non-centrosymmetric space group Im, which allows for proper ferroelectricity in this compound [257]. These two examples show nicely that quadruple perovskites are also interesting study objects for proper as well as improper ferroelectricity.

Detailed experimental and theoretical studies for the quadruple perovskites with Cu on the A'-site and Fe on the B-site were performed by Yamada *et al.* [236] and Rezaei *et al.* [237], respectively. Depending on the size of the lanthanide cation on the A-site, these compounds exhibit either inter-site charge transfer (A = La, Pr, Nd, Sm, Eu, Gd, Tb) or charge disproportionation phenomena (A = Dy, Ho, Er, Tm, Yb, Lu). The ISCT is accompanied by metal-to-insulator, antiferromagnetic and isostructural phase transitions with a negative thermal expansion of the volume upon heating. In contrast to the ISCT, the CD is accompanied by metal-to-semiconductor, ferrimagnetic and structural phase transitions without drastic volume changes. In addition to the CD, a rock-salt type charge ordering of the B-site can be observed. Rezaei *et al.* [237] performed density functional theory calculations and showed "that the strength of the crystal-field splitting and the relative energy ordering between Cu $3d_{xy}$ and Fe $3d$ states are the key parameters determining the ISCT/CD in light/heavy lanthanides". Although similar ISCT and CD phenomena were found for other quadruple perovskites (e.g. $BiCu_3Fe_4O_{12}$ (ISCT) [244, 245], $CaCu_3Fe_4O_{12}$ (CD) [242, 247, 248], $CeCu_3Fe_4O_{12}$ (CD) [249], $YCu_3Fe_4O_{12}$ (CD) [250]), it is not yet clear if exactly the same mechanisms are causal for these transitions.

However not only the substitution of the A-site cations leads to different phenomena; also the substitution of the Fe cation on the B-site (for example by Cr cations) can differ from the above described mechanisms. For instance the two quadruple perovskites $LaCu_3Cr_4O_{12}$ and $YCu_3Cr_4O_{12}$ reveal both an ISCT effect between Cu and Cr [246], although the yttrium analogue $YCu_3Fe_4O_{12}$ possess a CD effect [250]. Different from the Fe analogues, they show also a metallic Pauli paramagnetic behavior over the entire temperature range as well as a positive thermal expansion upon heating, which is in contrast to the given properties of $LaCu_3Fe_4O_{12}$ and $YCu_3Fe_4O_{12}$ in table 5.1. This is a clear indicator that the mechanisms of the quadruple perovskites with Cr on the B-site can differ from the Fe analogues.

In order to shed light on the properties of other Cr-containing compounds, the high-pressure synthesized quadruple perovskite with the chemical formula $BiCu_3Cr_4O_{12}$ was investigated in this work. A detailed synchrotron X-ray Powder Diffraction study was carried out to reveal all structural properties of this compound in the temperature range from 100 K to 350 K. The obtained diffraction results are supported by magnetic susceptibility and electric resistivity measurements.

Table 5.1: Properties of different quadruple perovskites. Used abbreviations are as follows: inter-site charge transfer (ISCT), charge disproportionation (CD), positive thermal expansion (PTE), negative thermal expansion (NTE), ferromagnetic (FM), ferrimagnetic (FiM), antiferromagnetic (AFM). Please note that for many quadruple perovskites the change of properties occurs concordantly at the same critical temperature/pressure. Please note also that the classification of the conductivity with metal/metallic, semiconductor and insulator is given by the authors in the corresponding literature (often the term semiconductor covers a huge range of conductivity/resistivity from heavily p-doped semiconductors to heavily n-doped semiconductors). In general this table gives only an overview of selected publications, thus some information in this table can be already revised.

Quadruple perovskite	Space group	Charge phenomena (ISCT, CD)	Volume change (PTE, NTE)	Magnetism (FM, FiM, AFM)	Metal / semiconductor / insulator	Electric resistivity ρ ($\Omega \cdot cm$)	Literature
B = Fe							
$CaCu_3Fe_4O_{12}$	$Im\bar{3}$ (T = RT) $Pn\bar{3}$ (T = 90 K)	CD: $Ca^{2+}Cu_3^{2+}Fe_4^{4+}O_{12}^{2-}$ $\rightarrow Ca^{2+}Cu_3^{2+}Fe_2^{3+}Fe_2^{5+}O_{12}^{2-}$	PTE	FiM below T_c = 210 K	insulator	$\rho \approx 2 \cdot 10^{-2}$ (T = 300 K) $\rho \approx 1 \cdot 10^{-1}$ (T = 0 K)	[242, 247, 248]
$CeCu_3Fe_4O_{12}$	$Im\bar{3}$ (T = RT) $Im\bar{3}$ (T = 100 K)	CD: $Ce^{4+}Cu_3^{2+}Fe_4^{3.5+}O_{12}^{2-}$ $\rightarrow Ce^{4+}Cu_3^{2+}Fe_3^{3+}Fe_1^{5+}O_{12}^{2-}$	-	AFM ? below T_c $T_c \approx$ 260-280 K	semiconductor	$\rho \approx 1 (T = 300K)$ $\rho \approx 1 \cdot 10^{6}$ (T = 0 K)	[249]
$YCu_3Fe_4O_{12}$	$Im\bar{3}$ (T = RT) $Pn\bar{3}$ (T = 100 K)	CD: $Y^{3+}Cu_3^{2+}Fe_4^{3.75+}O_{12}^{2-}$ $\rightarrow Y^{3+}Cu_3^{2+}Fe_{2.5}^{3+}Fe_{1.5}^{5+}O_{12}^{2-}$	PTE	FiM below T_c = 250 K	metal / semiconductor	$\rho \approx 1$ (T = 300 K) $\rho \approx 1.2 \cdot 10^{1}$ (T = 0 K)	[250]
$SrCu_3Fe_4O_{12}$	$Im\bar{3}$ (T = RT) (isostr. transition)	Mössbauer: CD: $Sr^{2+}Cu_3^{2+}Fe_4^{4+}O_{12}^{2-}$ $\rightarrow Sr^{2+}Cu_3^{2+}Fe_{3.2}^{3+}Fe_{0.8}^{5+}O_{12}^{2-}$ XRD: ISCT: $Cu^{2.20+} + Fe^{3.55+}$ $\rightarrow Cu^{2.35+} + Fe^{3.43+}$	NTE	AFM below T_c = 180 K	semiconductor	$\rho \approx 1$ (T = 300 K) $\rho \approx 2 \cdot 10^{3}$ (T = 20 K)	[233–235]
$LnCu_3Fe_4O_{12}$ (Ln = Dy, Ho, Er, Tm, Yb, Lu)	$Im\bar{3}$ (T = RT) $Pn\bar{3}$ (T = 100 K)	CD: $Ln^{3+}Cu_3^{2+}Fe_4^{3.75+}O_{12}^{2-}$ $\rightarrow Ln^{2+}Cu_3^{2+}Fe_{2.5}^{3+}Fe_{1.5}^{5+}O_{12}^{2-}$	PTE	FiM below T_c T_c = 250-260 K	metal / semiconductor		[236, 237]
$LnCu_3Fe_4O_{12}$ (Ln = La, Pr, Nd, Sm, Eu, Gd, Tb)	$Im\bar{3}$ (T = RT) (isostr. transition)	ISCT: $Ln^{3+}Cu_3^{2+}Fe_4^{3.75+}O_{12}^{2-}$ $\rightarrow Ln^{3+}Cu_3^{3+}Fe_4^{3+}O_{12}^{2-}$	NTE	AFM below T_c T_c = 360-240 K with decreasing Ln size	metal / insulator		[236, 237]
$LaCu_3Fe_4O_{12}$	$Im\bar{3}$ (T = RT) (isostr. transition)	ISCT: $La^{3+}Cu_3^{2+}Fe_4^{3.75+}O_{12}^{2-}$ $\rightarrow La^{3+}Cu_3^{3+}Fe_4^{3+}O_{12}^{2-}$	NTE	AFM below T_c = 393 K	metal / insulator	$\rho \approx 1 \cdot 10^{-2}$ (P = 8 GPa) $\rho \approx 4 \cdot 10^{1}$ (P = 0.5 GPa)	[238–240] [241–243]
$BiCu_3Fe_4O_{12}$	$Im\bar{3}$ (T = RT) (isostr. transition)	ISCT: $Bi^{3+}Cu_3^{2+}Fe_4^{3.75+}O_{12}^{2-}$ $\rightarrow Bi^{3+}Cu_3^{3+}Fe_4^{3+}O_{12}^{2-}$	NTE	AFM below T_c = 428 K	metal / semiconductor		[244, 245]
B = Cr							
$CaCu_3Cr_4O_{12}$	$Im\bar{3}$ (T = RT)			Pauli paramagnetic	metal	$\rho \approx 1 \cdot 10^{-3}$ (T = 300 K) $\rho \approx 4 \cdot 10^{-4}$ (T = 0 K)	[258]
$LaCu_3Cr_4O_{12}$	$Im\bar{3}$ (T = RT) (isostr. transition at T_c = 220 K)	ISCT: $La^{3+}Cu_3^{2+}Cr_4^{3.75+}O_{12}^{2-}$ $\rightarrow La^{3+}Cu_3^{3+}Cr_4^{3+}O_{12}^{2-}$	PTE	Pauli paramagnetic	metal	$\rho \approx 6 \cdot 10^{-3}$ (T = 350 K) $\rho \approx 10 \cdot 10^{-3}$ (T = 0 K)	[246]
$YCu_3Cr_4O_{12}$	$Im\bar{3}$ (T = RT) (isostr. transition at T_c = 250 K)	ISCT: $Y^{3+}Cu_3^{2+}Cr_4^{3.75+}O_{12}^{2-}$ $\rightarrow Y^{3+}Cu_3^{3+}Cr_4^{3+}O_{12}^{2-}$	PTE	Pauli paramagnetic	metal	$\rho \approx 2 \cdot 10^{-3}$ (T = 350 K) $\rho \approx 2 \cdot 10^{-3}$ (T = 0 K)	[246]
B = Mn							
$BiCu_3Mn_4O_{12}$	$Im\bar{3}$ (T = RT)	?	?	FiM (T_c = 350 K)	semiconductor / metallic	$\rho \approx 12.5 \cdot 10^{-3}$ (T = 300 K) $\rho \approx 7 \cdot 10^{-3}$ (T = 0 K)	[248, 259]

Continued on next page

Table 5.1 – *Continued from previous page*

Quadruple perovskite	Space group	Charge phenomena (ISCT, CD)	Volume change (PTE, NTE)	Magnetism (FM, FiM, AFM)	Metal / semi-conductor / insulator	Electric resistivity ρ ($\Omega \cdot cm$)	Literature
$CaCu_3Mn_4O_{12}$	$Im\bar{3}$ (T = RT)	?	?	FM (T_c = 355 K)	semiconductor	$\rho \approx 1.8 \cdot 10^3$ (T = 300 K) $\rho \approx 0.7 \cdot 10^{-1}$ (T = 0 K)	[260, 261]
$LaCu_3Mn_4O_{12}$	$Im\bar{3}$ (T = RT)	?	?	FiM (T_c = 361 K)	metallic	$\rho \approx 1.3 \cdot 10^{-1}$ (T = 300 K) $\rho \approx 0.7 \cdot 10^{-1}$ (T = 0 K)	[262]
$BiMn_3Mn_4O_{12}$	$I2/m$ (T = RT) $Im\bar{3}$ (T = RT) depending on oxygen content (for ferroelectricity Im (T = RT))	?	?	FM (T_c = 59 K) (spin canting?) AFM (T_c = 28 K) for cubic phase only AFM ($T_c \approx$ 27 K)	insulator / semiconductor	$\rho \approx 1 \cdot 10^4$ (T = 300 K)	[257, 263, 264]
$CaMn_3Mn_4O_{12}$	$Im\bar{3}$ $R\bar{3}$ (transition interval between T = 409 K and T = 448 K)	CD: $Ca^{2+}Mn_3^{3+}Mn_4^{3.25+}O_{12}^{2-}$ $\rightarrow Ca^{2+}Mn_3^{3+}Mn_3^{3+}Mn_1^{4+}O_{12}^{2-}$	NTE	AFM ($T_{c,1}$ = 90 K) (helical ordered) AFM ($T_{c,2}$ = 48 K) (???)			[255, 256, 265]
$NaMn_3Mn_4O_{12}$	$Im\bar{3}$ (T = RT - 168 K) $I2/m$ / $C2/m$ (T < 176 K)	CD: $Na^{2+}Mn_3^{2+}Mn_4^{3.5+}O_{12}^{2-}$ $\rightarrow Na^{2+}Mn_3^{2+}Mn_2^{3+}Mn_2^{4+}O_{12}^{2-}$	-	AFM (T_c = 125 K)	insulator	$\rho \approx 1.2$ (T = 300 K) $\rho \approx 1 \cdot 10^5$ (T = 100 K) $\rho \approx 1 \cdot 10^5$ (T = 100 K)	[251, 252] [253, 254]
B = V							
$MnCu_3V_4O_{12}$	$Im\bar{3}$ (T = RT / 100 K)			Paramagnetic	metal	$\rho \approx 1.7 \cdot 10^{-3}$ (T = 300 K) $\rho \approx 1.3 \cdot 10^{-3}$ (T = 0 K)	[266]
B = Ir							
$LaCu_3Ir_4O_{12}$	$Im\bar{3}$ (T = RT)			Paramagnetic	metallic	$\rho \approx 6.5 \cdot 10^{-1}$ (T = 300 K) $\rho \approx 5.0 \cdot 10^{-1}$ (T = 0 K)	[267]

5.2 Synthesis

High pressure synthesis of the quadruple perovskite $BiCu_3Cr_4O_{12}$ was carried out at the National Institute for Materials Science (NIMS) in Tsukuba (Ibaraki) / Japan by Dr. Hiroya Sakurai[1] and Dr. Masahiko Isobe. The synthesis of the black colored powder was done by using a stoichiometric mixture of Bi_2O_3, CuO, Cr_2O_3 and CrO_2 powders which were sealed in a gold capsule. The gold capsule was then subsequently pressed applying a pressure of 7.7 GPa and simultaneously heated to a temperature of 1473 K for 2 hours. For the high pressure synthesis a belt-type apparatus was used. After this treatment the sample was quenched to room temperature and the pressure was gradually released. The product of the synthesis is a polycrystalline black colored pellet.

5.3 Experimental setup

Synchrotron X-ray powder diffraction measurements were performed by Dr. Tomce Runcevski and Prof. Dr. Robert E. Dinnebier at the National Synchrotron Light Source (NSLS), Brookhaven at beamline X17B1. The collection of the diffraction patterns was done in Debye-Scherrer mode using a wavelength of $\lambda = 0.1839$ Å(= 67.42 keV) with a Si(311) sagittal focusing double Laue crystal monochromator. Diffracted X-rays were detected by using a Perkin Elmer image plate detector. The sample was sealed in a glass capillary of 0.5 mm diameter and cooled/heated with an Oxford cryostream 700 cold gas blower.
The sample was first measured at room temperature and then cooled down to 100 K in temperature steps of 4 K. Thereafter, the sample was heated from 100 K to 352 K with the same temperature steps. Unfortunately upon cooling the data sets between 140 K and 106 K are lost, as there was a technical issue with the beam shutter.

The integration of the collected two-dimensional Debye-Scherrer rings to one-dimensional powder diffraction patterns was subsequently performed by using the computer program FIT2D [152]. The parameters which were required for this integration were determined from a LaB_6 reference sample.
A simulated two-dimensional heating/cooling Guinier pattern of these temperature dependent synchrotron X-ray powder diffraction measurements can be found in figure 5.1.

1 Dr. Hiroya Sakura, National Institute for Materials Science (NIMS), 1-1 Namiki, Tsukuba, Ibaraki 305-0044, Japan

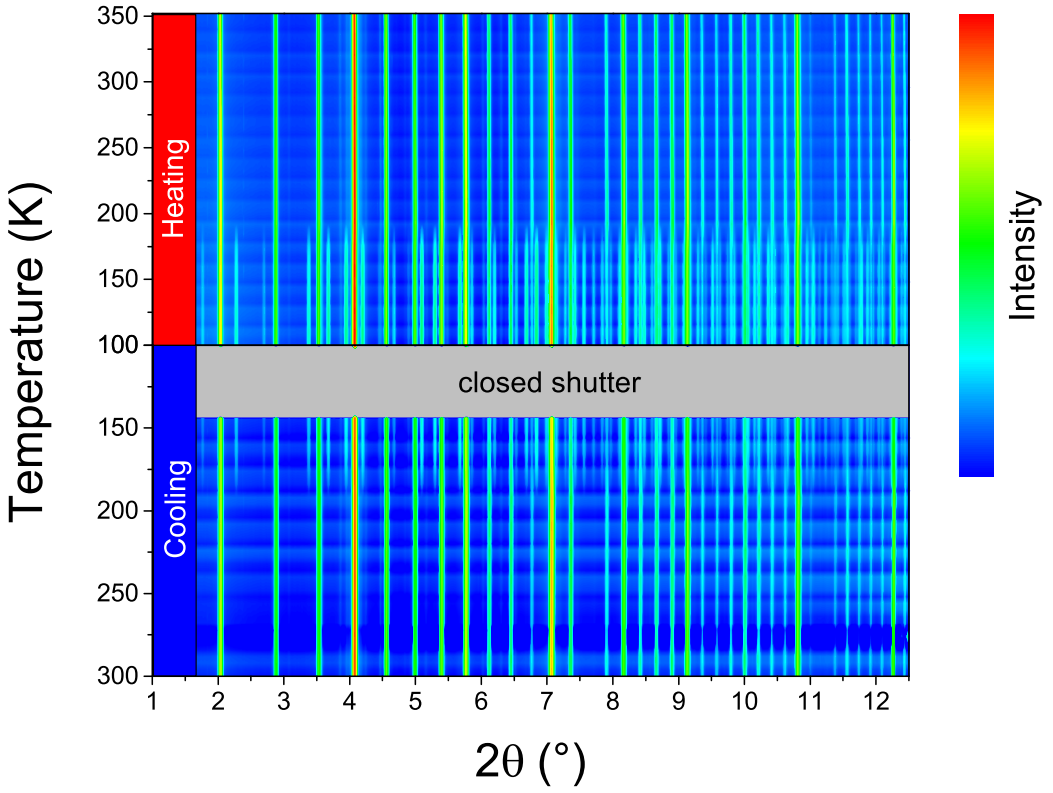

Figure 5.1: Simulated two-dimensional heating/cooling Guinier pattern of the temperature dependent *in situ* synchrotron X-ray powder diffraction measurements of $BiCu_3Cr_4O_{12}$. A first inspection of the graph indicates a reversible first order phase transition at approximately 188 K. On cooling the beam shutter was closed between 140 K and 106 K. In an interval of approximately 16 K, horizontal streaks with increased intensity can be observed in the simulated heating/cooling Guinier pattern. It seems that at these values the patterns have a higher intensity potentially due to a better position of the capillary (possibly caused by the spinning frequency of the capillary). However this small difference in the background intensity does not influence the refinement as it is compensated by the modeling of the background with variable Chebyshev polynomials[2].

The magnet susceptibility was measured using a SQUID magnetometer (MPMS, Quantum Design). The measured temperature range was 5 K to 350 K and the applied magnetic field strength was between 0 T and 5 T. Measurements of the direct current (DC) electric resistivity were performed using a Physical Property Measurement System (Quantum Design) in a temperature range of 2 K to 300 K. For the DC electric resistivity measurement a sample of the size 0.5 x 0.5 x 1.0 mm^3 was used. Measurements (raw data) of the electric resistivity and the magnetic susceptibility were kindly provided by Dr. Masahiko Isobe.

5.4 Sequential Rietveld refinement of temperature dependent synchrotron X-ray powder diffraction data

Sequential Rietveld refinements for all synchrotron X-ray powder diffraction data sets were performed by using the commercial version of the TOPAS 4.2 program [57] offered by the Bruker AXS Corporation. For all data sets the diffraction background was modeled by refineable Chebyshev polynomials and the peak shape modeling of the Bragg reflections was done using the fundamental parameter approach [159, 160]. The zero shift was determined to -0.00368(12)° 2θ for the room temperature measurement and kept fixed for all other temperature-dependent refinements. Peak broadening of all crystalline phases due to sample dependent effects were modeled by the integrated crystallite size and phenomenological strain macros (detailed explanation of these macros can be found in the TOPAS 4.2 manual [57] and partially in section 4.4). The synchrotron radiation was assumed to be 100% horizontally polarized.

5.4.1 Crystal structure at room temperature

$BiCu_3Cr_4O_{12}$ crystallizes at room temperature in space group $Im\bar{3}$ with cubic perovskite lattice parameters of $2a_p \times 2a_p \times 2a_p$ ($2a_p$ = 7.3028(1) Å with respect to the primitive cubic lattice parameters of a perovskite a_p) and a volume of V = 389.46(2) $Å^3$, isostructural to other A-Site ordered quadruple perovskites with chemical formula $ACu_3Cr_4O_{12}$ (A = La, Y)[246], $LnCu_3Fe_4O_{12}$ (Ln = lanthanide cation)[236], etc. (see table 5.1 for more examples and see figure 5.3 for a view of the crystal structure at room temperature. A description of the room temperature crystal structure is given below). A Rietveld refinement of the synchrotron X-ray powder diffraction data measured at room temperature structure is presented in figure 5.2. In addition to the main phase, small amounts of Cr_2O_3 (wt% 0.40(14)) and CrO (wt% 0.58(21)) were identified, which both persist over the entire investigated temperature range. These

2 The same phenomenon was observed for another compound which was measured during the same measurement period, so it can be excluded that it is a sample dependent effect. The time dependence which can be estimated by checking the time stamps of the collected raw data seems to be approximately 12 and/or 16 minutes which corresponds to a very low frequency of 0.00139 Hz and/or 0.00104 Hz, respectively.

impurities were satisfactory modeled by taking their structural models and refining the peak shapes and lattice parameters. Additionally to these impurity phases three other small peaks are observed which possibly belong to another impurity. Unfortunately this impurity could not be identified, therefore the phase was simply neglected during the refinement. As the peaks of this unidentifiable impurity persist also over the entire temperature range, they are not considered as superstructure reflections of the $BiCu_3Cr_4O_{12}$ phase as there is no change in intensity upon crossing the phase transition. Structural details as the Wyckoff positions, the atomic coordinates, the anisotropic/isotropic displacement parameters as well as the residual factors of the room temperature Rietveld refinement can be found in table 5.2.

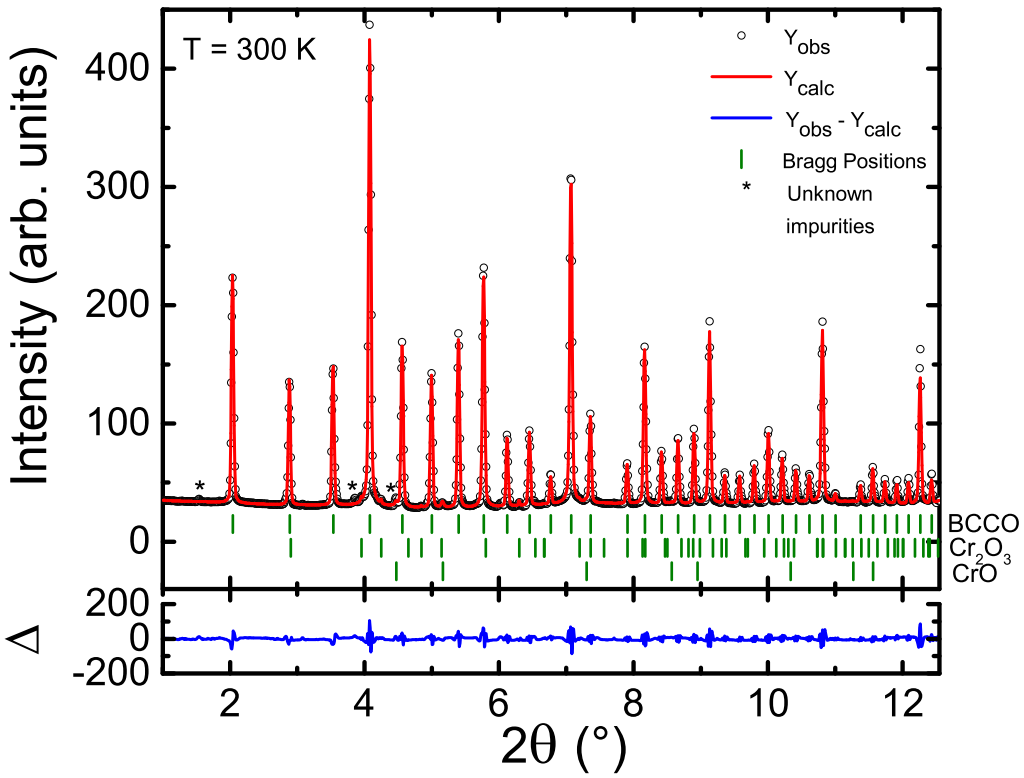

Figure 5.2: Rietveld plot of the $BiCu_3Cr_4O_{12}$ quadruple perovskite (BCCO) in space group $Im\bar{3}$ at room temperature. Known impurities like Cr_2O_3 (wt% 0.40(14)) and CrO (wt% 0.58(21)) were also modeled by the Rietveld method. Unknown impurities are marked by asterisks.

Table 5.2: Structural details as well as the residual factors of the room temperature structure of $BiCu_3Cr_4O_{12}$ in space group $Im\bar{3}$. All positions are fully occupied. Cubic lattice parameter is $a = 7.3028(1)$ Å with a cell volume of V = 389.46(2) Å^3. The residual factors are: $R_{Bragg} = 1.705$ %, $R_{exp} = 1.751$ %, $R_{wp} = 8.781$ %, GOF = 5.015 (as defined in TOPAS 4.2 [57]).

Atom	Wyckoff-Position	x	y	z	Anisotropic displacement parameters (Å^2)					
					u11	u22	u33	u12	u13	u23
Bi	2a	0	0	0	0.01943(44)	0.01943(44)	0.01943(44)	0	0	0
Cu	6b	0	1/2	1/2	0.0016(19)	0.0005(36)	0.0097(39)	0	0	0
Cr	8c	1/4	1/4	1/4	0.00272(47)	0.00272(47)	0.00272(47)	0.00062(97)	0.00062(97)	0.00062(97)
O	24g	0	0.3057(7)	0.1809(7)	Isotropic displacement parameter B: 0.18(13) (Å^2)					

The crystal structure of the $BiCu_3Cr_4O_{12}$ quadruple perovskite at room temperature is displayed in figure 5.3. Isostructural to the other members of the $AA'_3B_4O_{12}$ quadruple perovskite family (A = e.g. lanthanide cation; A', B = metallic cations) (for citations see table 5.1) the crystal structure consists of a three-dimensional framework of corner-sharing BO_6 polyhedra (here B = Cr). Interstitials are occupied by A cations in an icosahedral environment (here A = Bi) and square-planar coordinated $A'O_4$ configurations (here A' = Cu) which are aligned perpendicular to each other. The square-planar coordination of the A'-site can be explained by the occupation of this site with Jahn-Teller active cations like Cu^{2+} or Mn^{3+} cations [248]. In general, the nominal oxidation states of this quadruple perovskite can be presented as $Bi^{3+}Cu_3^{2+}Cr_4^{3.75+}O_{12}^{2-}$, which will be later experimentally confirmed by the calculation of the bond valence sums (BVS) in section 5.4.4. The nominal oxidation state of the Cr cation with a mixed valence state of 3.75+ explains also the absence of a Jahn-Teller effect of the CrO_6 octahedron, as only for Cr^{2+} cations a Jahn-Teller distorted octahedron can be expected.

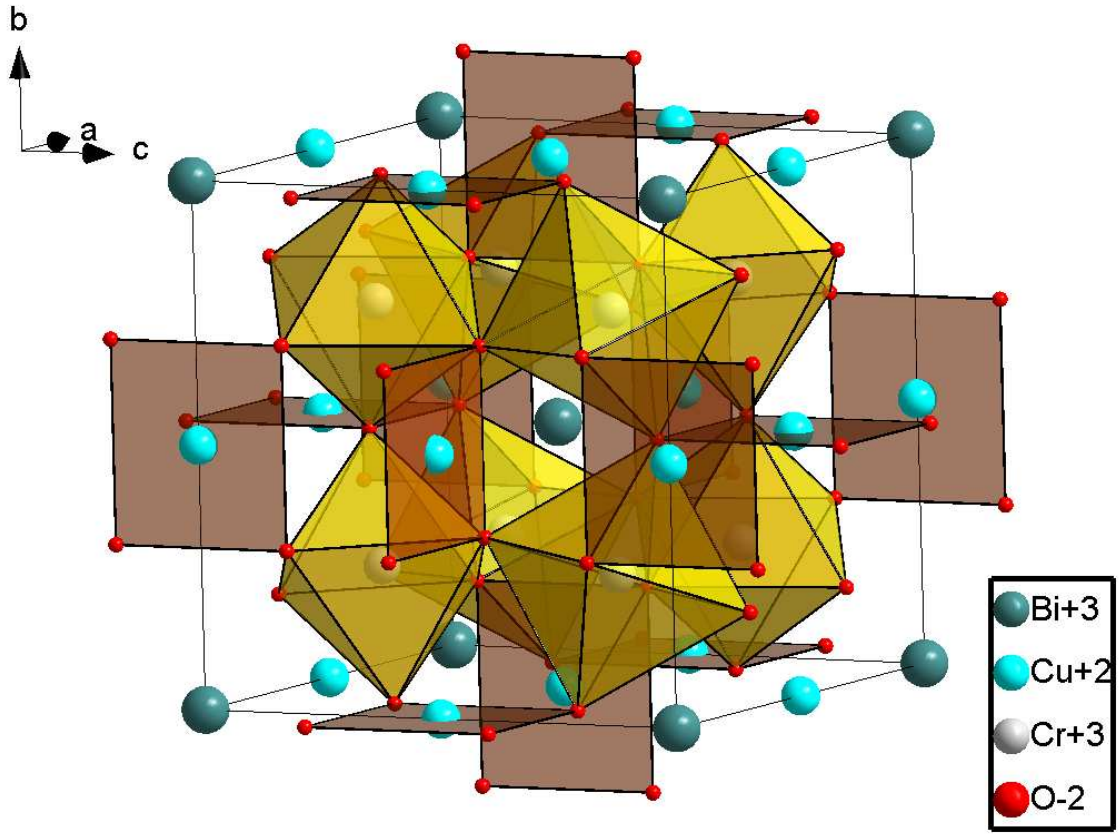

Figure 5.3: Crystal structure of the $BiCu_3Cr_4O_{12}$ quadruple perovskite with space group $Im\bar{3}$ at room temperature. The crystal structure consists of a three-dimensional framework of corner-sharing CrO_6 polyhedra. Interstitials are occupied by Bi cations in an icosahedral environment and square-planar coordinated CuO_4 configurations which are aligned perpendicular to each other.

5.4.2 Determination of the crystal structure at low temperatures

As already shown in the simulated two-dimensional heating/cooling Guinier pattern of the temperature dependent *in situ* synchrotron X-ray powder diffraction measurements in figure 5.1 in section 5.3 a reversible potential first order phase transition occurs upon cooling as well as upon heating at a temperature of approximately 188 K. A magnification of the phase transition region upon heating is presented in figure 5.4. Together with the overview in figure 5.1, this magnification shows that the intensity of the main Bragg reflections is unaffected during the phase transition and that additionally only satellite reflections are arising. This behavior suggests that the room temperature crystal structure is in general preserved and that the phase transition is leading to a commensurate or incommensurate modulation of the underlying quadruple perovskite crystal structure. Another aspect of this magnification is that the previously assumed potential first order phase transitions seems to be in fact rather a second order phase transition as the intensities of the satellite reflections are either slowly decreasing (on heating) or slowly increasing (on cooling) over a certain temperature range[1]. This observation of a second order phase transition simplifies the search for the crystal structure of the new phase, as the new space group can be found by looking for a subgroup of the parental space group $Im\bar{3}$ as a structural phase transition of second order always obeys group theory.

In order to narrow the possible solution space for a subgroup of the parental space group $Im\bar{3}$, the propagation vector (or also called modulation vector) of the new commensurate or incommensurate crystal structure must be found. This was done by using the program K_Search [83] from the FullProf program suite [83]. A first search for possible commensurate crystal structures gave a propagation vector of $\vec{k} = (0.5, 0.5, 0)^T$. Other commensurate solutions for propagation vectors which were close to the first solution are $\vec{k} = (0.5, 0, 0.5)^T$ and $\vec{k} = (0, 0.5, 0.5)^T$. A second search for incommensurate crystal structures gave propagation vectors which were close to the commensurate solutions, thus incommensurate solutions were no longer considered.

Investigations with the software ISODISTORT [64] revealed that the subgroup $Pn\bar{3}$ can be directly excluded from the search for applicable space groups as this space group posses a propagation vector of $\vec{k} = (0, 0, 0)^T$ or $\vec{k} = (1, 1, 1)^T$. Interestingly, this discovery, that the space group $Pn\bar{3}$ cannot be used, immediately excludes a phase transition to a simple rock-salt type order crystal structure as is usually found for the charge disproportionated quadruple perovskites mentioned in section 5.1. Using the ISODISTORT software different possible subgroups with a propagation vector of $\vec{k} = (0.5, 0.5, 0)^T$ were determined. Probable cubic space groups with matching propagation vectors were quite large in volume therefore smaller unit cells with lower symmetry were considered first. As no matching tetragonal space groups could be found by ISODISTORT, the focus went on to possible orthorhombic and trigonal space groups

1 This interpretation assumes that the investigated sample is of single phase at every temperature step. It will be later shown that this assumption is justified.

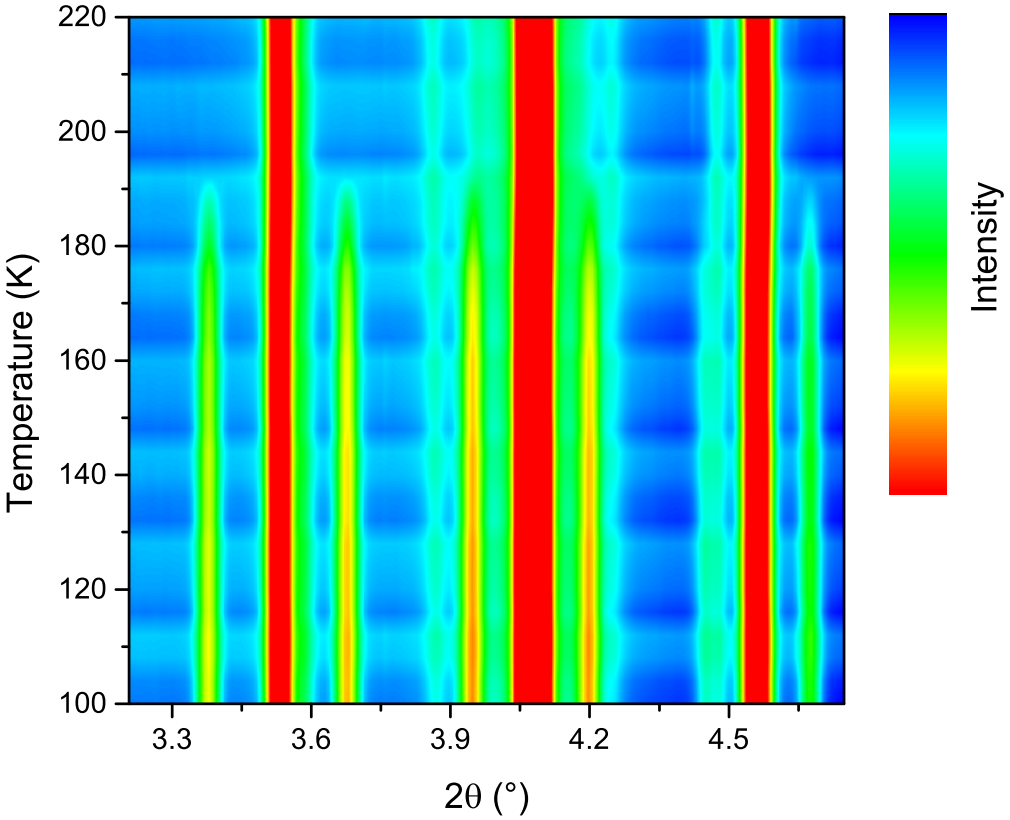

Figure 5.4: Magnified simulated two-dimensional heating Guinier pattern of the temperature dependent *in situ* synchrotron X-ray powder diffraction measurements of $BiCu_3Cr_4O_{12}$. The observable Bragg reflections of the main phase show no intensity changes during the phase transition. The potential first order phase transition cannot be maintained as the intensity of the satellite peaks is increasing/decreasing over a wider temperature range and therefore a second order phase transition is more likely.

(hexagonal space groups were also not considered by ISODISTORT). Structural fits of possible space group candidates with orthorhombic and trigonal space groups in $Cmmm$ and $R\bar{3}$, respectively, showed that the observed synchrotron powder pattern could be almost fitted, except for the problem of unrealistic large anisotropic displacement parameters (ADPs) for the Bi cations. As no other corrections could improve the fit and reduce the ADPs, a even lower symmetry was considered. As a possible candidate the triclinic space group $P\bar{1}$ with lattice parameters $a = 6.3271(467)$ Å, $b = 12.1016(1038)$ Å, $c = 12.1015(952)$ Å, $\alpha = 117.0501(1308)°$, $\beta = 99.8813(9171)°$ and $\gamma = 100.0542(9490)°$ was tested and the problem of unrealistic ADPs could be solved. A subsequent check with the software PLATON [268] for missed symmetries showed that the found triclinic crystal structure can be also described in the monoclinic space group $C2/m$ (in a first test of possible monoclinic space groups given by

ISODISTORT, the necessary origin shift was disregarded, which therefore led also to large ADPs for the Bi cation, which was the reason why the monoclinic solutions were at first not considered).

In figure 5.5 the final Rietveld refinement of the powder diffraction data set at a temperature of 100 K of $BiCu_3Cr_4O_{12}$ in space group $C2/m$ is presented. The monoclinic lattice parameters at a temperature of 100 K are $a = 10.34320(62)$ Å, $b = 7.29306(42)$ Å, $c = 10.32178(63)$ Å and $\beta = 90.09037(693)°$. These lattice parameters can be transformed into pseudo-cubic lattice parameters by using the given transformation matrix between space group $Im\bar{3}$ and space group $C2/m$ in appendix J. The calculated pseudo-cubic lattice parameters are $a = 7.30042(67)$ Å, $b = 7.29306(42)$ Å, $c = 7.31193(47)$ Å, $\beta = 90.11883(377)°$ and $\alpha = \gamma = 90°$. The monoclinic cell volume is $V_{monoclinic} = 778.6(1)$ Å^3 which is twice the unit cell volume of the cubic room-temperature crystal structure.

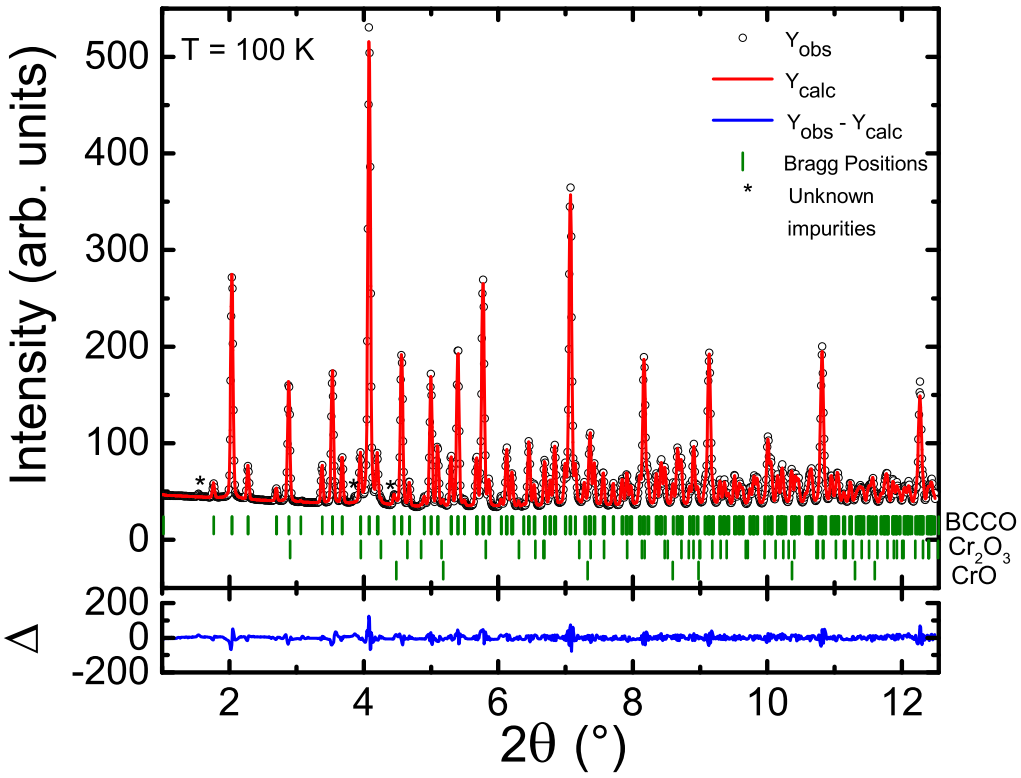

Figure 5.5: Rietveld plot of the $BiCu_3Cr_4O_{12}$ quadruple perovskite in space group $C2/m$ at a temperature of 100 K. Known impurities like Cr_2O_3 and CrO were also modeled by the Rietveld method. Unknown impurities are marked by asterisks.

The atomic positions at a temperature of 100 K were determined by the refinement of the amplitudes of symmetry modes which in turn were calculated using the ISODISTORT software [64]. The details of the final Rietveld refinement at a temperature of 100 K with the atomic positions and the isotropic and anisotropic displacement pa-

rameters can be found in table 5.3. The residual factors of this Rietveld refinement can be found in the caption of table 5.3.

Table 5.3: Structural details as well as the residual factors of the low-temperature monoclinic structure (at a temperature of 100 K) of the $BiCu_3Cr_4O_{12}$ quadruple perovskites. The space group is $C2/m$. All positions are fully occupied. Monoclinic lattice parameters are $a = 10.3432(6)$ Å, $b = 7.2931(4)$ Å, $c = 10.3218(6)$ Å, $\beta = 90.09(1)°$ with a cell volume of $V = 778.6(1)$ Å^3. The residual factors are: $R_{Bragg} = 2.005$ %, $R_{exp} = 1.355$ %, $R_{wp} = 6.077$ %, GOF = 4.485 (as defined in TOPAS 4.2 [57]).

Atom	Wyckoff-Position	x	y	z	Anisotropic displacement parameters (Å^2)					
					u11	u22	u33	u12	u13	u23
Bi	4i	0.7756(5)	0	0.2485(5)	0.00571(97)	0.0111(19)	0.0129(23)	0.0080(85)[1]	-0.0087(23)	0.0121(78)[1]
Cu1	4i	0.2535(1)	0	0.2487(1)	Overall isotropic displacement parameter B for Cu: 0.15(3) (Å^2)					
Cu2	2d	0	1/2	1/2						
Cu3	2a	0	0	0						
Cu4	2b	0	1/2	0						
Cu5	2c	0	0	1/2						
Cr1	8j	0.0083(8)	0.2573(1)	0.2473(2)	Overall isotropic displacement parameter B for Cr: 0.05(3) (Å^2)					
Cr2	4f	1/4	1/4	1/2						
Cr3	4e	1/4	1/4	0						
O1	4i	-0.0019(6)	0	0.3033(6)	Overall isotropic displacement parameter B for O: 0.0(2) (Å^2)					
O2	4i	0.4937(6)	0	0.8060(6)						
O3	4i	0.8239(6)	0	0.4853(6)						
O4	4i	0.3236(6)	0	-0.0090(6)						
O5	8j	0.8545(4)	0.3049(5)	0.3372(4)						
O6	8j	0.3492(4)	0.3088(5)	0.8414(4)						
O7	8j	0.9022(5)	0.1760(5)	0.0996(5)						
O8	8j	0.3962(5)	0.1779(5)	0.5924(5)						

The crystal structure of $BiCu_3Cr_4O_{12}$ at a temperature of 100 K is presented in figures 5.6a)-c). As the Cr cation splits into three distinct Wyckoff positions, a different color coding was used for the three different Cr positions (Cr1 = orange, Cr2 = purple, Cr3 = light blue). With this color coding it is obvious that the CrO_6 octahedra show a columnar ordering along the *b* axis. In contrast to the Cr position, the Cu position splits into 5 distinct crystallographic positions, however the square-planar coordination of the Cu cation is preserved. The square-planar CuO_4 configuration of the Cu4 and the Cu5 cation is oriented parallel to the *a*-*c*-plane, whereas the configuration of the Cu1 cation is perpendicular to the [-101] direction and the configuration of the Cu2 and Cu3 cations is perpendicular to the [101] direction. In general, the motif of the crystal structure in the cubic phase is preserved in the monoclinic crystal structure upon cooling.

The above described crystal structure of the $BiCu_3Cr_4O_{12}$ quadruple perovskite at 100 K is isostructrual to the recently discovered crystal structure of the quadruple perovskite $NaMn_3Mn_4O_{12}$ by Prodi *et al.* [254]. In this compound the manganese cation at the B position splits into the Wykoff positions 8j, 4e and 4f likewise to the Cr cation in $BiCu_3Cr_4O_{12}$. Later it will be shown that even similar oxidation states in equivalent positions will be adopted (see section 5.4.4).

The coordination spheres around the Cr and Bi cations at a temperature of 100 K are shown in figures 5.7a)-e). From these figures it is already obvious that the bond lengths within each polyhedron can differ considerably and that all of these polyhedra are no longer regular at low temperatures. Especially the coordination sphere of the Cr1 cation exhibits a huge distortion of the $Cr(1)O_6$ octahedron as the inner bond lengths between the Cr1 cation and the next oxygen ligands cover a range of 1.802 Å to 1.985 Å. A similar distortion can be found for the $Cr(2)O_6$ octehdron with a range of inner bond lengths between 1.862 Å to 2.039 Å. In contrast to the $Cr(1)O_6$ and $Cr(2)O_6$ octahedra the $Cr(3)O_6$ octahedron is much less distorted as the difference of inner bond lengths is smaller than 0.03 Å (1.955 Å to 1.980 Å). Besides the distorted CrO_6 octahedra a distortion at low temperatures can be also observed for the BiO_{12} icosahedron. Here the bond lengths between the central Bi cation to the oxygen cations differ from 2.369 Å to 2.841 Å. The development of different bond lengths and therefore the development of the distortion over temperature will be described in the next section.

1 Mathematically the anisotropic displacement parameters (ADPs) u12 and u23 parameter must be zero. Unfortunately no constraints were applied for the ADPs in this refinement. All results which are presented here for the low-temperature phase of $BiCu_3Cr_4O_{12}$ were refined without these constraints. In order to guarantee that these faults do not influence the results too much, selected temperatures were refined with the correct constraints for the ADPs for the low-temperature phase. Due to this reason the author can guarantee, that the error in the atomic positions and therefore the error in bond lengths and calculated bond valence sums is smaller than one estimated standard deviation compared to the refinements with the correct constraint ADPs.

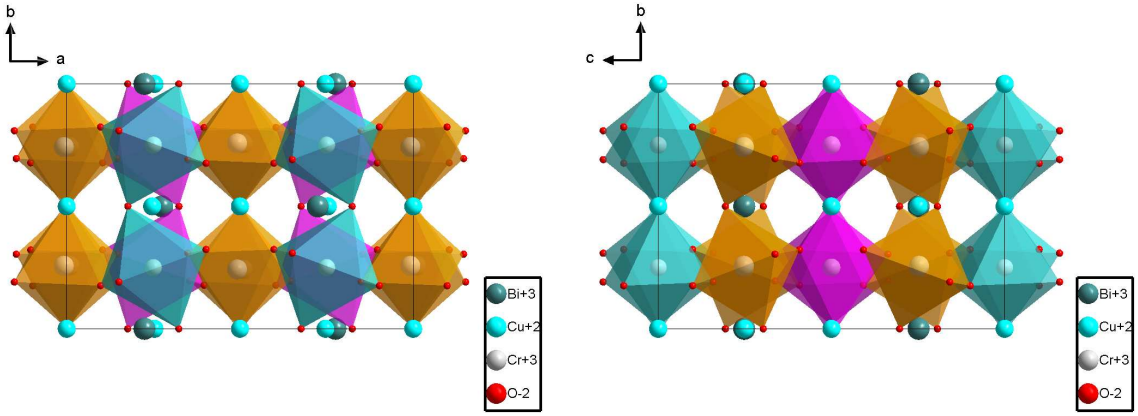

(a) view along *c*-direction

(b) view along *a*-direction

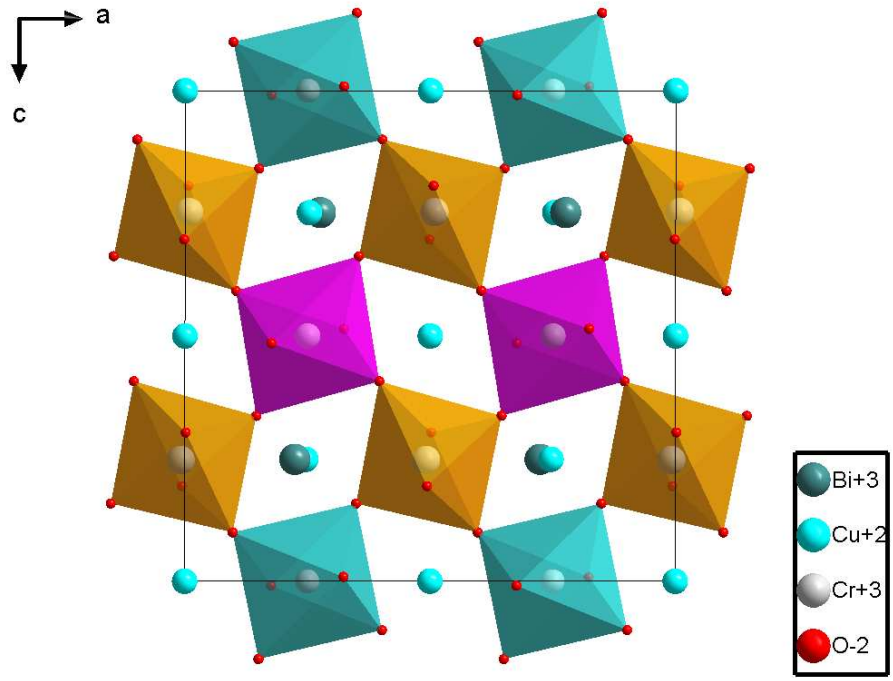

(c) view along *b*-direction

Figure 5.6: Projections of the crystal structure of the $BiCu_3Cr_4O_{12}$ quadruple perovskite in space group $Im\bar{3}$ at a temperature of 100 K: a) view along the *a*-axis, b) view along the *c*-axis and c) view along the *b*-axis. Likewise to the crystal structure at room temperature, the low temperature crystal structure consists of a three-dimensional framework of corner-sharing CrO_6 polyhedra. Interstitials are occupied by Bi cations in an icosahedral environment and square-planar coordinated CuO_4 configurations which are aligned perpendicular to each other. In contrast to the room temperature crystal structure, three different Cr positions are present (these different Cr positions are color coded: Cr1 = orange, Cr2 = purple, Cr3 = light blue). The view along the *b*-axis reveals that the different Cr positions are ordered in columns.

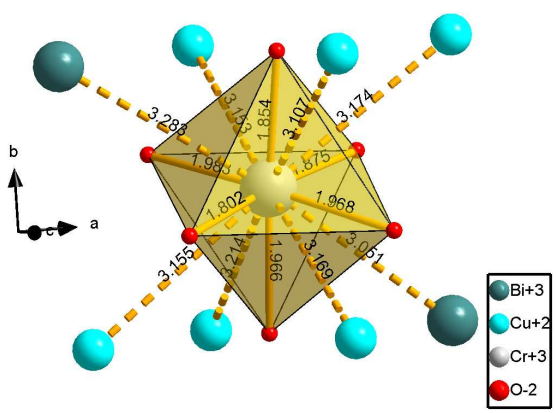

(a) Coordination sphere of Cr1

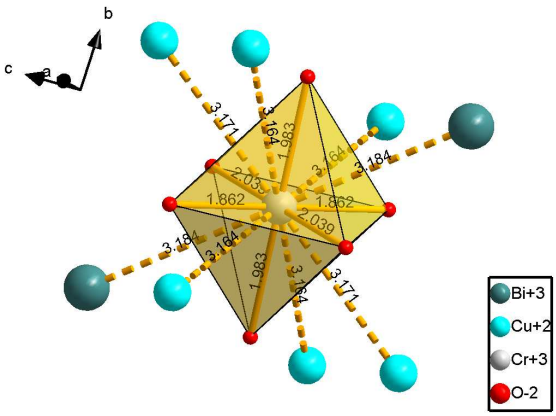

(b) Coordination sphere of Cr2

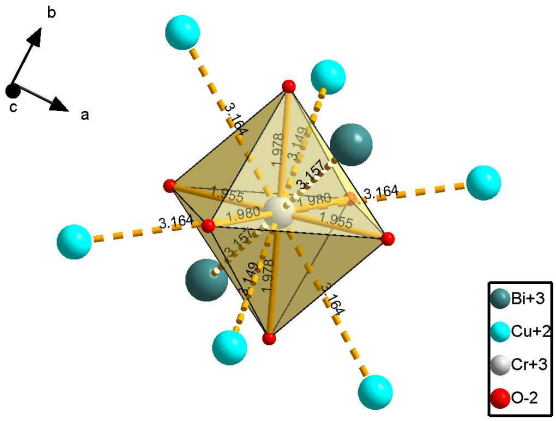

(c) Coordination sphere of Cr3

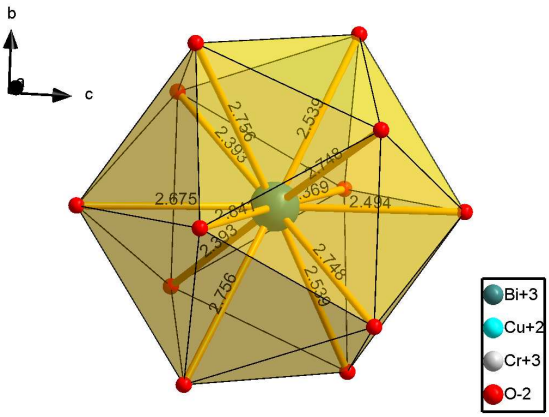

(d) Coordination sphere of Bi (close)

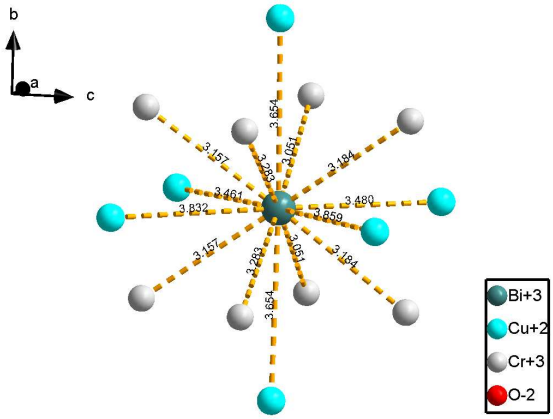

(e) Coordination sphere of Bi (distant)

Figure 5.7: Coordination spheres at a temperature of 100 K around the a) Cr1 cation, the b) Cr2 cation, the c) Cr3 cation and the d)+e) Bi cation of the $BiCu_3Cr_4O_{12}$ quadruple perovskite. Please note the distorted character of the corresponding polyhedra of Cr1, Cr2 and Bi.

5.4.3 Results of the sequential Rietveld refinement with symmetry modes

In order to get an overview and deeper insight into the structural phase transition all synchrotron X-ray Powder Diffraction patterns were treated with a sequential Rietveld refinement. In this sequential Rietveld refinement atomic coordinates of all patterns were refined using the amplitudes of a symmetry mode model, which was obtainedfrom the ISODISTORT software [64] (for this purpose the group-subgroup relationship between the cubic $Im\bar{3}$ phase and the monoclinic $C2/m$ phase was used). A list of order parameters and a list of all symmetry modes which were obtained by ISODISTORT can be found in appendix K.
The refinement of the monoclinic lattice parameters was performed by refining the pseudo-cubic lattice parameters and then transforming these lattice parameters with the transformation matrix given in appendix J to the monoclinic ones. This method allows a simultaneous investigation of the pseudo-cubic as well as of the monoclinic lattice parameters. The result of the refined lattice parameters is presented in figure 5.8.

Examining the behavior of the pseudo-cubic lattice parameters in figure 5.8 it is obvious that the cubic-monoclinic phase transition is completely reversible as the cooling and the heating data points are almost congruent. By looking carefully at the behavior of the different lattice parameters it can be deduced that the pseudo-cubic lattice parameters a and c are potentially showing a power-law behavior (which is expected for a structural second order phase transition according to Landau theory [68]), in contrast to the pseudo-cubic lattice parameter b. This situation becomes even clearer, if the monoclinic lattice parameter β is considered. The graph of this lattice parameter obviously shows a first order phase transition, as this angle does not approach the 90° angle in the cubic phase by a typical power-law behavior. Due to these reasons the assumption of a second order phase transition cannot be longer sustained[1]. Fortunately, this observation does not influence the modeling of the diffraction data by symmetry modes as the group-subgroup relationship between $Im\bar{3}$ and $C2/m$ is preserved and the values of the amplitudes of the symmetry modes must not necessarily be continuous.
In the same range (between $\approx$ 168 and 188 K), where the monoclinic β angle shows something like a peak, an interesting behavior of the monoclinic unit cell volume can be observed. In this region, the monoclinic unit cell volume shows a steep continuous decrease of the volume which can be understood as a large negative thermal expansion upon heating. This is in high contrast to other Cr-containing quadruple perovskites like $LaCu_3Cr_4O_{12}$ and $YCu_3Cr_4O_{12}$, where a positive thermal expansion was observed [246].

1 Another evidence for a weak first order phase transitions is given by the determination of the peak width. Using the fundamental parameter approach, the peak width in TOPAS is modeled by the Gaussian and Lorentzian crystallite size and the phenomenological Gaussian strain component. The typical weak first order phase transition behavior over temperature of this components is shown in figure L.1 in the appendix.

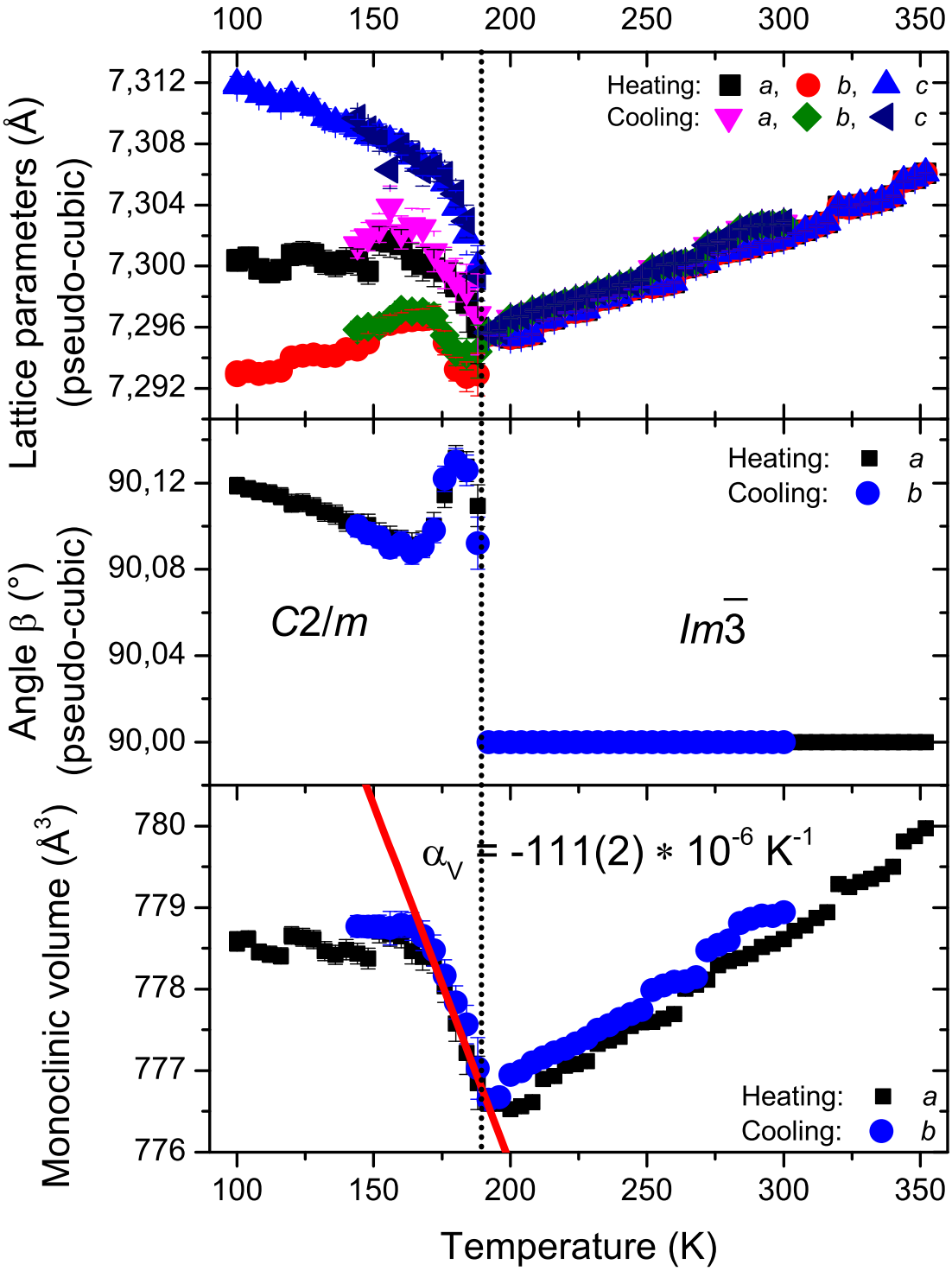

Figure 5.8: Pseudo-cubic lattice parameters, monoclinic β angle and monoclinic unit cell volume upon heating and cooling of the Rietveld refined synchrotron X-ray powder diffraction patterns of the $BiCu_3Cr_4O_{12}$ quadruple perovskite. The phase transition at a temperature of approximately 188 K is shown by the vertical dotted line. Please note that there are no data points for the cooling arm between 140 K and 106 K due to the closed beam shutter.

The observed negative thermal expansion of the monoclinic unit cell volume can be satisfactory modeled by the simple assumption of a linear thermal expansion of the volume given by the following equation:

$$V_{monoclinic}(T) = V_{0,monoclinic} \cdot (1 + \alpha_V \cdot \Delta T) \quad . \tag{5.1}$$

Here $V_{monoclinic}$ is the monoclinic unit cell volume at a given temperature T, $V_{0,monoclinic}$ is the monoclinic unit cell volume at a temperature of 0 K and α_V is the coefficient of the linear volume expansion.
If a fit of the monoclinic unit cell volume in the region between 168 K and 188 K is made, a linear volume contraction α_V of $-111(2)\cdot10^{-6}$ K^{-1} can be obtained. This value is even higher than the value which was reported by Yamada *et al.* for $SrCu_3Fe_4O_{12}$ (SCFO) [233]. They reported a linear expansion coefficient of $\alpha_{linear,SCFO} = -2.26 \cdot 10^{-5}$ K^{-1}. As SCFO is a cubic quadruple perovskite during all phases, this value can be easily transformed to the isotopic volume expansion value by the following equation:

$$\alpha_{V,SCFO} = 3 \cdot \alpha_{linear,SCFO} = -67.8 \cdot 10^{-6} K^{-1} \quad . \tag{5.2}$$

This shows intriguingly that the negative volume expansion value for $BiCu_3Cr_4O_{12}$ is almost twice the value of the $SrCu_3Fe_4O_{12}$ quadruple perovskite. At this point one should not draw the conclusion that $SrCu_3Fe_4O_{12}$ and $BiCu_3Cr_4O_{12}$ show similar ISCT and CD behavior as will be later seen during the bond valence sum calculations in section 5.4.4.

However, the behavior of the lattice parameters and unit cell volume within the temperature range from 168 K to 188 K is still not yet clear. Detailed investigations showed that this "transition region" is most likely single phase and that it can be only accurately modeled by the $C2/m$ space group. In general this "transition region" can be observed in the investigation of almost all refined and subsequent calculated parameters, for which reason this region will be assigned to the monoclinic phase as the possibility of an additional phase is speculative.

The behavior of the amplitudes of the symmetry modes is shown in figures 5.9a)-e). From these figures, especially from figures 5.9a)-c), it is obvious that the heating and the cooling values in the monoclinic phase are mirror symmetric. Such a behavior of the amplitude of the symmetry modes can happen, if there is a bigger gap between the refinement of two consecutive diffraction patterns (as it is the case when we start with a sequential Rietveld refinement of the cooling arm and approach the gap where the beam shutter was closed and therefore diffraction data is missing). In such cases the values of the amplitudes can jump to symmetry equivalent values if the crystal structure allows for such a behavior. In general this does not influence the behavior of bond lengths, etc., however the following investigations of bond lengths and bond valence sums will be done by simply investigating the heating arm.

The order of the phase transition can also be investigated by fitting a power-law be-

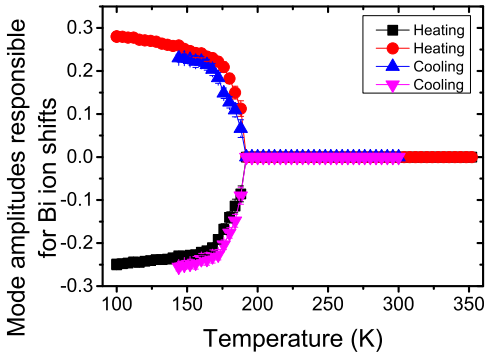

(a) Bi modes

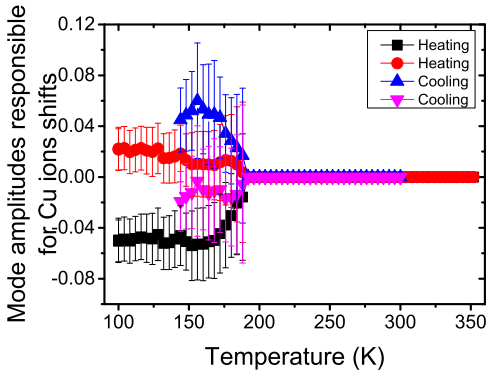

(b) Cu modes

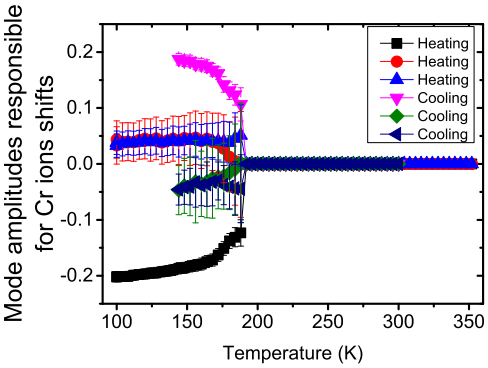

(c) Cr modes

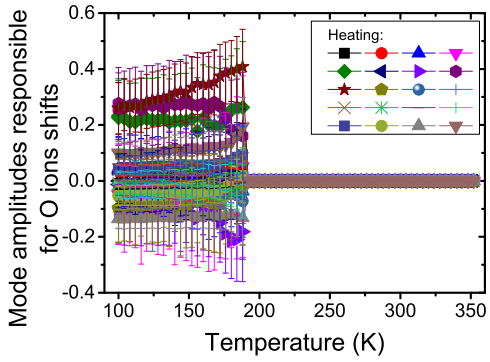

(d) O modes

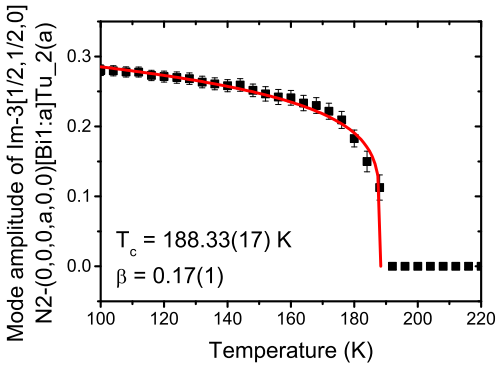

(e) Bi a2 mode

Figure 5.9: Temperature dependent amplitudes of the symmetry modes which are responsible for atomic coordinate shifts of the a) Bi cations, b) Cu cations, c) Cr cations and d) oxygen cations in the $BiCu_3Cr_4O_{12}$ quadruple perovskite. A detailed investigation of the a2 mode with a fit of a power-law behavior according to Landau theory is given in e).

havior to the amplitudes of selected symmetry modes. A suitable power-law behavior according to Landau theory is given by the following equation [67–69]:

$$a_{SM}(T) = a_{SM,0} \cdot \left(\frac{T_c - T}{T_c}\right)^{\beta} + \varepsilon \quad , \tag{5.3}$$

where a_{SM} is the value of the amplitude of the symmetry mode at a certain temperature T, $a_{SM,0}$ is the amplitude at a temperature of 0 K, T_c is the critical temperature, where the phase transition occurs, β is the critical exponent and ε is a possible shift away from zero (in this case ε is zero as there is no additional shift required as the amplitudes in the high symmetry phase are always zero).
Empirically, it seems that in particular the symmetry modes of heavy cations are suitable for such investigations, as the positions and therefore the mode amplitudes of these cations can be determined by X-ray diffraction with high accuracy. Therefore, one of the symmetry modes which is responsible for the shift of the Bi cation is taken in order to perform a power-law fit with equation 5.3 (see figure 5.9e)). The obtained critical values are T_c = 188.33(17) K for the critical temperature and β = 0.17(1) for the critical exponent. Especially the value for the critical exponent shows intriguingly that the monoclinic-to-cubic phase transition is not of second order but instead of weak first order[1]. This result is also supported by the behavior of other temperature dependent mode amplitudes as well as by the temperature dependent behavior of the lattice parameters, which all give a typicial indication for a weak first order phase transition.

In addition to the figures of the temperature dependent lattice parameters (see figure 5.8) and the temperature dependent amplitudes of the symmetry modes (see figure 5.9), the temperature dependent bond length behavior of all cations to the next oxygen cations is shown in figures 5.10 and 5.11.

The temperature dependent behavior of the bond lengths is very informative as it shows clearly that most of the cation coordination polyhedra are distorted to a large extent at lower temperatures. For instance for the Bi cation (see figure 5.10a)) the mean bond length is still preserved in the low temperature regime, although the icosahedron becomes completely distorted when the critical temperature on cooling is crossed. A similar behavior can be found for the three different CrO_6 octahedra despite the fact that the mean bond length is also changing by passing the critical temperature. By looking at figures 5.10b)-d) it is obvious that for the $Cr(1)O_6$ octahedron the mean bond length is decreasing while it is increasing for the $Cr(2)O_6$ and $Cr(3)O_6$ octahedra. Interestingly all three CrO_6 octahedra show a totally different distortion behavior. The $Cr(3)O_6$ octahedron shows only a slight distortion as all bond lengths are increasing by approximately the same extent, which leads to an enlargement of the octahedral volume. The uniform bond length of the $Cr(2)O_6$ octahedron splits into three different bond lengths, which leads to a small elongation in the vertical direction

1 The theoretical critical exponent for a perfect second order phase transition is β = 0.5.

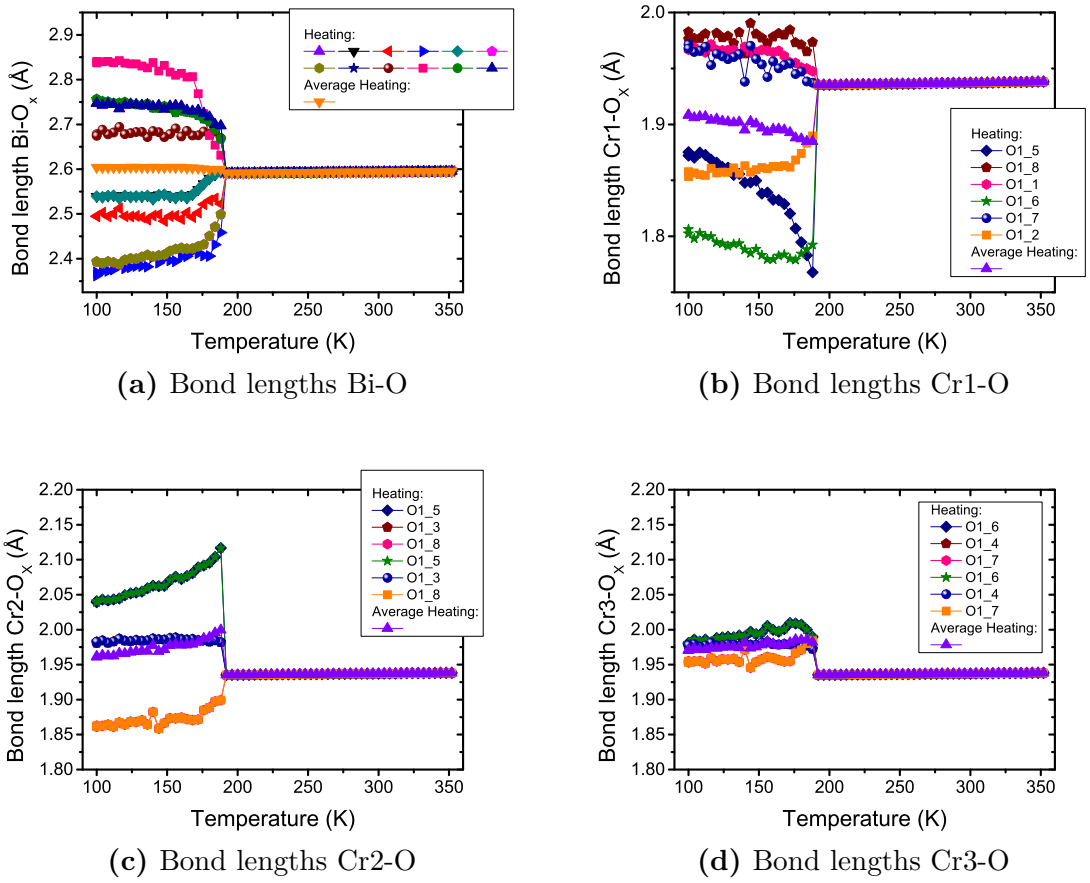

(a) Bond lengths Bi-O **(b)** Bond lengths Cr1-O

(c) Bond lengths Cr2-O **(d)** Bond lengths Cr3-O

Figure 5.10: Temperature dependent bond lengths of the a) Bi, b) Cr1, c) Cr2 and d) Cr3 coordination polyhedra in $BiCu_3Cr_4O_{12}$.

and into an elongation and also a compression within the plane (this description refers to the illustration in figure 5.7b)). In contrast to the bond lengths in the $Cr(2)O_6$ and $Cr(3)O_6$ octahedra, the bond lengths in the $Cr(1)O_6$ octahedron exhibit a very complicated temperature dependent behavior. Three of the six bond lengths are increasing when the $BiCu_3Cr_4O_{12}$ quadruple perovskite is cooled over its phase transition point. This leads to a slight elongation along these directions, whereas for the other three bond lengths partially a drastic compression can be observed. If the crystal structure is cooled further, two of the compressed bond lengths show only small changes (within a range of 0.05 Å), whereas the distance between the Cr1 cation and the O1_5 cation relaxes to a less compressed bond length by reducing the amount of compression by almost 0.1 Å. This means that the distortion of the $Cr(1)O_6$ octahedron slightly after the phase transition point is much higher than at lower temperatures, which is a crucial information if one tries to understand the behavior of the calculated bond valence sums in section 5.4.4. A comparison between the two CrO_6 octahedra at temperatures of 100 K and 188 K is given by the pictures of the coordination spheres in figure 5.12.

The behavior of the different Cu coordination polyhedra can be described in three

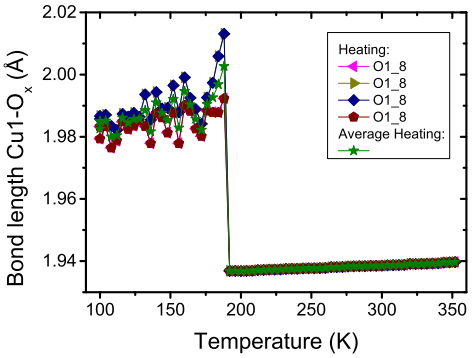

(a) Bond lengths Cu1-O

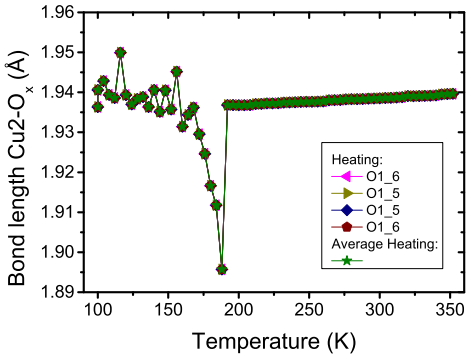

(b) Bond lengths Cu2-O

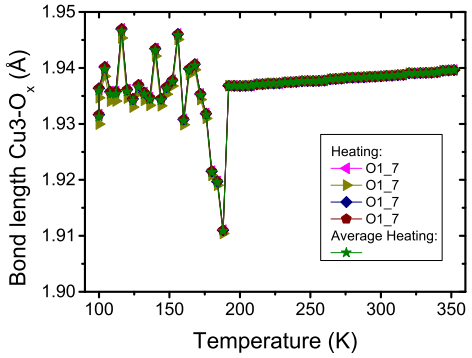

(c) Bond lengths Cu3-O

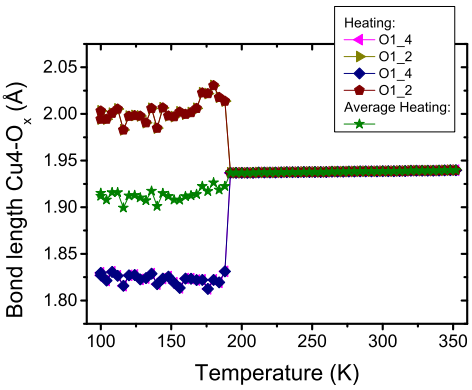

(d) Bond lengths Cu4-O

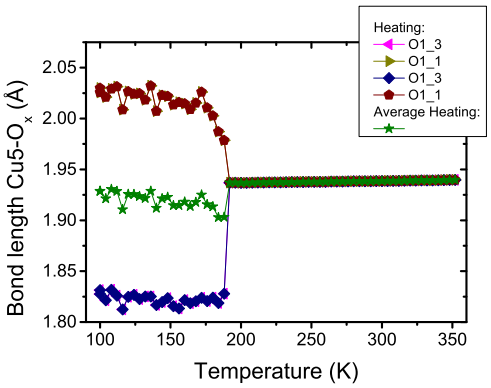

(e) Bond lengths Cu5-O

Figure 5.11: Temperature dependent bond lengths of the Cu coordination polyhedra in $BiCu_3Cr_4O_{12}$.

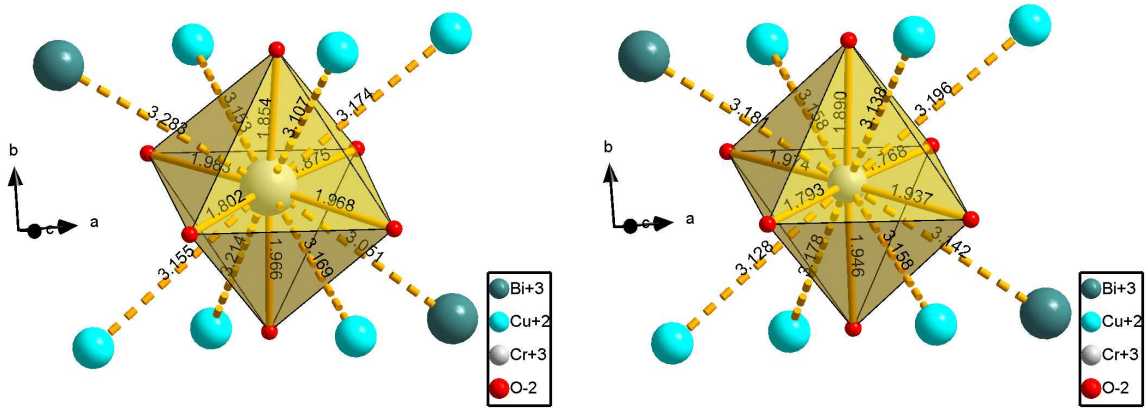

(a) Coord. sphere Cr1 (100K) **(b)** Coord. sphere Cr1 (188K)

Figure 5.12: Coordination spheres of the $Cr(1)O_6$ octahedron at temperatures of a) 100 K and b) 188 K in the $BiCu_3Cr_4O_{12}$ quadruple perovskite. Although it is not visible by bare eye, the octahedron at 188 K is much more distorted.

different groups. The first group is the group of the Cu1 square-planar coordination with site multiplicity 4 (see figure 5.11a)). For this coordination polyhedra an expansion of all bond lengths can be found by passing the critical transition point, which leads to an enlargement of the size of the coordination plane. An opposite behavior can be found for the Cu2 and Cu3 coordination polyhedra each with site multiplicity 2 (see figure 5.11b)+c)). Upon cooling, directly after the phase transition, the size of the coordination polyhedra is first decreasing until it relaxes over a range of 20 K to its previous size. The third group is built by the Cu4 and Cu5 coordination polyhedra with each site multiplicity 2 (see figures 5.11d)+e)). For these coordination polyhedra an elongation along one direction and a compression along the other direction can be observed.

Besides the investigation of the bond lengths, the distortion level of the different coordination polyhedra can also be investigated by calculating the shifts of the central cations away from the center of gravity of the corresponding coordination polyhedra. The shift of the Cr1-Cr3 and Bi cations along the monoclinic crystal axis away from the center of gravity of the corresponding coordination polyhedra is shown in figures 5.13a)-d), whereas the absolute shift/distance of these cations away from the center of gravity of the corresponding coordination polyhedra is shown in figures 5.13e)-f). From these figures it is clear, that the Cr2 and Cr3 cations are not shifted with respect to their center of gravity, in contrast to the Bi and Cr1 cations which show a quite large shift away from their center of gravity. Please note also that the shift of the Bi cation is approximately along a single crystallographic axis, whereas the Cr1 cation is moving along a body diagonal.

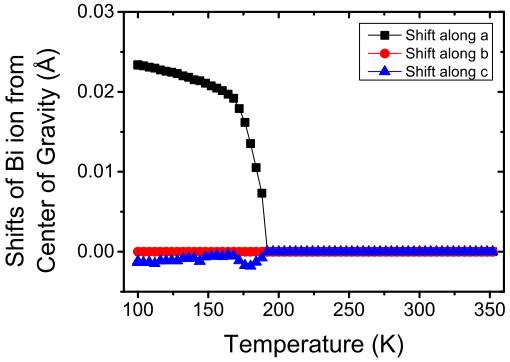

(a) Shift of Bi cation from BiO12-CoG

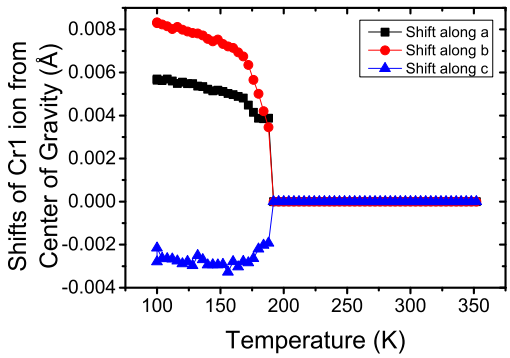

(b) Shift of Cr1 cation from CrO6-CoG

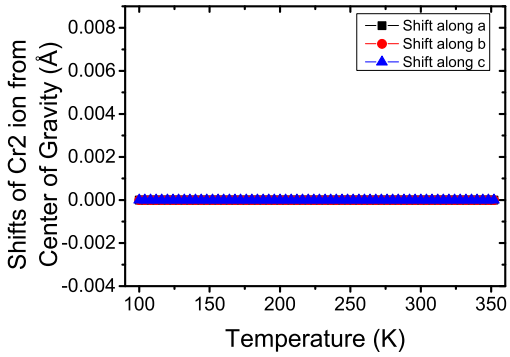

(c) Shift of Cr2 cation from CrO6-CoG

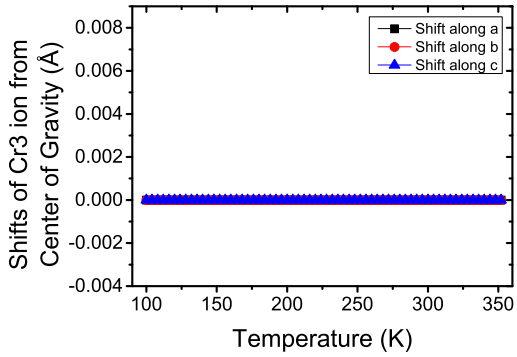

(d) Shift of Cr3 cation from CrO6-CoG

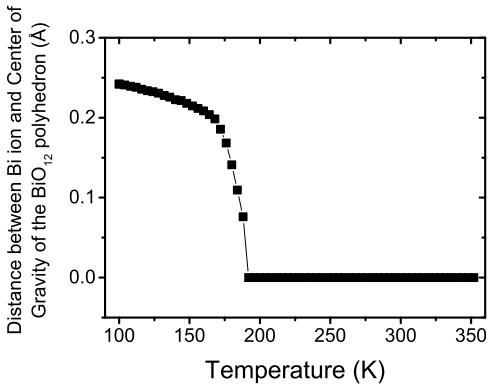

(e) Distance of Bi cation from BiO12-CoG

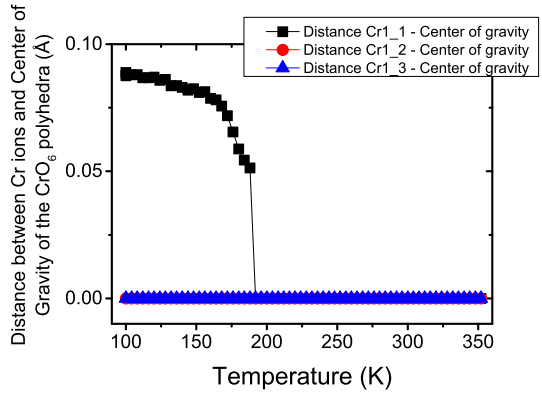

(f) Distance of Cr cations from CrO6-CoG

Figure 5.13: Temperature dependent shifts of the different cations (Cr1-3 and Bi) away from their center of gravity of the corresponding coordination polyhedra along the monoclinic crystal axis a)-d) in the $BiCu_3Cr_4O_{12}$ quadruple perovskite. e)-f) add up shifts away from the center of gravity of the corresponding coordination polyhedra.

5.4.4 Bond valence sum calculations

The temperature dependent bond valence sums (BVS) presented in figure 5.14 were calculated according to equations 5.4 and 5.5 [269], which are defined below.

$$V_i = \sum_j S_{ij} \tag{5.4}$$

where V_i is the bond valence sum of a certain cation i in its chemical environment and S_{ij} is a single bond valence which is empirically defined as

$$S_{ij} = e^{\frac{r_0 - r_ij}{b}} \tag{5.5}$$

where r_{ij} is the experimental determined bond length between an (oxygen) anion and a cation and r_0 is a tabulated bond valence parameter depending on the effective coordination number. The value of b in the denominator of the power of the exponential is empirically determined to 0.37 [269]. The tabulated bond valence parameters which were used for the calculations are $r_0 = 1.724$ for Cr^{3+} to O^{2-} valences [269], $r_0 = 1.756$ for Cr^{4+} to O^{2-} valences [246], $r_0 = 1.679$ for Cu^{2+} to O^{2-} valences [269] and $r_0 = 2.094$ for Bi^{3+} to O^{2-} valences [269].

As can be seen in figure 5.14, at room temperature, the value of 3.11 valence units (v.u.) of the Bi cation and the value of 1.98 v.u. of the Cu cation are very close to their ideal values of 3+ and 2+, respectively. In contrast, at room temperature, the BVS of Cr (which is calculated by the theoretical ratio of a mixed-valence state of 1:3 of Cr^{3+} and Cr^{4+} cations) with a value of 3.6 v.u. seems to be underestimated, as the theoretical BVS value of this mixed-valence Cr cation should be +3.75 v.u.. In general there are several possibilities to explain too low values of the observed BVS, of which the most likely is given here. For instance, if a partial substitution of B cations (B = Cr) by A' cations (A' = Cu) is assumed, than the effective BVS value is lowered[1]. In the case of the $BiCu_3Cr_4O_{12}$ quadruple perovskite this would mean that 8% Cu^{2+} cations should be present on the Cr site, which would lead to a theoretical BVS value of 3.61 v.u. which is almost in perfect agreement with the observed BVS value. However, the assumption of 8% Cu^{2+} on the Cr site must be also in agreement with the results of the Rietveld refinement. And indeed, if a Rietveld refinement of the room temperature synchrotron X-ray powder diffraction measurements is carried out with a ratio of 0.08:0.92 of Cu and Cr cations on the cubic Wyckoff position 8*c*, the refinement results are almost unaffected. The obtained parameters of such a refinement have values, which lie all within one estimated standard deviation as for a

1 The calculated values with 8% Cu^{2+} on the Cr site are shown in figure N.1 in the appendix. The difference of the models with and without Cu^{2+} is that marginal, so that the discussion of particular values even for the substituted model will be done by taking the values of the unsubstituted model presented in figure 5.14.

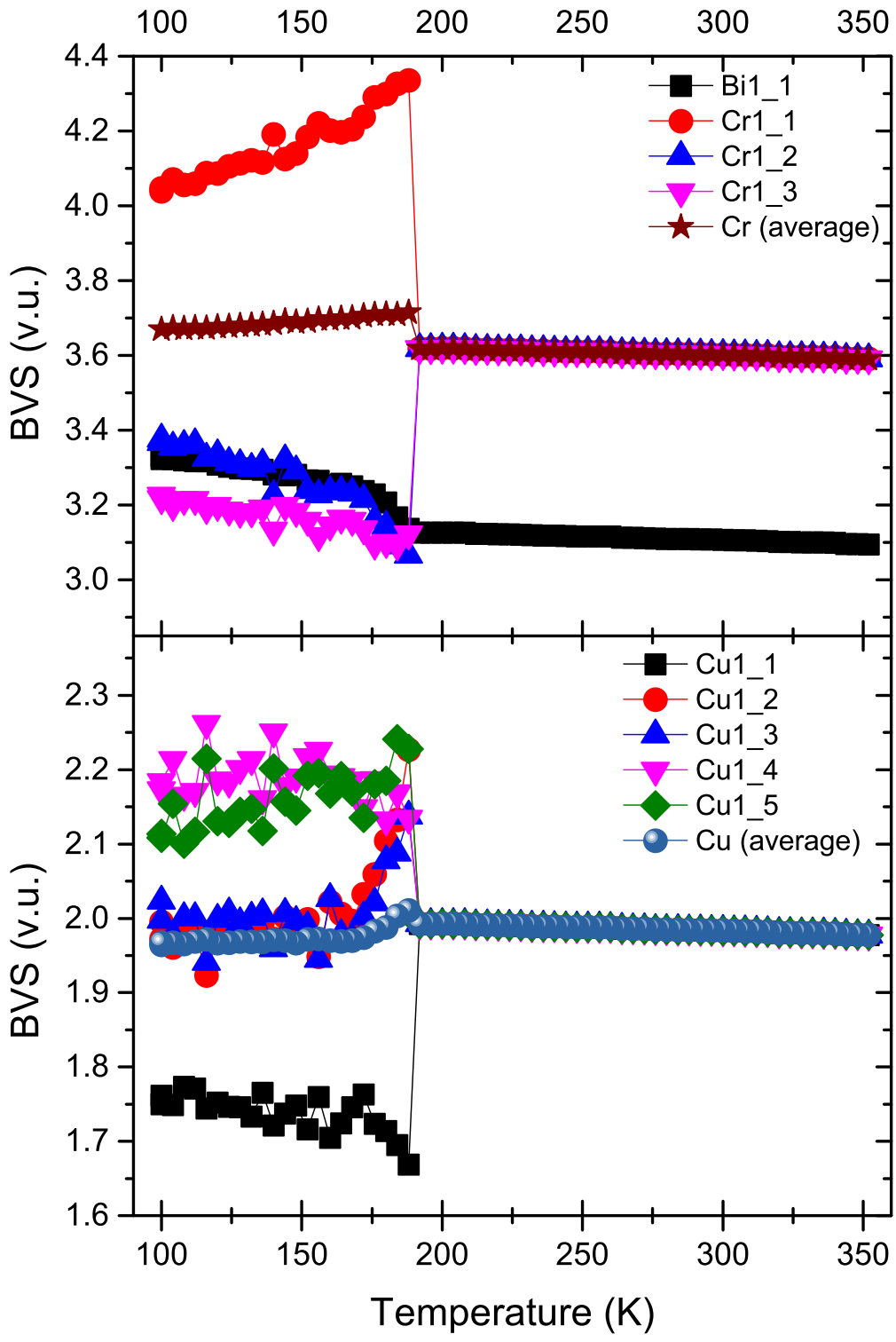

Figure 5.14: Temperature dependent bond valence sum calculations for all cations for the $BiCu_3Cr_4O_{12}$ quadruple perovskite. Detailed information about the calculation of the bond valence sums is given in the text.

refinement without Cu on the Cr site[1]. In addition, such a B-site substitution would also explain why only impurities of Cr_2O_3 and CrO are observed, but no impurities of Cu-compounds are found, although the synthesis was done with the correct stoichiometric ratio. Later it will be shown that the assumption of 8% Cu^{2+} on the Cr site will also give a better explanation of the observed saturated magnetization at low temperatures and high applied fields.

Below the transition temperature of 188 K, the BVS value of Cu splits into three arms, which can be explained by the distortion of the particular Cu coordination polyhedra (see also the behavior of the bond lengths of Cu in figure 5.11, which are also a measure for the distortion of the square-planar coordinated polyhedra). However, the average BVS value of all Cu cations in the low-temperature phase is still approximately 2+, thus an ISCT between the Cu and the Cr cations is rather unlikely. A similar distortion behavior as for the Cu cations can be found for the Bi cation. Below the critical temperature the BVS value of Bi starts to rise from approximately 3.1 v.u. to 3.3 v.u. at a temperature of 100 K. This behavior can be correlated with the bond lengths of the Bi cation to its coordinated oxygen anions (see figure 5.10a)) and also with the shift of the Bi cation away from its center of gravity of the corresponding coordination polyhedron (see figure 5.13a)+e)). To the same amount as the BiO_{12} icosahedron becomes distorted over the temperature by cooling, to the same amount the BVS value of the Bi cation is increasing. Intriguingly, this is a nice example to show how the empirical bond valence parameters r_0 are affected by the distortion of the corresponding coordination polyhedra (further literature about that phenomenon is given by Wang and Liebau [270]).

Besides the interesting behaviors of the BVS of the Bi and Cu cations, the behavior of the Cr cation leads to the most crucial part of the BVS investigations. Below the critical transition temperature of approximately 188 K, the unique BVS of Cr splits into three arms (due to the lowering of the symmetry and the splitting of the cubic Wyckoff position), where one arm jumps up to BVS values of approximately 4+ and the other two arms jump down to BVS values of approximately 3.5+. Therefore, the upper arm, which belongs to the Cr1 cation, is calculated with the corresponding bond valence parameters of a Cr^{4+} cation, whereas the two lower arms of the Cr2 and Cr3 cations are calculated with a ratio of 1:1 of Cr^{4+} and Cr^{3+} in order to keep the mean oxidation state of 3.75+. This implies that in summary the $BiCu_3Cr_4O_{12}$ quadruple perovskite undergoes a CD at the critical phase transition temperature, which ends up

1 The fact, that the refinement results are almost unaffected allows also the circumstance that all the refinements which were done above can be treated as there is no Cu^{2+} on the Cr-site. The reason for that is, that each refinement can not discriminate between the correct solution as both models have almost the exact same refinement minimum and therefore the results of both solutions will have nearly congruent error bars. This argument is also understandable if the difference in the scattering power of this atomic position is considered. A full occupation with Cr^{3+} cations means that 21 electrons contribute to the scattering power, whereas 8% Cu^{2+} on the Cr site gives a contribution of 21.48 electrons. For an X-ray diffraction experiment a difference in the scattering power of 0.48 electrons is not observable.

in a columnar checkerboard ordering of the Cr1 cation which has an oxidation state of 4+ and of the Cr2 and Cr3 cations which are in a mixed-valence state of 3.5+. Nevertheless, this a very simple model which is superimposed by other effects. For instance the observed BVS values of the Cr2 and Cr3 cations directly after the phase transition are too low (Cr2: 3.07 v.u. / Cr3: 3.13 v.u), although they are approaching values of 3.37 v.u. and 3.22 v.u. at a temperature of 100 K for the Cr2 and Cr3 cations, respectively, on further cooling. If the assumption of 8% Cu^{2+} on all Cr sites is valid, then a theoretical value of 3.38 v.u. can be calculated. This is in good agreement with the observed value for the Cr2 cation at 100 K, although this value is not perfectly reached by the BVS of the Cr3 cation at the same temperature (potentially this can be explained by the isotropic enlargement of the volume of the $Cr(3)O_6$ octahedron, which also leads to a decrease in the calculated BVS value). In contrast to the BVS of the Cr2 and Cr3 cations, the BVS value of the Cr1 cation shows a totally different behavior. For all temperatures below the critical phase transition temperature, the BVS value of the Cr1 cation is too high. An explanation for this behavior might be given by looking at the huge deformation which the $Cr(1)O_6$ octahedron undergoes directly after the phase transition upon cooling. Below 188 K the deformation of the $Cr(1)O_6$ octahedron has the largest value as can be estimated from the picture of its coordination polyhedron bond lengths in figure 5.10b). Although the bond length between the Bi cation and the oxygen O1_2 anion is further decreasing the bond length between the Bi cation and the oxygen O1_7 anion is increasing to a much larger extent giving rise to a reduction of the distortion of the $Cr(1)O_6$ octahedron. This reduction of the distortion explains also the trend of the BVS of the Cr1 cation as a reduced distortion leads to better BVS values. However the BVS value of Cr1 is still too high as the 8% Cu^{2+} on the Cr1 site should lead to a theoretical value of 3.84 v.u.. Possibly the high value at 100 K can still be attributed to the large distortion of the $Cr(1)O_6$ octahedron.

Howsoever, the reason for the large distortion of the $Cr(1)O_6$ octahedron can be explained by a visual inspection of the crystal structure over temperature. With a new simulation method for TOPAS, created by Etter and Dinnebier [271], it is possible to create video simulations for all temperature dependent results of the Rietveld refinements. With this visual inspection tool it is very convenient to see what happens within the crystal structure during the phase transition. If the simulation is started in the high temperature / high symmetry phase and then the crystal structure is cooled, it is easy to determine that the shift of the Bi cation in the low temperature / low symmetry phase forces a shift of the Cr1 cation, which causes the distortion of the corresponding $Cr(1)O_6$ octahedron.

Although the behavior of the different BVS is not easily explained, it seems that the $BiCu_3Cr_4O_{12}$ quadruple perovskite undergoes a typical CD phenomenon, which is quite similar to the one which occurs in the A-site ordered quadruple perovskite $NaMn_3Mn_4O_{12}$ [254], also in regard to the occurring distortions.

5.5 Measurements of the electric resistivity and magnetic susceptibility

In figure 5.15 the electric resistivity and the electric conductivity are shown, respectively. At a temperature of 300 K the electric resistivity (electric conductivity) is approximately $\rho \approx 5.2 \cdot 10^{-3} \Omega cm$ ($\sigma \approx 191.3\ \Omega^{-1} cm^{-1}$), which indicates that the $BiCu_3Cr_4O_{12}$ quadruple perovskite has a metallic behavior at room temperature. At a temperature of approximately 187 K (which is almost the same temperature as determined for the structural phase transition) the resistivity starts to increase until at approximately a temperature of 123 K a value of the resistivity of $\rho \approx 18.4 \cdot 10^{-3} \Omega cm$ is reached. On further cooling the electric resistivity starts to decrease until at a temperature of 2 K an electric resistivity (electric conductivity) of approximately $\rho \approx 13.1 \cdot 10^{-3} \Omega cm$ ($\sigma \approx 76.6\ \Omega^{-1} cm^{-1}$) is reached. Although there is a sharp increase below the structural transition point of 188 K, the $BiCu_3Cr_4O_{12}$ quadruple perovskite exhibits metallic conductivity in each phase and at all temperatures. The values of the temperature dependent electric resistivity/conductivity and the metallic behavior is comparable to other Cr-containing quadruple perovskites like $CaCu_3Cr_4O_{12}$ [258], $LaCu_3Cr_4O_{12}$ [246] and $YCu_3Cr_4O_{12}$ [246] (see also table 5.1).

The field-cooled (FC) measurement of the magnetic susceptibility shown in figure 5.16 exhibits a typical ferromagnetic behavior with a critical transition temperature which is the same one which is found for the electric resistivity and approximately the same one which is found for the structural phase transition. The paramagnetic region of the inverse susceptibility can be fitted with a Curie-Weiss law as it is given by the following equation:

$$\chi_m = \frac{C_{CW}}{T - T_{CW}} \quad . \tag{5.6}$$

In this equation the magnetic susceptibility is given by $\chi_m = \frac{\partial M}{\partial H}$, where H is the applied magnetic field strength and M is the magnetization of the material. The constant C_{CW} (sometimes also C_W) is the Curie constant, T is the temperature and T_c (sometimes also Θ_W) is the paramagnetic Curie-Weiss temperature (some authors prefer the term "Weiss temperature" or "Weiss constant").
The values which can be obtained by the fit with the Curie-Weiss law are a Curie constant of $C_{CW} = 2.38(1) \frac{emu \cdot K}{Mol}$ and a Curie-Weiss temperature of $T_{CW} = 148.2(2) K$. As other Cr-containing quadruple perovskites show a metallic Pauli paramagnetic behavior [246, 258] and the electric resistivity measurements from above suggests also a metallic behavior in the high-temperature phase, a Curie-Weiss law with an additional constant for the Pauli paramagnetism was tested. A fit with such a modified Curie-Weiss law was not successful, suggesting that no Pauli paramagnetic behavior in the high-temperature phase can be observed.

The field dependent isothermal magnetization at a temperature of 5 K and field strengths of H = -5 T to H = 5 T is presented in figure 5.17. From this figure it is obvious that the $BiCu_3Cr_4O_{12}$ quadruple perovskite shows no hysteresis effect but an

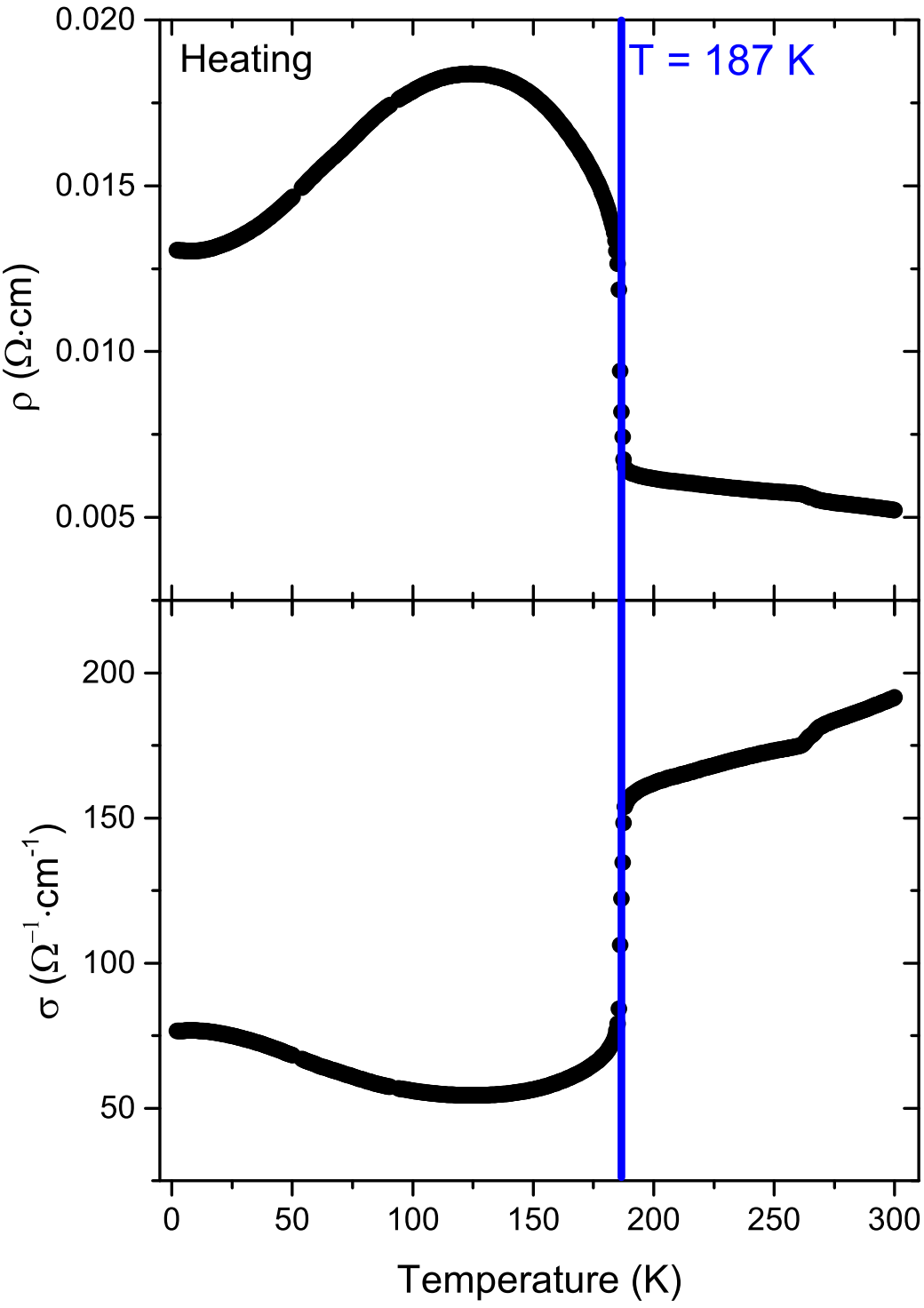

Figure 5.15: Temperature dependent electric resistivity of the $BiCu_3Cr_4O_{12}$ quadruple perovskite (upon heating). At 187 K there is a sharp increase in the resistivity, however, the values of the electric resistivity and the electric conductivity proves that $BiCu_3Cr_4O_{12}$ exhibits metallic behavior over the entire investigated temperature range.

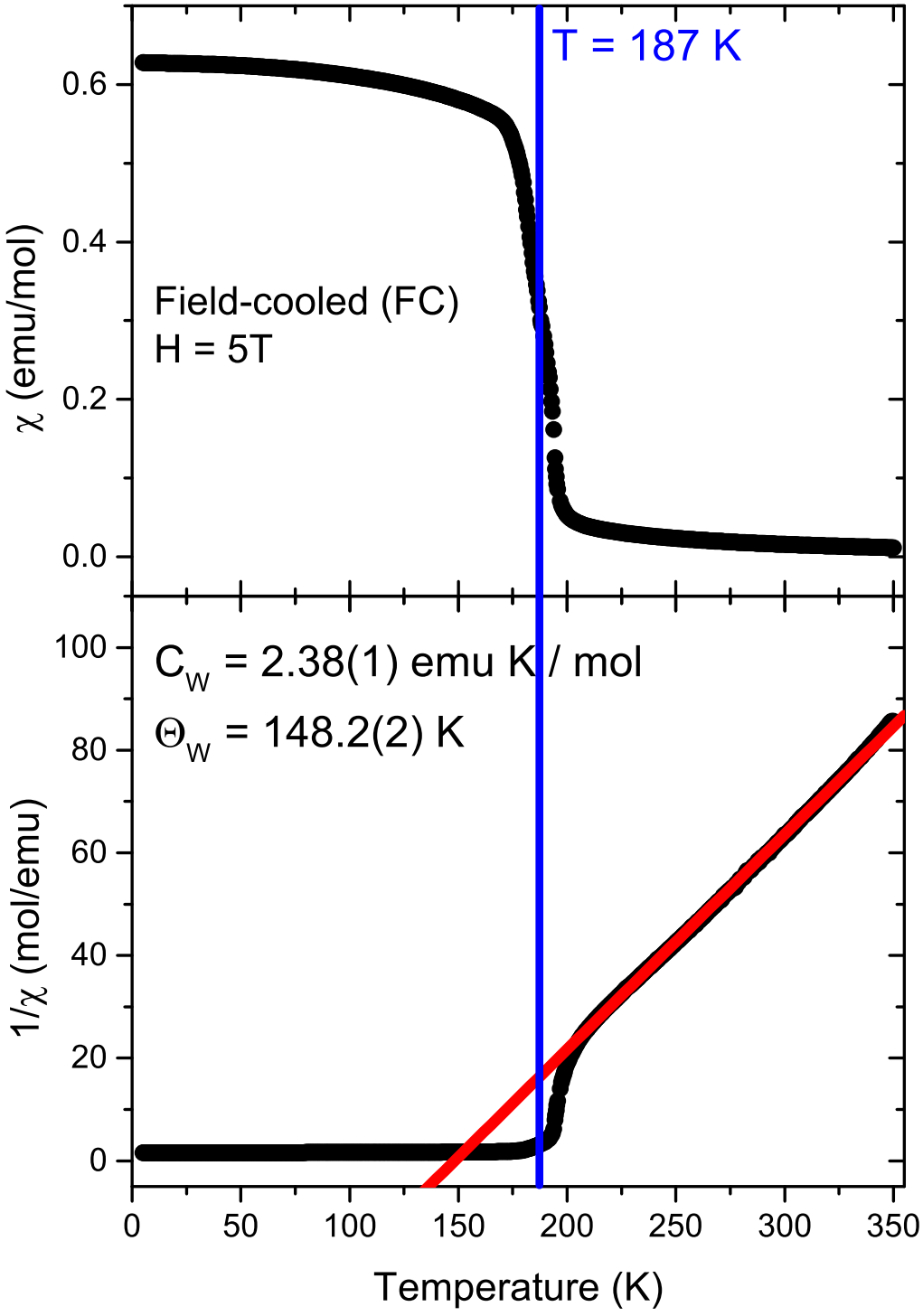

Figure 5.16: Upper picture: Field-cooled measurement of the temperature dependent magnetic susceptibility of the $BiCu_3Cr_4O_{12}$ quadruple perovskite at a field of H = 5 T. At 187 K the magnetic susceptibility increases showing a typical ferromagnetic behavior. Lower picture: inverse susceptibility. The paramagnetic region of the inverse susceptibility was fitted by a Curie-Weiss law.

early magnetic saturation at a field strength of H = ± 1.5 T. The maximum magnetization in Bohr magneton units is approximately M ≈ 5.63 μ_B.
In general, the magnetic saturation can be calculated approximately with the following simple equation (this equation can be derived by determining the low-temperature/high-field limit of the quantum mechanical treated paramagnetic magnetization):

$$M_S = g_S \cdot \sum_i S_i \quad , \tag{5.7}$$

where M_S is the magnetic saturation in Bohr magnetons, g_S is the electron spin g-factor (g stands for gyromagnetic) and its value is approximately ≈ 2 for a pure electron spin angular momentum without orbital angular momentum and S_i is the value of a single spin which contributes to the magnetic saturation.
If a ferromagnetic ordering between the Cu^{2+} ($3d^9 4s^0 \rightarrow S = 1/2$) and $Cr^{3.75+}$ [1] (Cr^{3+}: $3d^3 4s^0 \rightarrow S = 3/2$, Cr^{4+}: $3d^2 4s^0 \rightarrow S = 1$) magnetic moments is considered, a total magnetic saturation of 12 μ_B is obtained ($M_{S,\mathrm{FM}} = 2 \cdot (3 \cdot 1/2 + 1 \cdot 3/2 + 3 \cdot 1)$). This value is in contrast to the experimentally measured saturation magnetization.
Another possibility for the ordering of the magnetic moments is that the magnetic moments of the Cu cations are antiparallel aligned to the magnetic moments of the Cr cations. This would lead to a ferrimagnetic ordering and the calculated magnetic saturation for such a model is 6 μ_B ($M_{S,\mathrm{FiM}} = 2 \cdot (-3 \cdot 1/2 + 1 \cdot 3/2 + 3 \cdot 1)$). This calculated value of the magnetic saturation is in much better agreement with the experimentally observed magnetic saturation, for which reason the $BiCu_3Cr_4O_{12}$ quadruple perovskite is considered to be a ferrimagnet in its low-temperature phase. The difference between the theoretical and the observed value can be potentially attributed to the Cu^{2+} substitution of the Cr site. If it is assumed that the magnetic moments of the 8 % Cu^{2+} cations on the Cr site are parallel aligned to the magnetic moments of the Cr cations, a theoretical saturated magnetization of 5.6 μ_B can be obtained. This is in almost perfect agreement with the experimentally observed value of M ≈ 5.63 μ_B.
In general, the finding that $BiCu_3Cr_4O_{12}$ is ferrimagnetic stands in contrast to other Cr-containing quadruple perovskites as they show only Pauli paramagnetic behavior in all temperature dependent phases [246, 258] (see also table 5.1). On the other hand this result of a ferrimagnetic quadruple perovskite which undergoes a charge disproportionation is similar to the behavior in the charge disproportionated Fe analogues (see also table 5.1).

1 An average oxidation state of 3.75+ for the Cr cations can also be assumed in the low temperature phase, as suggested by the calculated average bond valence sum of all Cr cations which has a value close to 3.75+ (see figure 5.14).

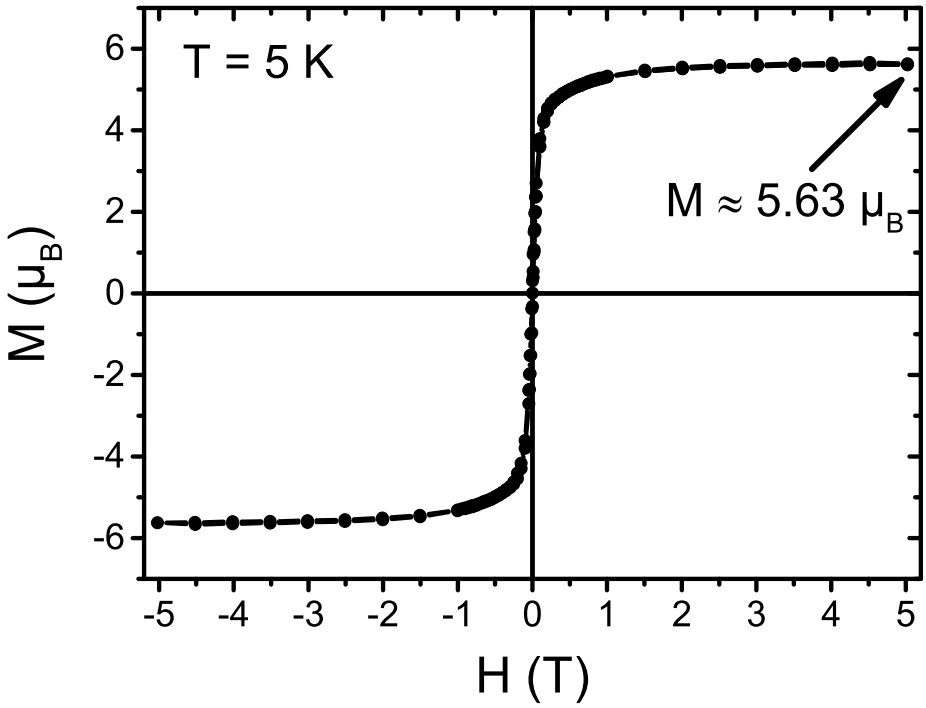

Figure 5.17: Field dependent isothermal magnetization at a temperature of 5 K and field strengths from H = -5 T to H = 5 T of the $BiCu_3Cr_4O_{12}$ quadruple perovskite.

5.6 Conclusion

Investigations of synchrotron X-ray powder diffraction measurements of $BiCu_3Cr_4O_{12}$ A-site ordered quadruple perovskite revealed that the compound has a typical cubic crystal structure at room temperature (space group $Im\bar{3}$), identical to all other A-site ordered quadruple perovskites listed in table 5.1. Below a temperature of 188 K the quadruple perovskite undergoes a structural weak first order phase transition to a monoclinic crystal structure (space group $C2/m$), which was previously only observed for $NaMn_3Mn_4O_{12}$ [254]. In a temperature range of 20 K between 168 K and 188 K a large negative thermal expansion of the volume with a volume expansion coefficient of $\alpha_V = -111(2) \cdot 10^{-6}$ K^{-1} is observed upon cooling, which is two times higher than the value which was observed for the quadruple perovskite $SrCu_3Fe_4O_{12}$ [233]. Extensive structural investigations in the low-temperature phase revealed that most of the coordination polyhedra around the cations are heavily distorted, which also influences the numerical results of the bond valence sum calculations. However, the bond valence sum calculations over the entire temperature range proofed, that the $BiCu_3Cr_4O_{12}$ quadruple perovskite shows a charge disproportionation phenomenon of the Cr cations on the B-site, which occurs simultaneously with the structural phase transition: $Bi^{3+}Cu_3^{2+}Cr_4^{3.75+}O_{12}^{2-} \rightarrow Bi^{3+}Cu_3^{2+}Cr_1^{3+}Cr_3^{4+}O_{12}^{2-}$. The distortions of the co-

ordination polyhedra and also the charge disproportionation seem to be very similar to the isostructural $NaMn_3Mn_4O_{12}$ quadruple perovskite [254], except for the charge disordered Wyckoff $4e$ and $4f$ sites.
Measurements of the electric resistivity/conductivity showed that this compound exhibits metallic behavior in both structural phases, although the resistivity is slightly increasing at the critical transition temperature. Measurements of the magnetic susceptibility illustrated, that this compound shows ferromagnetic behavior, which was further specified as ferrimagnetic behavior by the measurement of the field dependent isothermal magnetization.
For the BVS calculations as well as for the obtained saturated magnetization at low temperatures and high applied magnetic fields it could be shown that an assumption of 8 % Cu^{2+} on the Cr site leads to much better agreement of theoretically calculated and experimentally observed values. Furthermore it was also shown that this assumption of 8 % Cu^{2+} on the Cr site does not influence the results which were obtained by the Rietveld refinement of the synchrotron X-ray powder diffraction data.
Concerning the multiferroic properties, $BiCu_3Cr_4O_{12}$ seems to be a single-ferroic material as only a ferrimagnetic phase transition could be observed. From the centrosymmetric / non-polar space groups in the high- and low-temperature phase it can be excluded that this quadruple perovskite shows proper ferroelectricity. As the synchrotron X-ray powder diffraction measurements were only done down to a temperature of 100 K, another structural phase transition to a polar space group below 100 K cannot be fully excluded. However, the measurements of the electric resistivity and the magnetic susceptibility do not give a hint on a further structural phase transition below 100 K, so it is very unlikely that proper ferroelectricity occurs at lower temperatures. Other types of improper ferroelectricity are also unlikely as a collinear ferrimagnetic ordering does not break the inversion symmetry of the crystal structure and therefore a magnetically driven ferroelectricity is hindered. Also geometrical frustration combined with charge ordering can be excluded as mechanism for ferroelectricity, as the observed charge disproportionation leads to a columnar checkerboard charge ordering and no geometrical frustration of the corresponding sites is present. The only mechanism which can not be fully excluded at lower temperature is a lone pair driven ferroelectricity, but as already mentioned, the measurement of the electric resistivity and the magnetic susceptibility do not support another phase transition in this temperature regime.

Summary

The investigation of the crystal and magnetic structures of potential multiferroic perovskites by synchrotron X-ray and neutron powder diffraction is a first step in order to reveal ferroic orders. Moreover, the determined symmetries of the crystal and magnetic structures can give a hint on probable coupling effects between them, as it is the case of the $BiFeO_3$ perovskite, where the spin cycloid suppresses a linear magnetoelectric coupling between the ferroelectric and the antiferromagnetic order [3, 4, 8, 9] (see also chapter 1). In order to investigate the crystal and partially magnetic structures of interesting perovskites with possible multiferrroic behavior, numerous temperature or pressure dependent *in situ* synchrotron X-ray and neutron powder diffraction measurements of three different perovskite systems were carried out.

The first investigated compounds were the $Bi_{1-x}Sr_xFeO_{3-\delta}$ perovskites, which build a solid solution series between the two end members $BiFeO_3$ and $SrFeO_3$. A detailed Rietveld refinement study from synchrotron X-ray and high resolution neutron powder diffraction measurements of the $Bi_{1-x}Sr_xFeO_{3-\delta}$ perovskites (with x = 0..0.5) at room temperature revealed, that the crystal structure above a composition of $x \geq 0.2$ must be regarded as cubic with a centrosymmetric space group $Pm\bar{3}m$. This centrosymmetric space group already forbids the possibility of a proper ferroelectricity, which is in contrast to the $BiFeO_3$ end member (non-centrosymmetric polar space group $R3c$), where proper ferroelectricity is driven by the stereochemically active Bi $6s^2$ "lone pair". The analysis of the temperature dependent high resolution neutron powder diffraction data sets showed, that the composition level not only influences the crystal structure but also the magnetic structures. From the obtained neutron powder data of the $BiFeO_3$ perovskite, for instance, the spin cycloid could be observed due to a slight asymmetry of the magnetic Bragg reflections. Interestingly this asymmetry vanishes above a composition of $x \geq 0.2$ and a pure G-type antiferromagnetic ordering of the magnetic moments is established. It was found by Rietveld refinements with magnetic symmetry modes, that this magnetic ordering can be described by a tetragonal magnetic Shubnikov group with label I_c4/mcm (140.550) in the BNS setting, where the magnetic unit cell is 4 times larger than the crystallographic unit cell. The determination of the critical Néel temperatures from the refined temperature

dependent magnetic moments[1] revealed, that the antiferromagnetic to paramagnetic phase transitions of the $Bi_{1-x}Sr_xFeO_{3-\delta}$ perovskites (with x = 0, 0.2, 0.3 and 0.5) occur in a narrow temperature range between 650 and 660 K. Interestingly, the determination of the critical Néel temperatures of the $Bi_{1-x}Sr_xFeO_{3-\delta}$ perovskites (with x = 0.2, 0.3 and 0.5) from differential scanning calorimetry measurements gave elevated values, which can possibly be attributed to different oxygen environmental conditions during the measurements. Although the underlying quantitative dependency between oxygen vacancies and magnetic properties is not yet clear, it can be stated that an increase in oxygen vacancies in the crystal structure certainly leads to a reduction of the critical Néel temperature [172].

Investigations by Rietveld refinements of the high pressure synchrotron X-ray powder diffraction data of the $LaFeO_3$ orthoferrite perovskite confirmed two phase transitions up to a pressure of 50 GPa along the room temperature isotherm. The first phase transition at approximately 20.5(6) GPa was identified to be a structural second order phase transition from the lower centrosymmetric space group *Pbnm* to the higher centrosymmetric space group *Ibmm*. Applying different crystallographic approaches, like rigid bodies/constrainable atomic groups, symmetry modes and a recently developed approach with rotational symmetry modes of a rigid body/constrainable atomic group, for the modeling of the atomic coordinates in sequential Rietveld refinements, it could be demonstrated that this second order phase transition is mainly driven by the rotation of the FeO_6 octahedron and secondarily by a shift of the lanthanum cation. This is in contrast to the isostructural first order phase transition at approximately 38 GPa, which is driven by a pressure induced high-spin ($S = \frac{5}{2}$) to low-spin ($S = \frac{1}{2}$) transition of the Fe^{3+} cation. Interestingly, all observed phase transitions occur between centrosymmetric crystal structures, which instantly prohibits the occurrence of proper ferroelectricity. However, further investigation techniques are required in order to investigate the dependency between pressure and the at ambient conditions reported ferroelasticity and improper ferroelectricity.
In addition to the investigation of the different phase transitions in $LaFeO_3$, sequential and parametric Rietveld refinements were performed in order to determine the equation of state (EoS) parameters for the volume and the lattice parameters below the hydrostatic limit. Using a Murnaghan EoS for the pressure dependent volume of the $LaFeO_3$ perovskite, a bulk modulus of $B_0 = 172(2)$ GPa, a first pressure derivative of the bulk modulus of $B_0' = 4.3(3)$ and a volume at ambient conditions of $V_0 = 242.87(1)$ Å^3 could be obtained. Corresponding values for the lattice parameters were determined by an adapted inverted Murnaghan EoS as well as by a newly developed adpated inverted third order Vinet EoS approximation and the determined values were in quite good accordance with each other.

1 The values of the magnetic moments for the $Bi_{1-x}Sr_xFeO_{3-\delta}$ perovskites (with x = 0.2, 0.3 and 0.5) were determined by the refinement of amplitudes of magnetic symmetry modes, whereas the magnetic moments for the $BiFeO_3$ perovskite were directly determined from the refinement of the complex magnetic Fourier coefficients.

The third and last investigated compound was recently synthesized and belongs to the class of the quadruple perovskites. Synchrotron X-ray powder diffraction patterns of this $BiCu_3Cr_4O_{12}$ quadruple perovskite exhibited, that it possess a centrosymmetric crystal structure at room temperature, which can be described in the cubic space group $Im\bar{3}$. Rietveld refinements of temperature dependent synchrotron X-ray powder diffraction data sets showed, that a structural reversible weak first order phase transition from a cubic to a monoclinic crystal structure occurs upon cooling at approximately 188 K. The symmetry of this monoclinic crystal structure was determined to be centrosymmetric in space group $C2/m$ with a unit cell that is twice the unit cell of the cubic crystal structure at room temperature. Detailed investigations of the atomic coordinates and the different cation coordination polyhedra in the monoclinic phase revealed, that these polyhedra exhibit a high degree of distortion. Moreover, it could be shown from bond valence sum calculations that this cubic to monoclinic structural phase transition is accompanied by a charge disproportionation of the chromium cations into equal amounts of $Cr^{3.5+}$ and Cr^{4+}. Besides the charge disproportionation also a charge ordering of the chromium cations can be observed, which exhibits a checkerboard ordering of $Cr^{3.5+}$ and Cr^{4+} and a columnar ordering along the crystallographic *b*-axis. However, the structural investigations showed that proper ferroelectricity is forbidden by symmetry.
Besides the charge disproportionation and the charge ordering, which accompanies the structural phase transition, also a ferrimagnetic ordering of the magnetic moments of the copper and chromium cations, which was determined from magnetization and magnetic susceptibility measurement, can be simultaneously observed at the critical temperature. In contrast to the structural, magnetic and charge changes, the measured electric resistivity does not change over the entire investigated temperature range.
However, with respect to the possible multiferroic properties of the $BiCu_3Cr_4O_{12}$ quadruple perovskite, proper ferroelecticity cannot occur in the investigated temperature range, as was already mentioned above. Nevertheless the quadruple perovskites are certainly an interesting material class in order to search for magnetoelectric coupling effects which are connected with proper or improper ferroelectricity and which therefore allow their usage in industrial applications.

Zusammenfassung

Die Untersuchung der Kristall- und Magnetstrukturen möglicher multiferroischer Perowskite mittels Synchrotron Röngten- und Neutronenpulverdiffraktion ist ein erster Schritt um ferroische Ordnungen aufzudecken. Darüber hinaus können die ermittelten Kristall- und Magnetstruktursymmetrien Hinweise auf mögliche Kopplungsmechanismen entsprechender ferroischer Ordnungen geben, wie es zum Beispiel der Fall für den $BiFeO_3$ Perowskit ist, bei dem der vorhandene Spinzykloid eine lineare magnetoelektrische Kopplung zwischen ferroelektrischer und ferromagnetischer Ordnung unterdrückt [3, 4, 8, 9] (siehe auch Kapitel 1). Um die Kristall- und Magnetstrukturen interessanter Perowskite mit möglichen multiferroischen Verhalten zu untersuchen, wurden zahlreichen temperatur- und druckabhängige *in situ* Synchrotronröntgen- und Neutronenpulverdiffraktionsmessungen an drei verschiedenen Perowskitsystemen durchgeführt.

Die zuerst untersuchten Verbindungen waren die $Bi_{1-x}Sr_xFeO_{3-\delta}$ Perowskite, welche eine Mischkristallreihe mit den Engliedern $BiFeO_3$ und $SrFeO_3$ ausbilden. Eine detaillierte Rietveldverfeinerungsstudie von Synchrotronröntgen- und hochauflösenden Neutronenpulverdiffraktionsmessungen der $Bi_{1-x}Sr_xFeO_{3-\delta}$ Perowskite (mit x = 0 bis x = 0.5) bei Raumtemperatur ergab, dass die Kristallstruktur oberhalb einer Komposition von $x \geq 0.2$ als kubisch mit der zentrosymmetrischen Raumgruppe $Pm\bar{3}m$ angesehen werden muss. Dabei verbietet diese zentrosymmetrische Raumgruppe bereits die Möglichkeit eigentlicher Ferroelektrizität, was im Gegensatz zum $BiFeO_3$ Endglied (nicht-zentrosymmetrische polare Raumgruppe $R3c$) steht, bei dem eigentliche Ferroelektrizität aufgrund des stereochemisch aktiven Bi $6s^2$ "lone pair" gegeben ist. Die Analyse der temperaturabhängigen hochauflösenden Neutronenpulverdiffraktionsdatensätzen zeigte, dass der Kompositionsanteil nicht nur die Kristallstruktur sondern auch die magnetische Struktur beeinflusst. Zum Beispiel kann aus den gemessenen Neutronenpulverdaten des $BiFeO_3$ Perowskits der Spinzykloid aufgrund einer kleinen Asymmetrie der magnetischen Braggreflexe beobachtet werden. Interessanterweise verschwindet diese Asymmetrie oberhalb einer Komposition von $x \geq 0.2$ aber und eine reine G-Typ antiferromagnetische Anordnung der magnetischen Momente wird etabliert. Mit Hilfe der Rietveldverfeinerung mit magnetischen Symmetriemoden konnte gezeigt werden, dass diese magnetische Ordnung als tetragonale magnetische Shubnikov Gruppe mit der Bezeichnung I_c4/mcm (140.550) im BNS Setting beschrieben werden kann, wobei die magnetische Einheitszelle die vierfache Größe der kristallo-

graphischen Einheitszelle aufweist. Die Bestimmung der kritischen Néeltemperatur aus den verfeinerten temperaturabhängigen magnetischen Momenten[1] zeigte, dass der antiferromagnetische zu paramagnetische Phasenübergang der $Bi_{1-x}Sr_xFeO_{3-\delta}$ Perowskite (mit x = 0, 0.2, 0.3 und 0.5) in einem schmalen Temperaturband zwischen 650 K und 660 K zu finden ist. Interessanterweise ergab die Bestimmung der kritischen Néeltemperatur der $Bi_{1-x}Sr_xFeO_{3-\delta}$ Perowskite (mit x = 0.2, 0.3 und 0.5) durch die dynamische Differenzkalorimetrie erhöhte Werte, was womöglich auf die unterschiedliche Sauerstoffumgebungsbedingungen während der Messungen zurückgeführt werden kann. Obwohl die zugrundeliegende Abhängigkeit zwischen Sauerstoffleerstellen und magnetischen Eigenschaften noch nicht ganz klar ist, kann gesagt werden, dass der Anstieg an Sauerstoffleerstellen in der Kristallstruktur sicherlich zu einer Reduktion der kritischen Néeltemperatur führt [172].

Untersuchungen des $LaFeO_3$ Orthoferrit Perowskit durch Rietveldverfeinerungen von Hochdrucksynchrotronröntgenpulverdiffraktionsdaten offenbarten, dass zwei Phasenübergänge bis zu einem Druck von 50 GPa entlang der Raumtemperaturisothermen beobachtet werden können. Dabei wurde der erste Phasenübergang bei ungefähr 20.5(6) GPa als struktureller Phasenübergang zweiter Ordnung identifiziert, der einen Übergang von der niedrigeren zentrosymmetrischen Raumgruppe *Pbnm* zu der höheren zentrosymmetrischen Raumgruppe *Ibmm* darstellt. Unter Anwendung verschiedener kristallographischer Ansätze zur Modellierung der Atomkoordinaten in sequentiellen Rietveldverfeinerungen, wie den starren Körpern/verschränkten atomarer Gruppen, den Symmetriemoden und dem erst kürzlich entwickelten Ansatz der Rotationssymmetriemoden starrer Körper/verschränkter atomarer Gruppen, konnte gezeigt werden, dass dieser Phasenübergang zweiter Ordnung hauptsächlich von der Rotation des FeO_6 Oktaeders und sekundär von der Verschiebung des Lanthankations getragen wird. Dies steht im Gegensatz zu dem isostrukturellen Phasenübergang erster Ordnung bei ungefähr 38 GPa, welcher durch den druckinduzierten high-spin ($S = \frac{5}{2}$) to low-spin ($S = \frac{1}{2}$) Übergang des Fe^{3+} Kations getragen wird. Interessanterweise treten alle beobachteten Phasenübergänge zwischen zentrosymmetrischen Kristallstrukturen auf, welche instantan das Auftreten eigentlicher Ferroelektrizität verhindern. Allerdings wurden unter Umgebungsbedingungen Ferroelasitizität und uneigentliche Ferroelektrizität beobachtet, so dass weitere Untersuchungsmethoden von Nöten sind, um die Druckabhängigkeit dieser ferroischen Ordnungen aufzuklären.
Zusätzlich zu den untersuchten, in $LaFeO_3$ auftretenden, Phasenübergängen wurden sequentielle und parametrische Rietveldverfeinerungen durchgeführt, mit dem Hintergrund die Parameter der Zustandsgleichungen (EoS) für das Volumen und für die Gitterparameter unterhalb des hydrostatischen Limits zu bestimmen. Unter Verwendung einer Murnaghan EoS für das druckabhängige Volumen konnten folgende Werte

1 Die Werte der magnetischen Momente der $Bi_{1-x}Sr_xFeO_{3-\delta}$ Perowskite (mit x = 0.2, 0.3 and 0.5) wurden durch die Verfeinerung der Amplituden der magnetischen Symmetriemoden bestimmt, wohingegen die magnetischen Momente des $BiFeO_3$ Perowskits direkt aus der Verfeinerung der komplexen magnetischen Fourierkoeffizienten bestimmt wurden.

für den $LaFeO_3$ Perowskit bestimmt werden: Kompressionsmodul $B_0 = 172(2)$ GPa, erste Ableitung des Kompressionsmoduls nach dem Druck $B_0' = 4.3(3)$ und Volumen bei Umgebungsbedingungen $V_0 = 242.87(1)$ Å^3. Entsprechende Werte für die Gitterparameter wurden mittels einer adaptierten invertierten Murnaghan EoS sowie mit einer adaptierten invertierten und approximierten Vinet EoS dritter Ordnung bestimmt, wobei die bestimmten Werte eine gute Übereinstimmung aufwiesen.

Die dritte und letzte untersuchte Verbindung wurde erst kürzlich synthetisiert und gehört zu der Klasse der Quadrupelperowskite. Synchrotronröntgenpulverdiffraktionsbilder des $BiCu_3Cr_4O_{12}$ Quadrupelperowskits offenbarten, dass dieser eine zentrosymmetrische Kristallstruktur bei Raumtemperatur besitzt, welche mit der kubischen Raumgruppe $Im\bar{3}$ beschrieben werden kann. Rietveldverfeinerungen der temperaturabhängigen Synchrotronröntgenpulverdiffraktionsdatensätze zeigten, dass beim Abkühlen bei ungefähr 188 K ein strukturell reversibler Phasenübergang schwacher erster Ordnung von einer kubischen zu einer monoklinen Kristallstruktur auftritt. Die Symmetrie dieser monoklinen Kristallstruktur konnte mit der zentrosymmetrischen Raumgruppe $C2/m$ beschrieben werden, wobei die monokline Einheitszelle die zweifache Größe der kubischen Einheitszelle bei Raumtemperatur besitzt. Detaillierte Untersuchungen der Atomkoordinaten und der verschiedenen Kationenkoordinationspolyeder in der mononklinen Phase ergaben, dass die Polyeder Verzerrungen hohen Grades aufweisen. Mehr noch, es konnte mittels Bindungsvalenzsummenberechnungen gezeigt werden, dass diese strukturelle kubische zu monokline Phasenumwandlung von einer Ladungsdisproportionierung der Chromkationen in gleiche Anteile von $Cr^{3.5+}$ und Cr^{4+} begleitet wird. Neben dieser Ladungsdisproportionierung kann zudem eine Ladungsordnung der Chromkationen beobachtet werden, welche ein Schachbrettmuster der $Cr^{3.5+}$ und Cr^{4+} Kationen aufweist, welches in Säulen entlang der kristallographischen *b*-Achse angeordnet ist. Wie dem auch sei, die strukturellen Untersuchungen belegen, dass eigentliche Ferroelektrizität durch die Symmetrie verboten ist.
Neben der Ladungsdisproportionierung und der Ladungsordnung, welche den strukturelle Phasenübergang begleiten, kann simultan bei der kritischen Temperatur, durch Magnetisierungs- und magnetische Suszeptibilitätsmessungen, eine ferrimagnetische Ordnung der magnetischen Momente der Kupfer- und Chromkationen beobachtet werden. Im Gegensatz zu den strukturellen, magnetischen und Ladungsänderungen weißt die elektrische Widerstandsmessung allerdings im gesamten untersuchten Temperaturbereich keine Änderung auf.
Wie bereits oben erwähnt zeigt sich, dass in Bezug auf die möglichen multiferroischen Eigenschaften des $BiCu_3Cr_4O_{12}$ Quadrupelperowskit festgestellt werden kann, dass eigentliche Ferroelektrizität im untersuchten Temperaturbereich nicht auftreten kann. Nichtsdestotrotz sind die Quadrupelperowskite mit Sicherheit eine interessante Materialklasse um nach magnetoelektrischen Kopplungseffekten zu suchen, die mit eigentlicher oder uneigentlicher Ferroelektrizität verbunden sind und welche sich daher in industriellen Anwendungen verwenden lassen.

APPENDIX A

Calculation of the magnetic moments with general complex Fourier coefficients

The first part of equation 2.43 in subsection 2.4.1.1 gives the full description of the magnetic moment configuration by the general complex Fourier coefficients:

$$\vec{m}_{lj} = \sum_{\vec{k}} \frac{1}{2} \cdot \left(\vec{S}_{\vec{k}j} + \vec{S}^{*}_{-\vec{k}j} \right) \cdot e^{-2 \cdot \pi \cdot i \cdot \vec{k}_{\pm} \cdot \vec{R}_l} \quad , \tag{A.1}$$

where $\vec{S}_{\vec{k}j}$ is given by:

$$\vec{S}_{\vec{k}j} = \vec{R}_{\vec{k}j} + i \cdot \vec{I}_{\vec{k}j} \cdot e^{-2 \cdot \pi \cdot i \cdot \Phi_{\vec{k}j}} \quad . \tag{A.2}$$

Using equation A.1 and putting in A.2 gives:

$$\vec{m}_{lj} = \sum_{\vec{k}} \frac{1}{2} \cdot \left[\left(\vec{R}_{\vec{k}j} + i \cdot \vec{I}_{\vec{k}j} \cdot e^{-2 \cdot \pi \cdot i \cdot \Phi_{\vec{k}j}} \right) + \left(\vec{R}_{\vec{k}j} - i \cdot \vec{I}_{\vec{k}j} \cdot e^{2 \cdot \pi \cdot i \cdot \Phi_{\vec{k}j}} \right) \right] \cdot e^{-2 \cdot \pi \cdot i \cdot \vec{k} \cdot \vec{R}_l} \quad . \tag{A.3}$$

If now the positive and negative magnetic propagation vectors are considered, then equation A.3 can be written as follows:

$$\begin{aligned} \vec{m}_{lj} &= \sum_{\vec{k}} \frac{1}{2} \cdot \left[\left(\vec{R}_{\vec{k}j} + i \cdot \vec{I}_{\vec{k}j} \cdot e^{-2 \cdot \pi \cdot i \cdot \Phi_{\vec{k}j}} \cdot e^{-2 \cdot \pi \cdot i \cdot \vec{k} \cdot \vec{R}_l} \right) \right. \\ &\quad \left. + \left(\vec{R}_{\vec{k}j} - i \cdot \vec{I}_{\vec{k}j} \cdot e^{2 \cdot \pi \cdot i \cdot \Phi_{\vec{k}j}} \cdot e^{2 \cdot \pi \cdot i \cdot \vec{k} \cdot \vec{R}_l} \right) \right] \\ &= \sum_{\vec{k}} \frac{1}{2} \cdot \left[\left(\vec{R}_{\vec{k}j} + i \cdot \vec{I}_{\vec{k}j} \cdot e^{-2 \cdot \pi \cdot i \cdot \left(\Phi_{\vec{k}j} + \vec{k} \cdot \vec{R}_l \right)} \right) \right. \\ &\quad \left. + \left(\vec{R}_{\vec{k}j} - i \cdot \vec{I}_{\vec{k}j} \cdot e^{2 \cdot \pi \cdot i \cdot \left(\Phi_{\vec{k}j} + \vec{k} \cdot \vec{R}_l \right)} \right) \right] \quad . \end{aligned} \tag{A.4}$$

Using the Euler formula and substituting $2 \cdot \pi \cdot i \cdot \left(\Phi_{\vec{k}j} + \vec{k} \cdot \vec{R}_l \right)$ by u:

$$\begin{aligned}\vec{m}_{lj} &= \sum_{\vec{k}} \frac{1}{2} \cdot \Big[\Big(\vec{R}_{\vec{k}j} \cdot \cos(-u) + i \cdot \vec{R}_{\vec{k}j} \cdot \sin(-u) + i \cdot \vec{I}_{\vec{k}j} \cdot \cos(-u) - \vec{I}_{\vec{k}j} \cdot \sin(-u)\Big) \\ &\quad + \Big(\vec{R}_{\vec{k}j} \cdot \cos(u) + i \cdot \vec{R}_{\vec{k}j} \cdot \sin(u) - i \cdot \vec{I}_{\vec{k}j} \cdot \cos(u) + \vec{I}_{\vec{k}j} \cdot \sin(u)\Big)\Big] \quad . \quad \text{(A.5)}\end{aligned}$$

Using now the symmetry of the sine ($\sin(-x) = -\sin(x)$) and the cosine ($\cos(x) = -\cos(x)$) leads to the final result:

$$\begin{aligned}\vec{m}_{lj} &= \sum_{\vec{k}} \frac{1}{2} \cdot \Big[\Big(\vec{R}_{\vec{k}j} \cdot \cos(u) - i \cdot \vec{R}_{\vec{k}j} \cdot \sin(u) + i \cdot \vec{I}_{\vec{k}j} \cdot \cos(u) + \vec{I}_{\vec{k}j} \cdot \sin(u)\Big) \\ &\quad + \Big(\vec{R}_{\vec{k}j} \cdot \cos(u) + i \cdot \vec{R}_{\vec{k}j} \cdot \sin(u) - i \cdot \vec{I}_{\vec{k}j} \cdot \cos(u) + \vec{I}_{\vec{k}j} \cdot \sin(u)\Big)\Big] \\ &= \sum_{\vec{k}} \Big(\vec{R}_{\vec{k}j} \cdot \cos\Big(2 \cdot \pi \cdot \Big(\vec{k} \cdot \vec{R}_l + \Phi_{\vec{k}j}\Big)\Big) + \vec{I}_{\vec{k}j} \cdot \sin\Big(2 \cdot \pi \cdot \Big(\vec{k} \cdot \vec{R}_l + \Phi_{\vec{k}j}\Big)\Big)\Big) \quad \text{(A.6)}\end{aligned}$$

APPENDIX B

Calculation of the absorption correction for the refinements of neutron data

One of the phenomena which occur in matter, when it is probed by particles like X-ray photons, electrons or neutrons is absorption. This means that particles act in a way with the matter, so that they can no longer contribute to elastic scattering processes as they are used for instance in powder diffraction. In general that would not be a problem, if the absorption effect would be an isotropic phenomenon. However, in a powder diffraction experiment the investigated samples are limited objects often in a spherical shape like a capillary and therefore often the geometry of the experiment and the geometry of the probed sample prohibits an isotropic absorption effect. Especially for a transmission experiment (like the Debye-Scherrer geometry in a powder diffraction experiment), this argument is quite obvious. If we assume for instance an X-ray powder diffraction experiment in this geometry, it is geometrically clear, that at a higher diffraction angle the way for the diffracted X-rays through the sample is much shorter than for diffracted X-rays at a lower diffraction angle. Therefore a diffraction angle dependent absorption correction must be applied in a Rietveld refinement, where the absorption correction depends also on the type of matter[1]. Fortunately, the absorption of X-rays and neutrons in matter was quite good investigated allowing to calculate the correct absorption correction for a given chemical composition from tabulated values.

In most Rietveld refinement programs like TOPAS [57] or FullProf [83] the absorption correction for the refinement of a powder diffraction patterns is simply given by the linear attenuation factor μ and the radius R of the investigated sample or by the product of them. In the following it will be shown, how the product of $\mu \cdot R$ for the absorption correction of the neutron powder diffraction data of the $Bi_{1-x}Sr_xFeO_{3-\delta}$

1 In the case of light elements in X-ray diffraction, an absorption correction makes no big difference in a Rietveld refinement, therefore it is often simply neglected. The same holds true in neutron diffraction for atoms which show only small values for incoherent scattering and absorption of neutrons.

perovskites for the Rietveld refinement in Fullprof is calculated.

A suitable tool in order to calculate the absorption of neutrons in matter depending on the chemical composition, the wavelength of the neutrons and the crystal density is given online by the "NIST center of Neutron Research" [272]. This tool is very user friendly, as it calculates the linear attenuation factor by taking into account that the linear attenuation of neutrons in matter depends on the incoherent scattering and the absorption.

In the case of the $Bi_{1-x}Sr_xFeO_{3-\delta}$ perovskites, the chemical composition and also the used neutron wavelength is known, thus only the crystal density has to be calculated in order to use the online tool of NIST.

In order to calculate the crystal or crystallographic density, the connection between different formulas for the molar volume can be used:

$$V_m = \frac{V}{n} = \frac{M}{\rho} = \frac{N_A \cdot V_{cell}}{Z} \quad , \tag{B.1}$$

where V_m is the molar volume, V is the volume of the sample, n is the amount of the substance, M is the molar mass, ρ is the density of the sample, Z is the number of formula units in the unit cell, V_{cell} is the volume of the unit cell and N_A is the Avogadro constant.
By the rearrangement of equation B.1, we get an expression for the crystal density:

$$\rho = \frac{M \cdot Z}{V_{cell} \cdot N_A} \quad . \tag{B.2}$$

For a known or an assumed crystal structure, the number of formula units in the unit cell Z is known. The molar mass M can be calculated from the chemical composition by the following formula:

$$M = \sum_i k_i \cdot m_i \quad , \tag{B.3}$$

where i is the summation over all atom types, m_i is the atom weight of a particular element and k_i is the number of atoms inside the chemical composition of this particular element.
Finally, the unit cell volume can be determined by the knowledge of the unit cell parameters a, b, c, α, β and γ. These unit cell parameters can be determined by a whole powder pattern decomposition (WPPD) method according to Pawley [62] or Le Bail *et al.* [63]. With the formulas given in table B.1 it is possible to calculate the unit cell volume for each crystal system.

With the atomic weights from table B.2 it is now a straightforward calculation of

Crystal system	Formula for the unit cell volume
Cubic	$V = a^3$
Tetragonal	$V = a^2 \cdot c$
Hexagonal	$V = a^2 \cdot c \cdot \sin(60°)$
Trigonal (H)	$V = a^2 \cdot c \cdot \sin(60°)$
Trigonal (R)	$V = a^3 \cdot \sqrt{1 - 3 \cdot \cos^2 \alpha + 2 \cdot \cos^3 \alpha}$
Orthorhombic	$V = a \cdot b \cdot c$
Monoclinic	$V = a \cdot b \cdot c \cdot \sin(\beta)$
Triclinic	$V = a \cdot b \cdot c \cdot \sqrt{1 - \cos^2 \alpha - \cos^2 \beta - \cos^2 \gamma + 2 \cdot \cos \alpha \cdot \cos \beta \cdot \cos \gamma}$

Table B.1: Calculation of the unit cell volume V for different crystal systems [273] depending on the lattice parameters a, b, c, α, β and γ. For the trigonal system the formula for H = hexagonal setting and R = rhombohedral setting are given.

the molar mass and therefore of the crystal density for each compound[1].

Element	Atomic weight (u)
Bi	208.98
Sr	87.62
Fe	55.845
O	15.999

Table B.2: Atomic weights of Bi, Sr, Fe and O from [274].

The calculated molar mass of the $Bi_{1-x}Sr_xFeO_{3-\delta}$ perovskites as well as the corresponding unit cell volumes, the corresponding number Z of formula units in the unit cell and the corresponding density can be found in table B.3. In this table also the calculated linear attenuation factor μ as well as the product of μ and the radius R can be found. The radius R is given as 0.6 cm, as all used niobium or vanadium containers had a diameter of 1.2 cm.

1 In reality, the crystal density is lower than the calculated value, due to the loose packing of the material. Empirically, it can be determined that the "packing factor" is between 0.5 and 0.7. Therefore an average packing factor of 0.6 was assumed for the calculation of the linear attenuation factors for the $Bi_{1-x}Sr_xFeO_{3-\delta}$ perovskites.

Chemical composition	Molar mass M ($\frac{g}{mol}$)	Unit cell volume V_{cell} (Å^3)	Z	Crystal density ρ ($\frac{g}{cm^3}$)	Approximate packed density ρ ($\frac{g}{cm^3}$)	Linear attenuation factor μ ($\frac{1}{cm}$)	$\mu \cdot R$
$BiFeO_3$	312.822	374.159	6	8.330	4.998	0.025	0.0150
$Bi_{0.9}Sr_{0.1}FeO_{3-\delta}$	300.686	372.204	6	8.049	4.829	0.027	0.0162
$Bi_{0.8}Sr_{0.2}FeO_{3-\delta}$	288.55	61.803	1	7.753	4.652	0.028	0.0168
$Bi_{0.7}Sr_{0.3}FeO_{3-\delta}$	276.414	61.759	1	7.432	4.459	0.029	0.0174
$Bi_{0.5}Sr_{0.5}FeO_{3-\delta}$	252.142	61.466	1	6.812	4.087	0.031	0.0186
$Bi_{0.2}Sr_{0.8}FeO_{3-\delta}$	215.734	59.186	1	6.053	3.632	0.036	0.0216
$SrFeO_{3-\delta}$	191.462	57.405	1	5.539	3.323	0.039	0.0234

Table B.3: Molar mass, unit cell volume, number of formula units in the unit cell and density of the $Bi_{1-x}Sr_xFeO_{3-\delta}$ perovskites at room temperature. For the calculation of the molar mass, oxygen was assumed to have a stoichiometric value of 3. The approximate packed density is calculated using an empirical factor of ≈ 0.6. The wavelength for the calculation of the linear attenuation factor was 1.54814 Å for x = 0, 0.2, 0.5, 0.8, 1 and 1.548296 Å for x = 0.1 and x = 0.3. The linear attenuation factor was calculated with [272]. The radius of the niobium or vanadium containers was 0.6 cm.

APPENDIX C

Transformation between $Pm\bar{3}m$ and $R3c$

C.1 Lattice transformation

Mathematical details of lattice transformations are presented in appendix J.

The transformation from the lattice parameters of $Pm\bar{3}m$ to the lattice parameters of $R3c$ in subsection 3.5.3 is given by the following transformation matrix:

$$W = \begin{pmatrix} 1 & 0 & -2 \\ 0 & 1 & 2 \\ 1 & -1 & 2 \end{pmatrix} \tag{C.1}$$

The inverse of W is given by:

$$W^{-1} = \begin{pmatrix} \frac{2}{3} & \frac{1}{3} & \frac{1}{3} \\ \frac{1}{3} & \frac{2}{3} & -\frac{1}{3} \\ -\frac{1}{6} & \frac{1}{6} & \frac{1}{6} \end{pmatrix} \tag{C.2}$$

APPENDIX D

Heat capacity as second derivative of the Gibbs free energy

For the proof that the heat capacity of constant pressure can be expressed as second derivative of the Gibbs free energy, it is possible to start from the definition of the heat capacity:

$$C_p := \frac{\partial Q}{\partial T} \quad , \tag{D.1}$$

where Q is the heat and T is the temperature.
If we now assume that the inner energy U solely depends on the heat Q we can write[1]:

$$C_p := \frac{\partial Q}{\partial T} = \frac{\partial U}{\partial T} \quad . \tag{D.2}$$

In general, the inner energy U depends on the entropy S and the entropy S depends on the temperature T, so we can expand the last term by the chain rule:

$$C_p = \frac{\partial U}{\partial T} = \frac{\partial U}{\partial S}\frac{\partial S}{\partial T} \quad . \tag{D.3}$$

The term $\frac{\partial U}{\partial S}$ is given as temperature T, if we look at the definition of the total differential of the inner energy U:

$$dU = \underbrace{\frac{\partial U}{\partial S}}_{T} dS + ... \quad . \tag{D.4}$$

Further terms of volume, pressure, etc. are neglected as the heat capacity of constant pressure does not depend on these variables.

With the substitution by T the following expression can be received:

$$C_p = T \cdot \frac{\partial S}{\partial T} \quad . \tag{D.5}$$

1 This argument holds also true for the enthalpy H, why the heat capacity at constant pressure can be also written as $C_p = \frac{\partial H}{\partial T}$

For the term $\frac{\partial S}{\partial T}$, one can have a look at the definition of the total differential of the Gibbs free energy G:

$$dG = \underbrace{\frac{\partial G}{\partial T}}_{-S} dT + ... \qquad . \tag{D.6}$$

So the entropy S in equation D.5 can be replaced by the negative of the first derivative of the Gibbs free energy:

$$C_p = -T \cdot \frac{\partial^2 G}{\partial T^2} \qquad . \tag{D.7}$$

This equations proofs the assumption that the heat capacity at constant pressure can be expressed as second derivative of the Gibbs free energy.

APPENDIX E

Additional figures for the pressure dependent investigations of $LaFeO_3$ - Approach A

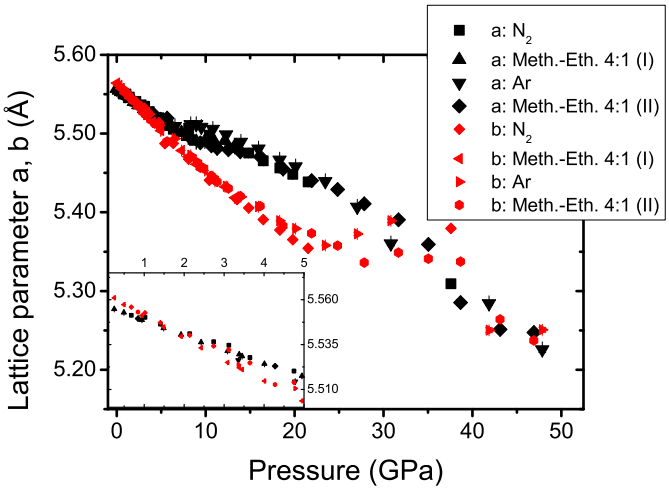

Figure E.1: Pressure dependent lattice parameters a and b of the $LaFeO_3$ perovskite. The crossing at approximately 2.1 GPa allows the description of the crystal structure with a tetragonal unit cell, although it does not indicate a phase transition to a tetragonal crystal structure.

APPENDIX F

Inverted third order Vinet EoS approximation

The "linearized" inverted third order Vinet EoS approximation is given by

$$a(P) = a_0 \times f(P) \qquad , \tag{F.1}$$

where a_0 is the lattice parameter at ambient conditions and $f(P)$ is given as

$$\begin{aligned}
f(P) = \; & \frac{4uv^3 + 3uv^2}{4uv^3} + \frac{1}{2}\Bigg[\frac{1}{4}\frac{(-4uv^3 - 3uv^2)^2}{u^2v^6} \\
& - \frac{9uv^2 - 6P + 6uv^3 + 6uv}{uv^3} + \frac{1}{uv^3}\Bigg(36u^2v^3P + 21u^2v^4P \\
& + 8u^3v^3 - 8P^3 + 24uv^3P^2 + 24uvP^2 - 6u^2v^2P + 36uv^2P^2 \\
& + \Bigg(-\frac{1}{v}\Big(-72u^4v^3 - 720u^3v^3P - 756u^2vP^2 - 432u^3v^4P \\
& - 3060u^2v^3P^2 - 3024P^3uv - 2664u^2v^4P^2 - 1296u^2v^2P^2 \\
& - 7920uv^2P^3 + 288P^3u - 825u^2v^5P^2 - 9576P^3uv^3 + 1152vP^4 \\
& - 6000uv^4P^3 + 576v^2P^4 + 1152P^4 - 2304uv^5P^3 + 192P^4v^3 \\
& - 512uv^6P^3\Big)\Bigg)^{\frac{1}{2}}uv^2\Bigg)^{\frac{1}{3}} + \Bigg(2\Big(-(u^2v^2) - 6uv^2P \\
& + 2P^2 - 4uv^3P - 4uvP\Big)\Bigg) \Bigg/ \Bigg(uv^3\Big(36u^2v^3P + 21u^2v^4P \\
& + 8u^3v^3 - 8P^3 + 24uv^3P^2 + 24uvP^2 - 6u^2v^2P + 36uv^2P^2 \\
& + \Big(-\frac{1}{v}(-72u^4v^3 - 720u^3v^3P - 756u^2vP^2 - 432u^3v^4P \\
& - 3060u^2v^3P^2 - 3024P^3uv - 2664u^2v^4P^2 - 1296u^2v^2P^2
\end{aligned}$$

$$
\begin{aligned}
&- 7920uv^2P^3 + 288P^3u - 825u^2v^5P^2 - 9576P^3uv^3 + 1152vP^4 \\
&- 6000uv^4P^3 + 576v^2P^4 + 1152P^4 - 2304uv^5P^3 + 192P^4v^3 \\
&- 512uv^6P^3))^{\frac{1}{2}}uv^2\Big)^{\frac{1}{3}}\Big) - \frac{-3uv^2 + 2P - 2uv^3 - 2uv}{uv^3}\Bigg]^{\frac{1}{2}} \\
&- \frac{1}{2}\Bigg[\frac{1}{2}\frac{(-4uv^3 - 3uv^2)^2}{u^2v^6} - \frac{9uv^2 - 6P + 6uv^3 + 6uv}{uv^3} \\
&- \frac{1}{uv^3}\Bigg(36u^2v^3P + 21u^2v^4P + 8u^3v^3 - 8P^3 + 24uv^3P^2 \\
&+ 24uvP^2 - 6u^2v^2P + 36uv^2P^2 + \Big(-\frac{1}{v}\Big(-72u^4v^3 \\
&- 720u^3v^3P - 756u^2vP^2 - 432u^3v^4P - 3060u^2v^3P^2 \\
&- 3024P^3uv - 2664u^2v^4P^2 - 1296u^2v^2P^2 - 7920uv^2P^3 \\
&+ 288P^3u - 825u^2v^5P^2 - 9576P^3uv^3 + 1152vP^4 \\
&- 6000uv^4P^3 + 576v^2P^4 + 1152P^4 - 2304uv^5P^3 + 192P^4v^3 \\
&- 512uv^6P^3\Big)\Big)^{\frac{1}{2}}uv^2\Bigg)^{\frac{1}{3}} - \Bigg(2\Big(-(u^2v^2) - 6uv^2P + 2P^2 \\
&- 4uv^3P - 4uvP\Big)\Bigg)\Bigg/\Bigg(uv^3 \cdot \Big(36u^2v^3P + 21u^2v^4P \\
&+ 8u^3v^3 - 8P^3 + 24uv^3P^2 + 24uvP^2 - 6u^2v^2P \\
&+ 36uv^2P^2 + \Big(-\frac{1}{v}(-72u^4v^3 - 720u^3v^3P - 756u^2vP^2 \\
&- 432u^3v^4P - 3060u^2v^3P^2 - 3024P^3uv - 2664u^2v^4P^2 \\
&- 1296u^2v^2P^2 - 7920uv^2P^3 + 288P^3u - 825u^2v^5P^2 \\
&- 9576P^3uv^3 + 1152vP^4 - 6000uv^4P^3 + 576v^2P^4 + 1152P^4 \\
&- 2304uv^5P^3 + 192P^4v^3 - 512uv^6P^3))^{\frac{1}{2}}uv^2\Big)^{\frac{1}{3}}\Big) \\
&+ \frac{-3uv^2 + 2P - 2uv^3 - 2uv}{uv^3}
\end{aligned}
$$

$$
\begin{aligned}
&+\left(\frac{(9uv^2-6P+6uv^3+6uv)(-4uv^3-3uv^2)}{u^2v^6}\right.\\
&\left.-\frac{2(-4uv^3-9uv^2-12uv-6u)}{uv^3}-\frac{(-4uv^3-3uv^2)^3}{4u^3v^9}\right)\Bigg/\\
&\left(\frac{1}{4}\frac{(-4uv^3-3uv^2)^2}{u^2v^6}-\frac{9uv^2-6P+6uv^3+6uv}{uv^3}\right.\\
&+\frac{1}{uv^3}\Big(36u^2v^3P+21u^2v^4P+8u^3v^3-8P^3+24uv^3P^2\\
&+24uvP^2-6u^2v^2P+36uv^2P^2+\Big(-\frac{1}{v}(-72u^4v^3\\
&-720u^3v^3P-756u^2vP^2-432u^3v^4P-3060u^2v^3P^2\\
&-3024P^3uv-2664u^2v^4P^2-1296u^2v^2P^2-7920uv^2P^3\\
&+288P^3u-825u^2v^5P^2-9576P^3uv^3+1152vP^4\\
&-6000uv^4P^3+576v^2P^4+1152P^4-2304uv^5P^3+192P^4v^3\\
&-512uv^6P^3)\Big)^{\frac{1}{2}}uv^2\Big)^{\frac{1}{3}}+\Big(2\Big(-(u^2v^2)-6uv^2P+2P^2\\
&-4uv^3P-4uvP\Big)\Big)\Big/\Big(uv^3\Big(36u^2v^3P+21u^2v^4P\\
&+8u^3v^3-8P^3+24uv^3P^2+24uvP^2-6u^2v^2P\\
&+36uv^2P^2+(-\frac{1}{v}(-72u^4v^3-720u^3v^3P-756u^2vP^2\\
&-432u^3v^4P-3060u^2v^3P^2-3024P^3uv-2664u^2v^4P^2\\
&-1296u^2v^2P^2-7920uv^2P^3+288P^3u-825u^2v^5P^2\\
&-9576P^3uv^3+1152vP^4-6000uv^4P^3+576v^2P^4+1152P^4\\
&-2304uv^5P^3+192P^4v^3-512uv^6P^3))^{\frac{1}{2}}uv^2\Big)^{\frac{1}{3}}\Big)\\
&\left.-\frac{-3uv^2+2P-2uv^3-2uv}{uv^3}\right)^{\frac{1}{2}}\Bigg]^{\frac{1}{2}}\qquad.
\end{aligned}
\tag{F.2}
$$

APPENDIX G

Additional figures for the pressure dependent investigations of $LaFeO_3$ - Approach B

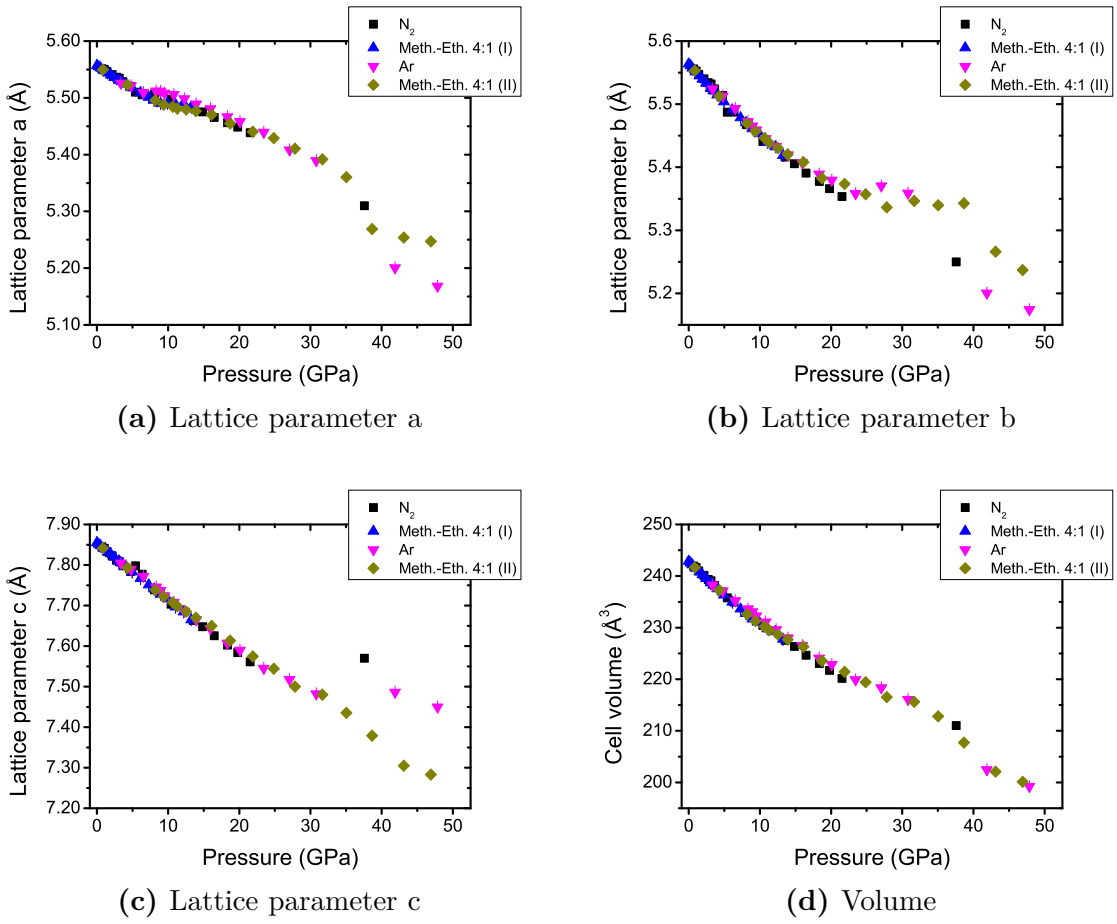

(a) Lattice parameter a

(b) Lattice parameter b

(c) Lattice parameter c

(d) Volume

Figure G.1: Pressure dependent orthorhombic a)-c) lattice parameters and d) unit cell volume of $LaFeO_3$.

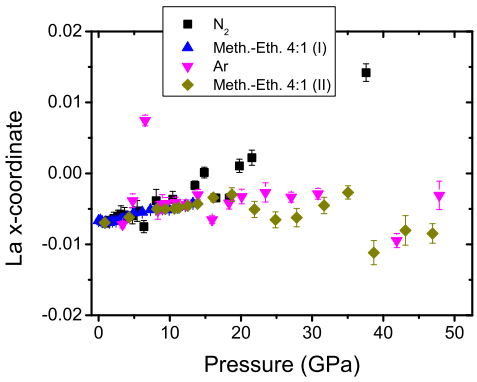

(a) La x-coordinate

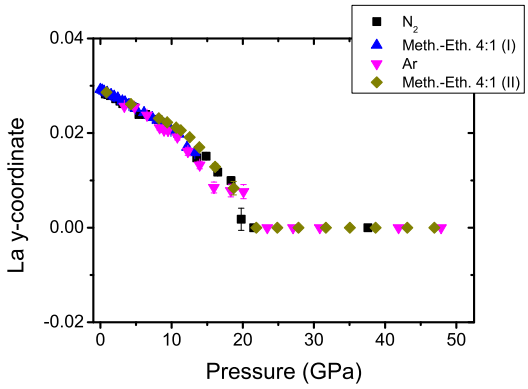

(b) La y-coordinate

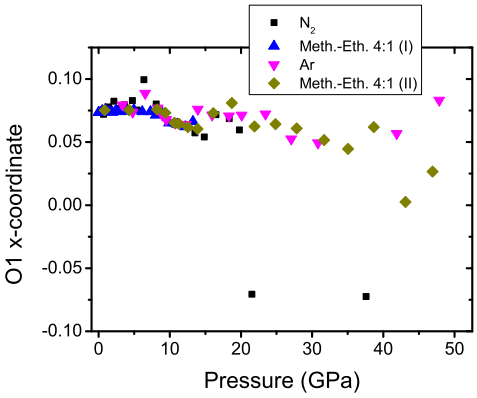

(c) O1 x-coordinate

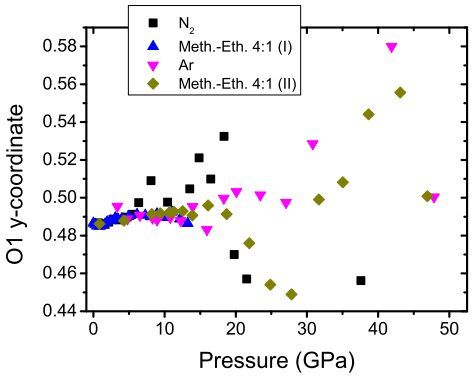

(d) O1 y-coordinate

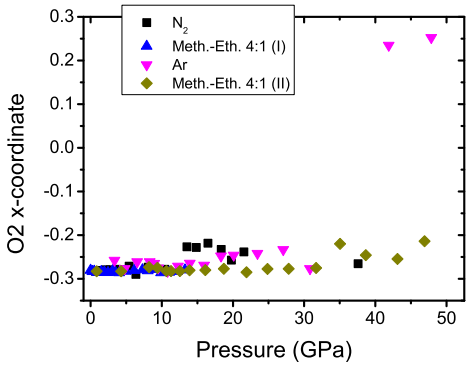

(e) O2 x-coordinate

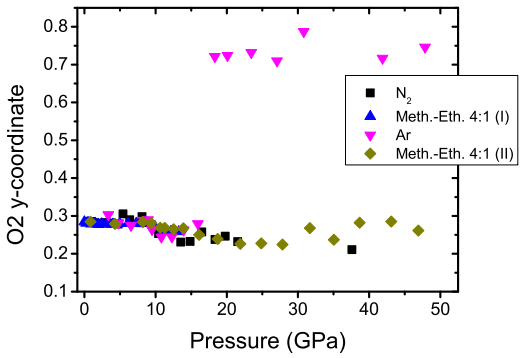

(f) O2 y-coordinate

Figure G.2: Pressure dependent atomic coordinates of the $LaFeO_3$ perovskite. The lanthanum y-coordinate in b) gives a clear indication of a structural second order phase transition (The figures of the atomic coordinates are continued in figure G.3).

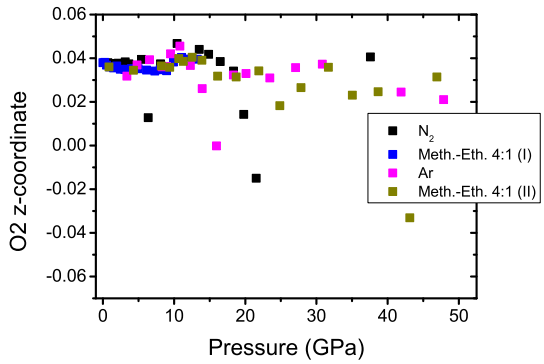

(a) O2 z-coordinate

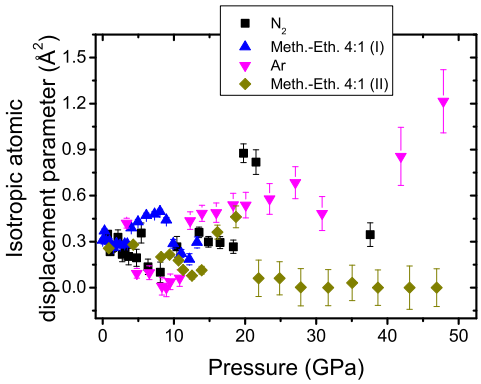

(b) Overall isotropic atomic displacement parameters

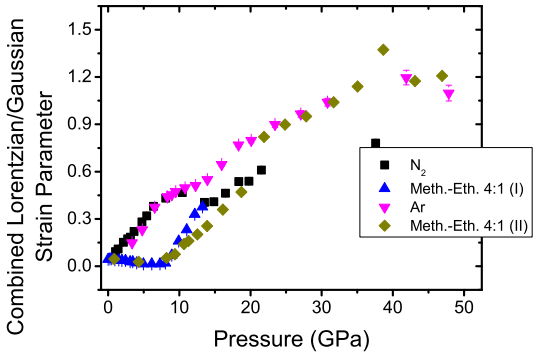

(c) Phenomenological strain parameter

Figure G.3: a) Continued pressure dependent atomic coordinates of the $LaFeO_3$ perovskite from figure G.2. b) Pressure dependent overall isotropic atomic displacement parameter for all datasets. b) Pressure dependent phenomenological strain parameters for the different pressure media dependent data sets. From this figure the onset of the non-hydrostatic regime for the different pressure media can be estimated (the definition of the phenomenological strain parameter is given in a footnote in section 4.4).

APPENDIX H

Additional figures for the pressure dependent investigations of $LaFeO_3$ - Approach C

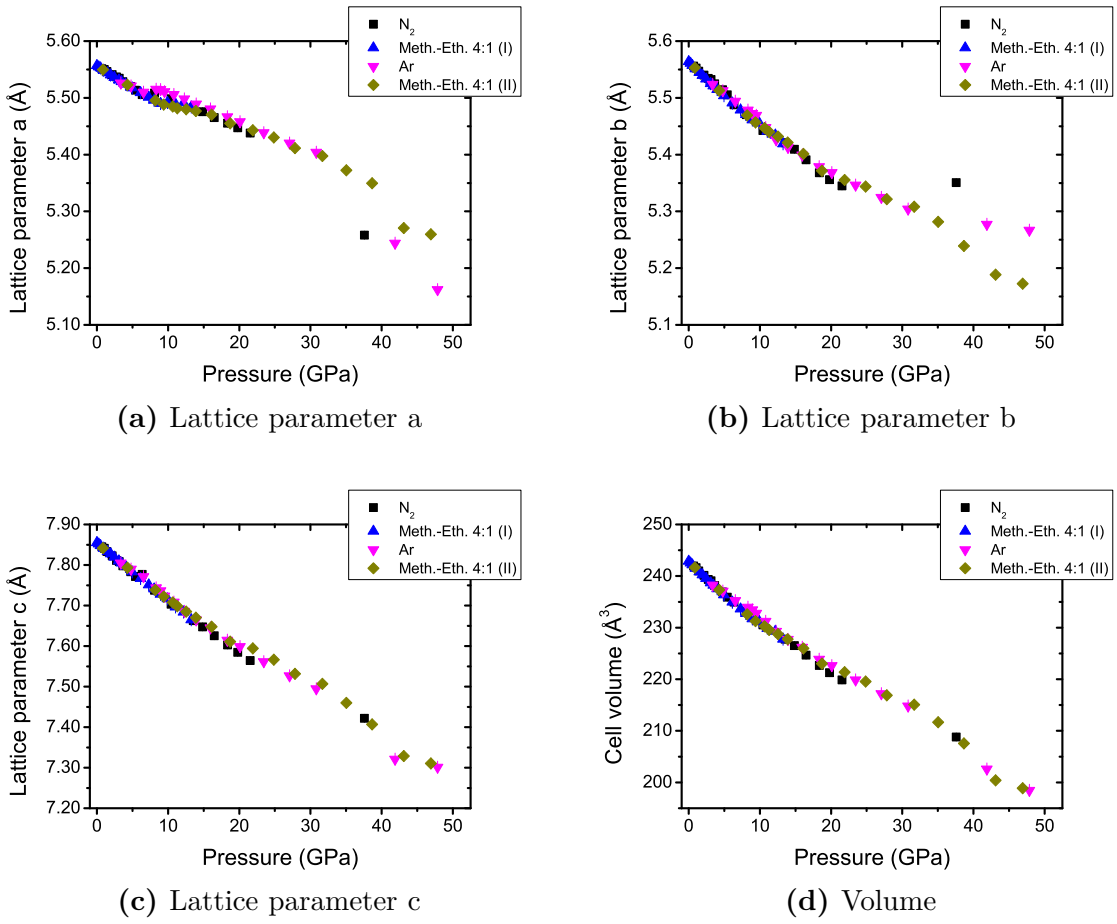

(a) Lattice parameter a

(b) Lattice parameter b

(c) Lattice parameter c

(d) Volume

Figure H.1: Pressure dependent orthorhombic a)-c) lattice parameters and d) unit cell volume of $LaFeO_3$.

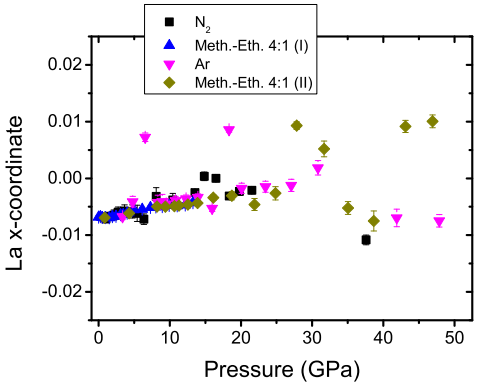

(a) La x-coordinate

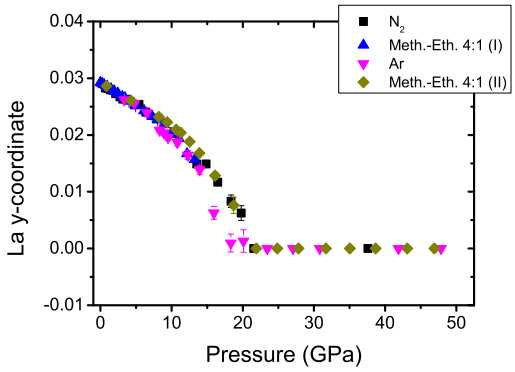

(b) La y-coordinate

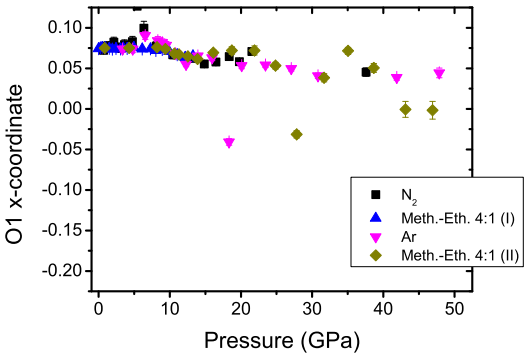

(c) O1 x-coordinate

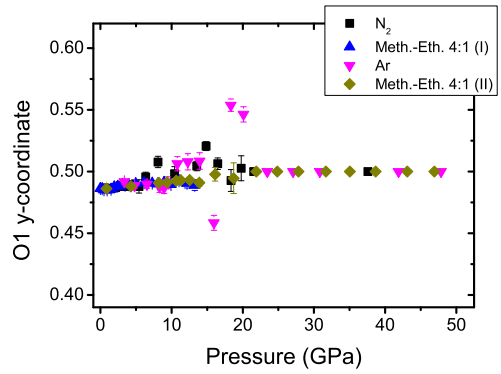

(d) O1 y-coordinate

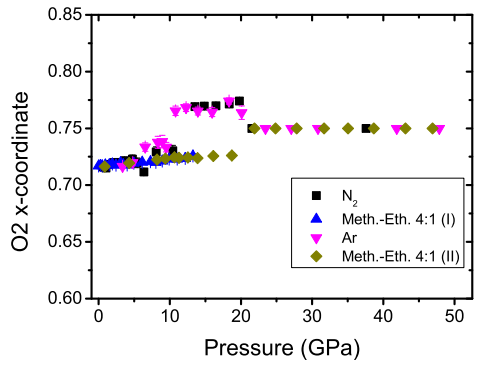

(e) O2 x-coordinate

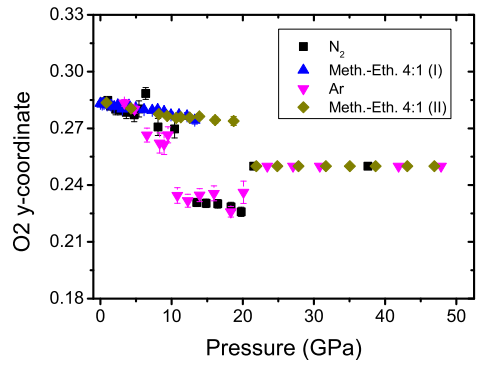

(f) O2 y-coordinate

Figure H.2: Pressure dependent atomic coordinates of the $LaFeO_3$ perovskite. The lanthanum y-coordinate in b) gives a clear indication of a structural second order phase transition (The figures of the atomic coordinates are continued in figure H.3).

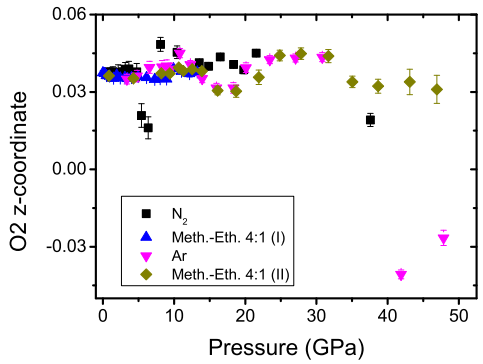

(a) O2 z-coordinate

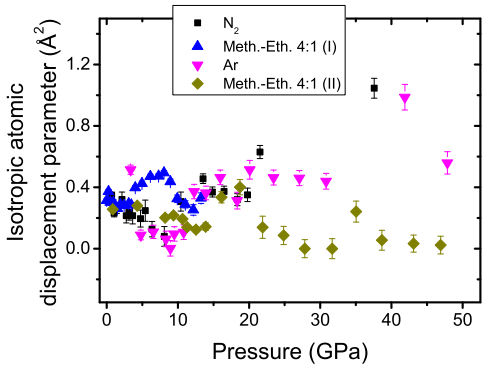

(b) Overall isotropic atomic displacement parameters

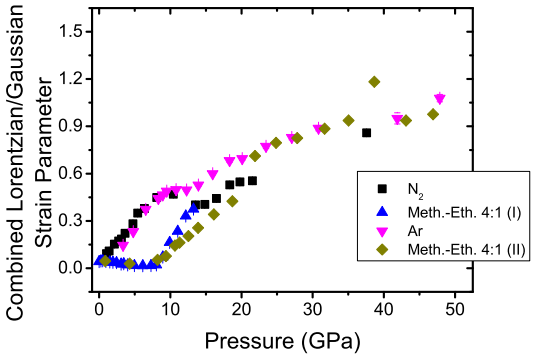

(c) Phenomenological strain parameter

Figure H.3: a) Continued pressure dependent atomic coordinates of the $LaFeO_3$ perovskite from figure H.2. b) Pressure dependent overall isotropic atomic displacement parameter for all datasets. b) Pressure dependent phenomenological strain parameters for the different pressure media dependent data sets. From this figure the onset of the non-hydrostatic regime for the different pressure media can be estimated (the definition of the phenomenological strain parameter is given in a footnote in section 4.4).

APPENDIX I

Additional figures for the pressure dependent investigations of $LaFeO_3$ - Approach D

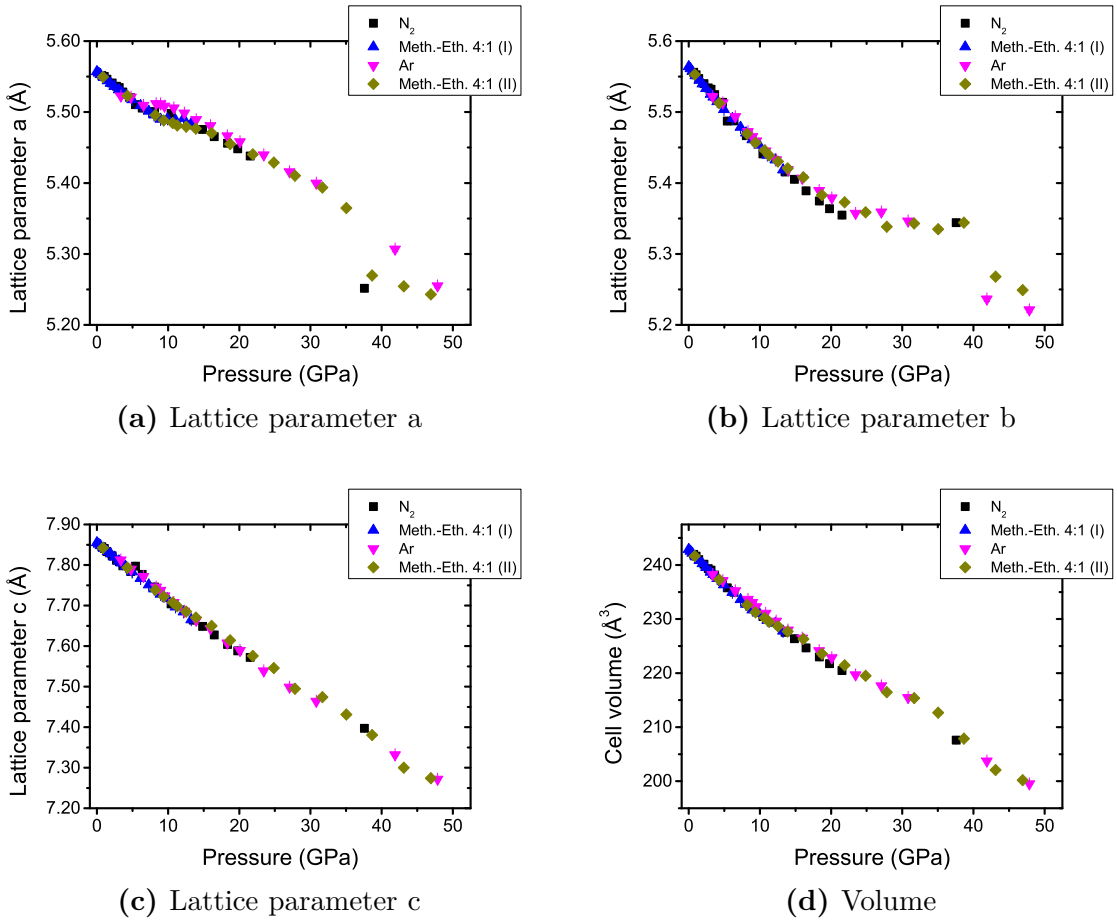

(a) Lattice parameter a

(b) Lattice parameter b

(c) Lattice parameter c

(d) Volume

Figure I.1: Pressure dependent orthorhombic a)-c) lattice parameters and d) unit cell volume of $LaFeO_3$.

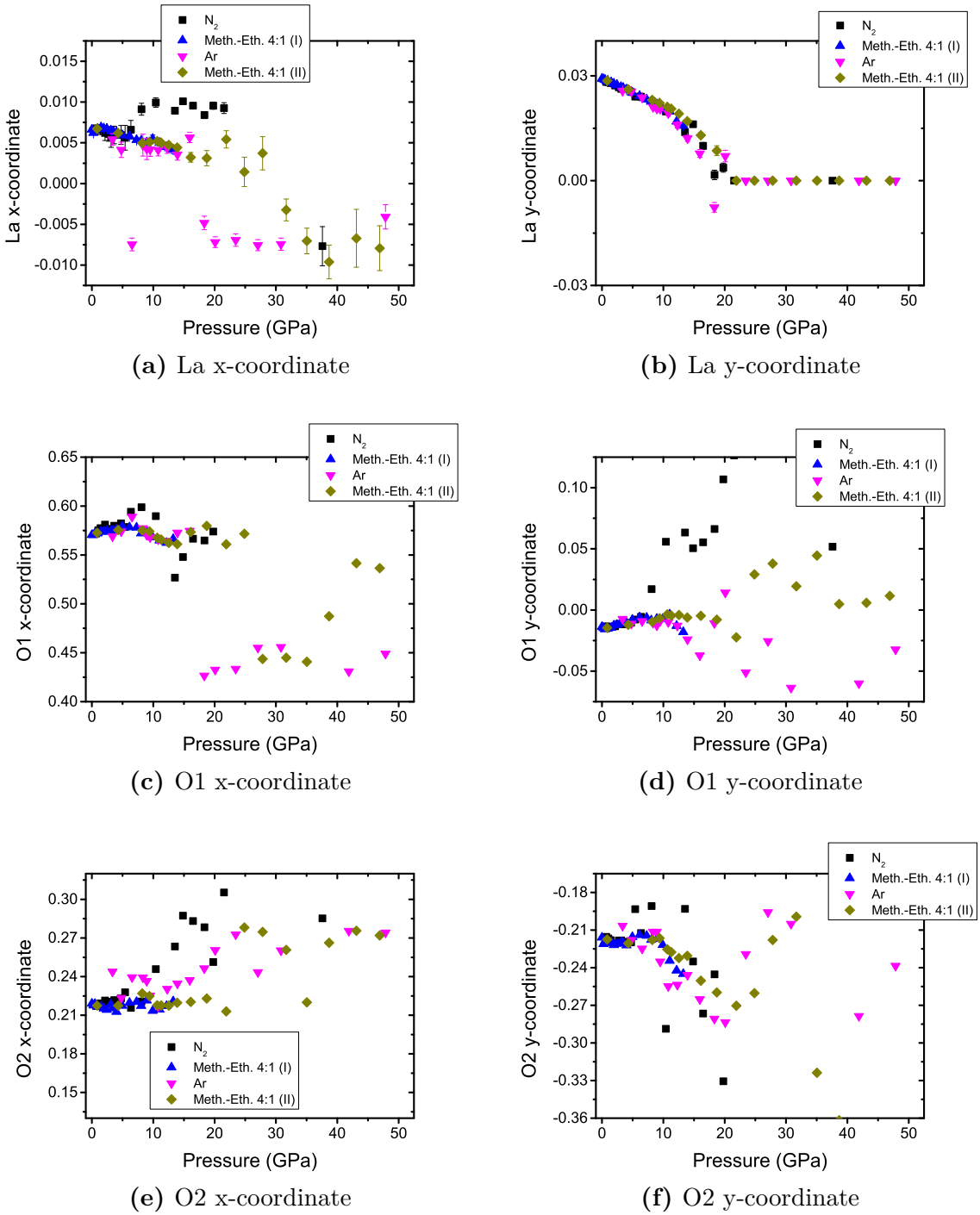

(a) La x-coordinate

(b) La y-coordinate

(c) O1 x-coordinate

(d) O1 y-coordinate

(e) O2 x-coordinate

(f) O2 y-coordinate

Figure I.2: Pressure dependent atomic coordinates of the $LaFeO_3$ perovskite. The lanthanum y-coordinate in b) gives a clear indication of a structural second order phase transition (The figures of the atomic coordinates are continued in figure I.3).

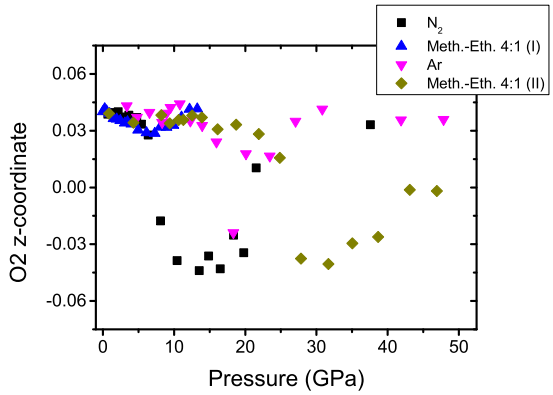

(a) O2 z-coordinate

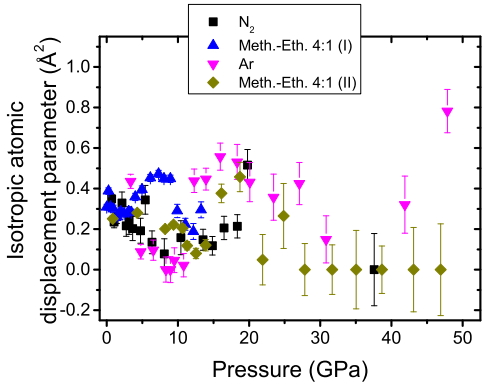

(b) Overall isotropic atomic displacement parameters

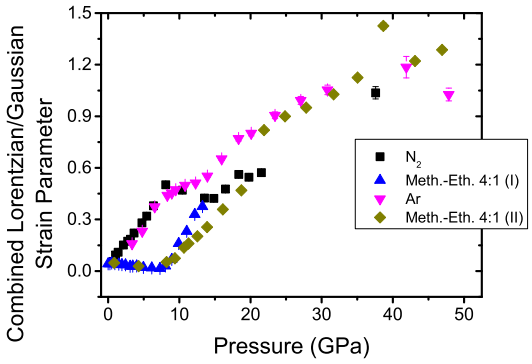

(c) Phenomenological strain parameter

Figure I.3: a) Continued pressure dependent atomic coordinates of the $LaFeO_3$ perovskite from figure I.2. b) Pressure dependent overall isotropic atomic displacement parameter for all datasets. b) Pressure dependent phenomenological strain parameters for the different pressure media dependent data sets. From this figure the onset of the non-hydrostatic regime for the different pressure media can be estimated (the definition of the phenomenological strain parameter is given in a footnote in section 4.4).

APPENDIX J

Transformation between $Im\bar{3}$ and $C2/m$

J.1 Lattice transformation

Generally, the transformation of a crystallographic space lattice A to a crystallographic space lattice B is given by a similarity transformation:

$$G_B = W^T \cdot G_A \cdot W \tag{J.1}$$

where G_A and G_B are the metric tensors (= fundamental matrices) of the corresponding crystallographic space lattices, W is the transformation matrix and W^T the transposed transformation matrix.

The metric tensor is defined as:

$$G = \begin{pmatrix} g_{11} & g_{12} & g_{13} \\ g_{21} & g_{22} & g_{23} \\ g_{31} & g_{32} & g_{33} \end{pmatrix} = \begin{pmatrix} a^2 & a \cdot b \cdot \cos\gamma & a \cdot c \cdot \cos\beta \\ a \cdot b \cdot \cos\gamma & b^2 & b \cdot c \cdot \cos\alpha \\ a \cdot c \cdot \cos\beta & b \cdot c \cdot \cos\alpha & c^2 \end{pmatrix} \tag{J.2}$$

where a, b, c, α, β and γ are the lattice parameters of a given crystallographic space lattice.

The transformation from the lattice parameters of $Im\bar{3}$ in section 5.4.1 to the lattice parameters of $C2/m$ in section 5.4.2 is given by the following transformation matrix:

$$W = \begin{pmatrix} 1 & 0 & -1 \\ 0 & 1 & 0 \\ 1 & 0 & 1 \end{pmatrix} \tag{J.3}$$

Thus the transformation is:

$$G_{C2/m} = W^T \cdot G_{Im\bar{3}} \cdot W \quad . \tag{J.4}$$

It is also possible to do the reverse transformation ($C2/m \rightarrow Im\bar{3}$), which is given

by:

$$W^{T^{-1}} \cdot G_{C2/m} \cdot W^{-1} = \underbrace{W^{T^{-1}} \cdot W^{T}}_{\mathbb{1}} \cdot G_{Im\bar{3}} \cdot \underbrace{W \cdot W^{-1}}_{\mathbb{1}} \quad . \tag{J.5}$$

The inverse of W is given by:

$$W^{-1} = \begin{pmatrix} \frac{1}{2} & 0 & \frac{1}{2} \\ 0 & 1 & 0 \\ -\frac{1}{2} & 0 & \frac{1}{2} \end{pmatrix} \tag{J.6}$$

J.2 Coordinate transformation

Generally, the transformation of a given atomic coordinate x, y, z of a crystallographic space lattice B to the atomic coordinate x', y', z' of a crystallographic space lattice A is given by a transformation which consists of a rotational part W (which is the above mentioned transformation matrix) and of an origin shift w (which is a vector):

$$X' = (W,w)X = W \cdot X + w \tag{J.7}$$

where $X = (x, y, z)^T$ and $X' = (x', y', z')^T$.

The transformation for the atomic coordinates of the crystal structure in space group $Im\bar{3}$ in section 5.4.1 to the atomic coordinates of the crystal structure in space group $C2/m$ in section 5.4.2 is given by the relation:

$$X_{C2/m} = W^{-1} \cdot (X_{Im\bar{3}} - w) \tag{J.8}$$

where W^{-1} is given in equation J.6 and the orgin shift w is given as:

$$w = (0, 0, 0.5)^T \quad . \tag{J.9}$$

In order to obtain all required atomic coordinates in space group $C2/m$, first all symmetry equivalent positions of each atom have to be calculated first. After the calculation of each atomic position in the unit cell, the transformation is carried out and a look into the International Tables Vol. A [275] shows which atomic position is a new one and which can be omitted due to symmetry equivalence. The full transformation calculation for all Bi, Cu, Cr and O atoms is listed in table J.1.

Table J.1: Transformation table of all Bi, Cu, Cr and O atomic positions in space group $Im\bar{3}$ to the atomic positions in space group $C2/m$. In the first column the atomic identifier is shown. In the second column the position in space group $Im\bar{3}$ is given. In the third column all symmetry equivalent atomic positions are calculated. The fourth column are the transformed coordinates in space group $C2/m$. And in the fifth column the Wyckoff positions in the new space group are identified as well as symmetry equivalent doublets, triplets, etc.. The tables with symmetry equivalent coordinates and Wyckoff positions can be obtained either by the International Tables Vol. A [275] or by the Bilbao Crystallographic Server (Online links: http://www.cryst.ehu.es/cgi-bin/cryst/programs/nph-wp-list?gnum=204 ($Im\bar{3}$) and http://www.cryst.ehu.es/cgi-bin/cryst/programs/nph-wp-list?gnum=12&gua=b ($C2/m$)).

Atom	Coordinate in $Im\bar{3}$	Symmetry equivalent coordinate in $Im\bar{3}$	Coordinate in $C2/m$	Wyckoff position in $C2/m$
Bi1_1	$\begin{pmatrix} 0 \\ 0 \\ 0 \end{pmatrix}$	$\begin{pmatrix} 0 \\ 0 \\ 0 \end{pmatrix}$	$\begin{pmatrix} -0.25 \\ 0 \\ -0.25 \end{pmatrix}$	4i
Bi1_2		$\begin{pmatrix} 0.5 \\ 0.5 \\ 0.5 \end{pmatrix}$	$\begin{pmatrix} 0.25 \\ 0.5 \\ -0.25 \end{pmatrix}$	4i ($\rightarrow$ Bi1_1)
Cu1_1	$\begin{pmatrix} 0 \\ 0.5 \\ 0.5 \end{pmatrix}$	$\begin{pmatrix} 0 \\ 0.5 \\ 0.5 \end{pmatrix}$	$\begin{pmatrix} 0 \\ 0.5 \\ 0 \end{pmatrix}$	2b
Cu1_2		$\begin{pmatrix} 0.5 \\ 0 \\ 0.5 \end{pmatrix}$	$\begin{pmatrix} 0.25 \\ 0 \\ -0.25 \end{pmatrix}$	4i
Cu1_3		$\begin{pmatrix} 0.5 \\ 0.5 \\ 0 \end{pmatrix}$	$\begin{pmatrix} 0 \\ 0.5 \\ -0.5 \end{pmatrix}$	2d
Cu1_4		$\begin{pmatrix} 0.5 \\ 0 \\ 0 \end{pmatrix}$	$\begin{pmatrix} 0 \\ 0 \\ -0.5 \end{pmatrix}$	2c
Cu1_5		$\begin{pmatrix} 0 \\ 0.5 \\ 0 \end{pmatrix}$	$\begin{pmatrix} -0.25 \\ 0.5 \\ -0.25 \end{pmatrix}$	4i ($\rightarrow$ Cu1_2)
Cu1_6		$\begin{pmatrix} 0 \\ 0 \\ 0.5 \end{pmatrix}$	$\begin{pmatrix} 0 \\ 0 \\ 0 \end{pmatrix}$	2a
Cr1_1	$\begin{pmatrix} 0 \\ 0.5 \\ 0.5 \end{pmatrix}$	$\begin{pmatrix} 0.25 \\ 0.25 \\ 0.25 \end{pmatrix}$	$\begin{pmatrix} 0 \\ 0.25 \\ -0.25 \end{pmatrix}$	8j
Cr1_2		$\begin{pmatrix} 0.75 \\ 0.75 \\ 0.25 \end{pmatrix}$	$\begin{pmatrix} 0.25 \\ 0.75 \\ -0.5 \end{pmatrix}$	4f

Cr1_3		$\begin{pmatrix} 0.75 \\ 0.25 \\ 0.75 \end{pmatrix}$	$\begin{pmatrix} 0.5 \\ 0.25 \\ -0.25 \end{pmatrix}$	8j (→ Cr1_1)
Cr1_4		$\begin{pmatrix} 0.25 \\ 0.75 \\ 0.75 \end{pmatrix}$	$\begin{pmatrix} 0.25 \\ 0.75 \\ 0 \end{pmatrix}$	4e
Cr1_5		$\begin{pmatrix} 0.75 \\ 0.75 \\ 0.75 \end{pmatrix}$	$\begin{pmatrix} 0.5 \\ 0.75 \\ -0.25 \end{pmatrix}$	8j (→ Cr1_1)
Cr1_6		$\begin{pmatrix} 0.25 \\ 0.25 \\ 0.75 \end{pmatrix}$	$\begin{pmatrix} 0.25 \\ 0.25 \\ 0 \end{pmatrix}$	4e (→ Cr1_4)
Cr1_7		$\begin{pmatrix} 0.25 \\ 0.75 \\ 0.25 \end{pmatrix}$	$\begin{pmatrix} 0 \\ 0.75 \\ -0.25 \end{pmatrix}$	8j (→ Cr1_1)
Cr1_8		$\begin{pmatrix} 0.75 \\ 0.25 \\ 0.25 \end{pmatrix}$	$\begin{pmatrix} 0.25 \\ 0.25 \\ -0.5 \end{pmatrix}$	4f (→ Cr1_2)
O1_1	$\begin{pmatrix} 0 \\ 0.3057 \\ 0.1809 \end{pmatrix}$	$\begin{pmatrix} 0 \\ 0.3057 \\ 0.1809 \end{pmatrix}$	$\begin{pmatrix} -0.15955 \\ 0.3057 \\ -0.15955 \end{pmatrix}$	8j
O1_2		$\begin{pmatrix} 0 \\ 0.6943 \\ 0.1809 \end{pmatrix}$	$\begin{pmatrix} -0.15955 \\ 0.6943 \\ -0.15955 \end{pmatrix}$	8j (→ O1_1)
O1_3		$\begin{pmatrix} 0 \\ 0.3057 \\ 0.8191 \end{pmatrix}$	$\begin{pmatrix} 0.15955 \\ 0.3057 \\ 0.15955 \end{pmatrix}$	8j (→ O1_1)
O1_4		$\begin{pmatrix} 0 \\ 0.6943 \\ 0.8191 \end{pmatrix}$	$\begin{pmatrix} 0.15955 \\ 0.6943 \\ 0.15955 \end{pmatrix}$	8j (→ O1_1)
O1_5		$\begin{pmatrix} 0.1809 \\ 0 \\ 0.3057 \end{pmatrix}$	$\begin{pmatrix} -0.0067 \\ 0 \\ -0.1876 \end{pmatrix}$	4i
O1_6		$\begin{pmatrix} 0.1809 \\ 0 \\ 0.6943 \end{pmatrix}$	$\begin{pmatrix} 0.1876 \\ 0 \\ 0.0067 \end{pmatrix}$	4i
O1_7		$\begin{pmatrix} 0.8191 \\ 0 \\ 0.3057 \end{pmatrix}$	$\begin{pmatrix} 0.3124 \\ 0 \\ -0.5067 \end{pmatrix}$	4i
O1_8		$\begin{pmatrix} 0.8191 \\ 0 \\ 0.6943 \end{pmatrix}$	$\begin{pmatrix} 0.5067 \\ 0 \\ -0.3124 \end{pmatrix}$	4i

O1_9		$\begin{pmatrix} 0.3057 \\ 0.1809 \\ 0 \end{pmatrix}$	$\begin{pmatrix} -0.09715 \\ 0.1809 \\ -0.40285 \end{pmatrix}$	8j
O1_10		$\begin{pmatrix} 0.6943 \\ 0.1809 \\ 0 \end{pmatrix}$	$\begin{pmatrix} 0.09715 \\ 0.1809 \\ -0.59715 \end{pmatrix}$	8j (→ O1_9)
O1_11		$\begin{pmatrix} 0.3057 \\ 0.8191 \\ 0 \end{pmatrix}$	$\begin{pmatrix} -0.09715 \\ 0.8191 \\ -0.40285 \end{pmatrix}$	8j (→ O1_9)
O1_12		$\begin{pmatrix} 0.6943 \\ 0.8191 \\ 0 \end{pmatrix}$	$\begin{pmatrix} 0.09715 \\ 0.8191 \\ -0.59715 \end{pmatrix}$	8j (→ O1_9)
O1_13		$\begin{pmatrix} 0.5 \\ 0.8057 \\ 0.6809 \end{pmatrix}$	$\begin{pmatrix} 0.34045 \\ 0.8057 \\ -0.15955 \end{pmatrix}$	8j (→ O1_1)
O1_14		$\begin{pmatrix} 0.5 \\ 0.1943 \\ 0.6809 \end{pmatrix}$	$\begin{pmatrix} 0.34045 \\ 0.1943 \\ -0.15955 \end{pmatrix}$	8j (→ O1_1)
O1_15		$\begin{pmatrix} 0.5 \\ 0.8057 \\ 0.3191 \end{pmatrix}$	$\begin{pmatrix} 0.15955 \\ 0.8057 \\ -0.34045 \end{pmatrix}$	8j
O1_16		$\begin{pmatrix} 0.5 \\ 0.1943 \\ 0.3191 \end{pmatrix}$	$\begin{pmatrix} 0.15955 \\ 0.1943 \\ -0.34045 \end{pmatrix}$	8j (→ O1_15)
O1_17		$\begin{pmatrix} 0.6809 \\ 0.5 \\ 0.8057 \end{pmatrix}$	$\begin{pmatrix} 0.4933 \\ 0.5 \\ -0.1876 \end{pmatrix}$	4i (→ O1_5)
O1_18		$\begin{pmatrix} 0.6809 \\ 0.5 \\ 0.1943 \end{pmatrix}$	$\begin{pmatrix} 0.1876 \\ 0.5 \\ -0.4933 \end{pmatrix}$	4i (→ O1_7)
O1_19		$\begin{pmatrix} 0.3191 \\ 0.5 \\ 0.8057 \end{pmatrix}$	$\begin{pmatrix} 0.3124 \\ 0.5 \\ -0.0067 \end{pmatrix}$	4i (→ O1_6)
O1_20		$\begin{pmatrix} 0.3191 \\ 0.5 \\ 0.1943 \end{pmatrix}$	$\begin{pmatrix} 0.0067 \\ 0.5 \\ -0.3124 \end{pmatrix}$	4i (→ O1_8)
O1_21		$\begin{pmatrix} 0.8057 \\ 0.6809 \\ 0.5 \end{pmatrix}$	$\begin{pmatrix} 0.40285 \\ 0.6809 \\ -0.40285 \end{pmatrix}$	8j (→ O1_9)
O1_22		$\begin{pmatrix} 0.1943 \\ 0.6809 \\ 0.5 \end{pmatrix}$	$\begin{pmatrix} 0.09715 \\ 0.6809 \\ -0.09715 \end{pmatrix}$	8j

O1_23		$\begin{pmatrix} 0.8057 \\ 0.3191 \\ 0.5 \end{pmatrix}$	$\begin{pmatrix} 0.40285 \\ 0.3191 \\ -0.40285 \end{pmatrix}$	8j ($\rightarrow$ O1_9)
O1_24		$\begin{pmatrix} 0.1943 \\ 0.3191 \\ 0.5 \end{pmatrix}$	$\begin{pmatrix} 0.09715 \\ 0.3191 \\ -0.09715 \end{pmatrix}$	8j ($\rightarrow$ O1_22)

APPENDIX K

Order parameters and symmetry modes for the quadruple perovskite $BiCu_3Cr_4O_{12}$

Im-3[0,0,0]GM1+(a)
Im-3[0,0,0]GM2+GM3+(a,b)
Im-3[0,0,0]GM4+(0,a,0)
Im-3[1/2,1/2,0]N2-(0,0,0,a,0,0)

Table K.1: Order parameters of the phase transition in $BiCu_3Cr_4O_{12}$.The order parameter descriptions are in the notation of Miller and Love [71].

a1	Im-3[1/2,1/2,0]N2-(0,0,0,a,0,0)[Bi1:a]Tu_1(a)
a2	Im-3[1/2,1/2,0]N2-(0,0,0,a,0,0)[Bi1:a]Tu_2(a)
a3	Im-3[1/2,1/2,0]N2-(0,0,0,a,0,0)[Cu1:b]B1u(a)
a4	Im-3[1/2,1/2,0]N2-(0,0,0,a,0,0)[Cu1:b]B2u(a)
a5	Im-3[1/2,1/2,0]N2-(0,0,0,a,0,0)[Cr1:c]Au(a)
a6	Im-3[1/2,1/2,0]N2-(0,0,0,a,0,0)[Cr1:c]Eu*_1(a)
a7	Im-3[1/2,1/2,0]N2-(0,0,0,a,0,0)[Cr1:c]Eu*_2(a)
a8	Im-3[0,0,0]GM1+(a)[O1:g]A'_1(a)
a9	Im-3[0,0,0]GM1+(a)[O1:g]A'_2(a)
a10	Im-3[0,0,0]GM2+GM3+(a,b)[O1:g]A'_1(a)
a11	Im-3[0,0,0]GM2+GM3+(a,b)[O1:g]A'_1(b)
a12	Im-3[0,0,0]GM2+GM3+(a,b)[O1:g]A'_2(a)
a13	Im-3[0,0,0]GM2+GM3+(a,b)[O1:g]A'_2(b)
a14	Im-3[0,0,0]GM4+(0,a,0)[O1:g]A'_1(a)
a15	Im-3[0,0,0]GM4+(0,a,0)[O1:g]A'_2(a)
a16	Im-3[0,0,0]GM4+(0,a,0)[O1:g]A"_1(a)
a17	Im-3[0,0,0]GM4+(0,a,0)[O1:g]A"_2(a)
a18	Im-3[1/2,1/2,0]N2-(0,0,0,a,0,0)[O1:g]A'_1(a)
a19	Im-3[1/2,1/2,0]N2-(0,0,0,a,0,0)[O1:g]A'_2(a)
a20	Im-3[1/2,1/2,0]N2-(0,0,0,a,0,0)[O1:g]A'_3(a)
a21	Im-3[1/2,1/2,0]N2-(0,0,0,a,0,0)[O1:g]A'_4(a)
a22	Im-3[1/2,1/2,0]N2-(0,0,0,a,0,0)[O1:g]A'_5(a)
a23	Im-3[1/2,1/2,0]N2-(0,0,0,a,0,0)[O1:g]A'_6(a)
a24	Im-3[1/2,1/2,0]N2-(0,0,0,a,0,0)[O1:g]A'_7(a)
a25	Im-3[1/2,1/2,0]N2-(0,0,0,a,0,0)[O1:g]A'_8(a)
a26	Im-3[1/2,1/2,0]N2-(0,0,0,a,0,0)[O1:g]A"_1(a)
a27	Im-3[1/2,1/2,0]N2-(0,0,0,a,0,0)[O1:g]A"_2(a)

Table K.2: Symmetry modes of the phase transition in $BiCu_3Cr_4O_{12}$.The order parameter descriptions are in the notation of Miller and Love [71].

APPENDIX L

Peak width modeling of the quadruple perovskite $BiCu_3Cr_4O_{12}$ by Gaussian and Lorentzian crystallite size and Gaussian strain

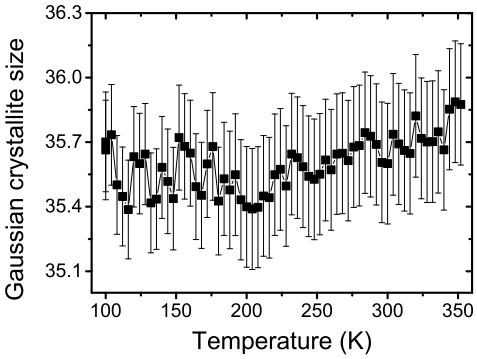

(a) Gaussian crystallite size parameter

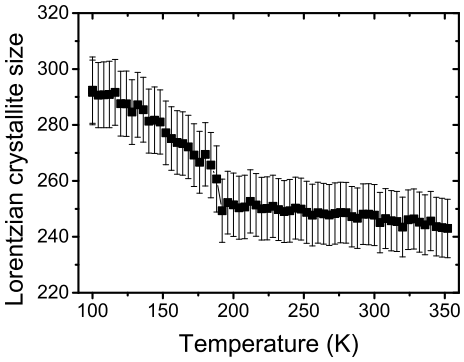

(b) Lorentzian crystallite size parameter

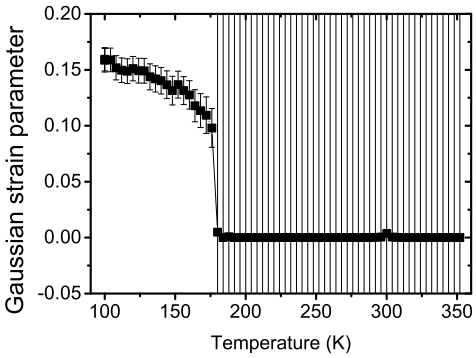

(c) Phenomenological Gaussian strain parameter

Figure L.1: Temperature dependent behavior of the Gaussian and Lorentzian crystallite size parameters as well as of the phenomenological Gaussian strain parameter (for information about these parameters see also section 4.4). The combination of these parameters is used to calculate the peak width of the $BiCu_3Cr_4O_{12}$ quadruple perovskite.

APPENDIX M

Strain calculation for the quadruple perovskite $BiCu_3Cr_4O_{12}$

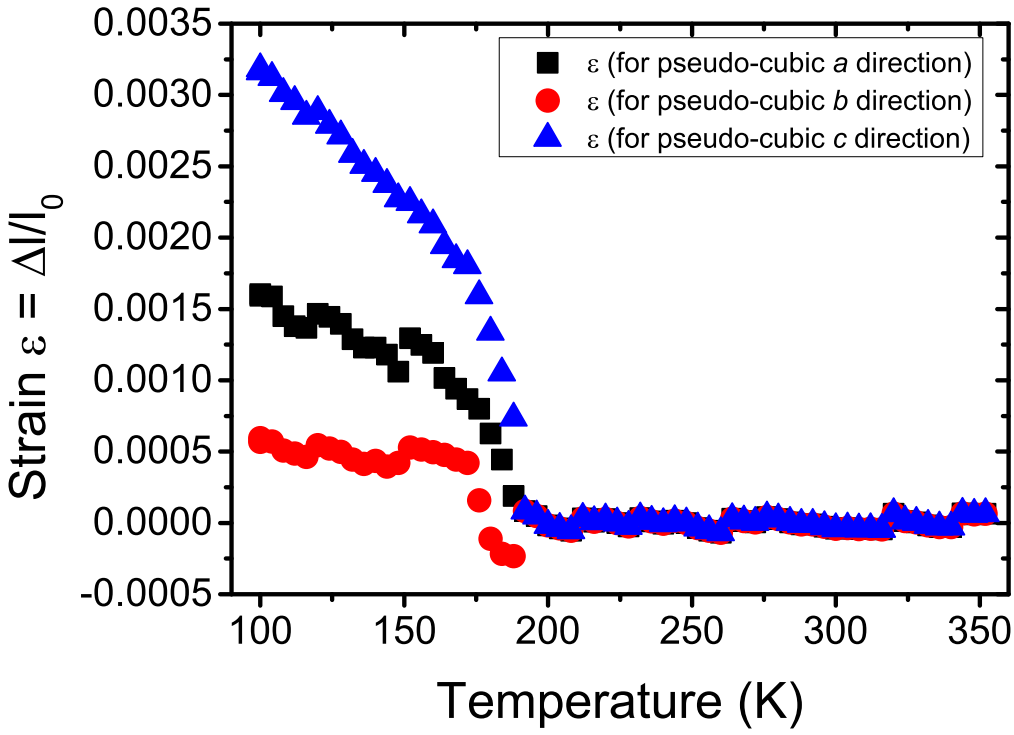

Figure M.1: Calculation of the temperature dependent pseudo-cubic lattice strains in the $BiCu_3Cr_4O_{12}$ quadruple perovskite. The cubic phase is assumed to be strain-free. The strains of the pseudo-cubic lattice parameters of the monoclinic phase are calculated in relation to the lattice parameters of the strain-free cubic phase at the same temperature.

APPENDIX N

Bond valence sum calculations for the quadruple perovskite $BiCu_3Cr_4O_{12}$ with 8% Cu^{2+} on the Cr-site

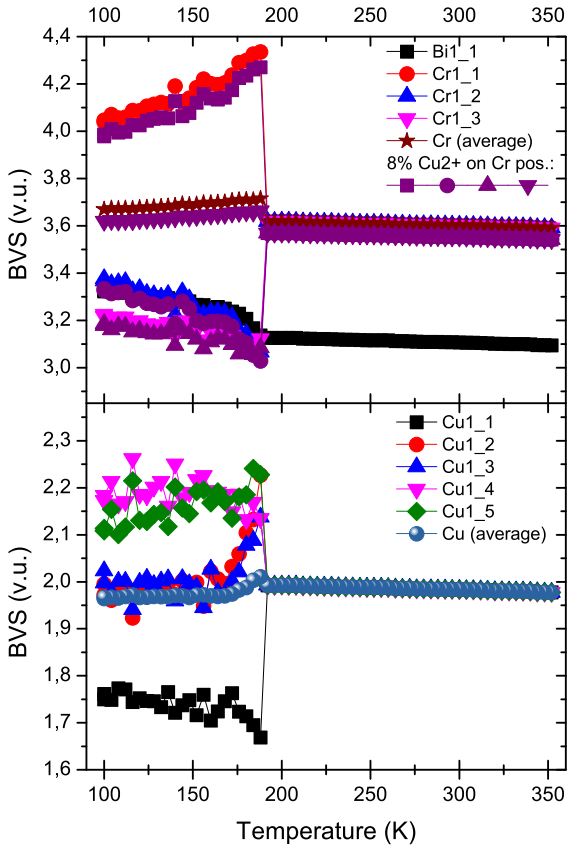

Figure N.1: Temperature dependent bond valence sum calculations for all cations in the $BiCu_3Cr_4O_{12}$ quadruple perovskite. This is in principle the same picture as given in figure 5.14, except that additional data points are calculated for a model where 8% Cu^{2+} is assumed on each Cr-site (see purple data points).

Symbols and Abbreviations

Symbols

Table 1: Physical constants from [276, table XLI].

Symbol	Value		Measurement unit	Description
c	2.99792458	10^{8}	$m \cdot s^{-1}$	speed of light in vacuum
e	1.602176565(35)	10^{-19}	C	elementary charge
eV	1.602176565(35)	10^{-19}	J	electronvolt
h	6.62606957(29)	10^{-34}	$J \cdot s$	Planck constant
h	4.135667516(91)	10^{-15}	$eV \cdot s$	
$\hbar$	1.054571726(47)	10^{-34}	$J \cdot s$	
$\hbar$	6.582118928(15)	10^{-16}	$eV \cdot s$	
k_B	1.3806488(13)	10^{-23}	$J \cdot K^{-1}$	Boltzmann constant
k_B	8.6173324(78)	10^{-5}	$eV \cdot K^{-1}$	
m_0	9.10938291(40)	10^{-31}	kg	electron mass
ε_0	8.854187817...	10^{-12}	$F \cdot m$	electric constant
μ_0	12.566370614...	10^{-7}	$N \cdot A^{-2}$	magnetic constant
G	6.67384(80)	10^{-11}	$m^3 \cdot kg^{-1} \cdot s^{-2}$	Newtonian constant of gravitation
N_A	6.02214129(27)	10^{23}	mol^{-1}	Avogadro constant
u	1.660538921(73)	10^{-27}	kg	(unified) Atomic mass unit $\frac{1}{12}$ m (^{12}C)

Abbreviations

ADP	anisotropic displacement parameter (dt. anisotroper Verschiebungsparameter)
AFM	antiferromagnetic (dt. antiferromagnetisch)
Bi	bismuth (dt. Bismut)
BNS	Belov, Neronova and Smirnova setting
BVS	bond valence sum (dt. Bindungsvalenzsumme)
CD	charge disproportionation (dt. Ladungsdisproportionierung)
CO	charge ordering (dt. Ladungsordnung)
Cu	copper (dt. Kupfer)
Cr	chromium (dt. Chrom)
DAC	diamond anvil cell (dt. Diamantstempelzelle)
DC	direct current (dt. Gleichstrom)
DFT	density functional theory (dt. Dichtefunktionaltheorie)
DSC	Differential Scanning Calorimetry (dt. Dynamische Differenzkalorimetrie)
EoS	equation of state (dt. Zustandsgleichung)
FC	field-cooled (dt. feldgekühlt)
Fe	iron (dt. Eisen)
FiM	ferrimagnetic (dt. ferrimagnetisch)
FM	ferromagnetic (dt. ferromagnetisch)
FOM	figure of merit (dt. Gütezahl)
FWHM	full width at half maximum (dt. Halbwertsbreite)
GOF	goodness of fit (dt. Güte der Anpassung)
HS	higher symmetry (dt. höhere Symmetrie)
ISCT	inter-site charge transfer (dt. Ladungstransfer zwischen verschiedenen Atomen)
La	lanthanum (dt. Lanthan)

LS	lower symmetry (dt. niedrigere Symmetrie)
NTE	negative thermal expansion (dt. negative thermische Ausdehnung)
O	oxygen (dt. Sauerstoff)
OG	Opechowski and Guccione setting
PTE	positive thermal expansion (dt. positive thermische Ausdehnung)
RB	rigid bbody (dt. starrer Körper)
Sr	strontium (dt. Strontium)
WPPD	whole powder pattern decomposition (dt. Zerlegung des gesamten Pulverdiffraktogramms)
WPPF	whole powder pattern fitting (dt. Anpassung des gesamten Pulverdiffraktogramms)

Bibliography

[1] N. A. Spaldin, M. Fiebig, *The Renaissance of Magnetoelectric Multiferroics*, Science **309**, 391 (2005) (cited on page 3)

[2] T. Lottermoser, *Multiferroika: Ein Material mit vielen Eigenschaften*, Online article at "Welt der Physik" (http://www.weltderphysik.de) (2009), Visited on 16-06-2015 (cited on page 3)

[3] W. Eerenstein, N. D. Mathur, J. F. Scott, *Multiferroic and magnetoelectric materials*, Nature **442**, 759 (2006) (cited on pages 3, 4, 35, 38, 169 and 173)

[4] R. Ramesh, N. A. Spaldin, *Multiferroics: progress and prospects in thin films*, Nature Materials **6**, 21 (2007) (cited on pages 3, 4, 37, 169 and 173)

[5] T. Lottermoser, *Multiferroika: Wie man Gegensätze vereint*, Online article at "Welt der Physik" (http://www.weltderphysik.de) (2009), Visited on 16-06-2015 (cited on page 3)

[6] *IEEE Standard on Magnetostrictive Materials: Piezomagnetic Nomenclature*, IEEE Std 319-1990 **319**, 1 (1991) (cited on page 3)

[7] V. K. Wadhawan, *Introduction to Ferroic Materials*, Gordon and Breach Science Publishers (2000) (cited on pages 3, 4, 32, 33, 36, 37, 38 and 257)

[8] C. Tabares-Munoz, J.-P. Rivera, A. Bezinges, A. Monnier, H. Schmid, *Measurement of the Quadratic Magnetoelectric Effect on Single Crystalline $BiFeO_3$*, Japanese Journal of Applied Physi **24**, 1051 (1985) (cited on pages 4, 169 and 173)

[9] G. Catalan, J. F. Scott, *Physics and Application of Bismuth Ferrite*, Advanced Materials **21**, 2463 (2009) (cited on pages 4, 41, 42, 169 and 173)

[10] H. M. Rietveld, *A Profile Refinement Method for Nuclear and Magnetic Structures*, Journal of Applied Crystallography **2**, 65 (1969) (cited on pages 4, 19 and 20)

[11] M. Etter, R. Dinnebier, *A Century of Powder Diffraction: a Brief History*, Zeitschrift fuer Anorganische und Allgemeine Chemie **640**, 3015 (2014) (cited on pages 7, 8, 10 and 19)

[12] E. Hecht, *Optik*, Oldenbourg Wissenschaftsverlag (2009) (cited on page 7)

[13] F. M. Grimaldi, *Physico mathesis de lumine, coloribus, et iride, aliisque annexis libri duo*, Vittorio Bonati (1665) (cited on page 7)

[14] W. C. Röntgen, *Ueber eine neue Art von Strahlen*, Aus den Sitzungsberichten der Würzburger Physik.-medic. Gesellschaft , 3 (1895) (cited on page 7)

[15] W. C. Röntgen, *Ueber eine neue Art von Strahlen*, Annalen der Physik **300**, 1 (1898) (cited on page 7)

[16] W. Friedrich, P. Knipping, M. von Laue, *Interferenzerscheinungen bei Röntgenstrahlen*, Bayerische Akademie der Wissenschaften / Mathematisch-Physikalische Klasse: Sitzungsberichte , 303 (1912) (cited on pages 7, 8 and 9)

[17] W. Friedrich, P. Knipping, M. von Laue, *Interferenzerscheinungen bei Röntgenstrahlen*, Annalen der Physik **346**, 971 (1913) (cited on pages 7, 8 and 9)

[18] M. von Laue, *Interferenzerscheinungen bei Röntgenstrahlen - Theoretischer Teil*, Naturwissenschaften **39**, 361 (1952) (cited on pages 7, 8 and 9)

[19] W. Friedrich, P. Knipping, *Interferenzerscheinungen bei Röntgenstrahlen - Experimenteller Teil*, Naturwissenschaften **39**, 364 (1952) (cited on page 7)

[20] P. P. Ewald (ed.), *Fifty Years of X-ray Diffraction*, International Union of Crystallography (1962) (cited on page 8)

[21] A. Authier, *Early Days of X-ray Crystallography*, International Union of Crystallography (Oxford University press) (2013) (cited on page 8)

[22] M. von Laue, *Eine quantitative Prüfung der Theorie für die Interferenzerscheinungen bei Röntgenstrahlen*, Annalen der Physik **346**, 989 (1913) (cited on page 8)

[23] F. D. Bloss, *Crystallography and Crystal Chemistry*, Holt, Rinehart and Winston, Inc. (1971) (cited on pages 8 and 247)

[24] R. E. Dinnebier, S. J. L. Billinge, *Powder Diffraction - Theory and Practice*, chap. Principles of Powder Diffraction pp. 1–19, The Royal Society of Chemistry (RCS) (2008) (cited on pages 8, 17, 247 and 248)

[25] W. L. Bragg, *The Diffraction of Short Electromagnetic Waves by a Crystal*, Proceedings of the Cambridge Philosophical Society **17**, 43 (1912) (cited on page 8)

[26] P. Debye, *Zerstreuung von Röntgenstrahlen*, Annalen der Physik **351**, 809 (1915) (cited on page 10)

[27] B. E. Warren, *X-ray diffraction*, Dover Publications Inc. (1990) (cited on page 10)

[28] W. Friedrich, *Eine Interferenzerscheinung bei Röntgenstrahlen*, Physikalische Zeitschrift **14**, 317 (1913) (cited on page 10)

[29] S. Nishikawa, S. Ono, *Transmission of X-Rays through Fibrous, Lamellar and Granular Substances*, Proceedings of the Tokyo Mathematico-Physical Society **7**, 131 (1913) (cited on page 10)

[30] P. Debye, P. Scherrer, *Interferenzen an regellos orientierten Teilchen im Röntgenlicht. I.*, Nachrichten von der Gesellschaft der Wissenschaften zu Göttingen, Mathematisch-Physikalische Klasse , 1 (1916) (cited on page 10)

[31] A. W. Hull, *A New Method of X-Ray Crystal Analysis*, Physical Review **10**, 661 (1917) (cited on pages 10 and 11)

[32] P. P. Ewald, *Zur Theorie der Interferenzen der Röntgenstrahlen in Kristallen*, Physikalische Zeitschrift **11**, 465 (1913) (cited on page 11)

[33] P. Scherrer, *Bestimmung der Größe und der inneren Struktur von Kolloidteilchen mittels Röntgenstrahlen*, Nachrichten von der Gesellschaft der Wissenschaften zu Göttingen, Mathematisch-Physikalische Klasse , 98 (1918) (cited on page 13)

[34] C. Runge, *Die Bestimmung eines Kristallsystems durch Röntgenstrahlen*, Physikalische Zeitschrift **18**, 509 (1917) (cited on page 15)

[35] T. Ito, *A General Powder X-Ray Photography*, Nature **164**, 755 (1949) (cited on page 15)

[36] P. de Wolff, *On the determination of unit-cell dimensions from powder diffraction patterns*, Acta Crystallographica **10**, 590 (1957) (cited on page 15)

[37] J. W. Visser, *A Fully Automatic Program for Finding the Unit Cell from Powder Data*, Journal of Applied Crystallography **2**, 89 (1969) (cited on page 15)

[38] R. Shirley, *Overview of powder-indexing program algorithms (history and strengths and weaknesses)*, International Union of Crystallography - Commission on Crystallographic Computing - Newsletter **2**, 48 (2003) (cited on page 15)

[39] A. Altomare, C. Giacovazzo, A. Moliterni, *Powder Diffraction - Theory and Practice*, chap. Indexing and Space Group Determination pp. 206–226, The Royal Society of Chemistry (RCS) (2008) (cited on pages 15, 17, 18 and 257)

[40] P. E. Werner, *Trial-and-error computer methods for the indexing of unknown powder patterns*, Zeitschrift für Kristallographie **120**, 375 (1964) (cited on page 15)

[41] D. Louër, *Indexing of Powder Diffraction Patterns*, Materials Science Forum **79–82**, 17 (1991) (cited on pages 15 and 17)

[42] D. Louër, M. Louër, *Méthode d'essais et erreurs pour l'indexation automatique des diagrammes de poudre*, Journal of Applied Crystallography **5**, 271 (1972) (cited on page 15)

[43] D. Louër, R. Vargas, *Indexation automatique des diagrammes de poudre par dichotomies successives*, Journal of Applied Crystallography **15**, 542 (1982) (cited on page 17)

[44] A. Boultif, D. Louër, *Indexing of powder diffraction patterns for low-symmetry lattices by the successive dichotomy method*, Journal of Applied Crystallography **24**, 987 (1991) (cited on page 17)

[45] P. M. de Wolff, *A simplified criterion for the reliability of a powder pattern indexing*, Journal of Applied Crystallography **1**, 108 (1968) (cited on pages 17 and 85)

[46] G. S. Smith, R. L. Snyder, *F_N: A criterion for rating powder diffraction patterns and evaluating the reliability of powder-pattern indexing*, Journal of Applied Crystallography **12**, 60 (1979) (cited on page 17)

[47] B. M. Kariuki, S. A. Belmonte, M. I. McMahon, R. L. Johnston, K. D. M. Harris, R. J. Nelmes, *A new approach for indexing powder diffraction data based on whole-profile fitting and global optimization using a genetic algorithm*, Journal of Synchrotron Radiation **6**, 87 (1999) (cited on page 17)

[48] A. A. Coelho, *Indexing of powder diffraction patterns by iterative use of singular value decomposition*, Journal of Applied Crystallography **36**, 86 (2003) (cited on page 17)

[49] A. L. Bail, *Monte Carlo indexing with McMaille*, Powder Diffraction **19**, 249 (2004) (cited on page 17)

[50] C. Giacovazzo, *Fundamental of Crystallography*, chap. Crystallographic Computing pp. 67–151, No. 7 in IUCr Texts on Crystallography. Oxford University Press, 2 edn. (2002) (cited on pages 18, 19 and 257)

[51] H. M. Rietveld, *The Crystal Structure of some Alkaline Earth Metal Uranates of the Type M_3UO_6*, Acta Crystallographica **20**, 508 (1966) (cited on page 19)

[52] H. M. Rietveld, *Line profiles of neutron powder-diffraction peaks for structure refinement.*, Acta Crystallographica **22**, 151 (1967) (cited on page 19)

[53] G. Malmros, J. O. Thomas, *Least-Squares Structure Refinement Based on Profile Analysis of Powder Film Intensity Data Measured on an Automatic Microdensitometer*, Journal of Applied Crystallography **10**, 7 (1977) (cited on page 19)

[54] C. P. Khattak, D. E. Cox, *Profile Analysis of X-ray Powder Diffractometer Data: Structural Refinement of* $La_{0.75}Sr_{0.25}CrO_3$, Journal of Applied Crystallography **10**, 405 (1977) (cited on page 19)

[55] R. A. Young, P. E. Mackie, R. B. von Dreele, *Application of the Pattern-Fitting Structure-Refinement Method to X-ray Powder Diffractometer Patterns*, Journal of Applied Crystallography **10**, 262 (1977) (cited on page 19)

[56] V. K. Pecharsky, P. Y. Zavalij, *Fundamentals of Powder Diffraction and Structural Characterization of Materials*, Springer Science+Business Media, LLC, 2nd edn. (2009) (cited on pages 20, 21 and 23)

[57] Bruker AXS, Karlsruhe, Germany, *Bruker AXS (2008): TOPAS V4.2: General profile and structure analysis software for powder diffraction data. - User's Manual, Bruker AXS, Karlsruhe, Germany* (2008) (cited on pages 20, 21, 49, 75, 76, 85, 98, 118, 137, 139, 145, 179 and 260)

[58] R. Dinnebier, M. Müller, *Modern Diffraction methods*, chap. Modern Rietveld Refinement, a Practical Guide pp. 27–60, Wiley-VCH Verlag GmbH & Co. KGaA (2013) (cited on pages 20, 21 and 23)

[59] R. B. von Dreele, *Powder Diffraction - Theory and Practice*, chap. Rietveld refinement pp. 266–281, The Royal Society of Chemistry (RCS) (2008) (cited on pages 21 and 98)

[60] A. C. Larson, R. B. V. Dreele, *General Structure Analysis System (GSAS)*, Los Alamos National Laboratory Report LAUR 86-748 (2004) (cited on page 21)

[61] G. W. Stinton, J. S. O. Evans, *Parametric Rietveld refinement*, Journal of Applied Crystallography **40**, 87 (2007) (cited on page 22)

[62] G. S. Pawley, *Unit-Cell Refinement From Powder Diffraction Scans*, Journal of Applied Crystallography **14**, 357 (1981) (cited on pages 22 and 180)

[63] A. Le Bail, H. Duroy, J. L. Fourquet, *Ab-initio Structure Determination of* $LiSbWO_6$ *by X-ray Powder Diffraction*, Materials Research Bulletin **23**, 447 (1988) (cited on pages 22, 77, 85 and 180)

[64] B. J. Campbell, H. T. Stokes, D. E. Tanner, D. M. Hatch, *ISODISPLACE: a web-based tool for exploring structural distortions*, Journal of Applied Crystallography **39**, 607 (2006) (cited on pages 24, 56, 109, 110, 111, 118, 120, 141, 143, 149 and 259)

[65] J. Rodríguez-Carvajal, F. Bourée, *Symmetry and magnetic structures*, EPJ Web of Conferences **22**, 1 (2012) (cited on pages 24, 25, 26, 27, 29, 30 and 56)

[66] B. J. Campbell, J. S. O. Evans, F. Perselli, H. T. Stokes, *Rietveld refinement of structural distortion-mode amplitudes*, International Union of Crystallography - Commission on Crystallographic Computing - Newsletter **8**, 81 (2007) (cited on page 24)

[67] L. D. Landau, E. F. Lifshitz, *Statistical Physics - Part 1*, Course of theoretical Physics **5**, Pergamon Press, 3rd edn. (1980) (cited on pages 24, 32, 33, 63, 82 and 153)

[68] E. K. H. Salje, *Phase transitions in Ferroelastic and co-elastic crystals - Student edition*, Cambridge University Press, cambridge topics in mineral physics and chemistry edn. (1993) (cited on pages 24, 32, 33, 38, 63, 82, 149 and 153)

[69] M. T. Dove, *Theory of displacive phase transitions in minerals*, American Mineralogist **85**, 212 (1997) (cited on pages 24, 63, 82 and 153)

[70] J. M. Perez-Mato, D. Orobengoa, M. I. Aroyo, *Mode crystallography of distorted structures*, Acta Crystallographica Section A: Foundations of Crystallography **66**, 558 (2010) (cited on page 24)

[71] S. C. Miller, W. F. Love, *Tables of Irreducible Representations of Space Groups and Co-Representations of Magnetic Space Groups*, Pruett Press, Boulder (1967) (cited on pages 24, 109, 110, 120, 211, 212, 259 and 261)

[72] H. T. Stokes, D. M. Hatch, J. D. Wells, *Group-theoretical methods for obtaining distortions in crystals: Application to vibrational modes and phase transitions*, Physical Review B **43**, 11010 (1991) (cited on page 24)

[73] H. T. Stokes, D. M. Hatch, *Isotropy subgroups of the 230 crystallographic space groups*, World Scientific Publishing Co. Pte. Ltd. (1988) (cited on page 24)

[74] D. M. Hatch, H. T. Stokes, *Complete listing of order parameters for a crystalline phase transition: A solution to the generalized inverse Landau problem*, Physical Review B **65**, 014113 (2001) (cited on page 24)

[75] D. Orobengoa, C. Capillas, M. I. Aroyo, J. M. Perez-Mato, *AMPLIMODES: symmetry-mode analysis on the Bilbao Crystallographic Server*, Journal of Applied Crystallography **42**, 820 (2009) (cited on page 24)

[76] M. I. Aroyo, J. M. Perez-Mato, D. Orobengoa, E. Tasci, G. de la Flor, A. Kirov, *Crystallography online: Bilbao Crystallographic Server*, Bulgarian Chemical Communications **43**, 183 (2011) (cited on pages 25 and 56)

[77] M. I. Aroyo, J. M. Perez-Mato, C. Capillas, E. Kroumova, S. Ivantchev, G. Madariaga, A. Kirov, H. Wondratschek, *Bilbao Crystallographic Server I: Databases and crystallographic computing programs*, Zeitschrift für Kristallographie **221**, 15 (2006) (cited on pages 25 and 56)

[78] M. I. Aroyo, A. Kirov, C. Capillas, J. M. Perez-Mato, H. Wondratschek, *Bilbao Crystallographic Server II: Representations of crystallographic point groups and space groups*, Acta Crystallographica Section A: Foundations of Crystallography **62**, 115 (2006) (cited on pages 25 and 56)

[79] F. D. Bergevin, M. Brunel, *Observation of magnetic superlattice peaks by X-ray diffraction on an antiferromagnetic NiO crystal*, Physics Letters A **39**, 141 (1972) (cited on page 25)

[80] M. J. Cooper, *X-RAY MAGNETIC SCATTERING*, Acta Physica Polonica A **82**, 137 (1992) (cited on page 25)

[81] M. J. M. J. Cooper, W. G. Stirling, *Magnetic X-ray scattering*, Radiation Physics and Chemistry **56**, 85 (1999) (cited on page 25)

[82] W. G. Stirling, M. J. Cooper, *X-ray magnetic scattering*, Journal of Magnetism and Magnetic Materials **200**, 755 (1999) (cited on page 25)

[83] J. Rodríguez-Carvajal, *Recent advances in magnetic structure determination by neutron powder diffraction*, Physica B **192**, 55 (1993) (cited on pages 25, 26, 27, 49, 53, 54, 58, 141 and 179)

[84] R. J. Harrison, *Neutron diffraction of magnetic materials*, Reviews in Mineralogy and Geochemistry **63**, 113 (2006) (cited on pages 25, 26, 27 and 56)

[85] N. Belov, N. Neronova, T. Smirnova, *The 1651 Shubnikov groups*, Trudy Instituta Kristallografii Akad. Nauk. S.S.S.R. **11**, 33 (1955) (cited on page 30)

[86] N. V. Belov, N. N. Neronova, T. S. Smirnova, *Shubnikov groups*, Soviet Physics, crystallography **2**, 311 (1957) (cited on page 30)

[87] W. Opechowski, R. Guccione, *Magnetism - Statistical models, magnetic symmetry, hyperfine interactions, and metals*, Magnetism **IIA**, chap. Magnetic Symmetry pp. 105–165, New York Academic Press, New York (1965) (cited on page 30)

[88] W. Opechowski, *Crystallographic and metacrystallographic groups*, Amsterdam, North-Holland (1986) (cited on page 30)

[89] D. B. Litvin, *Changes in the Opechowski-Guccione Symbols for Magnetic Space Groups due to changes in the International Tables Crystallography*, Ferroelectrics **204**, 211 (1997) (cited on page 30)

[90] D. B. Litvin, *On Opechowski-Guccione Magnetic Space-Group Symbols*, Acta Crystallographica Section A: Foundations of Crystallography **54**, 257 (1998) (cited on page 30)

[91] D. B. Litvin, *Magnetic space-group types*, Acta Crystallographica Section A: Foundations of Crystallography **57**, 729 (2001) (cited on page 30)

[92] P. Ehrenfest, *Phasenumwandlungen im ueblichen und erweiterten Sinn, classifiziert nach den entsprechenden Singularitaeten des thermodynamischen Potentiales*, Proceedings Koninklijke Akademie van Wetenschappen **36**, 153 (1933) (cited on pages 31, 32 and 65)

[93] W. Nolting, *Spezielle Relativitätstheorie, Thermodynamik*, Springer Verlag, grundkurs theoretische physik edn. (2005) (cited on pages 31 and 32)

[94] W. Nolting, *Statistische Physik*, Springer Verlag, grundkurs theoretische physik edn. (2005) (cited on pages 31, 32, 33 and 64)

[95] U. Müller, *Symmetriebeziehungen zwischen verwandten Kristallstrukturen*, Vieweg+Teubner Verlag (2012) (cited on pages 32 and 33)

[96] P. Chandra, P. B. Littlewood, in *Physics of Ferroelectrics*, eds. K. M. Rabe, H. Ahn, J.-M. Triscone, Topics in Applied Physics **105**, pp. 69–116. Springer (2007) (cited on page 32)

[97] S.-W. Cheong, M. Mostovoy, *Multiferroics: a magnetic twist for ferroelectricity*, Nature Materials **6**, 13 (2007) (cited on pages 36 and 37)

[98] S. Picozzi, C. Ederer, *First principles studies of multiferroic materials*, Journal of Physics: Condensed Matter **21**, 303201 (2009) (cited on pages 36 and 38)

[99] B. Hillebrands, S. Blügel, in *Festkörper*, ed. R. Kassing, Bergmann, Schaefer - Lehrbuch der Experimentalphysik **6**, chap. 5 pp. 401–484. Walter de Gruyter (2005) (cited on pages 37 and 38)

[100] H. Schmid, *Multi-ferroic magnetoelectrics*, Ferroelectrics **162**, 317 (1994) (cited on page 38)

[101] M. Fiebig, *Revival of the magnetoelectric effect*, Journal of Physics D: Applied Physics **38**, R123 (2005) (cited on page 38)

[102] A. K. Agyei, J. L. Birman, *On the linear magnetoelectric effect*, Journal of Physics: Condensed Matter **2**, 3007 (1990) (cited on page 38)

[103] C. Michel, J.-M. Moreau, G. D. Achenbach, R. GErson, W. J. James, *The atomic structure of $BiFeO_3$*, Solid State Communications **7**, 701 (1969) (cited on page 41)

[104] J. R. Teague, R. Gerson, W. J. James, *Dielectric Hysteresis in single crystal $BiFeO_3$*, Solid State Communications **8**, 1073 (1970) (cited on page 41)

[105] V. A. Khomchenko, D. A. Kiselev, J. M. Vieira, L. Jian, A. L. Kholkin, A. M. L. Lopes, Y. G. Pogorelov, J. P. Araujo, M. Maglione, *Effect of diamagnetic Ca, Sr, Pb, and Ba substitution on the crystal structure and multiferroic properties of the $BiFeO_3$ perovskite*, Journal of Applied Physics **103**, 024105 (2008) (cited on pages 41, 42, 44, 45 and 49)

[106] P. Ravindran, R. Vidya, A. Kjekshus, H. Fjellvag, *Theoretical investigation of magnetoelectric behavior in $BiFeO_3$*, Physical Review B **74**, 224412 (2006) (cited on page 41)

[107] Y.-H. Chu, L. W. Martin, M. B. Holcomb, R. Ramesh, *Controlling magnetism with mulitferroics*, Materials Today **10**, 16 (2007) (cited on pages 41 and 42)

[108] D. C. Arnold, K. S. Knight, F. D. Morrison, P. Lightfoot, *Ferroelectric-Paraelectric Transition in $BiFeO_3$: Crystal Structure of the Orthorhombic β Phase*, Physical Review Letters **102**, 027602 (2009) (cited on page 41)

[109] S. Kiselev, R. Ozerov, G. Zhdanov, *Detection of magnetic arrangement in $BiFeO_3$ ferroelectric by means of neutron diffraction study*, DOKLADY AKADEMII NAUK SSSR **145**, 1255 (1962) (cited on pages 41, 55 and 64)

[110] S. V. Kiselev, R. P. Ozerov, G. S. Zhdanov, *Detection of magnetic order in ferroelectric $BiFeO_3$ by neutron diffraction*, Soviet Physics - Doklady **7**, 742 (1963), Translation of DOKLADY AKADEMII NAUK SSSR (cited on pages 41, 55 and 64)

[111] J. M. Moreau, C. Michel, R. Gerson, W. J. James, *Ferroelectric $BiFeO_3$ X-ray and Neutron Diffraction Study*, Journal of Physics and Chemistry of Solids **32**, 1315 (1971) (cited on pages 41 and 55)

[112] I. Sosnowska, T. Peterlin-Neumaier, E. Steichele, *Spiral magnetic ordering in bismuth ferrite*, Journal of Physics C: Solid State Physics **15**, 4835 (1982) (cited on pages 42, 55, 56 and 58)

[113] I. Sosnowska, M. Loewenhaupt, W. I. F. David, R. M. Ibberson, *Investigation of the unusual magnetic spiral arrangement in $BiFeO_3$*, Physica B: Condensed Matter **180–181**, 117 (1992) (cited on pages 42, 55 and 58)

[114] A. A. Gippius, D. F. Khozeev, E. N. Morozova, A. V. Zalessky, *Observation of spin modulated magnetic structure at Bi- and Fe-sites in $BiFeO_3$ by nuclear magnetic resonance*, Physica Status Solidi A: Applications and Materials Science **196**, 221 (2003) (cited on page 42)

[115] A. A. Bush, A. A. Gippius, A. V. Zalesskii, E. N. Morozova, *^{209}Bi NMR spectrum of $BiFeO_3$ in the presence of spatial modulation of hyperfine fields*, Journal of Experimental and Theoretical Physics Letters **78**, 389 (2003) (cited on page 42)

[116] P. Fischer, M. Polomska, I. Sosnowska, M. Szymanski, *Temperature dependence of the crystal and magnetic structure of $BiFeO_3$*, Journal of Physics C: Solid State Physics **13**, 1931 (1980) (cited on pages 42 and 64)

[117] R. Przenioslo, A. Palewicz, M. Regulski, I. Sosnowska, R. M. Ibberson, K. S. Knight, *Does the modulated magnetic structure of $BiFeO_3$ change at low temperatures?*, Journal of Physics: Condensed Matter **18**, 2069 (2006) (cited on page 42)

[118] J. Herrero-Albillos, G. Catalan, J. A. Rodriguez-Velamazan, M. Viret, D. Colson, J. F. Scott, *Neutron diffraction study of the $BiFeO_3$ spin cycloid at low temperature*, Journal of Physics: Condensed Matter **22**, 256001 (2010) (cited on page 42)

[119] M. Ramazanoglu, W. Ratcliff, Y. J. Choi, S. Lee, S.-W. Cheong, V. Kiryukhin, *Temperature-dependent properties of the magnetic order in single-crystal $BiFeO_3$*, Physical Review B **83**, 174434 (2011) (cited on page 42)

[120] D. Lebeugle, D. Colson, A. Forget, M. Viret, A. M. Bataille, A. Gukasov, *Electric-Field-Induced Spin Flop in $BiFeO_3$ Single Crystal at Room Temperature*, Physical Review Letters **100**, 227602 (2008) (cited on page 42)

[121] S. Lee, W. Ratcliff, S.-W. Cheong, V. Kiryukhin, *Electric field control of the magnetic state in $BiFeO_3$ single crystals*, Applied Physics Letters **92**, 192906 (2008) (cited on page 42)

[122] C. Ederere, N. A. Spaldin, *Weak ferromagnetism and magnetoelectric coupling in bismuth ferrite*, Physical Review B **71**, 060401 (2005) (cited on page 42)

[123] J. Wang, J. B. Neaton, H. Zhen, V. Nagarajan, S. B. Ogale, B. Liu, D. Viehland, V. Vaithyanathan, D. G. Schlom, U. V. Waghmare, N. A. Spaldin, K. M. Rabe, M. Wuttig, R. Ramesh, *Epitaxial $BiFeO_3$ Multiferroic Thin Film Heterostructures*, Science **299**, 1719 (2003) (cited on page 42)

[124] X. Zhang, Y. Sui, X. Wang, J. Tang, W. Su, *Influence of diamagnetic Pb doping on the crystal structure and multiferroic properties of the $BiFeO_3$ perovskite*, Journal of Applied Physics **105**, 07D918 (2009) (cited on page 42)

[125] M. Al-Haj, *X-ray diffraction and magnetization studies of $BiFeO_3$ multiferroic compounds substituted by Sm3+, Gd3+, Ca2+*, Crystal Research and Technology **45**, 89 (2010) (cited on page 42)

[126] I. Sosnowska, W. Schäfer, W. Kockelmann, K. H. Andersen, I. O. Troyanchuk, *Crystal structure and spiralmagnetic ordering of $BiFeO_3$ doped with manganese*, Applied Physics A: Materials Science & Processing **74**, S1040 (2002) (cited on page 42)

[127] J. B. MacChesney, J. J. Jetzt, J. F. Potter, H. J. Williams, R. C. Sherwood, *Electric and Magnetic Properties of the System $SrFeO_3$-$BiFeO_3$*, Journal of the American Ceramic Society **49**, 644 (1966) (cited on pages 42, 43, 44, 58 and 60)

[128] J. Li, Y. Duan, H. He, D. Song, *Crystal structure, electronic structure, and magnetic properties of bismuth-strontium ferrites*, Journal of Alloys and Compounds **315**, 259 (2001) (cited on pages 43, 44, 58, 60 and 61)

[129] C. Lepoittevin, S. Malo, N. Barrier, N. Nguyen, G. vanG. van Tendeloo. Hervieu, *Long-range ordering in the $Bi_{(1-x)}Ae_xFeO_{3-x/2}$ perovskites: $Bi_{1/3}Sr_{2/3}FeO_{2.67}$ and $Bi_{1/2}Ca_{1/2}FeO_{2.75}$*, Journal of Solid State Chemistry **181**, 2601 (2008) (cited on pages 43, 44 and 60)

[130] V. V. Pokatilov, V. S. Pokatilov, A. S. Sigov, V. M. Cherepanov, *Magnetic Properties and Valence States of The Fe Ions in $Bi_{0.5}Sr_{0.5}FeO_{3-y}$*, Inorganic Materials **45**, 683 (2009) (cited on pages 43, 60 and 64)

[131] V. S. P. V. V. Pokatilov, A. S. Sigov, V. M. Cherepanov, *Magnetic States of Iron Ions in $Bi_{0.75}Sr_{0.25}FeO_{3-y}$*, Bulletin of the Russian Academy of Sciences. Physics **73**, 956 (2009) (cited on pages 43, 45, 60 and 64)

[132] A. A. Gippius, A. V. Tkachev, N. E. Gervits, V. S. Pokatilov, A. O. Konovalova, A. S. Sigov, *Evolution of spin-modulated magnetic structure in multiferroic compound $Bi_{(1-x)}Sr_xFeO_3$*, Solid State Communications **152**, 552 (2012) (cited on page 43)

[133] V. S. Pokatilov, A. O. Konovalova, A. S. Sigov, *Features of Local Crystallographic, Magnetic, and Valence State of Iron Ions in $Bi_{1-x}Sr_xFeO_3$ Perovskites at x = 0-0.67*, Bulletin of the Russian Academy of Sciences. Physics **77**, 695 (2013) (cited on pages 43 and 67)

[134] Y. Takeda, K. Kanno, T. Takada, O. Yamamoto, M. Takano, N. Nakayama, Y. Bando, *Phase Relation in the Oxygen Nonstoichiometric System $SrFeO_x$ ($2.5 \leq x \leq 3.0$)*, Journal of Solid State Chemistry **63**, 237 (1986) (cited on page 43)

[135] J. P. Hodges, S. Short, J. D. Jorgensen, X. Xiong, B. Dabrowski, S. M. Mini, C. W. Kimball, *Evolution of Oxygen-Vacancy Ordered Crystal Structures in the Perovskite Series $Sr_nFe_nO_{3n-1}$ (n = 2, 4, 8, and ∞), and the Relationship to Electronic and Magnetic Properties*, Journal of Solid State Chemistry **151**, 190 (2000) (cited on page 43)

[136] M. Schmidt, S. J. Campbell, *In situ neutron diffraction study (300-1273 K) of non-stoichmetric strontium ferrite $SrFeO_x$*, Journal of Physics and Chemistry of Solids **63**, 2085 (2002) (cited on page 43)

[137] M. Reehuis, C. Ulrich, A. Maljuk, C. Niedermayer, B. Ouladdiaf, A. Hoser, T. Hofmann, B. Keimer, *Neutron diffraction study of spin and charge ordering in $SrFeO_{3-\delta}$*, Physical Review B **85**, 184109 (2012) (cited on page 43)

[138] A. S. Anokhin, A. G. Razumnaya, V. I. Torgashev, V. G. Trotsenko, Y. I. Yuzyuk, A. A. Bush, V. Y. Shkuratov, B. P. Gorshunov, E. S. Zhukova, L. S. Kadyrov, G. A. Komandin, *Dynamic Spectral Response of Solid Solutions of the Bismuth-Strontium Ferrite $Bi_{1-x}Sr_xFeO_{3-\delta}$ in the Frequency Range 0.3-200 THz*, Physics of Solid State **55**, 1417 (2013) (cited on pages 43, 58 and 60)

[139] K. Brinkman, T. Iijima, H. Takamura, *The oxygen permeation characteristics of $Bi_{1-x}Sr_xFeO_3$ mixed ionic and electronic conducting ceramics*, Solid State Ionics **181**, 53 (2010) (cited on pages 43, 58 and 60)

[140] M. Zheng-Zheng, L. Jian-Qing, C. Zi-Peng, T. Zhao-Ming, H. Xiao-Jun, H. Hai-Jun, *Multiferroic properties and exchange bias in $Bi_{1-x}Sr_xFeO_3$ (x = 0-0.6) ceramics*, Chinese Physics B **23**, 097505 (2014) (cited on pages 43, 44, 45 and 60)

[141] V. A. Khomchenko, D. A. Kiselev, J. M. Vieira, A. L. Kholkin, M. A. Sá, Y. G. Pogorelov, *Synthesis and multiferroic properties of $Bi_{0.8}A_{0.2}FeO_3$ (A=Ca,Sr,Pb) ceramics*, Applied Physics Letters **90**, 242901 (2007) (cited on pages 44 and 45)

[142] V. A. Khomchenko, D. A. Kiselev, E. K. Selezneva, J. M. Vieira, A. M. L. Lopes, Y. G. Pogorelov, J. P. Araujo, A. L. Kholkin, *Weak ferromagnetism in diamagnetically-doped $Bi_{1-x}A_xFeO_3$ (A=Ca, Sr, Pb, Ba) multiferroics*, Materials Letters **62**, 1927 (2008) (cited on pages 44 and 45)

[143] V. A. Khomchenko, D. A. Kiselev, M. Kopcewicz, M. Maglione, V. V. Shvartsman, P. Borisov, W. Kleemann, A. M. L. Lopes, Y. G. Pogorelov, J. P. Araujo, R. M. Rubinger, N. A. Sobolev, J. M. Vieira, A. L. Kholkin, *Doping strategies for increased performance in $BiFeO_3$*, Journal of Magnetism and Magnetic Materials **321**, 1692 (2009) (cited on pages 44 and 45)

[144] R. L. Withers, L. Bourgeois, K. Balamurugan, N. H. Kumar, P. N. Santhosh, P. M. Woodward, *A TEM investigation of the $(Bi_{1-x}Sr_x)Fe^{3+}O_{3-x/2}$, $0.2 \leq x \leq 0.67$, solid solution and a suggested superspace structural description thereof*, Journal of Solid State Chemistry **182**, 2176 (2009) (cited on page 44)

[145] R. L. Withers, J. Schiemer, L. Bourgeois, L. Norén, Y. Liu, *A careful phase analysis and TEM investigation of the incommensurately modulated, $(Bi_{1-x}M^{II})Fe^{III}O_{3-x/2}$ (M = Ca and Sr), solid solution phases*, Journal of Physics: Conferences Series **226**, 012015 (2010) (cited on page 44)

[146] I. O. Troyanchuk, D. V. Karpinskii, M. V. Bushinskii, A. N. Chobot, N. V. Pushkarev, O. Prohnenko, M. Kopcewicz, R. Szymczak, *Crystal and Magnetic Structures of the $Bi_{1-x}Sr_xFeO_{3-\delta}$ and $Bi_{1-x}A_xFe_{1-x}Mn_xO_3$ (A = Sr, Ca) Solid Solutions*, Crystallography Reports **54**, 1172 (2009) (cited on pages 44, 45, 49, 52 and 54)

[147] I. O. Troyanchuk, M. V. Bushinsky, D. V. Karpinsky, V. Sirenko, V. Sikolenko, V. Efimov, *Structural and magnetic phases of $Bi_{1-x}A_xFeO_{3-\delta}$ (A = Sr, Pb) perovskites*, The European Physical Journal B **73**, 375 (2010) (cited on pages 44, 45, 49, 51, 52, 54, 58, 60 and 67)

[148] E. Pachoud, Y. Bréard, C. Martin, A. Maignan, A. M. Abakumov, E. Suard, R. I. Smith, M. R. Suchomel, *$Bi_{0.75}Sr_{0.25}FeO_{3-\delta}$: Revealing order/disorder phenomena by combining diffraction techniques*, Solid State Communications **152**, 331 (2012) (cited on pages 44, 45, 51 and 54)

[149] L. Y. Wang, D. H. Wang, H. B. Huang, Z. D. Han, Q. Q. Cao, B. X. Gu, Y. W. Du, *The magnetic properties of polycrystalline $Bi_{1-x}Sr_xFe_{1-x}Mn_xO_3$ ceramics*, Journal of Alloys and Compounds **469**, 1 (2009) (cited on page 44)

[150] A. Wedig, *Oxygen Exchange Kinetics of the Potential Solid Oxide Fuel Cell Cathode Material (Bi,Sr)(Co,Fe)$O_{3-\delta}$*, Ph.D. thesis, Fakultät Chemie der Universität Stuttgart (2013) (cited on pages 46 and 48)

[151] L. A. Chick, L. R. Pederson, G. D. Maupin, J. L. Bates, L. E. Thomas, G. J. Exarhos, *Glycine-nitrate combustion synthesis of oxide ceramic powders*, Materials Letters **10**, 6 (1990) (cited on page 46)

[152] A. P. Hammersley, S. O. Svensson, M. Hanfland, A. N. Fitch, D. Hausermann, *Two-Dimensional Detector Software: From Real Detector to Idealised Image of Two-Theta Scan*, High Pressure Research **14**, 235 (1996) (cited on pages 47, 74 and 135)

[153] A. Hoelzel, A. Senyshyn, N. Juenke, H. Boysen, W. Schmahl, H. Fuess, *High-resolution neutron powder diffractometer SPODI at research reactor FRMII*, Nuclear Instruments and Methods in Physics Research Section A: Accelerators, Spectrometers, Detectors and Associated Equipment **667**, 32 (2012) (cited on pages 47 and 58)

[154] R. Merkle, J. Maier, *How Is Oxygen Incorporated into Oxides? A Comprehensive Kinetic Study of a Simple Solid-State Reaction with $SrTiO_3$ as a Model Material*, Angewandte Chemie International Edition **47**, 3874 (2008) (cited on page 48)

[155] R. Merkle, J. Maier, *Wie wird Sauerstoff in Oxide eingebaut? Kinetische Studie einer "simplen" Feststoffreaktion am Modellmaterial $SrTiO_3$*, Angewandte Chemie **120**, 3936 (2008) (cited on page 48)

[156] C.-J. Shin, H.-I. Yoo, *Al-doped $SrTiO_3$: Part II, unusual thermodynamic factor and chemical diffusivity*, Solid State Ionics **78**, 1089 (2007) (cited on page 48)

[157] A. K. Eriksson, F. Lindberg, G. Svensson, P. Svedlindh, P. F. Henry, S.-G. Eriksson, C. S. Knee, *Influence of iron addition on the oxygen-deficient $Sr_{0.85}Bi_{0.15}Co_{1-x}Fe_xO_{3-\delta}$ $(0.0 \leq x \leq 1.0)$ perovskites*, Journal of Solid State Chemistry **181**, 2031 (2008) (cited on pages 49 and 52)

[158] G. Caglioti, A. Paoletti, F. Ricci, *Choice of collimators for a crystal spectrometer for neutron diffraction*, Nuclear Instruments **3**, 223 (1958) (cited on page 49)

[159] R. W. Cheary, A. Coelho, *A Fundamental Parameters Approach to X-ray Line-Profile Fitting*, Journal of Applied Crystallography **25**, 109 (1992) (cited on pages 49, 76 and 137)

[160] R. W. Cheary, A. A. Coelho, J. P. Cline, *Fundamental Parameters Line Profile Fitting in Laboratory Diffractometers*, Journal of Research of the National Institute of Standards and Technology **109**, 1 (2004) (cited on pages 49, 76 and 137)

[161] L. W. Finger, D. E. Cox, A. P. Jephcoat, *A correction for powder diffraction peak asymmetry due to axial divergence*, Journal of Applied Crystallography **27**, 892 (1994) (cited on page 50)

[162] B. E. Warren, *X-Ray Diffraction in Random Layer Lattices*, Physical Review B **59**, 693 (1941) (cited on page 53)

[163] S. Bette, R. E. Dinnebier, D. Freyer, *Structure solution and refinement of stacking faulted NiCl(OH)*, to be published in Journal of Applied Crystallography (cited on page 53)

[164] J. M. Perez-Mato, S. V. Gallego, E. S. Tasci, L. Elcoro, G. de la Flor, M. I. Aroyo, *Symmetry-Based Computational Tools for Magnetic Crystallography*, Annual Review of Materials Research **45**, 13.1 (2015) (cited on page 56)

[165] G. Shirane, *A Note on the Magnetic Intensities of Powder Neutron Diffraction:*, Acta Crystallographica **12**, 282 (1959) (cited on page 56)

[166] R. D. Shannon, *Revised effective ionic radii and systematic studies of interatomic distances in halides and chalcogenides*, Acta Crystallographica Section A: Crystal Physics, Diffraction, Theoretical and General Crystallography **32**, 751 (1976) (cited on page 60)

[167] H. W. Williams, B. L. Chamberland, *Determination of Curie, Néel, or crystallographic transition temperatures via differential scanning calorimetry*, Analytical Chemistry **41**, 2084 (1969) (cited on pages 64, 65 and 66)

[168] L. Pál, *First-Order magnetic phase transitions*, Acta Physica Academiae Scientiarum Hungaricae **27**, 47 (1969) (cited on page 65)

[169] M. S. Leu, C. S. Tsai, C. S. Lin, S. T. Lin, *The determination of Curie temperature by differential scanning calorimetry under magnetic field*, IEEE Transactions on Magnetics **27**, 5414 (1991) (cited on page 65)

[170] G. W. H. Höhne, W. F. Hemminger, H.-J. Flammersheim, *Differential Scanning Calorimetry*, Springer-Verlag, Berlin Heidelberg, GmbH, 2nd edn. (2003) (cited on page 65)

[171] P. Grosseau, B. Guilhot, A. Bachiorrini., *Curie temperature measurement by thermomagnetic analysis (TMA) and differential scanning calorimetry (DSC)*, in *XIV Convegno Nazionale di Calorimetria e di Analisi Termica*, pp. .281–285 (1992) (cited on page 66)

[172] V. S. Borisov, I. V. Maznichenko, D. Böttcher, S. Ostanin, A. Ernst, J. Henk, I. Mertig, *Magnetic exchange interactions and antiferromagnetism of ATcO3 (A = Ca, Sr, Ba) studied from first principles*, Physical Review B **85**, 134410 (2012) (cited on pages 69, 170 and 174)

[173] M. Etter, M. Müller, M. Hanfland, R. Dinnebier, *High-pressure phase transitions in the rare-earth orthoferrite $LaFeO_3$*, Acta Crystallographica Section B: Structural Science, Crystal Engineering and Materials **70**, 452 (2014) (cited on page 71)

[174] M. Etter, M. Müller, M. Hanfland, R. Dinnebier, *Possibilities and limitations of parametric Rietveld refinement on high pressure data: The case study of $LaFeO_3$*, Zeitschrift für Kristallographie - Crystalline Materials **229**, 246 (2014) (cited on page 71)

[175] M. Etter, R. E. Dinnebier, *Direct parameterization of the pressure-dependent volume by using an inverted approximate Vinet equation of state*, Journal of Applied Crystallography **47**, 384 (2014) (cited on pages 71 and 94)

[176] L. Gao, Y. Y. Xue, F. Chen, Q. Xiong, R. L. Meng, D. Ramirez, C. W. Chu, *Superconductivity up to 164 K in $HgBa_2Ca_{m-1}Cu_mO_{2m+2+\delta}$ (m=1, 2, and 3) under quasihydrostatic pressures*, Physical Review B **50**, 4260 (1994) (cited on page 71)

[177] W. C. Koehler, E. O. Wollan, *Neutron-diffraction study of the magnetic properties of perovskite-like compounds $LaBO_3$*, Journal of Physical and Chemical Solids **2**, 100 (1957) (cited on page 71)

[178] T. Peterlin-Neumaier, E. Steichele, *Antiferromagnetic structure of $LaFeO_3$ from high resolution TOF neutron diffraction.*, Journal of Magnetism and Magnetic Materials **59**, 351 (1986) (cited on pages 72 and 73)

[179] J. W. Seo, E. E. Fullerton, F. Nolting, A. Scholl, J. Fompeyrine, J.-P. Locquet, *Antiferromagnetic $LaFeO_3$ thin films and their effect on exchange bias*, Journal of Physics: Condensed Matter **20**, 264014 (2008) (cited on page 72)

[180] T. Fujii, I. Matsusue, J. Takada, in *Advanced Aspects of Spectroscopy*, ed. M. A. Farrukh, chap. 13 pp. 373–390. InTech (2012) (cited on page 72)

[181] G. R. Hearne, M. P. Pasternak, R. D. Taylor, P. Lacorre, *Electronic structure and magnetic properties of $LaFeO_3$ at high pressure*, Physical Review B **51**, 11495 (1995) (cited on pages 72, 86 and 88)

[182] S. C. Abrahams, R. L. . Barns, J. L. Bernstein, *Ferroelastic effect in lanthanum orthoferrite*, Solid State Communications **10**, 379 (1972) (cited on page 72)

[183] A. Fossdal, M.-A. Einarsrud, T. Grande, *Mechanical properties of $LaFeO_3$ ceramics*, Journal of the European Ceramic Society **25**, 927 (2005) (cited on page 72)

[184] S. Acharya, J. Mondal, S. Ghosh, S. K. Roy, P. K. Chakrabarti, *Multiferroic behavior of lanthanum orthoferrite ($LaFeO_3$)*, Materials Letters **64**, 415 (2010) (cited on pages 72 and 130)

[185] S. M. Selbach, J. R. Tolchard, A. Fossdal, T. Grande, *Non-linear thermal evolution of the crystal structure and phase transitions of $LaFeO_3$ investigated by high temperature X-ray diffraction*, Journal of Solid State Chemistry **196**, 249 (2012) (cited on pages 72, 73 and 81)

[186] S. Stolen, F. Gronvold, H. Brinks, T. Atake, H. Mori, *Heat capacity and thermodynamic properties of $LaFeO_3$ and $LaCoO_3$ from $T = 13$ K to $T = 1000$ K*, Journal of Chemical Thermodynamics **30**, 365 (1998) (cited on page 72)

[187] M. Eibschütz, S. Shtrikman, D. Treves, *Mössbauer Studies of Fe^{57} in Orthoferrites*, Physical Review **156**, 562 (1967) (cited on page 72)

[188] A. M. Glazer, *The classification of tilted octahedra in perovskites*, Acta Crystallographica B **28**, 3384 (1972) (cited on pages 72, 107 and 109)

[189] S. Geller, P. M. Raccah, *Phase Transitions in Perovskitelike Compounds of the Rare Earths*, Physical Review B **2**, 1167 (1970) (cited on page 72)

[190] V. M. Goldschmidt, *Die Gesetze der Krystallochemie*, Naturwissenschaften **14**, 477 (1926) (cited on page 72)

[191] W. M. Xu, O. Naaman, G. K. Rozenberg, M. P. Pasternak, R. D. Taylor, *Pressure-induced breakdown of a correlated system: The progressive collapse of the Mott-Hubbard state in $RFeO_3$*, Physical Review B **64**, 094411 (2001) (cited on pages 72, 86, 88, 129 and 130)

[192] S. Javaid, M. J. Akhtar, I. Ahmad, M. Younas, S. H. Shah, I. Ahmad, *Pressure driven spin crossover and isostructural phase transition in $LaFeO_3$*, Journal of Applied Physics **114**, 243712 (2013) (cited on pages 72, 86, 88 and 130)

[193] S. Javaid, M. J. Akhtar, *Pressure-induced magnetic, structural, and electronic phase transitions in $LaFeO_3$: a density functional theory (generalized gradient approximation) + U study*, Journal of Applied Physics **116**, 023704 (2014) (cited on pages 72, 86, 88 and 130)

[194] H. K. Mao, J. Xu, P. M. Bell, *Calibration of the Ruby Pressure Gauge to 800 kbar under Quasi-Hydrostatic Conditions*, Journal of Geophysical Research **91**, 4673 (1986) (cited on page 74)

[195] P. W. Stephens, *Phenomenological model of anisotropic peak broadening in powder diffraction*, Journal of Applied Crystallography **32**, 281 (1999) (cited on page 77)

[196] H. Shimizu, H. Tashiro, T. Kume, S. Sasaki, *High-Pressure Elastic Properties of Solid Argon to 70 GPa*, Physical Review Letters **86**, 4568 (2001) (cited on page 77)

[197] L. W. Finger, R. M. Hazen, G. Zou, H. K. Mao, P. M. Bell, *Structure and compression of crystalline argon and neon at high pressure and room temperature*, Applied Physics Letters **39**, 892 (1981) (cited on page 77)

[198] F. Datchi, P. Loubeyre, R. LeToullec, *Extended and accurate determination of the melting curves of argon, helium, ice (H_2O), and hydrogen (H_2)*, Physical Review B **61**, 6535 (2000) (cited on page 77)

[199] G. W. Stinton, I. Loa, L. F. Lundegaard, M. I. McMahon, *The crystal structures of δ and $\delta*$ nitrogen*, The Journal of Chemical Physics **131**, 104511 (2009) (cited on page 77)

[200] J. Belak, R. LeSar, R. D. Etters, *Calculated thermodynamic properties and phase transitions of solid N_2 at temperatures $0 \leq T \leq 300$ K and pressures $0 \leq P \leq 100$ GPa*, The Journal of Chemical Physics **92**, 5430 (1990) (cited on page 77)

[201] R. L. Mills, D. H. Liebenberg, J. C. Bronson, *Melting properties and ultrasonic velocity of nitrogen to 20 kbar*, The Journal of Chemical Physics **63**, 4026 (1975) (cited on page 77)

[202] A. K. MacMahan, *Structural transitions and metallization in compressed solid argon*, Physical Review B **33**, 5344 (1986) (cited on page 77)

[203] H. Katzke, P. Tolédano, *Theoretical descritpion of pressure- and temperature-induced structural phase transition mechanisms of nitrogen*, Physical Review B **78**, 064103 (2008) (cited on page 77)

[204] S. Geller, E. A. Wood, *Crystallographic studies of perovskite-like compounds. I. Rare earth orthoferrites and $YFeO_3$, $YCrO_3$, $YAlO_3$*, Acta Crystallographica **9**, 563 (1956) (cited on pages 77, 78 and 258)

[205] M. Marezio, P. D. Dernier, *The bond lengths in $LaFeO_3$*, Materials Research Bulletin **6**, 23 (1971) (cited on pages 77, 78 and 258)

[206] X. Yang, P. Juhás, S. J. L. Billinge, *On the estimation of statistical uncertainties on powder diffraction and small-angle scattering data from two-dimensional X-ray detectors*, Journal of Applied Crystallography **47**, 1273 (2014) (cited on page 77)

[207] N. L. Ross, J. Zhao, R. J. Angel, *High-pressure structural behavior of $GdAlO_3$ and $GdFeO_3$ perovskites*, Journal of Solid State Chemistry **177**, 3768 (2004) (cited on page 81)

[208] H. Bärnighausen, *Group-subgroup relations between space groups: A useful tool in crystal chemistry*, Match **9**, 139 (1980) (cited on pages 84, 86 and 250)

[209] G. K. Rozenberg, M. P. Pasternak, W. M. Xu, L. S. Dubrovinsky, S. Carlson, R. D. Taylor, *Consequence of pressure-instigated spin crossover in $RFeO_3$ perovskites; a volume collapse with no symmetry modification*, Europhysics Letters **71**, 228 (2005) (cited on pages 86 and 88)

[210] R. J. Angel, M. Bujak, J. Zhao, G. D. Gatta, S. D. Jacobsen, *Effective hydrostatic limits of pressure media for high-pressure crystallographic studies*, Journal of Applied Crystallography **40**, 26 (2007) (cited on pages 89, 90, 93, 97, 108, 114, 258 and 259)

[211] S. Klotz, J.-C. Chervin, P. Munsch, G. L. Marchand, *Hydrostatic limits of 11 pressure transmitting media*, Journal of Physics D: Applied Physics **42**, 075413 (2009) (cited on page 90)

[212] F. Birch, *Finite Elastic Strain of Cubic Crystals*, Physical Review **71**, 809 (1947) (cited on page 91)

[213] R. Jeanloz, *Universal equation of state*, Physical Review B **38**, 805 (1988) (cited on page 91)

[214] F. D. Murnaghan, *The Compressibility of Media under Extreme Pressures*, Proc. Natl. Acad. Sci USA **30**, 244 (1944) (cited on pages 91, 93, 97, 108, 114, 258 and 259)

[215] P. Vinet, J. R. Smith, J. Ferrante, J. H. Rose, *Temperature effects on the universal equation of state of solids*, Physical Review B **35**, 1945 (1987) (cited on pages 91 and 93)

[216] I. Halasz, R. Dinnebier, R. Angel, *Parametric Rietveld refinement for the evaluation of powder diffraction patterns collected as a function of pressure*, Journal of Applied Crystallography **43**, 504 (2010) (cited on pages 92, 93 and 258)

[217] R. J. Angel, in *Reviews in Mineralogy & Geochemistry Volume 39: Transformation Processes in Minerals*, eds. S. Redfern, M. Carpenter, P. Ribbe, Reviews in Mineralogy & Geochemistry Volume **39**, chap. 4 pp. 85–104. Mineralogical Society of America, Washington D.C. (2000) (cited on pages 92, 93, 94 and 258)

[218] R. J. Angel, in *Reviews in Mineralogy & Geochemistry Volume 41: High-Temperature and High-Pressure Crystal Chemistry*, eds. R. Hazen, R. Downs,

P. Ribbe, Reviews in Mineralogy & Geochemistry Volume **41**, chap. 2 pp. 35–59. Mineralogical Society of America, Geochemical Society, Washington D.C. (2000) (cited on pages 92, 93, 94 and 258)

[219] I. R. Shein, K. I. Shein, V. L. Kozhevnikov, A. L. Ivanoskii, *Band Structure and the Magnetic and Elastic Properties of $SrFeO_3$ and $LaFeO_3$ Perovskites*, Physics of the Solid State **47**, 2082 (2005), Translated from Fizika Tverdogo Tela, Vol. 47, No. 11, 2005, pp. 1998-2003 (cited on pages 92, 93 and 258)

[220] F. Birch, *Finite strain isotherm and velocities for single-crystal and polycrystalline NaCl at high pressures and 300°K*, Journal of Geophysical Research: Solid Earth **83**, 1257 (1978) (cited on pages 92, 93 and 258)

[221] N. L. Ross, J. Zhao, B. J. Burt, T. D. Chaplin, *Equations of state of $GdFeO_3$ and $GdAlO_3$ perovskites*, Journal of Physics: Condensed Matter **16**, 5721 (2004) (cited on pages 93 and 258)

[222] P. Vinet, J. H. Rose, J. Ferrante, J. R. Smith, *Universal features of the equation of state of solids*, Journal of Physics: Condensed Matter **1**, 1941 (1989) (cited on page 93)

[223] R. E. Cohen, O. Gülseren, R. J. Hemley, *Accuracy of equation-of-state formulations*, American Mineralogist **85**, 338 (2000) (cited on page 93)

[224] R. E. Dinnebier, *Rigid bodies in powder diffraction*, Powder Diffraction **14**, 84 (1999) (cited on page 98)

[225] K. S. Aleksandrov, *The sequences of structural phase transitions in perovskites*, Ferroelectrics **14**, 801 (1976) (cited on pages 107 and 109)

[226] P. M. Woodward, *Octahedral Tilting in Perovskites. I. Geometrical Considerations*, Acta Crystallographica Section B: Structural Science, Crystal Engineering and Materials **53**, 32 (1997) (cited on pages 107 and 109)

[227] P. M. Woodward, *Octahedral Tilting in Perovskites. II. Structure Stabilizing Forces*, Acta Crystallographica Section B: Structural Science, Crystal Engineering and Materials **53**, 44 (1997) (cited on pages 107 and 109)

[228] C. J. Howard, H. T. Stokes, *Group-Theoretical Analysis of Octahedral Tilting in Perovskites*, Acta Crystallographica Section B: Structural Science, Crystal Engineering and Materials **54**, 782 (1998) (cited on pages 107 and 109)

[229] R. J. Angel, J. Zhao, N. L. Ross, *General Rules for Predicting Phase Transitions in Perovskites due to Octahedral Tilting*, Physical Review Letters **95**, 025503 (2005) (cited on pages 107 and 109)

[230] D. Wang, R. J. Angel, *Octahedral tilts, symmetry-adapted displacive modes and polyhedral volume ratios in perovskite structures*, Acta Crystallographica Section B: Structural Science, Crystal Engineering and Materials **67**, 302 (2011) (cited on pages 107 and 109)

[231] M. Müller, R. E. Dinnebier, A.-C. Dippel, H. T. Stokes, B. J. Campbell, *A symmetry-mode description of rigid-body-rotations in crystalline solids: a case study of $Mg[H_2O]_6RbBr_3$*, Journal of Applied Crystallography **47**, 532 (2014) (cited on page 117)

[232] C. J. Howard, B. J. Kennedy, P. M. Woodward, *Ordered double perovskites - a group-theoretical analysis*, Acta Crystallographica Section B: Structural Science, Crystal Engineering and Materials **59**, 463 (2003) (cited on page 131)

[233] I. Yamada, K. Tsuchida, K. Ohgushi, N. Hayashi, J. Kim, N. Tsuji, R. Takahashi, M. Matsushita, N. Nishiyama, T. Inoue, T. Irifune, K. Kato, M. Takata, M. Takano, *Giant Negative Thermal Expansion in the Iron Perovskite $SrCu_3Fe_4O_{12}$*, Angewandte Chemie International Edition **50**, 6579 (2011) (cited on pages 131, 133, 151 and 166)

[234] I. Yamada, K. Shiro, H. Etani, S. Marukawa, N. Hayashi, M. Mizumaki, Y. Kusano, S. Ueda, H. Abe, T. Irifune, *Valence Transitions in Negative Thermal Expansion Material $SrCu_3Fe_4O_{12}$*, Inorganic Chemistry **53**, 10563 (2014) (cited on pages 131 and 133)

[235] H. Li, S. Liu, L. Chen, J. Zhao, B. Chen, Z. Wang, J. Meng, X. Liu, *First-principles study of negative thermal expansion mechanism in A-site-ordered perovskite $SrCu_3Fe_4O_{12}$*, RSC Advances **5**, 1801 (2015) (cited on pages 131 and 133)

[236] I. Yamada, H. Etani, K. Tsuchida, S. Marukawa, N. Hayashi, T. Kawakami, M. Mizumaki, K. Ohgushi, Y. Kusano, J. Kim, N. Tsuji, R. Takahashi, N. Nishiyama, T. Inoue, T. Irifune, M. Takano, *Control of Bond-Strain-Induced Electronic Phase Transitions in Iron Perovskites*, Inorganic Chemistry **52**, 13751 (2013) (cited on pages 131, 132, 133 and 137)

[237] N. Rezaei, P. Hansmann, M. S. Bahramy, R. Arita, *Mechanism of charge transfer/disproportionation in $LnCu_3Fe_4O_{12}$ (Ln = lanthanides)*, Physical Review B **89**, 125125 (2014) (cited on pages 131, 132 and 133)

[238] Y. W. Long, N. Hayashi, T. Saito, M. Azuma, S. Muranaka, Y. Shimakawa, *Temperature-induced A-B intersite charge transfer in an A-site-ordered $LaCu_3Fe_4O_{12}$ perovskite*, Nature **458**, 60 (2009) (cited on pages 131 and 133)

[239] Y. wen Long, T. Kawakami, W. tin Chen, T. Saito, T. Watanuki, Y. Nakakura, Q. qing Liu, C. qing Jin, Y. Shimakawa, *Pressure Effect on Intersite Charge*

Transfer in A-site-Ordered Double-Perovskite-Structure Oxide, Chemistry of Materials **24**, 2235 (2012) (cited on pages 131 and 133)

[240] H. Li, S. Lv, Z. Wang, Y. Xia, Y. Bai, X. Liu, J. Meng, *Mechanism of A-B intersite charge transfer and negative thermal expansion in A-site-ordered perovskite $LaCu_3Fe_4O_{12}$*, Journal of Applied Physics **111**, 103718 (2012) (cited on pages 131 and 133)

[241] R. Allub, B. Alascio, *A thermodynamic model for the simultaneous charge/spin order transition in $LaCu_3Fe_4O_{12}$*, Journal of Physics: Condensed Matter **24**, 495601 (2012) (cited on pages 131 and 133)

[242] W.-T. Chen, T. Saito, N. Hayashi, M. Takano, Y. Shimakawa, *Ligand-hole localization in oxides with unusual valence Fe*, Scientific Reports (Nature Group) **2**, 1 (2012) (cited on pages 131, 132 and 133)

[243] I. Yamada, S. Marukawa, M. Murakami, S. Mori, *"True" negative thermal expansion in Mn-doped $LaCu_3Fe_4O_{12}$ perovskite*, Applied Physics Letters **105**, 231906 (2014) (cited on pages 131 and 133)

[244] Y. Long, T. Saito, T. Tohyama, K. Oka, M. Azuma, Y. Shimakawa, *Intermetallic Charge Transfer in A-Site-Ordered Double Perovskite $BiCu_3Fe_4O_{12}$*, Inorganic Chemistry **48**, 8489 (2009) (cited on pages 131, 132 and 133)

[245] H. Li, S. Lv, X. Liu, J. Meng, *First-principles investigation of A-B intersite charge transfer and correlated electrical and magnetic properties in $BiCu_3Fe_4O_{12}$*, Journal of Computational Chemistry **32**, 1235 (2011) (cited on pages 131, 132 and 133)

[246] S. Zhang, T. Saito, M. Mizumaki, Y. Shimakawa, *Temperature-Induced Intersite Charge Transfer Involving Cr ions in A-Site-Ordered Perovskites $ACu_3Cr_4O_{12}$ (A=La and Y)*, Chemisty A European Journal **20**, 9510 (2014) (cited on pages 131, 132, 133, 137, 149, 158, 162 and 165)

[247] I. Yamada, K. Takata, N. Hayashi, S. Shinohara, M. Azuma, S. Mori, S. Muranaka, Y. Shimakawa, M. Takano, *A Perovskite Containing Quadrivalent Iron as a Charge-Disproportionated Ferrimagnet*, Angewandte Chemie **47**, 7032 (2008) (cited on pages 131, 132 and 133)

[248] Y. Shimakawa, *A-Site-Ordered Perovskites with Intriguing Physical Properties*, Inorganic Chemistry **47**, 8562 (2008) (cited on pages 131, 132, 133 and 140)

[249] I. Yamada, H. Etani, M. Murakami, N. Hayashi, T. Kawakami, M. Mizumaki, S. Ueda, H. Abe, K.-D. Liss, A. J. Studer, T. Ozaki, S. Mori, R. Takahashi, T. Irifune, *Charge-Order Melting in Charge-Disproportionated Perovskite $CeCu_3Fe_4O_{12}$*, Inorganic Chemistry **53**, 11794 (2014) (cited on pages 131, 132 and 133)

[250] H. Etani, I. Yamada, K. Ohgushi, N. Hayashi, Y. Kusano, M. Mizumaki, J. Kim, N. Tsuji, R. Takahashi, N. Nishiyama, T. Inoue, T. Irifune, M. Takano, *Suppression of Intersite Charge Transfer in Charge-Disproportionated Perovskite $YCu_3Fe_4O_{12}$*, Journal of the American Chemical Society **135**, 6100 (2013) (cited on pages 131, 132 and 133)

[251] M. Marezio, P. Dernier, J. Chenavas, J. Joubert, *High pressure synthesis and crystal structure of $NaMn_7O_{12}$*, Journal of Solid State Chemistry **6**, 16 (1973) (cited on pages 131 and 134)

[252] A. Prodi, E. Gilioli, A. Gauzzi, F. Licci, M. Marezio, F. Bolzoni, Q. Huang, A. Santoro, J. W. Lynn, *Charge, orbital and spin ordering phenomena in the mixed valence manganite $(NaMn_3^{+3})(Mn_3^{+2}Mn_4^{+2})O_{12}$*, Nature Materials **3**, 48 (2004) (cited on pages 131 and 134)

[253] S. V. Streltsov, D. I. Khomskii, *Jahn-Teller distortion and charge, orbital, and magnetic order in $NaMn_7O_{12}$*, Physical Review B **89**, 201115 (2014) (cited on pages 131 and 134)

[254] A. Prodi, A. Daoud-Aladine, F. Gozzo, B. Schmitt, O. Lebedev, G. van Tendeloo, E. Gilioli, F. Bolzoni, H. Aruga-Katori, H. Takagi, M. Marezio, A. Gauzzi, *Commensurate structural modulation in the charge- and orbitally ordered phase of the quadruple perovskite $(NaMn_3)Mn_4O_{12}$*, Physical Review B **90**, 180101 (2014) (cited on pages 131, 134, 146, 161, 166 and 167)

[255] G. Zhang, S. Dong, Z. Yan, Y. Guo, Q. Zhang, S. Yunoki, E. Dagotto, J.-M. Liu, *Multiferroic properties of $CaMn_7O_{12}$*, Physical Review B **84**, 174413 (2011) (cited on pages 131 and 134)

[256] R. D. Johnson, L. C. Chapon, D. D. Khalyavin, P. Manuel, P. G. Radaelli, C. Martin, *Giant Improper Ferroelectricity in the Ferroaxial Magnet $CaMn_7O_{12}$*, Physical Review Letters **108**, 067201 (2012) (cited on pages 131 and 134)

[257] A. Gauzzi, G. Rousse, F. Mezzadri, G. L. Calestani, G. André, F. Bourée, M. Calicchio, E. Gilioli, R. Cabassi, F. Bolzoni, A. Prodi, P. Bordet, M. Marezio, *Magnetoelectric coupling driven by inverse magnetostriction in multiferroic $BiMn_3Mn_4O_{12}$*, Journal of Applied Physics **113**, 043920 (2013) (cited on pages 132 and 134)

[258] M. A. Subramanian, W. J. Marshall, T. G. Calvarese, A. W. Sleight, *Valence degeneracy in $CaCu_3Cr_4O_{12}$*, Journal of Physics and Chemistry of Solids **64**, 1569 (2003) (cited on pages 133, 162 and 165)

[259] K. Takata, I. Yamada, M. Azuma, M. Takano, Y. Shimakawa, *Magnetoresistance and electronic structure of the half-metallic ferrimagnet $BiCu_3Mn_4O_{12}$*, Physical Review B **76**, 024429 (2007) (cited on page 133)

[260] Z. Zeng, M. Greenblatt, M. A. Subramanian, M. Croft, *Large Low-Field Magnetoresistance in Perovskite-type $CaCu_3Mn_4O_{12}$ without Double Exchange*, Physical Review Letters **82**, 3164 (1999) (cited on page 134)

[261] J. Sánchez-Benítez, J. A. Alonso, M. J. Martínez-Lope, M. T. Casais, J. L. Martínez, A. de Andrés, M. T. Fernández-Díaz, *Preparation, Crystal and Magnetic Structure, and Magnetotransport Properties of the Double Perovskite $CaCu_{2.5}Mn_{4.5}O_{12}$*, Chemistry of Materials **15**, 2193 (2003) (cited on page 134)

[262] J. A. Alonso, J. Sánchez-Benítez, A. D. Andrés, M. J. Martínez-Lope, M. T. Casais, J. L. Martínez, *Enhanced magnetoresistance in the complex perovskite $LaCu_3Mn_4O_{12}$*, Applied Physics Letters **83**, 2623 (2003) (cited on page 134)

[263] N. Imamura, M. Karppinen, T. Motohashi, D. Fu, M. Itoh, H. Yamauchi, *Positive and Negative Magnetodielectric Effects in A-Site Ordered $(BiMn_3)Mn_4O_{12}$ Perovskite*, Journal of the American Chemical Society **130**, 14948 (2008) (cited on page 134)

[264] N. Imamura, M. Karppinen, H. Yamauchi, *Synthesis and Properties of Monoclinic and Cubic Forms of the A-Site-Ordered $(BiMn_3)Mn_4O_{12}$ Perovskite*, Chemistry of Materials **21**, 2179 (2009) (cited on page 134)

[265] R. Przenioslo, I. Sosnowska, E. Suard, A. Hewat, A. N. Fitch, *Phase coexistence in the charge ordering transition in $CaMn_7O_{12}$*, Journal of Physics: Condensed Matter **14**, 5747 (2002) (cited on page 134)

[266] Y. Akizuki, I. Yamada, K. Fujita, N. Nishiyama, T. Irifune, T. Yajima, H. Kageyama, K. Tanaka, *A-Site-Ordered Perovskite $MnCu_3V_4O_{12}$ with a 12-Coordinated Manganese(II)*, Inorganic Chemistry **52**, 11538 (2013) (cited on page 134)

[267] M.-R. Li, M. Retuerto, Z. Deng, T. Sarkar, J. Sánchez-Benítez, M. C. Croft, T. S. Dasgupta, T. Das, T. A. Tyson, D. Walker, M. Greenblatt, *Strong Electron Hybridization and Fermi-to-Non-Fermi Liquid Transition in $LaCu_3Ir_4O_{12}$*, Chemistry of Materials **27**, 211 (2015) (cited on page 134)

[268] A. L. Spek, *Single-crystal structure validation with the program PLATON*, Journal of Applied Crystallography **36**, 7 (2003) (cited on page 142)

[269] I. D. Brown, D. Altermatt, *Bond-valence parameters obtained from a systematic analysis of the Inorganic Crystal Structure Database*, Acta Crystallographica Section B: Structural Science, Crystal Engineering and Materials **41**, 244 (1985) (cited on page 158)

[270] X. Wang, F. Liebau, *Influence of polyhedron distortions on calculated bond-valence sums for cations with one lone electron pair*, Acta Crystallographica Section B: Structural Science, Crystal Engineering and Materials **63**, 216 (2007) (cited on page 160)

[271] M. Etter, R. Dinnebier, *Preliminary title: Visual simulation of variable dependent crystal structures in TOPAS*, in preparation (cited on page 161)

[272] *Compute Neutron Attenuation and Activation*, http://www.ncnr.nist.gov/instruments/bt1/neutron.html (2015) (cited on pages 180, 182 and 260)

[273] R. C. Buchanan, T. Park, *Materials Crystal Chemistry*, Marcel Dekker Inc. (1997) (cited on pages 181 and 260)

[274] M. E. Wieser, T. B. Coplen, *Atomic weights of the elements 2009 (IUPAC Technical Report)*, Pure Applied Chemistry **83**, 359 (2011) (cited on pages 181 and 260)

[275] T. Hahn (ed.), *International Tables For Crystallography - Volume A: Space-Group Symmetry*, International Tables For Crystallography **A**, International Union of Crystallography D. Reidel Publishing Company (1983) (cited on pages 206, 207 and 261)

[276] P. J. Mohr, B. N. Taylor, D. B. Newell, *CODATA Recommended Values of the Fundamental Physical Constants: 2010*, arXiv , (2012) (cited on pages 219 and 261)

List of Figures

List of Tables

Publications

During the course of this PhD thesis, the following publications were made:

Journal Publications

1. *Martin Etter and Robert E. Dinnebier*
   Direct parameterization of the volume on pressure dependence by using an inverted approximative Vinet equation of state
   Journal of Applied Crystallography (J. Appl. Cryst.) 47 (2014), Part 1, pages 384-390, DOI: 10.1107/S1600576713032287

2. *Martin Etter, Melanie Müller, Michael Hanfland and Robert E. Dinnebier*
   High pressure phase transitions in the rare-earth orthoferrite $LaFeO_3$
   Acta Crystallographica B (Acta Crystallogr. B) 70 (2014), Part 3, pages 452-458, DOI: 10.1107/S2052520614007379

3. *Martin Etter, Melanie Müller, Michael Hanfland and Robert E. Dinnebier*
   Possibilities and limitations of parametric Rietveld refinement on high pressure data: The case study of $LaFeO_3$
   Zeitschrift für Kristallographie (Z. Kristallogr.) 229 (2014), Issue 3, pages 246-258, DOI: 10.1515/zkri-2013-1668

4. *Martin Etter, Melanie Müller and Robert E. Dinnebier*
   Rotational rigid body symmetry modes: A tool for the investigation of phase transitions
   Zeitschrift für anorganische und allgemeine Chemie (Z. anorg. allg. Chem.) 640 (2014), Issue 15, pages 3079-3087, DOI: 10.1002/zaac.201400324

5. *Martin Etter and Robert E. Dinnebier*
   A Century of Powder Diffraction: a Brief History
   Zeitschrift für anorganische und allgemeine Chemie (Z. anorg. allg. Chem.) 640 (2014), Issue 15, pages 3015-3028, DOI: 10.1002/zaac.201400526

6. *Martin Etter, Asifa Nigar, Naveed Zafar Ali, Zareen Akhter and Robert E. Dinnebier*

Synthesis and structural perspective on new ferrocenyl amide
submitted to Solid State Sciences (Solid State Sci.)

7. *Martin Etter, Maximilian J. Krautloher, Nakheon Sung, Joel Bertinshaw, Bumjoon Kim and Robert E. Dinnebier*
Crystal structure determination of non-stoichiometric $Ca_{4-x}RuO_{6-x}$ (x = 1.17) from X-ray powder diffraction data
Accepted in Powder Diffraction (Powder Diffr.)

Talks

1. *Martin Etter, Anja Wedig, Dominik Samuelis, Rotraut Merkle, Joachim Maier, Anatoliy Senyshyn and Robert E. Dinnebier*
Magnetic structure determination of $BiFeO_3$ from neutron powder diffraction
Joint Workshop on Materials Chemistry, September 25th, 2012, Stuttgart

2. *Martin Etter*
Magnetic and structure determination of $BiFeO_3$ from neutron powder diffraction with TOPAS v5
DMG Doktorandenkurs: "Grundlagen und Anwendung der Rietveld Verfeinerung", March 4-7, 2013, Stuttgart

3. *Martin Etter, Melanie Müller, Michael Hanfland and Robert E. Dinnebier*
Analyzing high pressure diffraction data of perovskites with parametric Rietveld refinement and rotational symmetry modes of a rigid body
Spring Meeting of the German Physical Society (DPG), Section "Condensed Matter" (SKM), March 30 - April 4, 2014, Dresden

4. *Martin Etter, Melanie Müller and Robert E. Dinnebier*
Analyzing in-situ powder diffraction data of minerals and inorganic compounds with symmetry mode approaches
92nd Annual Meeting Deutsche Mineralogische Gesellschaft (DMG), September 21 - 24, 2014, Jena

5. *Martin Etter, Melanie Müller and Robert E. Dinnebier*
Alternative descriptions of crystal structures
Summer School: Theory and Practice of Modern Powder Diffraction, October 5 - 8, 2014, Ellwangen

6. *Martin Etter*
Methods for Analyzing in situ powder diffraction data: sequential and parametric Rietveld refinement

DMG/DGK Doktorandenkurs: “Grundlagen und Anwendung der Rietveld Verfeinerung”, March 9-12, 2015, Stuttgart

7. *Martin Etter, Masahiko Isobe, Hiroya Sakurai, Robert E. Dinnebier und Hidenori Takagi*
A new monoclinic crystal structure type for A-site ordered quadruple perovskites
23rd Annual Meeting of the German Crystallographic Society, March 16 - 19, 2015, Göttingen

Posters

1. *Martin Etter, Anja Wedig, Dominik Samuelis, Anatoliy Senyshyn, Joachim Maier and Robert E. Dinnebier*
Oxygen Content in $SrFeO_3$ obtained from Neutron and X-ray Powder Diffraction modeled by Distribution Functions
21st Annual Conference of the German Crystallographic Society (DGK), March 19-22, 2013, Freiberg (Sachsen)

2. *Martin Etter, Melanie Müller, Michael Hanfland and Robert E. Dinnebier*
Using an innovative Vinet EoS approximation for parametric refinement of high pressure powder diffraction data
Workshop of the IUCr Commission on High Pressure: “Advance in Static and Dynamic High-Pressure Crystallography”, September 8-11, 2013, Hamburg (DESY)

3. *Martin Etter and Robert E. Dinnebier*
Parametric Rietveld refinements combined with the new approach of rotational rigid body symmetry modes: Investigation of high pressure powder diffraction data
22st Annual Conference of the German Crystallographic Society (DGK), March 17-20, 2014, Berlin

4. *Martin Etter, Melanie Müller, Michael Hanfland and Robert E. Dinnebier*
Analyzing high pressure diffraction data of perovskites with parametric Rietveld refinement and rotational symmetry modes of a rigid body
Spring Meeting of the German Physical Society (DPG), Section “Condensed Matter” (SKM), March 30 - April 4, 2014, Dresden

5. *Martin Etter and Robert E. Dinnebier*
Using an innovative Vinet EoS approximation for parametric refinement of high pressure powder diffraction data
Spring Meeting of the German Physical Society (DPG), Section “Condensed Matter” (SKM), March 30 - April 4, 2014, Dresden

Further Contributions

1. *Robert E. Dinnebier und Martin Etter*
   100 Jahre nach Max von Laue - Phasenübergänge und parametrisierte Symmetriemoden: Innovative Methoden in der Kristallographie
   Jahrbuch 2013 der Max-Planck Gesellschaft, http://www.mpg.de/6793735/MPI-FKF_JB_20131?c=7291695 or http://www.fkf.mpg.de/590603/research_report_6793735?c=164385

2. *Martin Etter, Masahiko Isobe, Hiroya Sakurai, Robert E. Dinnebier und Hidenori Takagi*
   Electronic ordering in perovskites and the effects on the symmetry of crystal structures
   Jahrbuch 2014 des Max-Planck Instituts für Festkörperforschung, http://www.fkf.mpg.de/5247193/I_04_Dinnebier

Acknowledgement

Last but not least I would like to thank and to appreciate all the people, which made this work and my PhD directly or indirectly possible. My special thanks go to...

- Prof. Dr. Robert E. Dinnebier for giving me the opportunity to work in his group. Personally I think his training in being a crystallographer was excellent and the time in his group will be one of the most enjoyable in my life.
- Prof. Dr. Bernhard Keimer for the acceptance of being the main reporter of my PhD thesis.
- Prof. Dr. Peter Michler for being the co-reporter of my PhD thesis.
- Prof. Dr. Hans Peter Büchler for being the head of my examination committee.
- Prof. Dr. Martin Jansen for the hosting in his department (first half) and for the fruitful discussions as well as for all the collaborations.
- Prof. Dr. Hidenori Takagi for the hosting in his department (second half) and the possibility to collaborate with him and his scientists in the $BiCu_3Cr_4O_{12}$ quadruple perovskite project.
- Dr. Reinhard Kremer for being the external advisor of my PhD committee. I would like to thank him also for the support and the discussions about magnetic structures and for lots of further fruitful discussion.
- Frank Adams for all the technical help during most of my experiments and for the nice collegial atmosphere.
- Christine Stefani for filling a lot of capillaries and for measurements and for the nice collegial atmosphere.
- Dr. Melanie Müller for all the collaborations with successful publications and all the discussions. Especially I would like to thank her for the jointly mineralogical excursions and for the nice collegial atmosphere.
- Dr. Tomce Runcevski for all the discussions and the collaborations. Special thanks to him for his explanations how to solve organic crystal structures and for the nice collegial atmosphere.

- Dr. Oxana Magdysyuk for all the discussions and the collaborations as well as for the collegial atmosphere
- Dr. Liana Vella-Zarb for all the discussions and for the nice collegial atmosphere.
- All the colleagues of the Jansen and Takagi department. Especially to the secretary Mrs. Sabine Paulsen and to Dr. Ulrich Wedig, Dr. Jürgen Nuss, Prof. Dr. Christian Schön, Dr. Thomas Bräuniger, Sabine Prill-Diemer, Claus Mühle, Kersten Schunke who helped me with all the scientific or bureaucratic questions and of course to all other people of the departments which I forgot to mention.
- Prof. Dr. Peter Michler for the opportunity to work as a tutor on his Bachelor and Master course of molecule and solid state physics.
- Prof. Dr. Joachim Maier, Dr. Dominik Samuelis, Dr. Rotraut Merkle, Dr. Anja Wedig and Nils Ohmer for the opportunity to collaborate with them on the $Bi_{1-x}Sr_xFeO_{3-\delta}$ project. Special thanks go to Dr. Anja Wedig for the synthesis and to Dr. Rotraut Merkle and Dr. Dominik Samuelis for fruitful discussions.
- Dr. Anatoliy Senyshyn for the great support during our two measurement times at the FRMII neutron reactor in Garching.
- Eva Brücher for carrying out the measurements of the magnetic susceptibility of the $Bi_{1-x}Sr_xFeO_{3-\delta}$ compounds.
- Ewald Schmitt for carrying out the DSC measurements of the $Bi_{1-x}Sr_xFeO_{3-\delta}$ compounds.
- Dr. Masahiko Isobe for giving me to opportunity to collaborate with him on the $BiCu_3Cr_4O_{12}$ quadruple perovskite project.
- Dr. Hiroya Sakurai for the synthesis of the $BiCu_3Cr_4O_{12}$ quadruple perovskite.
- Dr. Yoshiro Nohara and Dr. Alexander Yaresko for carrying out the DFT calculations of the $BiCu_3Cr_4O_{12}$ quadruple perovskite.
- Dr. Naveed Zafar Ali for providing me the opportunity to test my skills on the structure solution of organic crystal structures and for the nice collaboration.
- Dr. Alexandra Gibbs and Joanne Quiggin for proof reading of my publications.
- The staff of the library of the Max Planck institutes in Stuttgart for providing me copies of lots of old publications. Without their help the extensive review of the history of powder diffraction would not have been possible.
- My family and closest friends who supported me a lot.
- Miriam who never gave up to handle her bear.

Erklärung über die Eigenständigkeit der Dissertation

Ich versichere, dass ich die vorliegende Arbeit mit dem Titel “Crystal and magnetic structures of multiferroics from powder diffraction data” selbständig verfasst und keine anderen als die angegebenen Quellen und Hilfsmittel benutzt habe; aus fremden Quellen entnommene Passagen und Gedanken sind als solche kenntlich gemacht.

Martin Etter Stuttgart, 24.06.2015

Declaration of Authorship

I hereby certify that the dissertation entitled "Crystal and magnetic structures of multiferroics from powder diffraction data" is entirely my own work except where otherwise indicated. Passages and ideas from other sources have been clearly indicated.

Martin Etter Stuttgart, 24.06.2015